Coupling Quantum Point Contacts via Ballistic Electron Optics

Im Fachbereich Physik
der Freien Universität Berlin
eingereichte

Dissertation

zur Erlangung des Grades eines
Doktors der Naturwissenschaften (Dr. rer. nat.)
vorgelegt von

Jaan Freudenfeld

Berlin, im Oktober 2020

1. Gutachter: PD Dr. Stefan Ludwig
2. Gutachter: Prof. Dr. Kirill Bolotin
Tag der Disputation: 12.02.2021

Selbstständigkeitserklärung

Hiermit versichere ich, dass ich alle verwendeten Hilfsmittel und Hilfen angegeben und die vorliegende Arbeit auf dieser Grundlage selbstständig verfasst habe. Diese Arbeit ist nicht schon einmal in einem früheren Promotionsverfahren eingereicht worden.

Berlin, 15.10.2020

Jaan Freudenfeld

Kurzfassung

In der zukünftigen Elektronik werden Quanteneffekte in integrierten Schaltkreisen mit gekoppelten Nanostrukturen eine Schlüsselrolle spielen. In diesem Rahmen könnte die Kopplung zwischen entfernten On-Chip-Komponenten durch den Austausch von ballistischen Elektronen realisiert werden. Die vorliegende Dissertation zielt auf die Optimierung des Austauschs von ballistischen Elektronen zwischen Quantenpunktkontakten (QPCs) ab, fundamentalen Bausteinen von Quantenschaltkreisen. Um entfernte QPCs zu koppeln, wird das Konzept der ballistischen Elektronenoptik verwendet.

Im ersten experimentellen Teil dieser Dissertation wird zunächst die tatsächliche elektrostatische Potentialform eines einzelnen gatterdefinierten QPCs anhand seiner gemessenen, eindimensionalen Subbandabstände bestimmt. Die Potentialform ist zentral für den Emissionsprozess ballistischer Elektronen sowie für Wechselwirkungseffekte. Nach Vergleich der gemessenen Subbandabstände des QPCs mit dem lateral Parabolischen- bzw. Hard-Wall-Einschlusspotential-Modell stellt sich heraus, dass dieser vor dem Abschnüren mit dem parabolischen Sattelpunkt-Szenario kompatibel ist. Sobald jedoch mehrere Subbänder bevölkert werden, bewirkt Coulomb-Abschirmung ein Abflachen des Potentialbodens. Hier ist eine Beschreibung durch das Hard-Wall-Potential realistischer.

Im zweiten Experiment wird der Transport ballistischer und lateral kohärenter Elektronen durch zwei entfernte QPCs in Serie betrachtet. Die Emissions- und Detektionseigenschaften der QPCs werden im Detail durch Ablenkung ballistischer Elektronen in einem senkrechten Magnetfeld untersucht. Zusätzlich wird die Serientransmission durch eine Feldeffekt-Linse für Elektronen verstärkt. Anhand des Vergleichs der Messungen mit quantenmechanischen sowie klassischen Rechnungen werden generische Eigenschaften des Quantenschaltkreises diskutiert. Es wird gezeigt, wie die kohärente und ballistische Dynamik von den Details des QPC-Einschlusspotentials abhängt.

In einem dritten Experiment wird eine offene, ballistische elektronische Kavität untersucht, welche durch vier QPCs realisiert wird. Mithilfe von Bias-Voltage-Spektroskopie werden kohärente, Fabry-Pérot-artige Resonanzen charakterisiert. Darüber hinaus liefern Magnetotransportmessungen Hinweise auf einen Übergang von chaotischer zu integrabler Dynamik in der Kavität, sobald diese verkleinert wird.

Schließlich wird eine parabolische, offene und ballistische Kavität untersucht. Bei erhöhter elektronischer Temperatur, bei welcher QPCs besser als klassische Blendenöffnungen ohne kohärente Modenstruktur beschrieben werden, wird gezeigt, wie die Serientransmission durch zwei Blenden über die Kavität erhöht werden kann.

Abstract

In future electronics, quantum effects in integrated circuits containing coupled nanostructures will play a key role. In this framework, the coupling between distant on-chip components could be realized by the exchange of ballistic electrons. The present thesis aims at optimizing the exchange of ballistic electrons between quantum point contacts (QPCs), fundamental building blocks of quantum circuits. To couple distant QPCs, we use the concept of ballistic electron optics.

In the first experimental part of this thesis, we study the actual electrostatic potential shape of a gate-defined single QPC by measuring its one-dimensional subband spacings. The potential shape is central for the emission process of ballistic electrons as well as interaction effects. Comparing the measured subband spacings of the QPC to models of lateral parabolic versus hard-wall confinement, we find that it is compatible with the parabolic saddle-point scenario near pinch-off. However, as we increase the number of populated subbands, Coulomb screening flattens the potential bottom and a description in terms of a hard-wall potential becomes more realistic.

In the second experiment, we consider the ballistic and laterally coherent electron transport through two distant QPCs in series in a three terminal configuration. We study the emission and detection properties of the QPCs in detail via magnetic deflection of ballistic electrons in a perpendicular magnetic field. Additionally, we enhance the serial transmission by using a field effect electron lens. Comparing our measurements with quantum mechanical and classical calculations we discuss generic features of the quantum circuit and demonstrate how the coherent and ballistic dynamics depend on the details of the QPC confinement potentials.

In a third experiment, we consider an open ballistic electronic cavity formed by four QPCs. Performing bias voltage spectroscopy measurements, we characterize coherent Fabry-Pérot-like resonances. Furthermore, we find fingerprints of a transition from chaotic to integrable cavity dynamics in magnetotransport measurements, as we decrease the size of the cavity.

Finally, in a fourth experiment, we investigate a parabolic, open and ballistic electronic cavity. Working at a higher temperature, where the QPCs are better described as classical pinholes without coherent mode structure, we demonstrate how the serial transmission through the two pinholes can be enhanced by the cavity.

Contents

Introduction and overview

Since more than 50 years, the miniaturization of components in integrated circuits used in information technology has been the driving force for increasing computational power. However, as today's transistors are approaching the size of atoms, conventional electronics is facing a fundamental limit. In future electronics, quantum effects in integrated circuits containing coupled nanostructures will be play a key role. The coupling of distant on-chip components could then be realized by the exchange of ballistic electrons.

Our work aims at optimizing the exchange of ballistic electrons between quantum point contacts (QPCs), fundamental building blocks of quantum circuits. These short, tunable one-dimensional (1D) constrictions in a two-dimensional electron system (2DES) display a rich spectrum of physics. In 1988, the observation of 1D conductance quantization [1–3] was the starting shot for a vast spectrum of research. This includes shot noise measurements [4], scanning gate spectroscopy [5, 6], thermoelectric studies [7], phototransport [8], magnetotransport out of equilibrium [9, 10], quantum transport through freely suspended devices [11] or many-body interaction effects such as the 0.7-anomaly [12–14]. Single QPCs are used as charge detectors [15] or to split quantum-Hall edge channels [16, 17]. Serial QPCs and their ballistic dynamics have been investigated within magnetic deflection experiments [9, 10, 18], spin-orbit coupling [19, 20], defect scattering [21], diffraction at a QPC [22] or in terms of non-Ohmic resistance [23–27] .

We first study the actual potential shape of a gate-defined QPC before we investigate the transport of ballistic electrons in three different sample geometries containing distant QPCs. The quantum circuits are based on the concept of ballistic electron optics [28–32]. We are interested in maximizing the transmission efficiency of ballistic electrons through serial QPCs via a region of free, grounded 2DES. For possible applications in devices, the QPCs could in principle be replaced by quantum dots hosting spin- or charge qubits, entangled by the exchange of ballistic and coherent electrons. However, the transmission efficiency strongly depends on the ballistic carrier emission and detection via the QPCs, as well as the local disorder potential in the 2DES. To enhance the coupling between distant QPCs, we control ballistic electrons on the mesoscopic scale using magnetic fields, electrostatic lenses and -mirrors.

While this thesis aims at obtaining a PhD title at the Freie Universität Berlin, the actual project was conducted at the facilities of the Paul-Drude-Institut for solid state electronics in Berlin.

The present thesis is organized as follows:

In **chapter 1**, we introduce the concept of a high mobility 2DES, the basis for our ballistic low temperature quantum transport experiments. We additionally describe the fabrication

process of our customized mesoscopic quantum circuits by optical- as well as electron beam lithography in detail.

In **chapter 2** we address the experimental setup by means of the ^{3}He cryostat, the dewar containing a superconducting magnet as well as the ensemble of the electrical wiring and all measurement devices.

In **chapter 3** we introduce the theoretical background for our experiments. Starting at the Drude model, we discuss scattering mechanisms in high mobility 2DES as well as the ballistic and coherent transport regime. After the introduction of the Landauer-Büttiker formalism including an example for its application within a real sample, we present the transfer and scattering matrix method. At the end of the chapter, we show an overview of our numerical quantum mechanical model used for simulations in the following chapters.

In **chapter 4** we characterize the potential shape of a gate-defined QPC by measuring its 1D subband spacings. We directly compare our experimental results to the lateral hard-wall and the parabolic confinement potential model. At the end of the chapter, we calculate the expected beam pattern by implementing the experimentally found subband spacings into our numerical model.

In **chapter 5**, we introduce the concept of ballistic electron optics, used to design the quantum circuits discussed in the following chapters.

In **chapter 6** we consider two serial QPCs spaced by a region of free (grounded) 2DES. We study the lateral current distribution between the QPCs in a magnetic deflection experiment. Additionally, we tune the serial transmission using an electrostatic electron lens. We compare our experimental results to coherent as well as classical model calculations.

In **chapter 7** we discuss an open ballistic cavity with four QPCs. We characterize the QPCs and their leads and translate the measured currents to transmissions and reflections within the Landauer-Büttiker formalism. By performing spectroscopy measurements as a function of the source-drain voltage and the size of the cavity, we characterize coherent, Fabry-Pérot-like cavity modes. Furthermore, we investigate the carrier dynamics, as we decrease the size of the cavity in magnetotransport experiments.

In **chapter 8** we present an open ballistic cavity formed by two parabolic mirrors which contain QPCs at their focal points. Operating at an elevated temperature of 6 K, where the QPCs are better described as classical pinholes without coherent mode structure, we demonstrate how the serial transmission through the two pinholes can be enhanced by tuning the cavity size.

Finally, in **chapter 9**, we summarize the results of the present thesis.

1 Two-dimensional electron system and sample fabrication

The sample fabrication process can be divided into (i) the growth of the wafer material providing a high quality two-dimensional electron system (2DES) and (ii) further processing of the wafer to engineer customized quantum circuits. Since the wafer material used here has been provided by other groups we skip the growth process via molecular beam epitaxy (MBE) [33] and focus on the processing of the wafer. First, we introduce the concept of the 2DES, the basis for all experiments presented in this thesis. We further present the electric field-effect approach used to control the electron carrier density of the 2DES by applying voltages to metallic nanostructures on the wafer surface. In the last section of the chapter we describe the relevant fabrication processes in detail.

1.1 Heterostructure containing a two-dimensional electron system

All experiments presented in this thesis were carried out using a GaAs/AlGaAs based high mobility wafer grown in the research group of V. Umansky (Weizmann Institute, Tel Aviv, Israel; wafer no. mbe8-309). The bare heterostructure is a single crystal consisting of various layers of semiconductor material, MBE-grown on a (100) GaAs substrate as illustrated in Fig. 1.1(a). While the thin GaAs layer forming the wafer surface only serves to prevent oxidation, the functional part of the heterostructure consists of a layer of AlGaAs grown on GaAs. The AlGaAs layer additionally contains a monolayer of Si dopants (δ-doping [34]).

We sketch the resulting conduction band scheme of the heterostructure with respect to the growth (z) direction in Fig. 1.1(b). At cryogenic temperatures, the dopants are partially ionized, supplying their electrons either to surface states or to the triangular quantum well with localized states formed at the lower AlGaAs/GaAs interface. By a proper combination of x, the doping density and the spacing, only the lowest subband of the well is occupied, confining electrons into a 2DES within a plane parallel to the wafer surface. The spatial separation of the doping layer from the 2DES increases the carrier density and mobility of the 2DES. The depth of the 2DES for the wafer used in this thesis is around 110 nm measured from the surface.

Due to almost identical lattice constants and identical crystal structures of GaAs and AlGaAs, the GaAs/AlGaAs interface exhibits an excellent quality with very low defect density, making it one of the best interfaces for bandgap engineering. The bandgap of

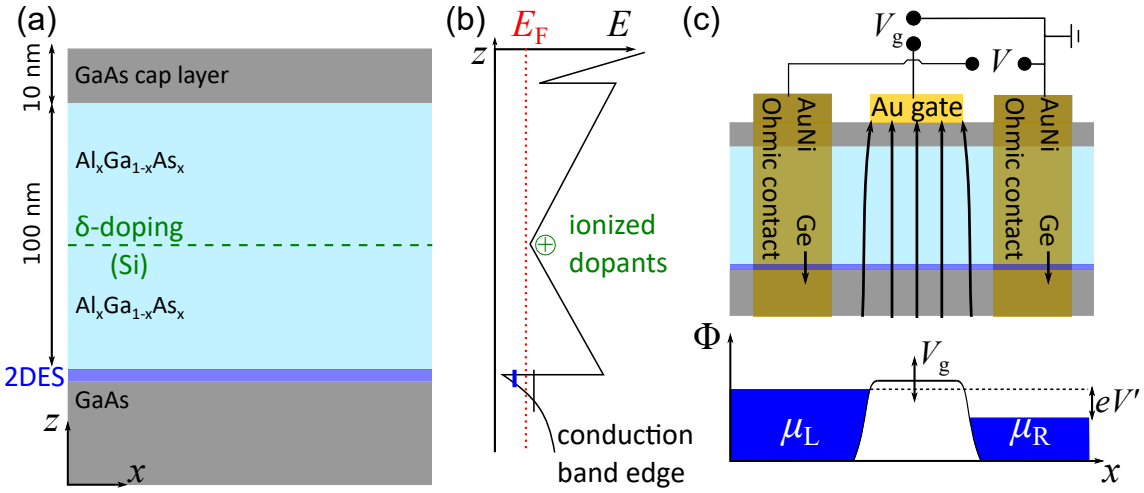

Figure 1.1: (a) Sketch of a typical δ-doped GaAs-AlGaAs based heterostructure hosting a 2DES. (b) Conduction band along the growth (z) direction. Red dotted line: Fermi level. At low temperatures, only the ground state (blue line) of the triangular well at the lower GaAs/AlGaAs interface is occupied as excited states (black line) are above the Fermi level. (c) Top sketch: of a processed heterostructure cross section; the 2DES is electrically contacted after annealing AuGeNi contacts into the wafer surface by diffused Ohmic contacts (see main text). A metal gate on the sample is used to locally tune the 2DES carrier density by applying a gate voltage V_g. Lower sketch: energy scheme for two contacts at chemical potentials $\mu_{L/R}$ with $\mu_L - \mu_R = eV'$ separated by a barrier controlled by the gate voltage V_g.

$Al_xGa_{1-x}As$ can be tuned between that of pure AlAs (2.16 eV at room temperature) to that of pure GaAs (1.42 eV) by varying the fraction x in the alloy between $0 \leq x \leq 1$ [35]. Typically, growers use $0.2 \leq x \leq 0.4$.

1.1.1 Field-effect structures

To electrically contact the 2DES for our transport experiments we use AuGeNi contacts deposited locally, cf. Fig. 1.1(c). By annealing the sample, in particular the Germanium atoms diffuse into the wafer to electrically contact the 2DES buried below the surface. In contrast, the gold atoms remain mostly on the surface and can be wire-bonded to establish the electrical connections to measurement devices. Our contacts are optimized to show an Ohmic (linear) I/V behavior even at low temperatures.

Applying a gate voltage V_g to a metallic structure deposited on the sample surface permits to locally change the carrier density of the 2DES below via the electric field-effect, cf. Fig. 1.1(c). For $V_g < 0$, we realize potential barriers within the 2DES resembling the shape of the gate. While we control the barrier height by adjusting V_g, we tune the chemical potentials on both sides of the leads by applying a finite bias voltage $\widetilde{V} = (\mu_L - \mu_R)/e$ between different Ohmic contacts. Designing nanoscaled field effect structures enables to further constrain the motion of electrons from two dimensions to one (e.g. in nanowires and

quantum point contacts) or even to zero (in quantum dots). Local electrostatic potentials can alternatively be created by other techniques like etching or strain in piezoelectric semiconductors. However, a key advantage of field effect structures consists in their wide range tunability of the local carrier density. This makes metal gates in particular useful components of integrated quantum circuits.

For a basic characterization of the wafer material used for all experiments in this thesis, we in the following present quantum Hall [36] measurements in a perpendicular magnetic field B. In Fig. 1.2(a), we present a top view of a sample containing a 2DES 110 below the

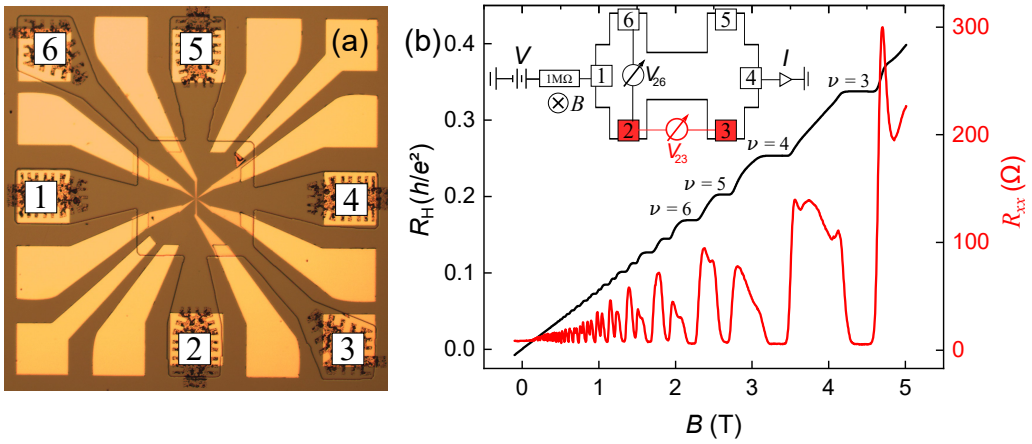

Figure 1.2: (a) Top view of the sample with numbered Ohmic contacts. We ground all gates for the quantum Hall measurement shown in (b). (b) Inset: measurement setup with the Ohmic contacts shown in (a) indicated by the same number. Black solid line, left axis: Hall resistance $R_{\mathrm{H}} = V_{26}/I$ and red solid line, right axis: longitudinal resistance $R_{\mathrm{xx}} = V_{23}/I$, as a function of the perpendicular magnetic field B.

surface with six numbered Ohmic contacts that are arranged in a Hall bar-like geometry. We sketch the setup used for the quantum Hall measurement with the Ohmic contacts from panel (a) indicated by the same numbers respectively in Fig. 1.2(b). For this measurement, we keep all gates grounded as we are interested in characterizing the bulk 2DES, without additional electrostatic potentials due to gate voltages. After cooling the sample down to 280 mK, we apply a source-drain voltage $V = -0.4\,\mathrm{V}$ at a 1MΩ resistor in series with the Hall bar. It causes an approximately constant current of $I \simeq 400\,\mathrm{nA}$ flowing from contact 1 into the grounded contact 4, as sketched in the inset. For better accuracy we also measure the current using a current-voltage converting amplifier. From the measured voltage between the contacts 2 and 6 perpendicular to the current flow, $V_{26}(B)$, we obtain the Hall resistance $R_{\mathrm{H}} = V_{26}/I$ plotted as black solid line. From the measured voltage between the contacts 2 and 3 in current direction, $V_{23}(B)$, we obtain the longitudinal resistance $R_{\mathrm{xx}} = V_{23}/I$ (red solid line). For magnetic fields $|B| \gtrsim 1\,\mathrm{T}$, the Hall resistance shows pronounced plateaus at $R_{\mathrm{H}} = h/(e^2\nu)$, where h is the Planck constant, e is the elementary charge and $\nu = 1,2,3,...$ is the filling factor. The longitudinal resistance shows Shubnikov-de Haas oscillations [37] with maxima occurring between the Hall plateaus, while R_{xx} drops to $R_{\mathrm{xx}} \simeq 3\,\Omega$ at the plateaus of R_{H}. We attribute the finite longitudinal

resistance (the finite voltage drop after subtracting the internal offset voltage of the voltage amplifier) to a second, weakly conducting layer parallel to the 2DES, located in the plane of the donor atoms [38,39]. From the slope of the Hall resistance at low fields, $\mathrm{d}R_\mathrm{H}/\mathrm{d}B$, or the period of the Shubnikov-de Haas oscillations in $1/B$, $\Delta(1/B)$, we calculate the carrier density of the 2DES,

$$n_s = \left(-e\frac{\mathrm{d}R_\mathrm{H}}{\mathrm{d}B}\right)^{-1} = \frac{2e}{h\Delta(1/B)}. \tag{1.1}$$

From both methods, we find $n_s = 3.1 \times 10^{11}\,\mathrm{cm}^{-2}$, corresponding to a Fermi energy of the free (*i.e.* without additional potentials) 2DES $E_\mathrm{F}^0 = \pi\hbar^2 n_s/m^\star = 11\,\mathrm{meV}$, where $m^\star = 0.067m_0$ is the effective electron mass in GaAs at low temperatures with the free electron mass m_0 and $\hbar = h/2\pi$ is the reduced Planck constant. This coincides with the specifications given by the grower. Using the van der Pauw method [40], we can calculate the mobility from the measured $R_\mathrm{xx}(B = 0)$,

$$\mu = -\frac{\pi}{en_s \ln(2) R_\mathrm{xx}}. \tag{1.2}$$

After structuring the sample shown in Fig. 1.2(a), we find $\mu = 2.27 \times 10^6\,\mathrm{cm}^2/(\mathrm{Vs})$. As the fabrication process induces defects in the crystal, this mobility is smaller than nominal mobility of the bare wafer material (before the fabrication of gated structures) indicated by the grower, $\mu = 6.1 \times 10^6\,\mathrm{cm}^2/(\mathrm{Vs})$.

The high electron mobility and large carrier density in this high quality 2DES are essential for ballistic transport experiments. We show the detailed growth protocol of the wafer material in the appendix, section A.1.

1.2 Optical lithography

In the following we introduce the structures processed on the wafer surface and describe the underlying fabrication process in detail. We carried out the processing in clean room facilities at the Kotthaus chair of the LMU of Munich and at the Paul-Drude-Institute in Berlin.

1.2.1 Overview of optically fabricated structures

The optical lithography process aims at the fabrication of the following structures [illustrated in Fig. 1.3(a)] in chronological order:

Mesa

We begin by etching specific areas of the sample down to the level of the 2DES ($\simeq 110\,\mathrm{nm}$). This way we destroy the 2DES in these areas and thereby define a cohesive conducting area of the sample - the so called mesa [spanish for table, blue area in Fig. 1.3(a)].

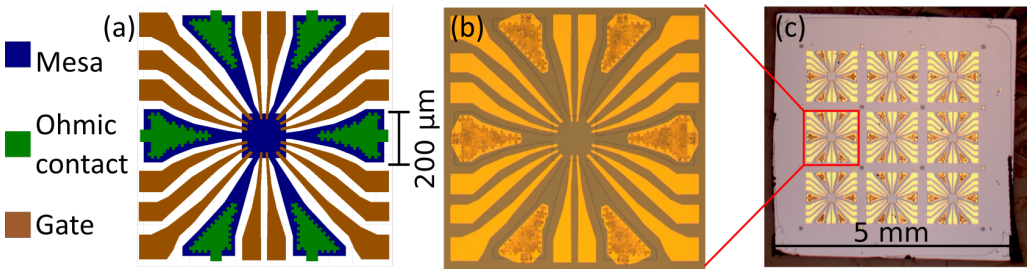

Figure 1.3: (a) Sample layout with components fabricated by optical lithography: mesa (blue), Ohmic contacts (green) and Au/Ti gates (brown). (b) Optical microscope image of a processed structure, after annealing of the Ohmic contacts. (c) Photograph of a 5x5 µm chip containing 9 sample fields after the optical lithography process.

Ohmic contacts

To electrically contact the 2DES embedded below the sample surface, we first evaporate a layer of 60 nm Au_xGe_{1-x} followed by 10 nm Ni and finally 60 nm Au_xGe_{1-x} (where $x = 0.88$) on the peripheral parts of the mesa. Using an annealing oven with a programmable heating and cooling sequence, we anneal the contacts into the wafer down to the plane of the 2DES. For the wafer used in our experiments, we applied a maximum annealing temperature of 480° C for 50 s in a constant flow of nitrogen (flushing mode) at 300 mbar. We add a detailed listing of the sequence containing all temperatures, hold times and ramping rates in the appendix, section A.2. We show the annealed contacts covered by additionally evaporated bond pads in the optical microscope image in Fig. 1.3(b).

The contacts have a meander-like structure [cf. green areas in Fig. 1.3(a)] to maximize the length between the metallic germanium contact and the 2DES embedded in the semiconductor. This reduces the contact resistance between the two materials. A small overlap of the contacts beyond the edge of the mesa makes sure that the chiral edge channels forming at the plateaus in the quantum Hall regime at specific values of the perpendicular magnetic field do not result in an electrical isolation of the Ohmic contacts.

Gates

In the last step of the optical lithography, we define the local gate structures by evaporating a 10 nm titanium adhesion layer, followed by 90 nm of gold, cf. brown areas in Fig. 1.3(a) and corresponding regions in the optical microscope image in panel (b). They feature wide bond pads on the periphery of the structures but taper towards to the center of the mesa where they serve as connections to nanosized gates to be fabricated within the subsequent electron beam lithography process.

To make optimal use of the precious wafer material, we fabricate 9 nominally identical structures on each wafer piece during the optical lithography process. In Fig. 1.3(c) we show an optical microscope image of a processed wafer piece after the optical lithography.

1.2.2 The fabrication process

In the following, we describe the fabrication process of the structures introduced above in more detail.

We begin by cleaving a small (typically 5 mm ×5 mm) rectangle from the larger wafer piece. This is done with high precision under an optical microscope by carefully scratching the wafer along a cleaving axis using a sharp diamond tip. We then flip the wafer and position it on a sterile clean room tissue on a flat surface. By carefully applying local pressure at the scratch (e.g. using the dull backside of tweezers) we break the crystal along the cleaving axis starting at the scratch. In the following, we process the cleaved wafer piece in the optical lithography process illustrated in Fig. 1.4. The detailed process parameters are listed in the appendix, section A.2.

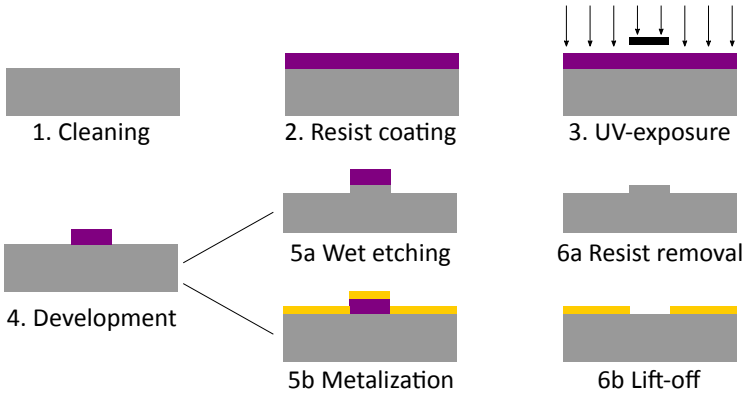

Figure 1.4: Typical sequence of an etch- or metallization process based on UV-light exposure using positive photo resist. The GaAs wafer surface is sketched in gray, photo resist in purple and metal in gold.

First, we carefully clean the sample surface using acetone or a commercial wafer cleaner followed by isopropanol. Small particles originating from the cleaving procedure and other contaminations on the surface might be removed by carefully wiping it with a smooth foam tip while keeping the sample inside the solvent. During the entire lithography process, we take great care not to scratch the surface, as this would likely destroy the 2DES along the scratch. We additionally avoid the usage of ultrasonic baths as these can induce defects in the crystal lattice, affecting the quality of the 2DES.

After cleaning the wafer surface, we spin-coat it with photo resist (photo-reactive long polymer chains) to form a homogeneous layer of specified thickness. To stabilize the photo resist we subsequently put the sample on a hot plate for the so-called pre-bake. Using a patterned photo mask and a mask aligner device, areas mimicking the customized design of the photo mask are in the following exposed to ultra violet (UV) light. After the exposure, we put the sample again on a hot plate for the post-bake. During the following development process the resist is removed from the wafer where it had previously been exposed to UV light for positive resist. For negative resist, areas not exposed by UV light

are removed. The remaining areas covered by photo resist are protecting the surface from the following etch process in diluted persulfuric acid. We stop the etching process in water and remove the remaining photo-resist in acetone, followed by an isopropanol bath.

To define Ohmic contacts, bond pads and metal gates with feature sizes beyond $\approx 1\,\mu m$ we also use optical lithography. For every structure, we repeat the process described above of resist coating - pre-bake - UV-exposure - post-bake - development. However, instead of etching we metallize the processed sample surface using an evaporation machine. In the final lift-off step we remove all photo resist in an acetone bath. During this process, the metal film covering areas coated with resist is removed, while the metal evaporated on the surface remains.

1.3 Electron beam lithography

The resolution in the optical lithography process is limited to $\approx 1\,\mu m$ related to the wavelength of the UV-light used in the mask aligner due to diffraction at the photo mask close to the sample. To realize much smaller nanostructures we use electron beam lithography (EBL).

The EBL process is schematically similar to the optical lithography. However, instead of UV light, we expose the sample to a focused electron beam. We list the detailed processing parameters of the EBL process in the appendix, section A.2. Due to the much smaller wavelength of electrons (typically on the picometer scale) compared to the UV-light used for exposure within the optical lithography process (typically around 400 nm), a beam of accelerated electrons provides a much higher resolution. Instead of using photo resist, we here spin-coat the sample with polymethyl methacrylate (PMMA or plexiglass) [41], a polymer-based resist. Inside the EBL-device, the PMMA-coated sample is exposed to a focused electron beam in vacuum. PMMA behaves like positive resist for moderate exposure doses $\lesssim 400\,\mu C/cm^2$ while a high electron dose leads to cross-linking of the polymer chains [42] and the formation of a transparent, insulating plexiglass layer. In that limit, it acts as a negative resist.

For moderate exposure doses, the PMMA polymer chains are broken into smaller pieces. In a subsequent development step, the PMMA can be removed to reveal the surface for a later metallization. The pattern to be written by the beam can be programmed using a special software. The resolution of our EBL instrument, a Raith 150two, is $\approx 8\,nm$ [43]. However, in our case the specific development process of the PMMA limits the resolution to around 20 nm [41]. We write the nanostructure at the low acceleration voltage of 5 kV to minimize possible damage due to high energetic electrons which can create defects near the 2DES, decreasing the mobility and stability of the latter. This precaution is in particular reasonable for ballistic transport experiments requiring high mean free paths and a stable local electrostatic potential. Before the actual writing process, we align the EBL write field with respect to the structures defined during the previous optical lithography process. The nanostructure itself is written in the center of the mesa. We show an example in the close-up of a sample in Fig. 1.5. Every gate of the nanostructure [cf. Fig. 1.5(c)] is connected to one of the macroscopic gates such that the larger gates fabricated by optical

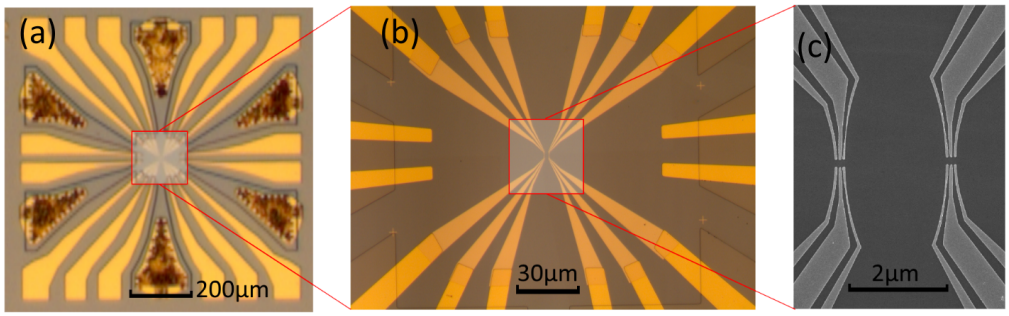

Figure 1.5: (a) Optical microscope image of the surface of a sample fabricated in one of the 9 fields on a 5 mm×5 mm chip, cf. Fig. 1.3. (b) Enlarged image of the center of the sample, showing the metal gates fabricated by EBL, each overlapping with a gate fabricated by optical lithography. (c) Scanning electron microscope (SEM) image of the central part of the nanostructure.

lithography serve as leads [cf. panels (b,c)]. For the metallization of the nanosized gates we use thinner layers (5 nm Ti + 35 nm Au) compared to the larger gates defined in the optical lithography process. A major challenge of the EBL process consists of finding the correct exposure dose for the sample. First, this becomes particularly difficult for very small structures of widths comparable to the height of the gate layer (≈ 40 nm) which can cause lift-off problems and surface roughness. Second, a fraction of the focused electron beam is (back)scattered by the PMMA resist and the semiconductor crystal, leading to finite exposure doses even in the proximity of the beam. This proximity effect has to be especially accounted for if different structures are written in close proximity to each other. In this case, the individual doses have to be carefully adjusted by performing systematic dose tests. For the nanosized gates fabricated within this project, typical exposure doses are $\rho \approx 50\,\mu\mathrm{C/cm^2}$.

After metal evaporation and lift-off we make use of the dielectric properties of PMMA and fabricate an insulating layer covering the nanostructure, cf. blue region in Fig. 1.6(a). To

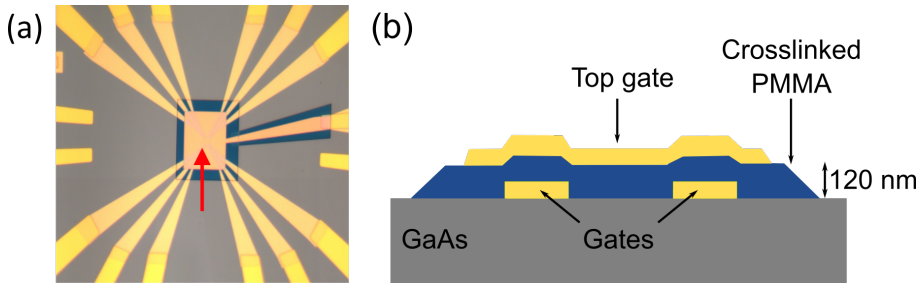

Figure 1.6: (a) Optical microscope image of a nanostructure covered by cross-linked PMMA (blue) and a global top gate isolated from the other gates by cross-linked PMMA. (b) Sketch of the cross section of the final structure on the GaAs surface including a PMMA layer between the gates deposited on the sample surface and the top gate.

form an insulating layer, we expose the PMMA-coated sample to a high dose of electrons, typically $\rho = 2400\,\mu C/cm^2$, which is 40-50 times higher compared to the dose used for writing the nanosized gates. The high dose leads to a cross-linking of polymer chains, creating a solid insulating layer in the exposed regions. The excessive, unexposed regions covered by PMMA can be removed by solvents. Besides providing mechanical and oxidation protection for the delicate center of the nanostructure, the insulating layer permits to fabricate a macroscopic top gate on top of the central nanostructure in Fig. 1.6(a). Such a global top gate is marked by a red arrow with the blue cross-linked PMMA layer below. We add a cross section of the final structure containing gates, cross-linked PMMA and the top gate in Fig. 1.6(b). Applying voltages to the top gate allows us to globally tune the carrier density in the covered regions, a key parameter to investigate disorder or interaction effects.

2 Cryostat, dewar and setup

Ballistic and coherent transport experiments in a 2DES require special efforts in terms of the measurement setup, which we introduce in this chapter. In the first section, we briefly describe the ^{3}He cryostat used for all experiments in this thesis. In the second section, we present the electrical setup used for the quantum transport experiments.

2.1 ^{3}He cryostat and dewar

Cryogenic temperatures are required to study ballistic and coherent effects in semiconductor nanostructures and to resolve the low energy scales of electron confinement in GaAs-AlGaAs based quantum point contacts (typically on the order of a few meV) or quantum dots ($\lesssim$ 1meV). For our experiments, we use a ^{3}He cryostat with a base temperature of $T \simeq 280\,\mathrm{mK}$, corresponding to thermal excitations of $k_\mathrm{B}T = 24\,\mu\mathrm{eV}$, where k_B is the Boltzmann constant. This temperature is sufficiently low for transport experiments with distant quantum point contacts. In Fig. 2.1(a), we show a mechanical drawing of the cryostat with labels indicating important components.

The cooling principle is based on evaporation cooling of liquid ^{3}He. In the following, we briefly explain the operation principle of the ^{3}He system. More detailed explanations can be found in Ref. [45]. During operation, the insert of the cryostat containing the sample is pumped and sealed at a pressure of $< 5 \times 10^{-4}\,\mathrm{mbar}$ in the inner vacuum chamber (IVC). We keep the cryostat in a dewar containing a liquid ^{4}He reservoir vacuum insulated from a shield filled with liquid nitrogen, cf. Fig. 2.1(b). Using an external rotary pump, we continuously pump liquid ^{4}He from the main bath of the dewar through thin capillaries into the 1 K pot of the cryostat. Here, we reduce the temperature of the liquid ^{4}He to around 1 K through the lower vapor pressure in the pumping line. The 1 K pot cools the ^{3}He gas reservoir stored in the cryostat below its boiling point of around 3.2 K. Now the ^{3}He gas condenses slowly into the ^{3}He pot at the lowest stage of the cryostat. The vapor pressure of the liquid ^{3}He is further reduced by an internal charcoal sorption pump, cooling the ^{3}He pot to its base temperature. The hold time of the condensate is several days and limited by the amount of ^{3}He gas as well as heat leaks. Once the liquid ^{3}He has evaporated, we heat the sorption pump to 40 K to restart the condensation process.

The dewar additionally contains a superconducting magnet able to create vertical magnetic fields of up to 8 T. We mount the sample horizontally on a sample holder located in the center of the magnetic field below the ^{3}He pot and cool the sample via a thermally treated ultra high purity 5N silver stick tightly clamped to the ^{3}He pot.

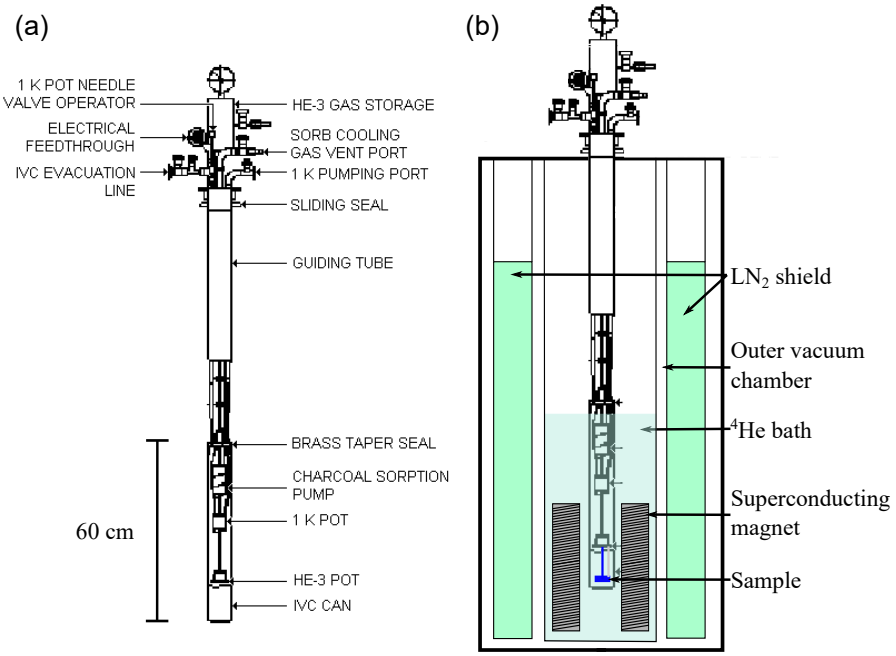

Figure 2.1: (a) Mechanical drawing of the Janis ^{3}He cryostat used for the experiments (copied from Ref. [44]). (b) Sketch of the cryostat inserted into the ^{4}He bath of the dewar insulated from the environment by a vacuum chamber and a nitrogen shield.

2.2 Electrical setup

We optimize the electrical wiring, filter components and measurement devices to achieve high stability of the voltages applied to the sample as well as high signal-to-noise ratios in the measured output signals. For the experiments presented in this thesis we used two different setups containing different measurement devices and wiring, which we introduce in the following.

2.2.1 Setup used for the experiments presented in chapters 6 and 8

For the measurements shown in 'Coherent electron optics with ballistically coupled quantum point contacts' (chapter 6) and 'Parabolic cavity' (chapter 8) we used the setup sketched in Fig. 2.2. We place the wire-bonded sample on a sample holder at the lowest temperature stage of the cryostat at $T = 250\,\mathrm{mK}$. We distinguish between current carrying leads (light blue) connected to Ohmic contacts of the sample and leads for voltages (magenta) applied to gates. Inside the cryostat, all used leads are twisted pair manganin wires. To minimize heating effects, the wires are thermally anchored at three low temperature stages of the cryostat: ^{3}He pot (250 mK), 1 K pot (1 K) and at the temperature of the ^{4}He bath (4.2 K).

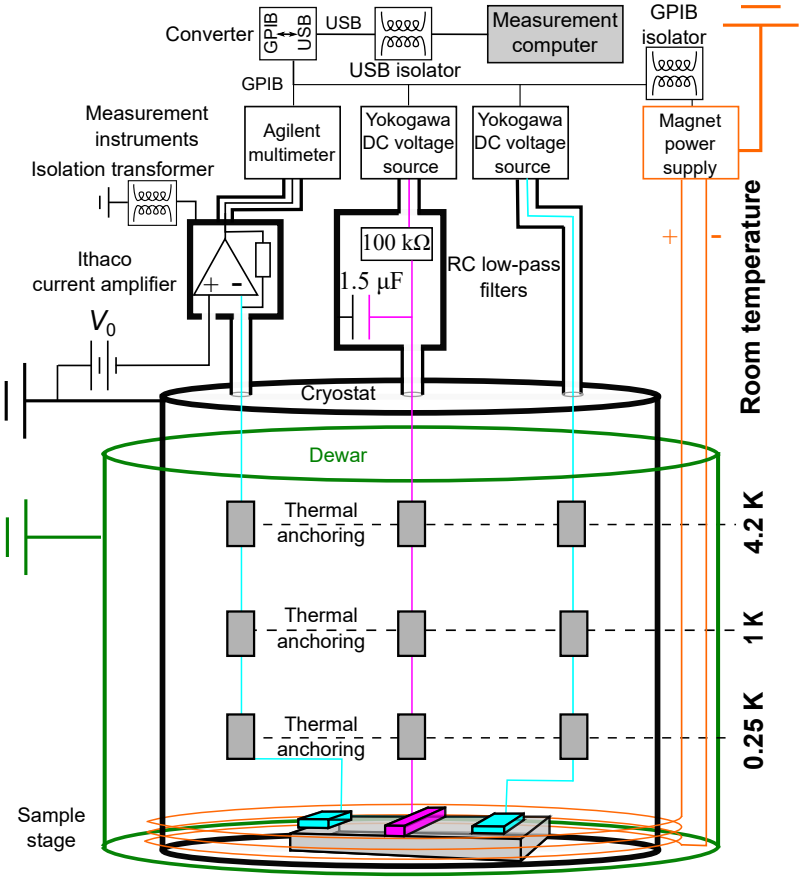

Figure 2.2: Sketch of the measurement setup used for the experiments presented in chapters 6 and 8 with the sample mounted in the cold cryostat kept in the dewar. The sample is electrically connected to RC low-pass filters and measurement devices at room temperature. Current carrying leads are light blue, leads connected to gates are magenta. The cryostat and the devices connected by thick black lines are kept on the measurement ground potential. We separately ground the dewar (green lines) and magnet power supply (orange lines), which are both electrically isolated from the cryostat.

At room temperature, double shielded coaxial Fischer- or BNC cables connect the wires of the cryostat to the different measurement instruments. We use programmable Yokogawa model 7651 DC voltage sources for the voltages applied to the gates. In the setup, the gates are protected by RC-filters at room temperature with a cutoff frequency $f_c \approx 1\,\mathrm{Hz}$. In contrast, the current carrying leads in this setup were not connected to room temperature RC low-pass filters. This was done to minimize the parasitic lead resistance for the ballistic transport experiments, at the cost of a lower signal to noise ratio. In table 2.1 and 2.2 we list the (approximate) individual cable lengths next to their resistances and capacitances to ground for both the current carrying- and the gate leads.

To measure currents in this setup, we connect one lead of the sample connected to an

Component	Cable length	Resistance	Capacitance to ground
BNC cable	0.4 m	$< 1\,\Omega$	40 pF
Fischer cable	1.5 m	$< 1\,\Omega$	150 pF
Manganin twisted pair wire	2 m	$50\,\Omega$	1 nF
Σ	3.9 m	$50\,\Omega$	1.19 nF

Table 2.1: Individual and total cable lengths, resistances and capacitances to ground of the current carrying leads for the setup sketched in Fig. 2.2.

Component	Cable length	Resistance	Capacitance to ground
BNC cable	1 m	$< 1\,\Omega$	100 pF
RC-Filter	-	$100\,\mathrm{k}\Omega$	1 µF
Fischer cable	1.5 m	$< 1\,\Omega$	150 pF
Manganin twisted pair wire	2 m	$50\,\Omega$	1 nF
Σ	4.5 m	$100\,\mathrm{k}\Omega$	1 µF

Table 2.2: Individual and total cable lengths, resistances and capacitances to ground of the leads carrying quasi-static voltages for the setup sketched in Fig. 2.2.

Ohmic contact of the sample to a DC voltage source. On a second lead connected to an Ithaco model 1211 current amplifier [46], we measure the dc current flowing through the sample. The input of the current amplifier generates a small offset voltage V_0 to the sample. For this model, the offset voltage can be adjusted down to a few µV by fine tuning a built-in potentiometer using a small screwdriver. A careful adjustment of the input voltage is essential before every measurement, since V_0 directly contributes to the (source-drain) voltage applied to the sample. Alternatively, V_0 can be determined by measuring the current through a known resistor, $V_0 = RI$. The current amplifier produces an output voltage proportional to the current which we measure in a downstream Keysight 34401A multimeter and read out with the measurement computer. We connect the individual leads of the gates to separate Yokogawa voltage sources which we likewise control via the measurement computer using a common GPIB interface.

To avoid ground loops, we use the cryostat connected to *one* common grounding point via a low resistive cable as the reference ground potential for our measurements. From here, all coaxial cable outer conductors, current amplifiers and measurement instruments obtain their ground potential (thick black lines in Fig. 2.2). To prevent ground loops with the supply line, we additionally decouple the current amplifier(s) from the supply ground using isolation transformers. Additionally, we add a galvanic USB isolator between the measurement instruments and the measurement computer as well as a GPIB isolator between the measurement instruments and the magnet power supply. To protect the delicate sample and the measurement devices from possible discharging events, we separately ground the dewar isolated from the cryostat (green lines). For the same reason, we use a third separate ground for the magnet power supply (orange lines). Other electrical components connected to the setup, such as vacuum pumps or pressure gauges have to be decoupled from the measurement ground by using plastic vacuum equipment close to the setup.

2.2.2 Setup used for the experiments presented in chapters 4 and 7

Within this project, we renewed the electrical wiring of the cryostat including all thermal anchorings from manganin twisted pair wires to single shielded 42 AWG micro coaxial cables. Both the inner and outer conductor of the coaxial cables are made of stainless steel, separated by a thin dielectric layer. Moreover, we purchased the current amplifier models SP 983-LSK389A [47] and SP 983-IF3602 [48] produced by Physics Basel and used them in the experiments presented in chapters 4 and 7. We show a sketch of the corresponding electrical setup in Fig. 2.3.

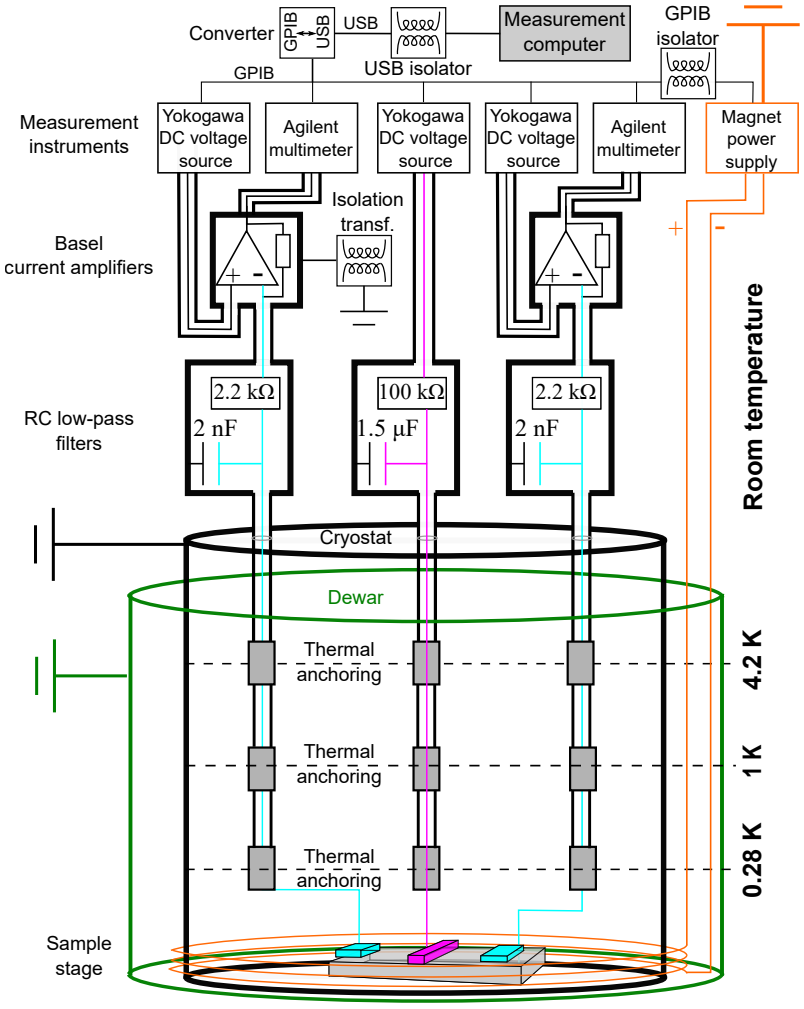

Figure 2.3: Sketch of the measurement setup used for chapters 4 and 7 with the sample mounted in the cryostat inserted in the cold dewar. Apart from the current amplifiers and the wiring (cf. main text), the setup is identical to the one shown in Fig. 2.2.

While the grounding scheme coincides with the one introduced in Fig. 2.2, the new wiring and the different current amplifiers have lead to the following changes:

The outer conductor of the coaxial cables is in direct contact with the cryostat at the thermal anchorings and thereby kept at the measurement ground potential, providing additional protection against external electromagnetic noise for the inner conductors carrying the voltages and currents. After the change of the wiring, the lowest ^{3}He-pot temperature reached in this cryostat in the Paul-Drude-Institute lab in Berlin increased from 270 mK to 280 mK. Additionally, the hold time of the condensate decreased from 4 days [49] to 3 days.[1] One possible explanation for the higher base temperature and shorter hold time is the additional heat leak generated by the outer conductor of the stainless steel coaxial cables.

Additionally, the Physics Basel current amplifier models SP 983-LSK389A and SP 983-IF3602 allow for a direct control of the offset voltage V_0 via a voltage source that can be connected to the input of the device, as sketched in Fig. 2.3. In this configuration, we can measure the current flow while controlling the voltage in one and the same lead, which is in particular useful for experiments with multi-terminal devices.

To optimize the signal to noise ratio for coherent measurements, we used RC low-pass filters at room temperature for both the gates and the current carrying lines, at the cost of a larger parasitic lead resistance in this setup. The cutoff frequency of the filter used for the current lines is $f_c \simeq 36\,\mathrm{kHz}$. In table 2.3 and 2.4 we list the (approximate) individual wire lengths next to their resistances and capacitances to ground for the current- and gate leads in this setup.

Component	Cable length	Resistance	Capacitance to ground
BNC cable	0.4 m	$< 1\,\Omega$	40 pF
RC-Filter	-	2.2 kΩ	2 nF
Fischer cable	1.5 m	$< 1\,\Omega$	150 pF
Micro coaxial cable	2 m	350 Ω	240 pF
Σ	3.9 m	2.55 kΩ	2.43 nF

Table 2.3: Individual and total cable lengths, resistances and capacitances to ground of the current carrying leads for the setup sketched in Fig. 2.3.

Component	Cable length	Resistance	Capacitance to ground
BNC cable	1 m	$< 1\,\Omega$	100 pF
RC-Filter	-	100 kΩ	1 µF
Fischer cable	1.5 m	$< 1\,\Omega$	150 pF
Micro coaxial cable	2 m	350 Ω	240 pF
Σ	4.5 m	100 kΩ	1 µF

Table 2.4: Individual and total cable lengths, resistances and capacitances to ground of the leads carrying voltages for the setup sketched in Fig. 2.3.

[1] In the LMU Munich lab, base temperatures of $T = 250\,\mathrm{mK}$ and hold times of up to 7 days were reached using the same cryostat with the inserts before the renewing of the wiring. The reason for the higher base temperature and shorter hold time with the same inserts in Berlin is unclear. We exclude the new arrangement of the pumping lines in the Berlin lab since the minimum temperatures reached at the 1 K pot and the sorption pump were identical compared to the Munich lab.

3 Theoretical background

This chapter contains the theoretical background of our experiments. We start with the Drude model [50] for diffusive electrical transport, which allows for the derivation of key parameters of our experiments, such as the electron mobility μ and mean free path l_{m}. We subsequently discuss scattering processes in high mobility heterostructures and introduce the ballistic transport regime. In this context, we introduce the realization of ballistic transport experiments on the basis of quantum point contacts and present the Landauer formula [51] describing the transmission through a ballistic conductor. In addition, we discuss the coherent transport regime and dephasing/decoherence mechanisms. Furthermore, we extend the transmission problem to ballistic and coherent multiterminal conductors within the Landauer-Büttiker formalism and introduce the transfer matrix method used to calculate the transmission through mesoscopic samples. We close the chapter with an overview of a numerical quantum mechanical model based on the transfer matrix method, used for simulations of the experiments shown in chapter 6.

3.1 Drude model

The Drude model [50] provides a microscopic description of carrier transport through a metal. Within this model, the conduction is described by free charge carriers that diffusively move through the 2DES. On the microscopic level, the electrical resistance occurs due to scattering processes between the charge carriers and the lattice. Without an external voltage, the diffusive motion of carriers is random in space and the net flux is zero. With an external electrical field $\vec{E}$, a steady state in which the momentum gain due to the external field matches the momentum loss due to scattering is reached:

$$-\Big(\frac{d\vec{p}}{dt}\Big)_{\text{scattering}} = \Big(\frac{d\vec{p}}{dt}\Big)_{\text{field}} \tag{3.1}$$

$$-\frac{m^\star \vec{v}_D}{\tau_m} = -q\vec{E}. \tag{3.2}$$

Here, $m^\star = 0.067 m_0$ denotes the effective mass of electrons in GaAs at low temperatures with the free electron mass m_0 and e the elementary charge with $q = -e$ for electrons and $q = e$ for holes. $\vec{v}_D$ is the average drift velocity of electrons (or holes) in the electric field and τ_m the mean scattering time between two subsequent elastic scattering processes causing randomization of the propagation direction. For electrons, $\vec{v}_D$ can be written as

$$\vec{v}_D = -\frac{e\tau_m}{m^\star}\vec{E} = -\mu\vec{E}, \tag{3.3}$$

with the mobility $\mu = e\tau_m/m^\star$ being the proportionality factor between drift velocity and external electrical field. For a given sheet carrier density n_s, the corresponding current density $\vec{j}$ is

$$\vec{j} = -e\vec{v}_D n_s = \sigma\vec{E}, \tag{3.4}$$

where $\sigma = e^2\tau_m n_s/m^\star$ denotes the conductivity. We can thus write the resistivity as

$$\rho = \sigma^{-1} = \frac{1}{en_s\mu} = \frac{m^\star}{n_s e\tau_m}, \tag{3.5}$$

stating that scattering events lead to limited mobilities and hence finite resistivities for a given carrier density.

3.2 Scattering in a 2DES

To realize low resistive, high mobility devices, scattering events between electrons and the lattice have to be minimized. In Fig. 3.1, we show the measured (dots) next to the calculated (lines) temperature dependence of the mobility of a modulation doped GaAs-AlGaAs heterostructure with a carrier density of $n_s = 3 \times 10^{11}\,\mathrm{cm}^{-2}$, found in Ref. [52]. This carrier density is very close to the carrier density in our experiments.

The main momentum scattering mechanisms for electrons in the 2DES are given by (i) electron-phonon scattering (ii) remote impurity scattering due to ionized dopants in the doping layer and (iii) scattering from background impurities in or close to the plane of the 2DES. Every scattering mechanism can be associated with a characteristic, temperature dependent elastic scattering timescale τ_i, and the total elastic scattering rate can be calculated from the sum of all scattering rates (Matthiessen's Rule),

$$\frac{1}{\tau_\mathrm{m}} = \sum_i \frac{1}{\tau_i}. \tag{3.6}$$

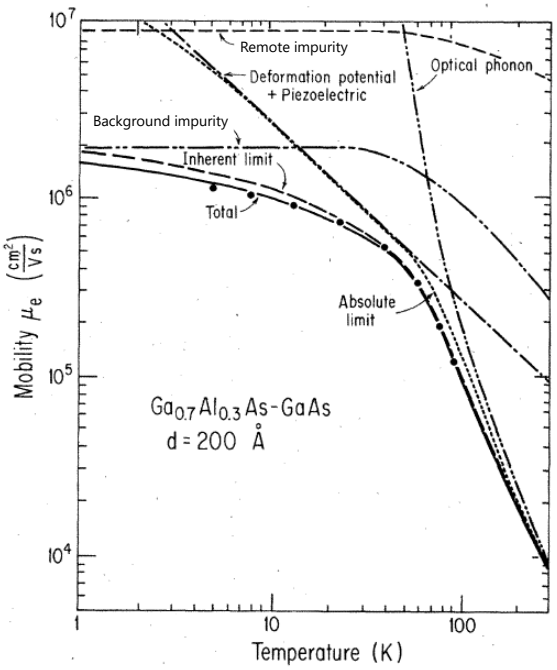

Figure 3.1: Measured (dots) and calculated (lines) temperature dependence of a modulation doped high mobility 2DES. Copied from Ref. [52].

In Fig. 3.1, calculated mobilities deduced from individual scattering mechanisms (*e.g.* optical phonon, remote impurity, background impurity) are plotted next to the total mobility obtained from the combined scattering rates as a function of temperature. The prediction is in very good agreement to the experimentally measured mobility (dots). Phonons

(lattice vibrations) are strongly temperature dependent and the limiting factor for the mobility at high temperatures. At low temperature, phonons freeze out and the mobility is limited by impurity scattering. The doping layer containing the remote impurities is typically spaced between 10 nm and 40 nm away from the 2DES. The spatial separation increases the mobility but still causes a weak, spatially random disorder potential in the 2DES due to Coulomb interaction, giving rise to small angle scattering for electrons in the 2DES. In contrast, background impurities very close to the 2DES lead to large angle scattering, which is the main limiting factor for the low-temperature mobility. For this reason, growers of high mobility 2DES focus on improving their growth techniques in regard to lower background impurities close to the GaAs/AlGaAs interface.

3.2.1 Ballistic transport

For an electron at the Fermi edge, the mean free path between two elastic scattering processes that strongly change the propagation direction can by calculated from the total elastic scattering time:

$$l_{\mathrm{m}} = v_{\mathrm{F}} \tau_{\mathrm{m}}, \tag{3.7}$$

where $v_{\mathrm{F}} = \sqrt{2E_{\mathrm{F}}^0/m^\star}$ is the Fermi-velocity. For a high mobility 2DES at low temperature, l_{m} is typically on the order of tens of microns ($l_{\mathrm{m}} = 55\,\mu\mathrm{m}$ for the wafer material used in this thesis). Technological progress and advanced lithography techniques, in particular EBL (cf. section 1.3), enabled continuous downscaling of gate defined structures. This progress paved the way toward 'ballistic' transport experiments, cf. Fig. 3.2. The elastic

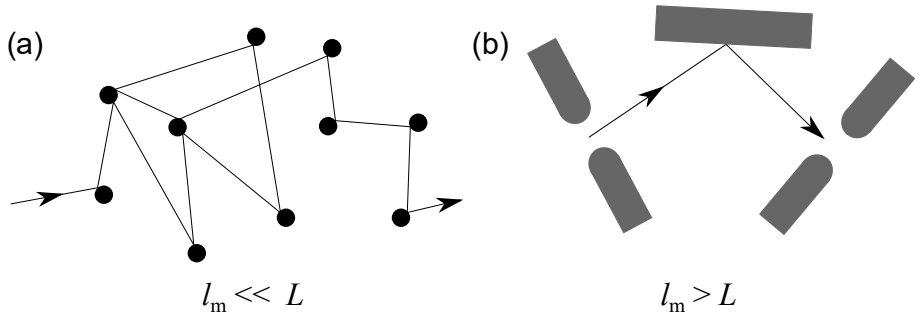

Figure 3.2: Illustration of diffusive (a) and ballistic (b) transport in samples of dimension L compared to the elastic mean free path l_{m}.

mean free path is the key quantity in this context: Diffusive transport is observed in samples of dimensions much larger than the mean free path, $L \gg l_{\mathrm{m}}$. In this regime, transport of carriers over a distance L can be understood as a series of elastic scattering events due to collisions and interactions with impurities, phonons or other electrons, as illustrated in Fig. 3.2(a).

In contrast, the large elastic mean free path in high mobility wafers and the high lithographic resolution of EBL enables to fabricate customized devices that are considerably smaller than the elastic mean free path, $L < l_{\mathrm{m}}$, cf. Fig. 3.2(b). In this regime, large angle

scattering predominantly occurs at the gated structures. Using this concept, circuits can be designed to control electrons on the mesoscopic level.

The possibility to fabricate ballistic devices also raised important theoretical questions, which we motivate on the basis of the sketch in Fig. 3.3(a). We consider a narrow ballistic

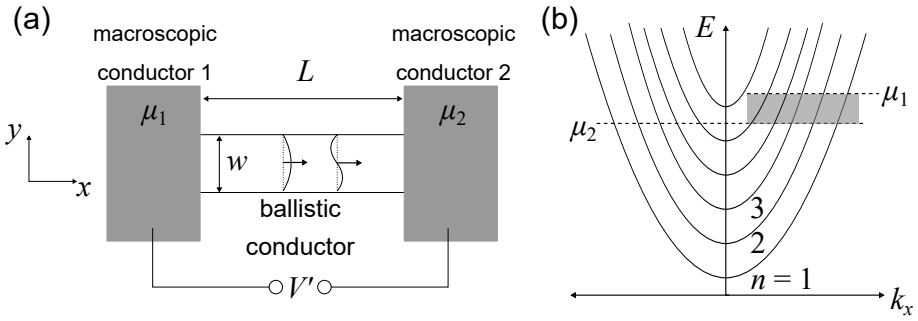

Figure 3.3: (a) Ballistic conductor carrying transverse modes between two macroscopic conductors at chemical potentials $\mu_{1,2}$. (b) Dispersion relations $E_n(k)$ of electrons inside the ballistic conductor.

conductor of length L sandwiched between two macroscopic conductors. The latter have dimensions much larger than the Fermi wavelength of the free 2DES λ_F, which is typically on the order of tens of nanometers for high mobility 2DES at low temperatures. The ballistic conductor between the contacts has a width w on the order of, but larger than λ_F. In this case, the dispersion relation in the macroscopic contacts is that of free electrons

$$E(k) = \frac{\hbar^2 k^2}{2m^\star}$$

confined in the z-plane of the 2DES with $k^2 = k_x^2 + k_y^2$, while electrons in the narrow ballistic conductor are additionally confined in the transverse (y-) direction. Here, the dispersion relation splits into a set of discrete subbands ('modes'), indexed n = 1,2,3,..., with individual dispersion relations

$$E_n(k_x) = E_n + \frac{\hbar^2 k_x^2}{2m^\star},$$

cf. Fig. 3.3(b). The total number of occupied modes is then $N(E) = \sum_n \Theta(E - E_n)$, where $\Theta(x)$ is the Heaviside step function with $\Theta(x) = 1$ for $x \geq 0$ and $\Theta(x) = 0$ for $x < 0$.

For a given width w, the conductance of the device sketched in panel (a) approaches a finite value (and hence a non-zero resistance) once its length L is decreased below the mean free path. This is surprising, as the conductance of macroscopic conductors scales like $G = \sigma w/L$, and intuitively one would assume zero resistance in the absence of backscattering. Instead, the finite resistance is caused by the rearrangement of the current as it propagates from the left macroscopic conductor at chemical potential μ_1 through the narrow ballistic conductor into the right macroscopic conductor at chemical potential μ_2, cf. Fig. 3.3(a,b): in the macroscopic two-dimensional conductors, the dispersion relation of

electrons is continuous and the current is carried by infinitely many modes. At the interface to the narrow, one-dimensional conductor with a finite set of N transverse modes, most of the current is reflected and the current redistributes, giving rise to an interface resistance, independently of the length of the ballistic conductor.

Next, we calculate the current I carried by a set of N transverse modes inside the ballistic conductor for a bias voltage V' causing a difference in the chemical potentials $\mu_1 - \mu_2 = eV'$ between the macroscopic conductors. We write the current as

$$I = \frac{e}{2} \sum_{n=1}^{N} \int_0^\infty D_{n,1\mathrm{D}}(E) v_n(E) t_n(E) \left[f_2(E) - f_1(E) \right] dE, \tag{3.8}$$

where

$$D_{n,1\mathrm{D}} = \frac{2}{\pi} \left(\frac{dE_n}{dk_x} \right)^{-1}$$

and

$$v_n = \frac{1}{\hbar} \frac{dE_n}{dk_x}$$

is the 1D density of states and the group velocity of mode n, respectively. Note that the energy dependence in the density of states and the group velocity cancels, such that every mode carries the same current, independently of the bandstructure (in 1D). $t_n(E)$ denotes the transmission probability of mode n at energy E and

$$f_i(E) = \frac{1}{\exp\left(\dfrac{E - \mu_i}{k_\mathrm{B} T} \right) + 1}$$

is the Fermi-Dirac distribution function representing the occupation probability of an electron with energy E in the macroscopic conductor $i = 1{,}2$ with local chemical potential μ_i at temperature T. Since all states below μ_2 are occupied in both macroscopic conductors, a net current is only carried by the $+k_x$ states of modes within the transport window $\mu_1 \geq E \geq \mu_2$ [cf. Fig. 3.3(b)], which we account for with the pre-factor $1/2$ in equation 3.8. Inserting into equation 3.8, the current is

$$I = \frac{2e}{h} \sum_{n=1}^{N} \int_0^\infty t_n(E) \left[f_2(E) - f_1(E) \right] dE.$$

Assuming a small bias window around the Fermi energy at $T = 0$, such that $t_n(E) \simeq t_n(E_\mathrm{F}^0)$ independently of energy we arrive at the expression

$$I = \frac{2e}{h} \sum_{n=1}^{N} t_n(E_\mathrm{F}^0) \left(\mu_1 - \mu_2 \right) = \frac{2e^2}{h} \sum_{n=1}^{N} t_n(E_\mathrm{F}^0) V'.$$

The conductance $G = I/V'$ can be written as

$$G(E_\mathrm{F}^0) = \frac{2e^2}{h} \sum_{n=1}^{N} t_n(E_\mathrm{F}^0) = \frac{2e^2}{h} T(E_\mathrm{F}^0), \tag{3.9}$$

where $\sum_{n=1}^{N} t_n(E_F^0) = T(E_F^0)$ is the total transmission of all N modes at the Fermi energy. Equation 3.9 - known as the Landauer formula [51] - demonstrates that 'conductance is transmission', in the sense that the conductance of a quantum conductor is directly proportional to the probability of a particle to transmit through it.

For N fully transmitting modes, $\sum_{n=1}^{N} t_n(E_F^0) = N$, we find the 1D conductance quantization, $G = NG_Q$ with the spin degenerate conductance quantum $G_Q = 2e^2/h = 7.7480917 \times 10^{-5}$ S.

3.2.1.1 Quantum point contact

In 1988, van Wees at al. [53] and Wharam et al. [3] independently of each other realized a quasi one-dimensional ballistic conductor in a 2DES, denoted quantum point contact (QPC). In a pioneering work, they deposited metallic split gates on top of a high mobility GaAs/AlGaAs heterostructure (cf. inset in Fig. 3.4), creating a constriction for electrons

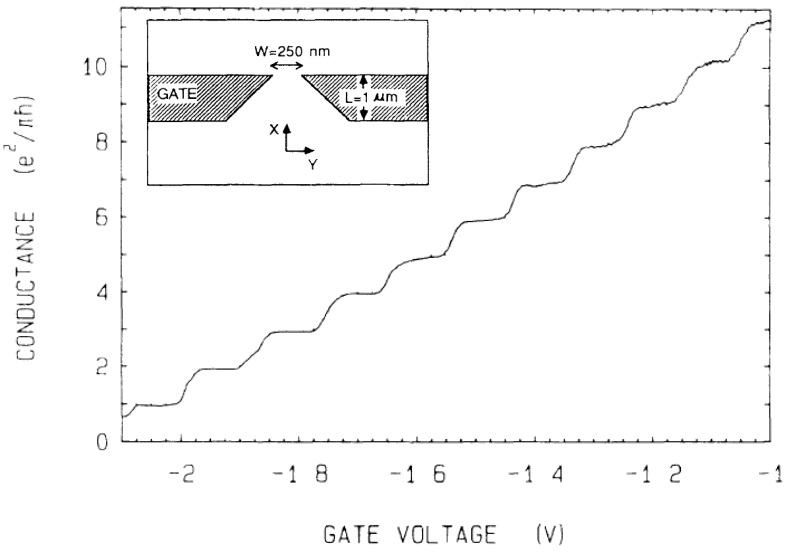

Figure 3.4: Historical data of a quantum point contact realized in a 2DES, copied from Ref. [53] (van Wees et al.).

by depleting the 2DES below the gates via a negative gate voltage (field-effect). The lithographic constriction width in the experiment was around 250 nm at a Fermi wavelength of 42 nm. Strikingly, after subtraction of the lead resistance, the conductance of the device decreased in steps at integers of G_Q for decreasing gate voltages, cf. main panel in Fig. 3.4. The conductance plateaus found here are a direct observation of the conductance quantization derived at the end of the previous section. By lowering the gate voltage, the depleted area of the 2DES below increases, giving rise to a more narrow constriction with less transverse modes contributing to conduction. For very negative voltages, the constriction is fully depleted and the channel is completely pinched off ($G = 0$, not shown in Fig. 3.4).

Note that the length of the 1D channel $L \approx 1\,\mu\text{m}$ shown in the inset of Fig. 3.4 is much shorter than the mean free path $l_\text{m} = 8.5\,\mu\text{m}$ of the sample, such that the conductance (the transmission) is mainly a property of the 'contacts' between the free 2DES and the 1D channel and not the 1D channel itself. The shape of the pinch-off curve thus strongly depends on the electrostatic potential shape of the constriction and the transition to the free 2DES. In the appendix (section A.4) we use the parabolic saddle point potential model to explain the smooth steps in QPC pinch-off curves.

3.2.2 Phase-coherent transport

Next to ballistic effects, the small dimensions of our devices and cryogenic temperatures allow us to study coherent effects related to the wave nature of electrons. The most famous ones include the Aharanov-Bohm effect [54], weak localization [55], (universal) conductance fluctuations [56] or a modified Young's double-slit experiment [57]. In all these works, the electron phase is manipulated, giving rise to quantum interference features that are not visible in a classical system. Experimentally, this is realized, for example, by applying a perpendicular magnetic field B, creating a phase difference between two electron paths proportional to the enclosed magnetic flux, or by applying local electric fields to tune the phase difference between two paths. Moreover, the electronic analog of a Fabry-Pérot resonator [58–60] can be studied by creating standing electron waves.

However, finite temperatures and finite source-drain voltages lead to a loss of the phase information, limiting the timescale of phase-coherent transport. In the following, we present the most relevant dephasing/decoherence mechanisms in a 2DES at low temperature.

Dephasing between different electrons

Finite source-drain voltages cause electronic excitations even for the degenerate Fermi gas at very low temperature. In a measurement under these conditions, different electrons with different energies within the transport window contribute to the current. Due to their different energies (k-states), the electrons accumulate a relative phase difference $\Delta\phi = \Delta k l$, where Δk is the momentum difference between two electrons at different energies and l their propagation distance. For an estimation of the dephasing length of an electron ensemble excited between E_F^0 and $E_\text{F}^0 + eV'$ (at $T = 0$), we calculate the propagation length after which two electrons at $E_1 = E_\text{F}^0$ and $E_2 = E_\text{F}^0 + eV'$ are exactly out of phase, such that $\Delta\phi = \pi$:

$$l_\phi(V') = \frac{\pi}{\Delta k(V')} = \frac{\pi}{\frac{\sqrt{2m^\star E_\text{F}^0}}{\hbar}\left(\sqrt{1+\frac{eV'}{E_\text{F}^0}}-1\right)}. \tag{3.10}$$

Decoherence of single electrons

Besides a dephasing of the electron ensemble, also single electrons can lose their phase memory. This occurs due to inelastic scattering events as discussed in the following.

At sufficiently low temperatures, electron-phonon scattering [61] freezes out, leaving behind inelastic electron-electron scattering as the main dephasing mechanism. In this context, we distinguish between inelastic electron-electron scattering events with (i) large energy transfer on the order of $k_{\mathrm{B}}T$ (eV') and (ii) small energy transfer interactions of single electrons with the fluctuating electromagnetic field of all other electrons (Nyquist noise [62]). These processes are inelastic by means that single electrons lose/gain energy. However, the total momentum and energy of the ensemble remains conserved as electrons exchange their momenta between each other.

(i) Chaplik [63] derived the inelastic scattering rate for an electronic excitation Δ above the Fermi level at $T = 0$:

$$\frac{1}{\tau_{e-e}(\Delta)} = \frac{E_{\mathrm{F}}^0}{4\pi\hbar}\left(\frac{\Delta}{E_{\mathrm{F}}^0}\right)^2\left[\ln\left(\frac{E_{\mathrm{F}}^0}{\Delta}\right) + \frac{1}{2} + \ln\left(\frac{2Q_{\mathrm{TF}}}{k_{\mathrm{F}}}\right)\right]. \tag{3.11}$$

Where $k_{\mathrm{F}} = \sqrt{2m^\star E_{\mathrm{F}}^0}/\hbar$ is the Fermi wave number and $Q_{\mathrm{TF}} = 0.2\,\mathrm{nm}^{-1}$ is the Thomas-Fermi screening vector in 2D for GaAs. Equation 3.11 holds for moderate excitation energies $\Delta << \hbar^3 k_{\mathrm{F}} Q_{\mathrm{TF}}/m^\star$. Note that Δ denotes the excitation energy relative to the Fermi level and equation 3.11 thus describes decoherence of electrons at a specific energy.

Giuliani et al. [64] extended the picture to finite temperatures with low electronic excitations in the regime $\Delta << k_{\mathrm{B}}T << E_{\mathrm{F}}^0$:

$$\frac{1}{\tau_{e-e}(T)} = -\frac{E_{\mathrm{F}}^0}{2\pi\hbar}\left(\frac{k_B T}{E_{\mathrm{F}}^0}\right)^2\left[\ln\left(\frac{k_B T}{E_{\mathrm{F}}^0}\right) - \ln\left(\frac{Q_{\mathrm{TF}}}{\hbar k_{\mathrm{F}}}\right) - \ln 2 - 1\right] \tag{3.12}$$

(ii) Additionally, scattering of electrons due to the fluctuating electromagnetic field created by the thermal motion of all other electrons causes decoherence, which is known as Nyquist noise [62]. The corresponding scattering rate for a disordered 2DES ($l_{\mathrm{m}} < L \leq l_\phi$) is [65]

$$\frac{1}{\tau_N(T)} = \frac{k_{\mathrm{B}}T}{2\pi\hbar}\frac{\lambda_F}{l_{\mathrm{m}}}\ln\left(\frac{\pi l_{\mathrm{m}}}{\lambda_{\mathrm{F}}}\right), \tag{3.13}$$

and the total dephasing rate due to electron-electron scattering can be obtained from $\tau_{\phi,e-e}^{-1} = \tau_{e-e}^{-1} + \tau_N^{-1}$, in agreement with an experiment [66].

In contrast, in clean, ballistic and coherent systems, $l_{\mathrm{m}} \geq l_\phi > L$, large energy transfer due to inelastic electron-electron scattering represents the main factor for a limited coherence length, $\tau_{\phi,e-e}^{-1} \simeq \tau_{e-e}^{-1}$, which has been confirmed experimentally using bias voltage spectroscopy at low temperature [57] (equation 3.11) as well as temperature dependent measurements at small bias [67] (equation 3.12).

In Fig. 3.5, we compare the dephasing length of an electron ensemble l_ϕ (dashed black line, cf. equation 3.10) to the inelastic electron-electron scattering length of a single electron $l_{e-e} = v_{\mathrm{F}}\tau_{e-e}$ (solid black line, with τ_{e-e} defined in equation 3.11) as a function of the energy $|eV'|$ relative to the Fermi level. For the comparison, we choose the actual Fermi energy of the wafer material used in our experiments, $E_{\mathrm{F}}^0 = 11\,\mathrm{meV}$ and consider $T = 0$. For a given source drain voltage, the electron ensemble first dephases, before single electrons lose their phase information, $l_\phi(|eV'|) < l_{e-e}(|eV'|)$. By applying sufficiently small

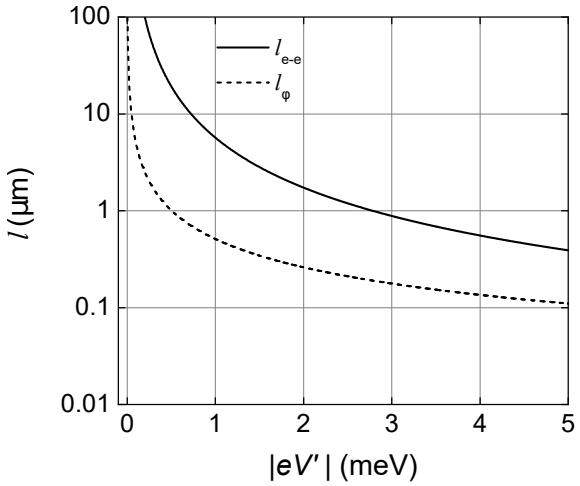

Figure 3.5: Calculated dephasing length of an electron ensemble l_ϕ (dashed black line, cf. equation 3.10) and inelastic electron-electron scattering length of a single electron $l_{e-e} = v_\mathrm{F}\tau_{e-e}$ (solid black line, with τ_{e-e} defined in equation 3.11) as a function of the energy $|eV'|$ relative to the Fermi level, for $E_\mathrm{F}^0 = 11\,\mathrm{meV}$ and $T = 0$, plotted on a logarithmic scale.

bias voltages, both phase breaking lengths reach values beyond a few microns, comparable to the dimensions of our samples. In this bias window, we can observe ballistic and coherent effects at low temperature.

3.3 Landauer-Büttiker formalism

The Landauer formula describing the transmission through a ballistic two terminal conductor (cf. equation 3.9) can be extended to ballistic samples with an arbitrary number of terminals indexed i,j within the Landauer-Büttiker formalism. We can write the total current flowing into lead j as [68]

$$I_j = \frac{2e}{h} \sum_i \left(T_{ij}\mu_j - T_{ji}\mu_i\right)$$

where

$$T_{ij}(E) = \sum_{m,n} t_{ij,mn}(E)$$

are the total pairwise transmissions after summation over all mode to mode transmission probabilities $t_{ij,mn}$ of mode n in lead j into mode m in lead i. With $V_i = \mu_i/e$, we can rewrite the current as

$$I_j = G_Q \sum_i \left(T_{ij}V_j - T_{ji}V_i\right).$$

To ensure that the current is zero for equal potentials in the leads ($V_i = V_j$) it must hold

$$\sum_i T_{ij} = \sum_i T_{ji},$$

such that we can rewrite the current in terms of potential differences (voltages),

$$I_j = G_Q \sum_i T_{ij} \left(V_j - V_i\right).$$

Time reversal symmetry gives the condition

$$T_{ij}(B) = T_{ji}(-B).$$

3.3.1 Ballistic cavity with four openings and diffusive leads

As an example for the application of the Landauer-Büttiker formalism introduced above, we consider a real sample shown in Fig. 3.6(a). In chapter 7, we discuss various experiments performed with this sample.

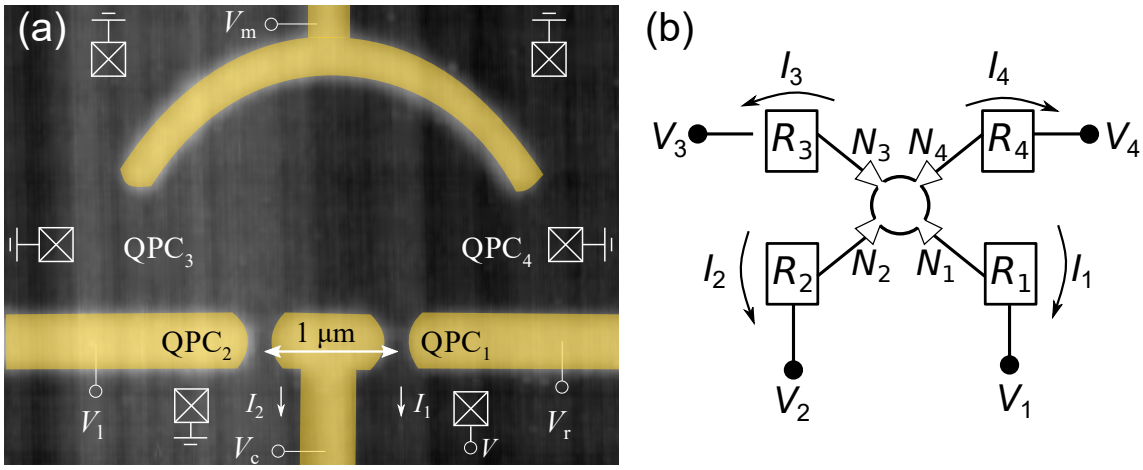

Figure 3.6: (a) Atomic force microscope (AFM) image of Ti/Au gates (yellow) on the sample surface (dark). Negative gate voltages V_r,V_c,V_l and V_m are used to define four QPCs and a mirror, forming a cavity in the 2DES 107 nm below the surface. Crossed boxes indicate Ohmic contacts far away from the nanostructure. We measure the currents I_1 and I_2 flowing through QPC$_{1,2}$ after applying a source-drain voltage V at QPC$_1$ and leaving all other Ohmic contacts grounded. (b) Ballistic four terminal device with lead resistances R_i, spin-degenerate channels N_i, potentials V_i and currents I_i flowing in lead i = 1,2,3,4.

By applying four negative voltages V_r,V_c,V_l and V_m to the gates highlighted in yellow, we realize four QPCs and a mirror gate in the 2DES below. Together, they form a cavity with four terminals.

For our transport experiments, we apply a source-drain voltage V to the lead of QPC$_1$, such that a current I_1 flows in the same lead, cf. Fig. 3.6(a). Additionally, we measure the current I_2 flowing in lead 2 behind QPC$_2$, which we keep as close as possible to the ground potential. Using Kirchhoff's law ($\sum_{i=1}^{4} I_i = 0$), we can determine the sum of the

currents I_3 and I_4 flowing in the leads of the wider QPC_3 and QPC_4, which we likewise keep at the ground potential. We sketch a simplified circuit diagram of the four terminal device with their lead resistances in Fig. 3.6(b).

As the dimensions of the cavity are considerably smaller than the measured mean free path in this sample ($l_m = 14\,\mu m$), the transport within the cavity is ballistic. Nevertheless, as we will justify below, we next treat the cavity as a node of an Ohmic circuit and assume diffusive transport to predict the diffusive current flow through the QPCs. We parameterize the resistance of QPC_i by $(N_i G_Q)^{-1}$, where N_i is the number of spin-degenerate channels in the respective QPC, with i = 1,2,3,4. The macroscopic Ohmic contacts far away from the cavity (indicated by crossed boxes) and their leads cause a known serial resistance R_i for QPC_i. Within this diffusive transport model, we can calculate the currents as a function of the effective resistances $\tilde{R}_i = (N_i G_Q)^{-1} + R_i$. The gate voltage dependence of N_i and R_i is determined experimentally, cf. section 7.2.

To quantify the transmission properties of the cavity and its four QPCs, we have to relate the measured currents to transmissions and reflections T_{ij} from lead j into lead i with i,j = 1,2,3,4 within the Landauer-Büttiker formalism introduced in section 3.3. In particular, we are interested in linking the measured 'emitter' current I_1 to the reflection amplitude T_{11} (corresponding to backscattered electrons returning into QPC_1) and the measured 'detector' current I_2 to the transmission amplitude T_{21} (corresponding to electrons transmitting through QPC_1 and QPC_2 in series). In general, the current measured at any of the four terminals depends on various transmission or reflection amplitudes, making the extraction of individual T_{ij} elements difficult. To still be able to derive good approximations for $T_{11}(I_1)$ and $T_{21}(I_2)$, we calculate the correction to the diffusive currents caused by the coherent and ballistic dynamic inside the cavity in leading order. For this purpose, we make the following assumptions:

(i) While the number of conducting channels coupling into/out of the cavity via the narrow emitter (QPC_1) and detector (QPC_2) are of order one, the number of conducting channels of the wider cavity side constrictions QPC_3 and QPC_4 are much larger and similar to each other, $N_3 \simeq N_4 >> N_{1,2}$. As we show in section 7.2, this is a reasonable assumption at least if we keep $N_{1,2}$ = 1,2.

(ii) We assume chaotic cavity physics [69–73] to estimate the background transmission/reflection amplitudes of the individual leads. Within this approximation, the transmission probability through lead j in a cavity with M leads is

$$t_j = \frac{N_j}{\sum_{i=1}^{M} N_i}. \tag{3.14}$$

The chaotic and the diffusive regime are equivalent by means of the distribution of currents proportional to the number of occupied spin-degenerate channels and the Ohmic resistances, respectively. On this basis, we motivate the application of the diffusive transport model introduced above.

(iii) To simplify the equation system to solve we assume that the leads 2,3,4 are at the ground potential, such that $V_2 = V_3 = V_4 = 0$. Experimentally, this assumption is reasonable since we are able to tune the voltage offset of the current amplifier connected to QPC_2 down to the ground potential within an accuracy of $|V_2| < 10\,\mu V$. Note that

this is an upper limit given by the specifications of the manufacturer [47, 48]. In our experiments, $|V_2|$ is typically on the order of very few microvolts, $|V_2| < 5\mu V$. For this reason, we in the following approximate $V_2 = V_3 = V_4 = 0$ and set $V_1 := V$.

Using these assumptions and the unitarity of the scattering matrix (defined in section 3.4 below), we arrive at the following approximations[1]:

$$I_1 = -V\left[G_1^{diff} + G_Q\left(\frac{N_1^2}{\sum_{j=1}^4 N_j} - T_{11}\right) + G_Q\frac{(N_1\delta T_{14} + N_1\delta T_{41})(N_3\tilde{R}_3 - N_4\tilde{R}_3)}{N_3N_4\left(\tilde{R}_3 + \tilde{R}_4\right)} + ...\right] \tag{3.15}$$

relates the measured emitter current I_1 to the reflection amplitude T_{11} for electrons emitted by QPC_1 to return into the same QPC. Here, we used the diffusive sample resistance

$$\frac{1}{G_1^{diff}} = \tilde{R}_1 + \left(\frac{1}{\tilde{R}_2} + \frac{1}{\tilde{R}_3} + \frac{1}{\tilde{R}_4}\right)^{-1} \tag{3.16}$$

In Fig. 3.7 we show G_1^{diff} as a function of V_m, obtained from the combined measured V_m-dependences of the four QPCs and their leads, for $N_{1,2} = 1,2,3$.

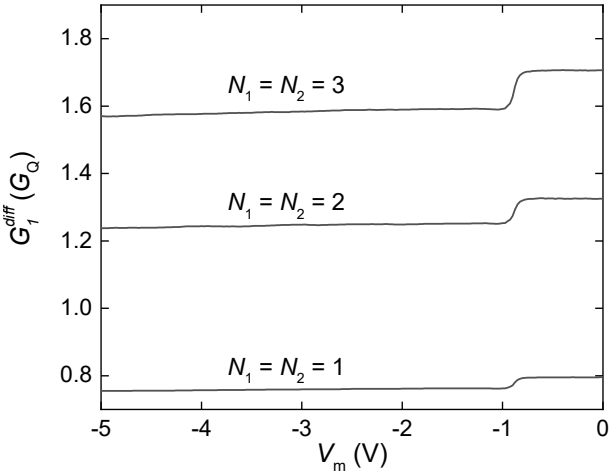

Figure 3.7: Measured diffusive conductance of QPC_1, $G_1^{diff}(V_m)$ obtained from inverting equation 3.16 with $N_1 = N_2 = 1,2,3$.

Similarly,

$$I_2 = V\left[G_2^{diff} + G_Q\left(T_{21} - \frac{N_1N_2}{\sum_{j=1}^4 N_j}\right) - G_Q\frac{(N_1\delta T_{24} + N_2\delta T_{41})(N_3\tilde{R}_3 - N_4\tilde{R}_4)}{N_3N_4\left(\tilde{R}_3 + \tilde{R}_4\right)} + ...\right] \tag{3.17}$$

with the diffusive serial transmission through QPC_1 and QPC_2

$$G_2^{diff} = \frac{1}{\tilde{R}_2}\left(1 - \frac{\tilde{R}_1}{\tilde{R}_1 + (\sum_{j=2}^4 1/\tilde{R}_j)^{-1}}\right) \tag{3.18}$$

links the measured detector current I_2 to the transmission amplitude T_{21} from QPC_1 into QPC_2.

The first terms of the two equations 3.15 and 3.17 are identical to the solution of the diffusive model, $I_{1,2} = \mp V G_{1,2}^{\text{diff}}$. T_{11} is the reflection amplitude which takes into account those carriers emitted into the cavity from QPC_1 and then backscattered through QPC_1. T_{21}

[1] The equations were derived by Piet W. Brouwer, head of the Dahlem Center for Complex Quantum Systems at the FU Berlin.

is the transmission coefficient which accounts for all carriers which are first emitted from QPC_1 into the cavity and then scattered into QPC_2. The second terms in parentheses describe the chaotic/diffusive limit of T_{11} and T_{21}, respectively. Hence, in the chaotic/diffusive transport limit, the correction terms in both equations vanish. The last terms in eq. 3.15 and 3.17 are of magnitude $1/N_{3,4}^{3/2}$, terms of lower magnitude are summarized by dots.

In the following, we omit these small terms and solve for T_{11} and T_{21}:

$$T_{11}(B,V_\mathrm{m},V) = \frac{1}{G_Q}\left(\frac{I_1(B,V_\mathrm{m})}{V} + G_1^{diff}(V_\mathrm{m}) + G_Q\frac{N_1^2}{\sum_{j=1}^4 N_j(V_\mathrm{m})}\right), \tag{3.19}$$

$$T_{21}(B,V_\mathrm{m},V) = \frac{1}{G_Q}\left(\frac{I_2(B,V_\mathrm{m})}{V} - G_2^{diff}(V_\mathrm{m}) + G_Q\frac{N_1N_2}{\sum_{j=1}^4 N_j(V_\mathrm{m})}\right). \tag{3.20}$$

In the equations above, we explicitly indicate the dependence on the experimental parameters B,V_m and V. The quantities $\tilde{R}_j$, N_j and $G_{1,2}^{diff}$ are or are composed of individual resistors without ballistic or coherent couplings. Therefor, these are magnetic field independent (for not too high fields $|B| \leq 100\,\mathrm{mT}$ applied in the experiments) and only affected by V_m. In contrast, the measured conductances $I_1(B,V_\mathrm{m})/V$ and $I_2(B,V_\mathrm{m})/V$ contain ballistic and coherent components which are sensitive to variations in B,V_m,V, as well as temperature. These are included in $T_{11}(B,V_\mathrm{m})$ and $T_{21}(B,V_\mathrm{m})$.

From the total reflection (transmission) amplitude T_{11} (T_{21}) we finally calculate the reflection probability

$$t_{11} = \frac{T_{11}}{N_1} \tag{3.21}$$

and the transmission probability

$$t_{21} = \frac{T_{21}}{N_1} \tag{3.22}$$

by dividing by the number of channels N_1 coupling into the cavity via the emitter QPC_1.

3.4 Transfer matrix and scattering matrix

Inside the quasi one-dimensional leads, the electronic wavefunctions propagating *towards* a scatterer in lead i can be written as

$$\Psi_{in,i}(x,y) = \sum_n a_{i,n}e^{\pm ik_x x}\chi_n(y).$$

Here, $\chi_n(y)$ denotes the transverse wavefunction with mode index n and $a_{i,n}$ the corresponding amplitude. In x-direction, the electrons propagate as plane waves and the sign of k_x is chosen such that it represents an *incoming* wave for the scatterer.

Similarly, we can write the *outgoing* wavefunction in lead i

$$\Psi_{out,i}(x,y) = \sum_n b_{i,n}e^{\mp ik_x x}\chi_n(y),$$

where the sign of the propagation direction is reverted and $b_{i,n}$ represent the amplitudes of the *outgoing* modes. In the following, we assume that the wave amplitudes $a_{i,n}$ and $b_{i,n}$ are directly proportional to the current carried by the corresponding mode (at fixed particle energy E).

The mode to mode transmission probabilities $t_{ij,mn}$ between different leads can be expressed in a illustrative matrix representation that relates the incoming wave amplitudes with the outgoing wave amplitudes. We explain this concept on the basis of an example, sketched in Fig. 3.8. We consider the transmission of a fully coherent electron with

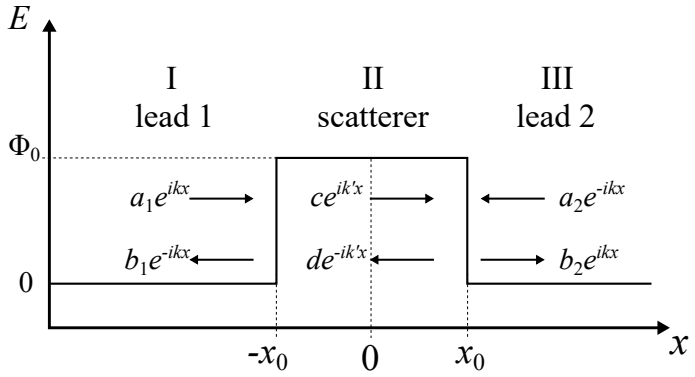

Figure 3.8: Potential barrier of height Φ_0 relative to the electronic energy E sandwiched between two ideal leads at zero potential. Arrows indicate the propagation direction of the corresponding wave amplitudes a_i (b_i) of a single transverse mode propagating into (out of) the scattering region.

kinetic energy E through a rectangular potential barrier of height Φ_0 placed between $-x_0 \leq x \leq x_0$. For simplicity but without loss of generality we assume only one transverse mode and define its amplitude propagating towards the scatterer in lead 1 (2) a_1 (a_2) and the outgoing amplitude b_1 (b_2). We denote the amplitude in the scattering region propagating along x ($-x$) as c (d).

We can connect the amplitudes a_1 and b_1 in lead 1 with the amplitudes c and d in the region of finite potential in a matrix representation

$$\begin{pmatrix} a_1 \\ b_1 \end{pmatrix} = \mathbf{T}_\mathrm{I} \begin{pmatrix} c \\ d \end{pmatrix}$$

with the transfer matrix

$$\mathbf{T}_\mathrm{I} = \begin{pmatrix} \left(\frac{ik+k'}{2ik}\right) e^{(ik-k')x_0} & \left(\frac{ik-k'}{2ik}\right) e^{(ik+k')x_0} \\ \left(\frac{ik-k'}{2ik}\right) e^{-(ik+k')x_0} & \left(\frac{ik+k'}{2ik}\right) e^{-(ik-k')x_0} \end{pmatrix}, \tag{3.23}$$

where k and k' are the wave numbers in the region of zero and finite potential, respectively. For the detailed derivation, please see section A.3 in the appendix.

In the same fashion, we can connect the amplitudes of the central region with finite potential and lead 2

$$\begin{pmatrix} c \\ d \end{pmatrix} = \mathbf{T}_{\mathrm{II}} \begin{pmatrix} b_2 \\ a_2 \end{pmatrix}$$

where $\mathbf{T}_{\mathrm{II}}$ is obtained by replacing $-x_0$ by x_0 and exchanging ik and k' in equation 3.23. Likewise, we can relate the amplitudes on both sides of the scatterer by concatenating the two transfer matrices, $\mathbf{T} = \mathbf{T}_{\mathrm{I}}\mathbf{T}_{\mathrm{II}}$,

$$\begin{pmatrix} a_1 \\ b_1 \end{pmatrix} = \mathbf{T} \begin{pmatrix} b_2 \\ a_2 \end{pmatrix}.$$

For given incoming amplitudes, we can now calculate the transmission coefficient t. Setting $a_1 = 1$ and $a_2 = 0$ (no incoming wave from lead 2 towards the scattering region), the transmission is

$$t = \left|\frac{b_2}{a_1}\right|^2 = \left|\frac{1}{\mathrm{T}_{11}}\right|^2 = \left[1 + \left(\frac{k^2 + k'^2}{2kk'}\right) \sinh\left(2k'x_0\right)\right]^{-1},$$

where T_{11} is the first entry of the total transfer matrix. Similarly, the reflection r into lead 1 is obtained via

$$r = \left|\frac{b_1}{a_1}\right|^2 = \left|\frac{\mathrm{T}_{21}}{\mathrm{T}_{11}}\right|^2.$$

The transmission through more complicated barriers of arbitrary shape can be calculated by discretizing the barrier $\Phi(x)$ into M slices of piecewise constant potentials $\Phi(x_i)$ with wave numbers

$$k'_i = \frac{\sqrt{2m^\star \left[E - \Phi(x_i)\right]}}{\hbar}$$

from which we calculate the transfer matrix of every slice i, $\mathbf{T}_i$. The total transfer matrix of the potential barrier is again obtained from the concatenation of all transfer matrices in the correct order,

$$\mathbf{T} = \prod_i^M \mathbf{T}_i.$$

The transfer matrix connects wave amplitudes on different sides of the scattering region. By rearranging the entries of the transfer matrix, we can likewise define the scattering matrix $\mathbf{S}$, which relates wave amplitudes moving into the scattering region with amplitudes moving out the scattering region. For the example above, we can relate the entries of the transfer matrix to those of the scattering matrix as follows:

$$t = |\mathrm{S}_{11}|^2 = \left|\frac{1}{\mathrm{T}_{11}}\right|^2;\ r = |\mathrm{S}_{21}|^2 = \left|\frac{\mathrm{T}_{21}}{\mathrm{T}_{11}}\right|^2$$

and write the scattering matrix $\mathbf{S}$ in

$$\begin{pmatrix} b_2 \\ b_1 \end{pmatrix} = \mathbf{S} \begin{pmatrix} a_1 \\ a_2 \end{pmatrix}$$

as

$$\mathbf{S} = \begin{pmatrix} t & r' \\ r & t' \end{pmatrix}$$

where t and r (t' and r') are the transmission and reflection amplitudes of the waves propagating from left to right (right to left). The scattering matrix is a unitary matrix, $\mathbf{S}^\dagger\mathbf{S} = \mathbb{1}$ which follows from the charge conservation condition

$$\sum_n |a_n|^2 = \sum_n |b_n|^2.$$

3.5 Quantum mechanical model for the transmission through a mesoscopic sample

Our numerical quantum mechanical model[2] allows for the calculation of pairwise mode to mode transmission probabilities $t_{ij,nm}$ between the $n \leq N$ ($m \leq M$) channels in contact j (i). These channels represent the transverse modes of a ballistic conductor within the Landauer-Büttiker formalism presented section 3.3. For k contacts, we consider $N_{tot} = \prod_{i=1}^{k} N_i$ pairwise transmission probabilities. In the following, we describe our method for the calculation, without loss of generality assuming only two contacts labeled j (i) with N (M) one-dimensional channels, cf. sketch in Fig. 3.9.

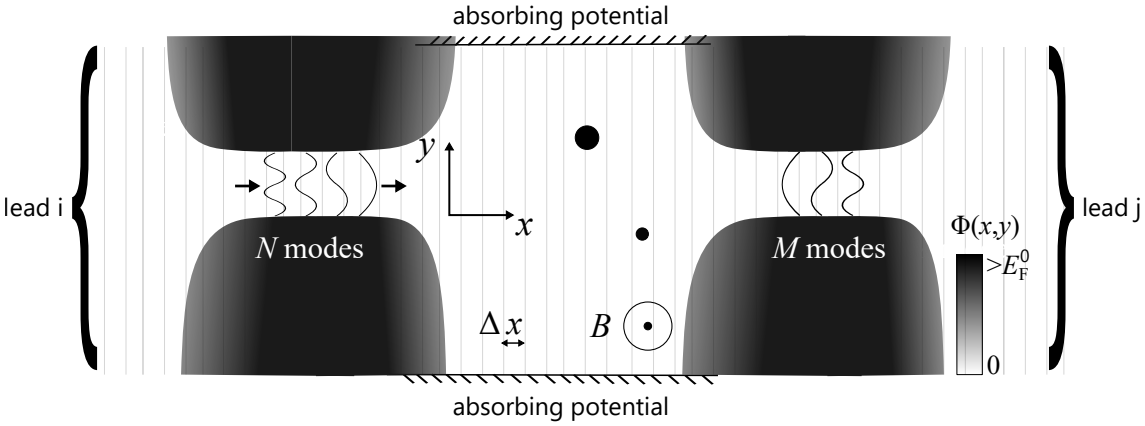

Figure 3.9: Sketch of the simulation region for our calculations. We numerically calculate the transmission through ideal reflectionless leads for a realistic 2D electrostatic potential landscape $\Phi(x,y)$ (greyscale) based on the actual sample layout. For the calculation, we divide the simulation region into parallel slices of width Δx along the y-direction where we solve the scattering problem exactly. To mimic grounded side drains of the 2DES, we implement absorbing potentials. Additional hard-wall impurity potentials (black circles) and a perpendicular magnetic field are added on demand.

Before the calculation, we first carefully model the electrostatic potential and its dependence on the gate voltages based on the lithographic sample layout as well as calibration measurements of the individual circuit components to result in a realistic 2D potential

[2]The model described in this section was realized and provided by Max Geier from the Dahlem Center for Complex Quantum Systems at the FU Berlin.

landscape of the actual sample. We attach ideal, reflectionless leads i,j to the two boundaries of the simulation region in x-direction, mimicking the measurement terminals in the experiment. To model macroscopic, grounded contacts connected to an intermediate region of free 2DES, we use an absorbing potential with periodic boundary conditions in y-direction, which allow an expansion in terms of plane waves, cf. upper and lower leads in Fig. 3.9.

For the calculation, we divide the simulation region into parallel slices of width $\Delta x = x_{i+1} - x_i = 15\,\mathrm{nm}$ for which we solve the Schrödinger equation for a given spatial electrostatic potential $\Phi(x_i,y)$ exactly. Additionally accounting for a perpendicular magnetic field B, the problem of a single electron in a spatial potential $\Phi(x_i,y)$ is described by the Hamiltonian

$$H = \frac{1}{2m^\star}\left(-i\hbar\frac{\partial}{\partial\vec{r}} - \frac{e}{c}\vec{A}(x_i,y)\right)^2 + \Phi(x_i,y)$$

where $\vec{A}(x_i,y)$ is the magnetic vector potential and c is the speed of light. While we calculate the solutions at fixed energy E, we account for the energy distribution of charge carriers due to finite temperature and source drain voltage by sampling over the energy distribution of the electrons. For solving the scattering problem for a given electrostatic potential and magnetic field at x_i, we expand the wavefunction along the vertical slices (in y-direction) in plane waves. Making use of the linearity of the scattering problem we calculate the scattering matrix of each individual slice separately. For each slice we further divide the problem into a free propagation without electrostatic potential and magnetic field between x_i and x_{i+1} setting $\Phi = 0$ and $\vec{A}(x_i,y) = 0$. Concatenation of the resulting slice-by-slice scattering matrices in the correct order yields the scattering matrix of the complete simulation region, from which we then extract the total transmission $T_{N,M} = \sum_{n=m=1}^{N,M} t_{n,m}$ between the two contacts with N and M conducting channels.

Additional hard-wall impurities or piezoelectric potentials are added on demand. However, we do not account for a weak, spatially random disorder potential due remote impurities in the donor layer. We also neglect any interaction effects due to electron-electron scattering or the electron spin.

4 Electrostatic potential shape of gate-defined quantum point contacts

Despite their role as fundamental building blocks in nanoelectronic circuits and the vast amount of literature about them [1–3,13,74], surprisingly little is known about the electrostatic potential shape of gate defined QPCs as a function of gate voltages. However, the precise potential shape is crucial for understanding interaction effects in QPCs [14,75–77] as well as their carrier emission dynamics [5,78], which is central for optimizing a quantum electronic circuit. The lateral confinement defines the mode structure of the 1D channel while the longitudinal potential shape governs the coupling of the 1D modes into the surrounding 2DES. A well designed QPC has several conductance steps that often are approximately equidistant in gate voltage as the QPC is opened up starting from pinch-off at $G = 0$. It is tempting to interpret equidistant conductance steps [2,79–83] as a signature of a parabolic lateral confinement potential [84] since such a potential has transverse modes at equally spaced energies. However, this interpretation is questionable as the distance of the conductance steps as a function of gate voltage is not necessarily proportional to the energy spacing between the 1D modes [82, 85]. Instead, populating the 1D channel with electrons by increasing the voltage applied to the split gates enhances Coulomb screening inside the constriction. As a consequence, the lateral confinement potential undergoes a transition from an unscreened approximately parabolic shape near pinch-off towards a screened potential for many occupied 1D subbands. This transition had been theoretically predicted [86]. Here, we experimentally investigate it using transport spectroscopy as a function of source-drain- and gate voltage. In the appendix (section A.4) we apply the parabolic saddle point potential model to our QPC, which would explain its almost perfectly equidistant conductance plateaus in the absence of screening. At first sight, the model describes the data qualitatively well. However, it is incompatible with the measured subband spectrum of the QPC. At the end of the present chapter, we use the experimentally found potential shape parameters into our numerical model (cf. section 3.5) to simulate beam profiles emitted from a QPC.[1]

In the top left inset of Fig. 4.1(a) we present an SEM image of the QPC under investigation. We realize the QPC by the usual split-gate technique on the surface of wafer mbe8-309 (see section A.1) hosting a 2DES 107 nm below the wafer surface. The 2DES Fermi energy is $E_{\mathrm{F}}^0 = 11\,\mathrm{meV}$ and the measured mean free path after processing the present sample $l_{\mathrm{m}} \simeq 24\,\mu\mathrm{m}$. A detailed description of the experimental setup used for the experiments described in this chapter is available in section 2.2.2. The smallest distance of the two gates defining the QPC is approximately 250 nm. The tips of the gates are designed as half circles with a radius of approximately 150 nm. To study the energetic spectrum of

[1] This chapter presents results of *Phys. Rev. B 101.* 165429 (2020) (Ref. [87]). See section B for the contributions of each author.

the 1D modes we measure the current as a function of both the voltage V_g applied to the gates and the source drain voltage V serving as an energy reference. In the main panel of Fig. 4.1(a), we plot a pinch-off curve of the QPC measured at a small source-

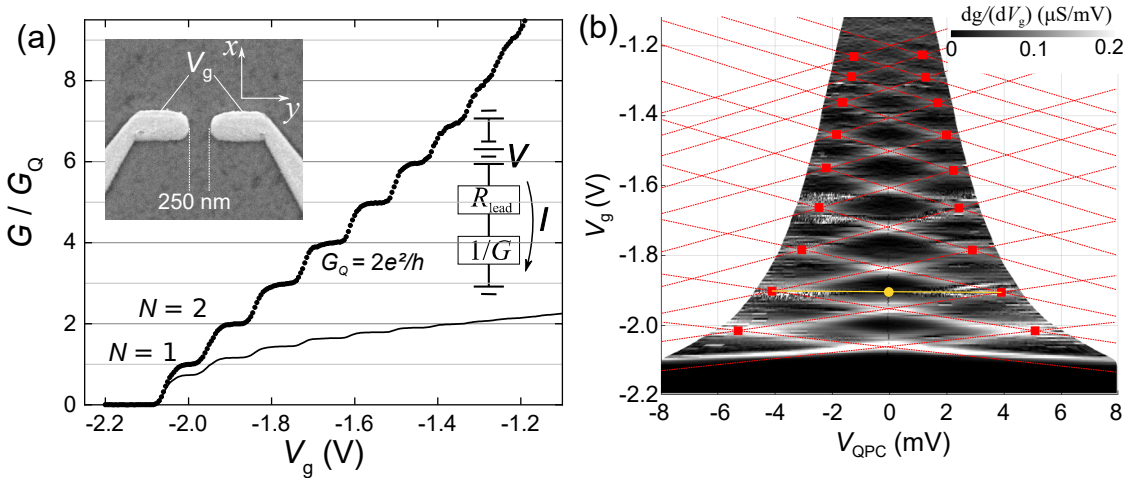

Figure 4.1: (a) Pinch-off curve $G(V_g)/G_Q$ of the QPC at source-drain voltage $V = -0.5\,\mathrm{mV}$; solid line: raw data; dots: corrected for lead resistance $R_{lead} = 4.62\,\mathrm{k\Omega}$ which includes $4.4\,\mathrm{k\Omega}$ resistance of external RC filters; left inset: SEM image of the QPC,; right inset: simplified circuit diagram of the measurement. (b) Differential transconductance $\mathrm{d}g/\mathrm{d}V_g$ as a function of V_g and the bias voltage $V_{QPC} = V - R_{lead}I$ dropping across the QPC. Local maxima of $\mathrm{d}g/\mathrm{d}V_g$ (white regions) indicate transitions between adjacent conductance plateaus. Red lines are a guide for the eye.

drain voltage, $V = -0.5\,\mathrm{mV}$. It features almost equidistant conductance plateaus in gate voltage. The line shows the measured conductance I/V of the sample, while black dots show the conductance of the QPC, G, after subtracting the finite lead resistance R_{lead}, cf. right inset in panel (a). Since the source-drain voltage V is applied across the QPC *and its leads* (which is always the case, because of the finite contact sizes even for a four-terminal measurement), the voltage drop across a QPC is $V_{QPC} = V - V_{lead} = V - R_{lead}I$, cf. sketch in Fig. 4.1(a). The lead resistance can be directly determined from the linear response pinch-off curves by fitting the conductance plateaus to their quantized values, $R_{lead} = V/I - (NG_Q)^{-1}$.

To experimentally determine the energies of the 1D modes we measure the differential conductance $g = \mathrm{d}I/\mathrm{d}V$ (e.g., using a lock-in amplifier) as a function of source-drain voltage V and the gate voltage. In Fig. 4.1(b) we plot the differential transconductance $\mathrm{d}g/\mathrm{d}V_g$ as a function of the gate voltage and the bias voltage V_{QPC} dropping across the QPC. In this plot, steps of the conductance $G(V_g,V_{QPC})$ appear as lines of positive differential transconductance (white). Red lines are a guide for the eye, indicating resonances between the 1D modes and the chemical potentials of the source and drain leads. Along the Nth line of positive (negative) slope counted from the bottom of the plot, the Nth 1D subband bottom potential is equal to the chemical potential in the source (drain) lead, $\varepsilon_N = \mu_S$ ($\varepsilon_N = \mu_D$). The lines frame diamond shaped regions. Within these regions the conductance takes the quantized values $G = NG_Q$. Intersection points at $V_{QPC} = 0$ indicate

steps of the linear response pinch-off curve, i.e., $G = (N - 0.5)G_{\mathrm{Q}}$. At intersection points at finite $V_{\mathrm{QPC}} \neq 0$ the chemical potential drop across a QPC equals the energy spacing between the corresponding 1D modes, $|\mu_{\mathrm{S}} - \mu_{\mathrm{D}}| = eV_{\mathrm{QPC}} = \varepsilon_N - \varepsilon_M$. The additional curved lines of enhanced differential transconductance within the $N = 1$ diamond indicate the 0.7-anomaly [13, 14, 75–77].

At the intersection points marked by red squares in panel (b), the bias V_{QPC} is precisely equal to the energy spacings between the highest occupied adjacent subbands,

$$\begin{aligned}\delta\varepsilon(N) &= \varepsilon_{N+1} - \varepsilon_N \\ &= eV_{\mathrm{QPC}}.\end{aligned} \tag{4.1}$$

We plot $\delta\varepsilon(N)$ in Fig. 4.2. We observe a strong decrease of $\delta\varepsilon(N)$ as the QPC is opened and N is increased. This result directly contradicts the very simple parabolic saddle potential model with constant curvature [84] since such a potential would give rise to a constant subband spacing $\delta\varepsilon$, independently of N (assuming that the potential offset depends linearly on the applied gate voltage).

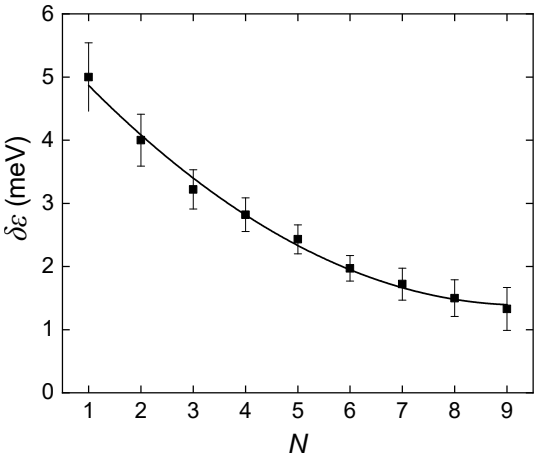

Figure 4.2: Subband spacings $\delta\epsilon(N)$ of the QPC presented in Fig. 4.1

For reflectionless coupling of the 1D modes into the free 2DES, the conductance of a QPC is limited by its strongest lateral confinement in the center of the constriction. In the following, we compare the two most common models describing the lateral confinement, namely a hard-wall versus a parabolic potential. These two models may be considered the extreme limits of a "continuum" of realistic scenarios for the transverse confinement.

4.1 Lateral hard-wall confinement potential

For the lateral hard-wall potential we model the transverse confinement potential $\Phi(y)$ as

$$\Phi(y) = \begin{cases} \Phi_0, & |y| \leq W/2 \\ \infty, & |y| > W/2\,, \end{cases} \tag{4.2}$$

where the two parameters W and Φ_0 are the width and offset of the hard-wall potential well. An offset can be caused by a partial depletion of the constriction related to the incomplete screening in a semiconductor with a small carrier density. The threshold energies for the transverse modes indexed $n = 1,2,3,...$ are

$$E_n = \frac{\pi^2\hbar^2 n^2}{2m^\star W^2} + \Phi_0 \tag{4.3}$$

Using Eq. (4.1) to relate the bias voltage at the intersection points marked by the red squares in Fig. 4.1(b) to the subband spacing $\delta\varepsilon(N) = E_{N+1} - E_N$, we calculate the widths

$$W(N) = \pi\hbar\sqrt{\frac{2N+1}{2m\delta\varepsilon(N)}}. \tag{4.4}$$

Neglecting additional screening effects due to the applied bias voltage, these values of $W(N)$ apply everywhere along the (almost horizontal) lines connecting pairs of red squares, see the yellow line for $N = 2$ in Fig. 4.1(b). In particular, this allows us to extend our estimate of the width $W(N)$ to $V_{\mathrm{QPC}} = 0$, indicated for $N = 2$ by the yellow dot in Fig. 4.1(b). Substituting W in Eq. (4.3) with $W(N)$ we then find the potential offset Φ_0 for $V_{\mathrm{QPC}} = 0$ using the relation $E_{\mathrm{F}}^0 \simeq E_N + 0.5\delta\epsilon(N)$, which gives

$$\Phi_0(N) \simeq E_{\mathrm{F}}^0 - \delta\varepsilon(N)\left(\frac{N^2}{2N+1} + \frac{1}{2}\right). \tag{4.5}$$

The potential shift by $0.5\delta\epsilon(N)$ accounts for the difference between the Nth subband bottom E_N and the Fermi level E_{F}^0 in the center of each diamond at $V_{\mathrm{QPC}} = 0$, assuming symmetric coupling between the 1D constriction and both leads. The assumption of symmetric coupling is confirmed by the fact that the lines connecting pairs of red squares in Fig. 4.1(b) are almost perfectly horizontal.

4.2 Lateral parabolic confinement potential with variable curvature

To model a lateral parabolic potential we use

$$\Phi(y) = \Phi_0 + \frac{m\omega_y^2 y^2}{2}, \tag{4.6}$$

where ω_y and Φ_0 are the characteristic frequency and offset of the parabolic potential well. The eigen energies of the modes within the parabolic confinement model are given by

$$E_n = \left(n - \frac{1}{2}\right)\hbar\omega_y + \Phi_0. \tag{4.7}$$

In analogy to the analysis assuming hard-wall potentials we determine the parameters ω_y and Φ_0 from the measured subband spacings. At the intersection points indicated with red squares in Fig. 4.1(b) we find

$$\hbar\omega_y(N) = eV_{\mathrm{QPC}} = \delta\varepsilon(N) \tag{4.8}$$

and in the centers of the diamonds at $V_{\mathrm{QPC}} = 0$ in addition

$$\Phi_0(N) \simeq E_{\mathrm{F}}^0 - N\hbar\omega_y\,. \tag{4.9}$$

Other than in the simple parabolic saddle-point potential with fixed curvature [84], here we consider a lateral potential curvature which varies with N, $\hbar\omega_y(N)$, and, hence, the gate voltage [82].

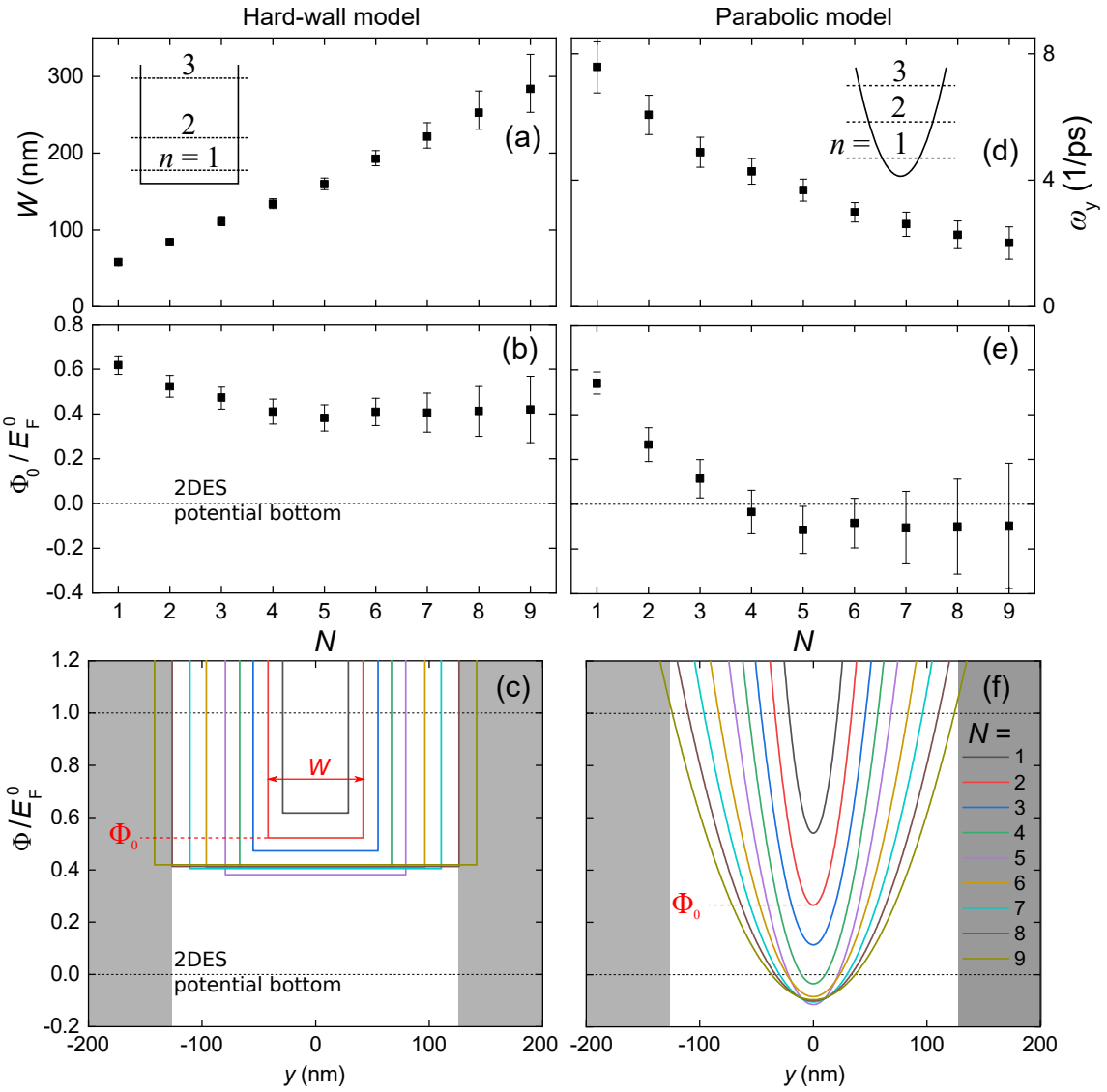

Figure 4.3: Comparison between hard-wall (left column) and parabolic (right column) potential models of the lateral confinement. (a) Width of hard-wall potential $W(N)$. (b) Offset of hard-wall potential $\Phi_0(N)$. (c) Shape of hard-wall potential for $1 \leq N \leq 9$, only for QPC_1. (d) Curvature of parabolic potential $\omega_y(N)$. (e) Offset of parabolic potential $\Phi_0(N)$. (f) Shape of parabolic potential for $1 \leq N \leq 9$, only for QPC_1. Error bars in panels (a), (b), (d) and (e) are calculated by error propagation from the error of $\delta\varepsilon(N)$, cf. Fig. 4.2. The gray shaded regions in (c,f) indicate the lithographic width of the gates forming the QPC constriction.

In Fig. 4.3 we directly compare our results for the hard-wall potential shown in the left column and for assuming parabolic confinement of variable curvature plotted on the right hand side. We present the parameters W and Φ_0 as a function of the subband number N for the hard-wall potential in panels (a) and (b) and ω_y and Φ_0 for the parabolic potential in panels (d) and (e). In panels (c) and (f) showing the actual potentials wells of the QPC

for the hard-wall and the parabolic model, we indicate the lithographic distance of 250 nm between the gates shown in the inset of Fig. 4.1(a) for comparison. It corresponds to the white area between regions shaded in gray. The width of the hard-wall potential slightly exceeds the lithographic width for $N = 9$. The QPC does not show further plateaus for $N > 9$.

Comparing the two models a substantial difference is visible in $\Phi_0(N)$. While for $N = 1$ the potential offset is similar for both models with $\Phi_0/E_\mathrm{F}^0 \simeq 0.6$, in case of the hard-wall potential it slowly decreases to $\Phi_0/E_\mathrm{F}^0 \simeq 0.4$ at $N = 4$ and stays approximately constant at that level as the QPC is opened further. In contrast, the decrease of the offset $\Phi_0(N)$ of the parabolic potential with N is much steeper, such that for $N \gtrsim 4$ it moves below the bottom of the conduction band in the 2D leads, indicated as a dashed line at $\Phi = 0$. We are not aware of a realistic mechanism that could lead to such an over-screening of the negative voltages applied to the gates.

The main result of our simple analysis starting from the measured subband spacings $\delta\varepsilon(N)$ is, that for $N \geq 4$ we can exclude a parabolic lateral confinement potential for our QPCs. Based on a self-consistent calculation it has been suggested that the increasing population of the 1D constriction as the QPC is opened up with N leads to an increased screening of the electric field originating from the charged control gates. For a gate-defined QPC, this causes a transition from a parabolic confinement for the case of little screening, i.e., $N = 1$ towards a truncated potential with a flat bottom at larger N where many carriers populate the constriction [86]. Our findings are in favor of such a scenario. The hard-wall potential presents the extreme limit of strong screening. Nevertheless, for $N \geq 4$, the hard-wall potential is more realistic than the other limit, namely the parabolic potential. The true shape of the lateral confinement potential of a QPC likely lies between these two extremes. For $N < 4$ it is closer to a parabola, but for $N \geq 4$ the parabola has a truncated, flat bottom, identical to that of a hard-wall potential but with smoothly increasing side walls of constant curvature as the case for a parabola [86, 88].

In summary, a parabolic saddle point potential is likely a realistic description of a QPC near pinch-off. However, as the QPC is opened up beyond $N \simeq 4$, the parabolic lateral confinement turns out to be a bad approximation. In this regime of enhanced screening, a hard-wall potential is the better approximation.

4.3 Coupling between control gates and the QPC

The electrostatic potential defining a QPC can be generated and controlled via the field effect by applying voltages to nearby metal gates. The size of the plateaus of quantized conductance in the pinch-off curves as a function of gate voltage, cf. Fig. 4.1, is proportional to the capacitive coupling between the control gates and the QPC, which we approximate as a conducting 1D-channel with the carrier density n_1D. We determine the approximate capacitance per unit length between gate and QPC as

$$c_\mathrm{1D} = e\delta n_\mathrm{1D}/\delta V_\mathrm{gate}\,, \tag{4.10}$$

where δn_1D is the increase of the carrier density as the voltage on the control gate is increased by δV_gate. If we take for δV_gate the voltage difference between two subsequent

intersection points of the source- and drain-resonances at $V_{\mathrm{QPC}} = 0$ in Fig. 4.1, $\delta n_{1\mathrm{D}}$ corresponds to the difference of the values of $n_{1\mathrm{D}}$ at these points corresponding to the N-th versus $(N+1)$st subband bottom at the Fermi level. The 1D carrier density is

$$n_{1\mathrm{D}}(N) = \int_0^\infty D_{1\mathrm{D}}(E) f(E) \mathrm{d}E \,, \tag{4.11}$$

where $D_{1\mathrm{D}} = \frac{1}{\pi\hbar}\sqrt{\frac{2m^\star}{E}}$ is the 1D electron density of states and $f(E)$ the Fermi-Dirac distribution. Given $k_{\mathrm{B}}T \ll E_{\mathrm{F}}^0$ we approximate $f(E) = 1$ for $E < E_{\mathrm{F}}^0$ and $f(E) = 0$ for $E > E_{\mathrm{F}}^0$. Summing up all 1D modes which are actually populated for the QPC tuned to the conductance $G = NG_{\mathrm{Q}}$ we find

$$\begin{aligned} n_{1\mathrm{D}}(N) &= \frac{\sqrt{2m^\star}}{\pi\hbar} \sum_{n=1}^{N} \int_{E_n}^{E_{\mathrm{F}}} \frac{1}{\sqrt{E - E_n}} dE \\ &= \frac{\sqrt{8m^\star}}{\pi\hbar} \sum_{n=1}^{N} \sqrt{E_{\mathrm{F}}^0 - E_n} \,. \end{aligned} \tag{4.12}$$

where E_n is the eigen energy of mode n for the hard-wall (parabolic) model given by equation 4.3 (4.7).

We plot $n_{1\mathrm{D}}(N)$ in Fig. 4.4 (right axis) for the hard-wall model (filled squares) and the parabolic model (open squares). Inserting $\delta n_{1\mathrm{D}}(N) = n_{1\mathrm{D}}(N+1) - n_{1\mathrm{D}}(N)$ from Eq. (4.12) in Eq. (4.10) we finally determine the 1D capacitance density as

$$c_{1\mathrm{D}}(N) = \frac{\sqrt{8m^\star e^2}}{\pi\hbar} \frac{\sqrt{E_{\mathrm{F}}^0 - E_{N+1}}}{\delta V_{\mathrm{gate}}(N)} \,, \tag{4.13}$$

where $\delta V_{\mathrm{gate}}(N)$ is the voltage difference between two adjacent conductance plateaus, cf. Fig. 4.1, measured between the conductance values $(N+0.5)G_{\mathrm{Q}}$ and $(N-0.5)G_{\mathrm{Q}}$. Substituting E_{N+1} with the according eigen-energy of the hard-wall (parabolic) potential using 4.3 (4.7) we can now determine the 1D capacitance density $c_{1\mathrm{D}}(N)$, cf. filled (open) blue circles in Fig. 4.4. $c_{1\mathrm{D}}(N)$ is the slope of the also shown 1D carrier density $n_{1\mathrm{D}}(N)$. The strong decrease of the capacitance with N for $N \leq 4$ is a direct signature of the increase of the screening of the electric field of the gates with growing carrier density.

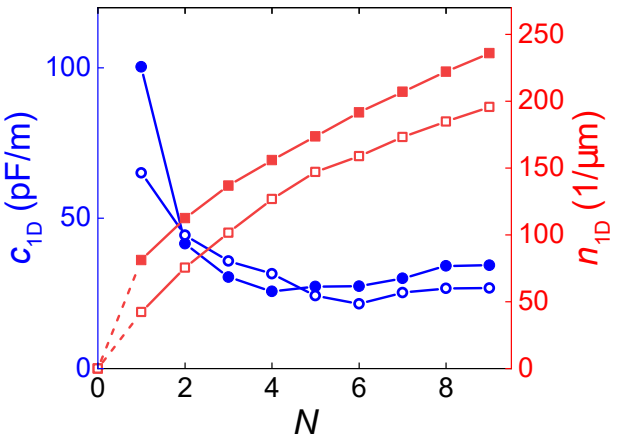

Figure 4.4: Blue circles, left axis: 1D capacitance and red squares, right axis: 1D carrier density of the QPC, deduced from $\delta\varepsilon(N)$ for a hard-wall confinement potential (filled symbols) and a parabolic potential (open symbols).

Clearly, the variations in capacitance as a function of N explain the counter-intuitive result that the subband spacings $\delta\epsilon(N)$ strongly vary in a region of almost equal widths of the plateaus of quantized conductance of the pinch-off curve, cf. Fig. 4.1 and Fig. 4.2.

4.4 QPC emission profiles

In this section, we use the experimentally determined subband spacings $\delta\varepsilon(N)$ shown in Fig. 4.2 and our quantum mechanical model introduced in section 3.5 to compare the emission properties of QPCs modeled by (i) the hard-wall potential and (ii) the parabolic saddle-point potential. Above, we described the analytic form of the hard-wall- and the parabolic potential at the point of maximum confinement at the center of the QPC constriction. Below show the two-dimensional continuation of both the hard-wall and parabolic potential as we used them in our quantum mechanical simulations.

Hard-wall potential. Within the hard-wall model, we write the 2D potential as

$$\Phi(x,y) = \begin{cases} e(x,\omega_x)\phi_0 & |y| \leq \frac{W}{2} + \sqrt{(R_0 - \frac{W}{2})^2 - x^2} \\ 4e(x,\omega_x)E_\mathrm{F}^0 & \text{else} \end{cases} \tag{4.14}$$

using the coordinate system indicated in Fig. 4.5(a). $e(x,\omega_x)$ is an envelope function as described below. The electrostatic potential defined in equation (4.14) has a discontinuity along two semicircles modeling the semicircular shape of the split gates defining the QPC. The width W and the offset potential Φ_0 at the QPC center determines the mode structure of the QPC. These parameters are directly obtained from the measured subband spacings and depend on $N(V_\mathrm{g})$ as shown in Fig. 4.3. The radius $R = R_0 - W/2$ of the semicircles decreases with increasing width of the QPC center modeling the shrinking of the gate depleted region when the gate voltage is increased, cf. sketch in Fig. 4.5(a). Since the precise shape of the electrostatic potential towards the free 2DES is not exactly known, we use R_0 as a fit parameter to match the lateral width of the experimentally determined beam profile. To model the transition of the electrostatic potential between the 1D channel and the free 2DES in current direction, we assume a smooth function in order to ensure reflectionless transmission through the QPC. This is implemented by a smooth version of the envelope function

$$e(x;\omega_x) = \begin{cases} 0, & |x| \geq \frac{L_\mathrm{QPC}}{2} \\ 1 - \frac{m\omega_x^2 x^2}{2E_\mathrm{F}^0}, & \text{else} \end{cases} \tag{4.15}$$

where the channel length $L_\mathrm{QPC} = \frac{2}{\omega_x}\sqrt{\frac{2E_\mathrm{F}^0}{m}} = 2R_0 - W$ such that the function $e(x,\omega_x)$ is continuous. We plot the envelope function in Fig. 4.5(b). In the quantum mechanical simulation, we use a version of $e(x,\omega_x)$ that connects smoothly to the free 2DES over a length $L_\mathrm{QPC}/12$ on both sides of the QPC. We show a top view of the final implementation of the hard-wall potential in Fig. 4.5(c).

Parabolic saddle point potential. For comparison, a parabolic saddle point potential connecting continuously to the free regions with vanishing potential can be defined as

$$\Phi(x,y) = e(x;\omega_x)\left(\Phi_0 + \frac{m\omega_y^2 y^2}{2}\right), \tag{4.16}$$

where $\hbar\omega_y = \delta\varepsilon(N)$ is the subband spacing. To simulate a parabolic QPC at the N'th conductance plateau we set $\Phi_0(N) = E_\mathrm{F}^0 - N\hbar\omega_y$. We show the corresponding two-dimensional QPC potential for $N = 7$ in Fig. 4.5(d).

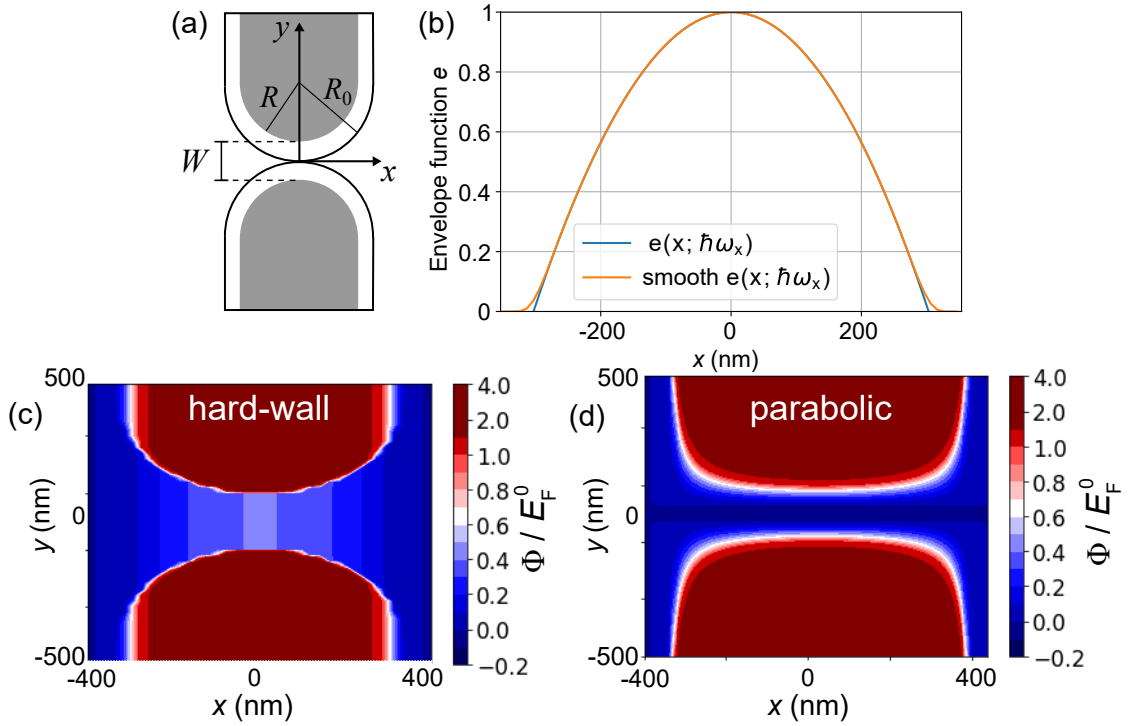

Figure 4.5: (a) Top view of a QPC with gate-voltage dependent width W and tip radius R. R_0 is a fit-parameter, cf. main text. (b) Envelope function $e(x;\omega_x)$ as defined in eq. (4.15) (blue) and the smoothed version used in the quantum mechanical simulation (orange). (c) Hard-wall potential modeling a QPC and (d) smooth potential modeling a parabolic QPC for $N = 7$. The lateral potential geometry at the center of the QPC (at $x = 0$) is obtained from the quantum well parameters shown in Fig. 4.3

In Fig. 4.6, we present calculated emitted probability densities in the free 2DES for a given electrostatic QPC potential, normalized such that $\int_{-\infty}^{\infty} |\Psi(y)|^2 \mathrm{d}y = 1$. We first consider $N = 1$ with the corresponding measured subband spacing $\delta\varepsilon(N = 1) \simeq 5\,\mathrm{meV}$ and directly compare the corresponding calculated spatial probability density $|\Psi(x',y)|^2$ behind the hard-wall QPC [panel (a)] and the parabolic QPC [panel (b)]. For the calculations, we choose $R_0 = 200\,\mathrm{nm}$. $x' = x - L_{\mathrm{QPC}}/2$ is the x-coordinate relative to the 'detachment point' where the QPC potential has vanished and the electron beam propagates in the free 2DES. We additionally plot the lateral beam profile $|\Psi(y)|^2$ at various x' in panel (c). For both QPCs, the lateral pattern resembles a symmetric Gaussian profile centered at $y = 0$. From the drop of the amplitude along y we deduce an emission angle θ. To quantify θ, we look at the lateral beam profile in the far field sufficiently far away from the QPC ($x' > 1\,\mu\mathrm{m}$) and define $\theta = \arctan(w(x)/x)$. $w(x)$ is the beam width obtained from the y-coordinate where the amplitude dropped to $1/e^2$ relative to the peak amplitude for a given x, $|\Psi(x,w(x))|^2 = |\Psi(x,0)|^2/e^2$. We find $\theta \simeq 20°$ for the hard-wall model and $\theta \simeq 24°$ for the parabolic model.

As the beam propagates along the free 2DES (in x-direction), the beam profile widens and

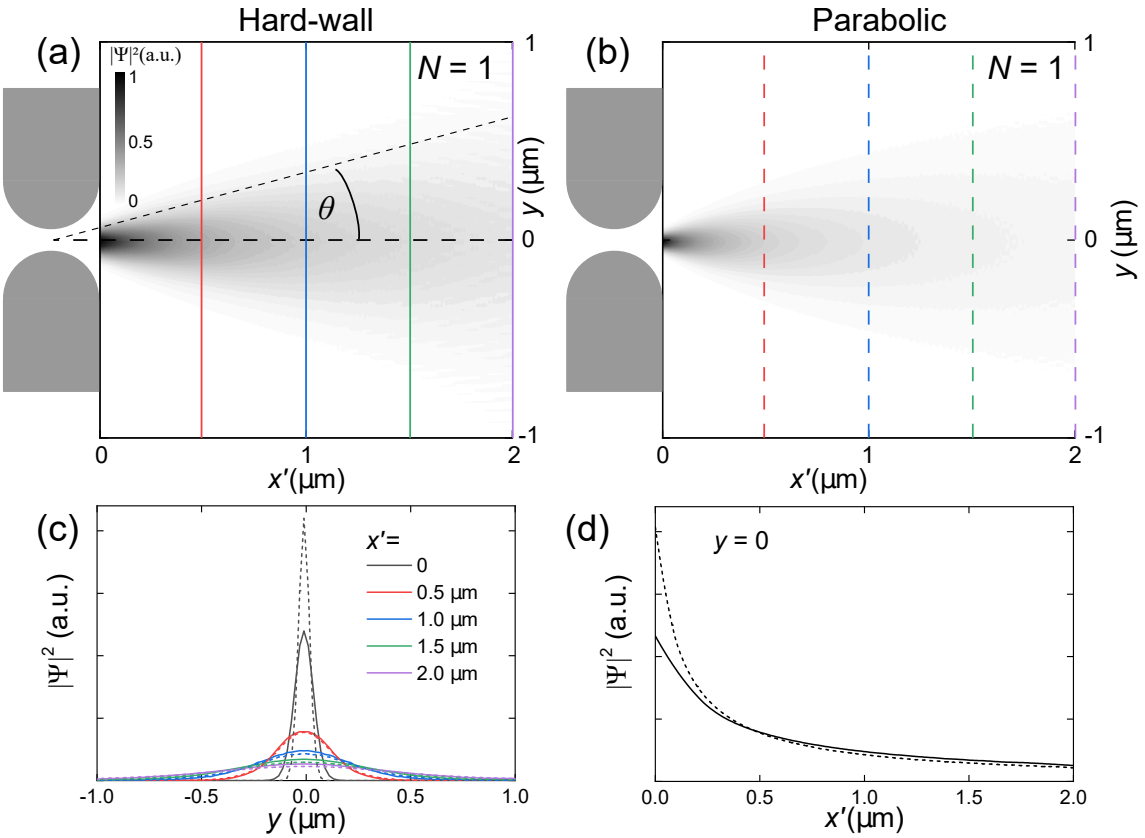

Figure 4.6: Spatial electronic probability density $|\Psi(x,y)|^2$ behind a QPC at $N = 1$ and $B = 0$, modeled by the hard-wall (a) and the parabolic saddle point potential model (b). The depleted QPC region is sketched for comparison. We indicate the emission angle θ in panel (a). x' is measured with respect to the point where the QPC potential vanishes. (c) $|\Psi(y)|^2$ for various x' of the corresponding color in (a, solid lines) and (b, dashed lines). (d) $|\Psi(x')|^2$ for $y = 0$. Solid lines: hard-wall model, dashed lines parabolic model.

the central maximum decays. We additionally show the decay of the peak height, $|\Psi(x')|^2$ for $y = 0$ in panel (d). Throughout the propagation, the integral over the lateral profile stays constant and equal to one (not shown), as we assume a perfectly flat (free) 2DES without reflections. Due to the parabolic confinement, the corresponding beam profile at the exit of the QPC at $x' = 0$ is slightly narrower.

Next, we extend the comparison between both QPC potentials to higher QPCs conductances $G = NG_Q$ with $N = 1,3,5$ and 7 and plot the corresponding calculated beam profiles in Fig. 4.7. Again, we model the QPCs using the subband spacings $\delta\varepsilon(N)$ shown in Fig. 4.2 and the QPC potential discussed above. For both the hard-wall and the parabolic model, the beam pattern clearly shows the coherent QPC mode structure by means of N local maxima of the lateral beam profile for $G = NG_Q$. Analog to the fundamental mode for $N = 1$, which we replot in the left two panels, all beam patterns broaden as they expand into the free 2DES. Additionally, higher conductances give rise to a wider beam pattern,

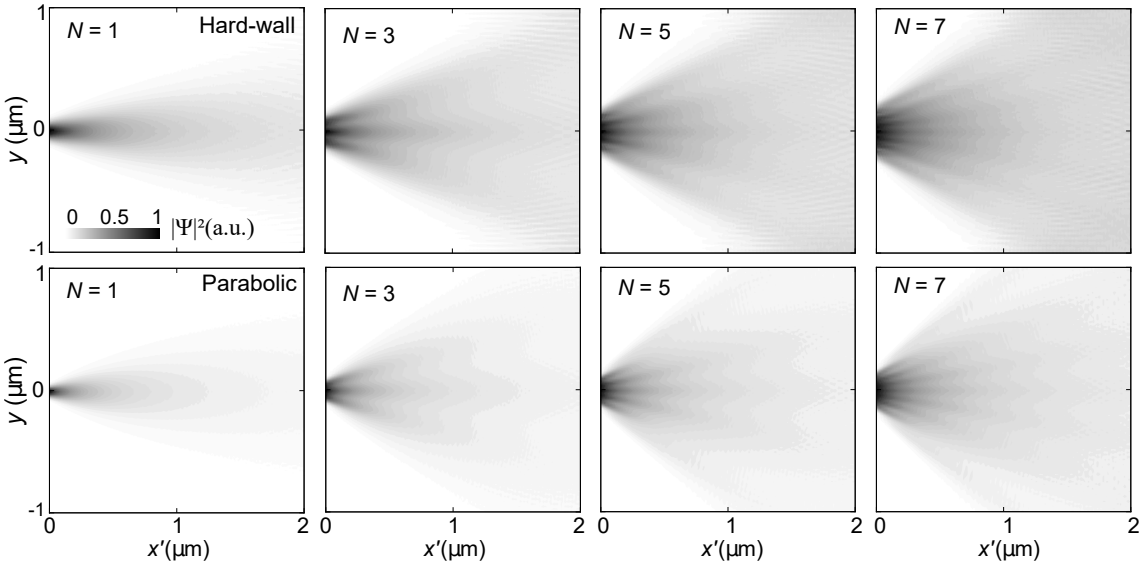

Figure 4.7: Calculated beam profiles for the hard-wall model (top panels) and the parabolic model (lower panels) for $N = 1,3,5$ and 7 (left to right).

reflecting the transverse momentum components increasing with N.

Next, we focus on the dependence of the emission angle θ introduced in Fig. 4.6(a) on N. In Fig. 4.8, we plot $\theta(N)$ for the hard-wall model [panel (a)] and the parabolic model

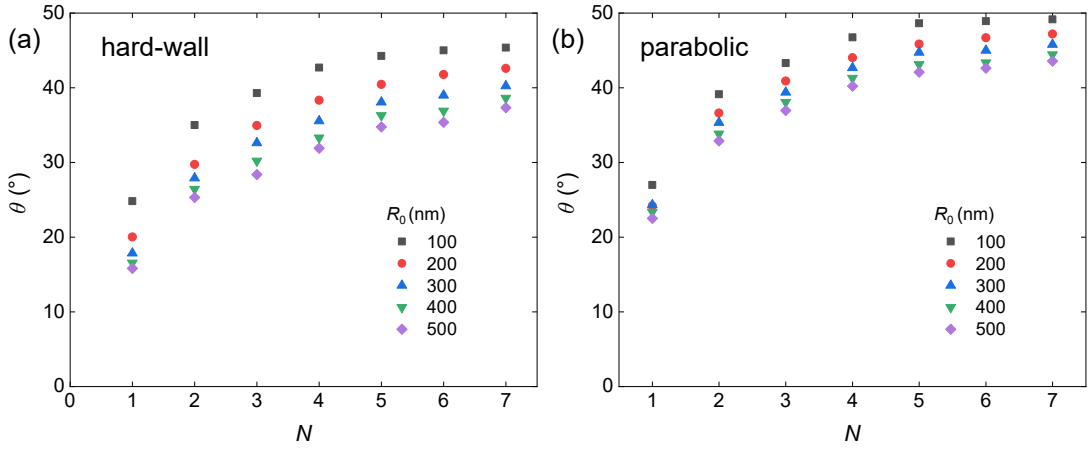

Figure 4.8: Calculated emission angles θ as a function of N for various R_0 for (a) the hard-wall model and (b) the parabolic model.

[panel (b)]. For both models, θ increases for a given value of R_0 as we open the QPC from $N = 1$ and saturates towards $N = 7$. The parabolic model gives rise to slightly larger emission angles than the hard-wall model for a given N. We additionally consider different values for the parameter R_0 (colored symbols), which is related to the longitudinal extent

of the QPC as explained above. Longer QPCs (larger R_0) result in smaller emission angles for given N.

The assumption of QPCs as perfect point sources is a starting point for the design of ballistic quantum circuits based on the simple laws of ray optics. However, as we demonstrate in Fig. 4.9, the realistic emission process of our gate defined QPC features deviations from this simple model. We display the calculated current density assuming the hard-wall potential with the experimentally determined subband spacings (cf. Fig. 4.2) and the corresponding gate voltage (and hence N-) dependent constriction widths W and tip radius R for $N = 1$,4 and 7 with $R_0 = 200\,\mathrm{nm}$. For $N = 4$ and 7, the coherent lateral mode structure features N local maxima. Due to interference, the local maxima do not propagate along straight trajectories but slightly bend as they enter the free 2DES (indicated by solid black lines as guide to the eye in Fig. 4.9). This behavior is also known from coherent laser beams frequently described by the Gaussian beam model [89]. Only sufficiently far away from the QPC the maxima diverge linearly, allowing us to indicate an approximate emission angle θ as discussed above. Due to this funnel-like emission process, every local lateral beam maximum has a slightly different apparent focus point for a given N, which we obtain from the intersection of the linear extrapolations of the beam pattern in the far-field back to the QPC, cf. dashed colored lines in Fig. 4.9. The QPC is thus not a perfect point source for electrons. This trend becomes stronger for larger N. Additionally, the course of the local maxima also varies as the length of the QPC (along x-axis) is changed with N: for larger N, the length of the QPC becomes shorter, and the beam detaches earlier from the QPC into the free 2DES. These issues make it impossible to design a gate layout for a coupling tool (such as an electrostatic lens or -mirror) which perfectly focuses the entire beam onto a single point, as there are slightly different angles of incidence for each local maximum (that additionally depend on N). However, the gate layout for a coupling device can in principle be optimized for a given mode, for example the fundamental mode at $N = 1$.

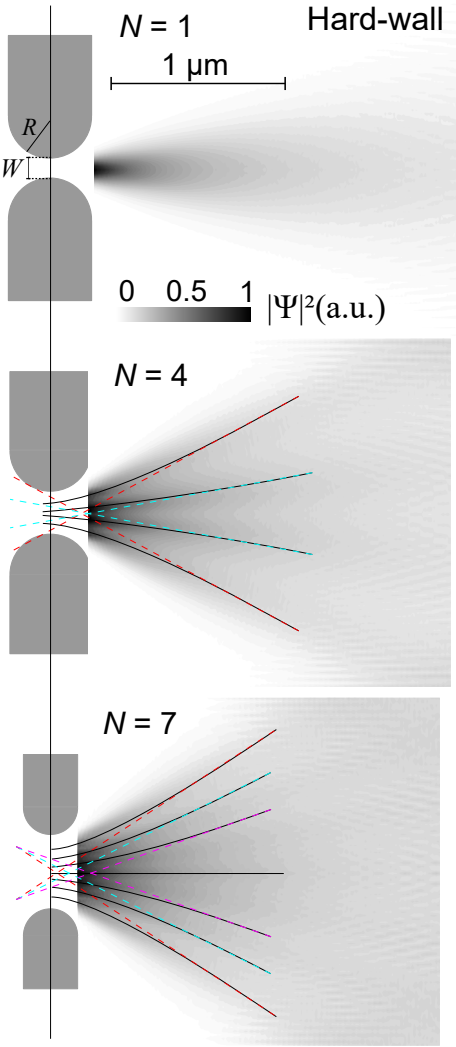

Figure 4.9: Calculated beam profiles using the hard-wall potential for $N = 1$,4 and 7. For $N = 4$ and 7, the funnel-like emission process becomes evident

The funnel-like carrier emission described above leads to losses due to slight astigmatisms for coupling tools like electrostatic lenses or mirrors, introduced in the following chapters, limiting the maximum possible serial transmission through distant QPCs. Furthermore, our calculations assume a perfect (flat) free 2DES without disorder. In contrast, a realistic

2DES always features a weak random background disorder potential due to ionized dopants in the donor layer [cf. Fig. 1.1(a)], giving rise to branched electron flow [5] even in high mobility wafers, further limiting the transmission through serial QPCs.

5 Ballistic electron optics

A thorough understanding of the carrier emission process from a single QPC into the free 2DES is central for the design of quantum circuits including multiple QPCs. In particular, in this project, we are interested in maximizing the transmission through two distant QPCs using the concept of ballistic electron optics [28–32]. In the most simple picture, QPCs serve as emitters and detectors for ballistic electrons which propagate through the 2DES at constant velocity along perfectly straight trajectories (similar to light rays in vacuum). Upon penetration of regions with a different nonzero carrier density than the surrounding free 2DES, ballistic electrons are refracted. On the boundary to depleted regions in the 2DES, they are specularly reflected.

In the following chapters, we use this picture to design an electrostatic electron lens (chapter 6), an elliptical mirror (chapter 7) and parabolic mirrors (chapter 8) to couple two distant QPCs via a region of grounded 2DES. In Fig. 5.1, we present exemplary measurements showing the transmission probability $t_{21} = T_{21}/N$ (with the transmission T_{21} defined in section 3.3 and N the number of incoming 1D channels) through two QPCs in series for all three devices. We add AFM (SEM) microscope images showing each device as insets.

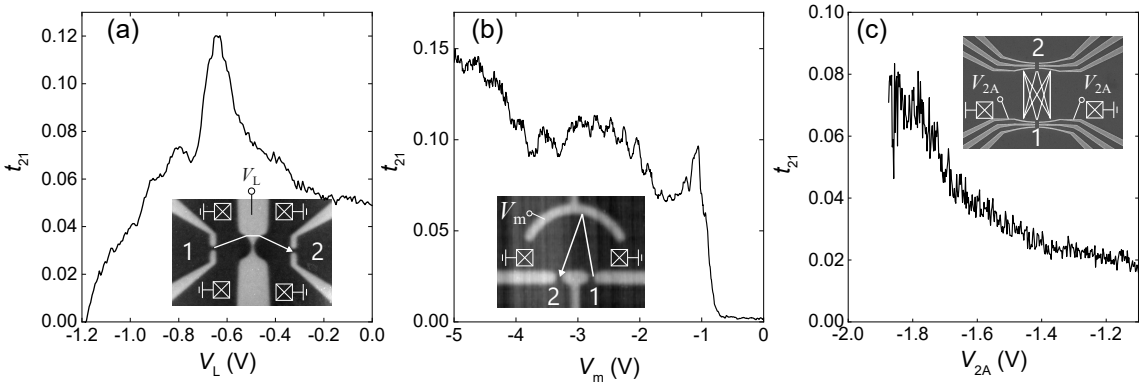

Figure 5.1: Gate voltage dependent transmission probability t_{21} through two serial QPCs at $B = 0$ in three different devices shown as insets. (a) Electrostatic electron lens. (b) Elliptical arc mirror. (c) Parabolic mirrors. The central region of the 2DES between the QPCs is electrically grounded.

For these measurements, we set the QPCs to a known conductance by adjusting the corresponding gate voltage (for example by tuning them to a quantized conductance plateau) and sweep the voltage applied to a gate used to tune the coupling between the QPCs.

We indicate the gate voltage swept for every measurement in the insets of Fig. 5.1. For practical applications, we aim at maximizing the transmission through two serial QPCs without an external magnetic field, at $B = 0$. Nevertheless, B represents an important experimental parameter to explore the spatial current distribution and to manipulate the phase of ballistic electrons.

For all three devices, the serial transmission can be enhanced by tuning the gate voltage, but stays limited to a transmission probability below 15 %. In the following chapters, we present a detailed analysis of the three devices shown above.

6 Coherent electron optics with ballistically coupled quantum point contacts

In this chapter, we consider two QPCs tuned to their quantized conductance regimes that interact by the exchange of ballistic electrons via a free, i.e., grounded, region of 2DES.[1] We demonstrate that the mutual coupling can be strongly enhanced by fine tuning an electrostatic lens [30,31] between the two QPCs. In Fig. 6.1 we display the surface partly covered by metal gates used to define the two QPCs and the lens.

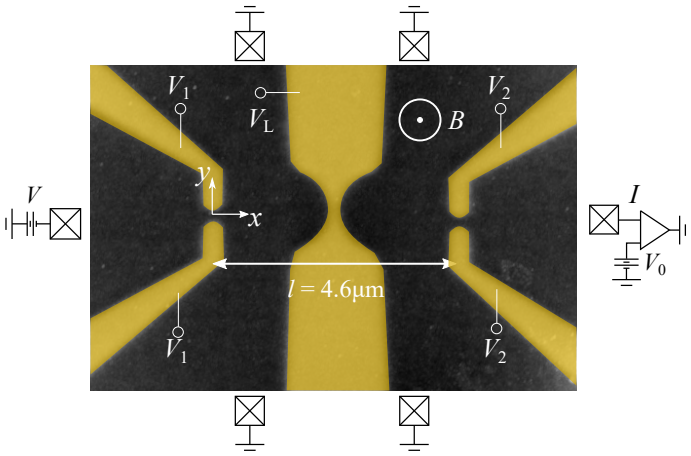

Figure 6.1: Atomic force microscope (AFM) image of the sample and corresponding circuit diagram. Metallic gates (light areas) are patterned on the sample surface (dark). Negative voltages V_1, V_2 and V_L electrostatically define QPC_1, QPC_2 and the concave lens. Crossed boxes display macroscopic Ohmic contacts far away from the nanostructure. A source-drain voltage V is applied at one of the QPCs while the detector current I is measured at the second QPC. The central region of the 2DES is electrically grounded. An external magnetic field B can be applied perpendicular to the 2DES.

The lens functions by refocusing carriers diverging from one QPC into the second QPC. For studying this *electrostatic focusing* we combine it with *magnetic deflection* [18,90] in a field perpendicular to the 2DES. (We avoid the common term *magnetic focusing*, as a homogeneous magnetic field merely deflects currents.) With this combination we determine

[1] This chapter presents results of *Phys. Rev. Lett. 125.* 107701 (2020) (Ref. [78]). See section B for the contributions of each author.

the angular resolved emission spectrum of the QPCs, which carries the coherent modes of the 1D constrictions, and explore electrostatic focusing between QPCs. The measurements presented in this chapter are performed within an (Al,Ga)As/GaAs heterostructure containing a 2DES located 107 nm beneath its surface on wafer mbe8-309 (see section A.1). The 2DESs Fermi energy and actual mean free path measured at cryogenic temperatures are $E_{\mathrm{F}}^{0} \simeq 11\,\mathrm{meV}$ and $l_{\mathrm{m}} \simeq 24\,\mu\mathrm{m}$.

6.1 QPCs

For a basic characterization we present linear response pinch-off curves of the individual QPCs in Fig. 6.2(a). The current as a function of voltages V_1, V_2 applied to the QPC gates

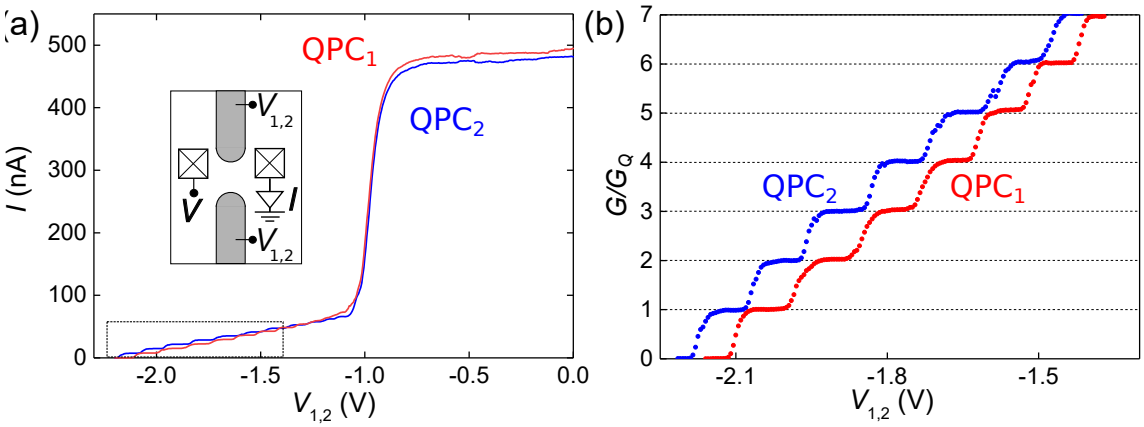

Figure 6.2: (a) Pinch-off curves $I(V_{1,2})$ for QPC_1 (red line) and QPC_2 (blue line) measured separately (with $V_{2,1} = 0$). (b) Conductance $G(V_{1,2})$ (with $V_{2,1} = 0$) of both QPCs in units of G_Q in the region indicated by a dotted rectangle in (a). The curves are corrected for the lead resistance of $300\,\Omega$.

decreases sharply as the constriction is formed at the depletion voltage around $-1\,\mathrm{V}$. For $V_{1,2} < -1\,\mathrm{V}$, both QPCs feature a series of quantized conductance plateaus, highlighted by the dashed rectangle. In Fig. 6.2(b), we plot the conductance as a function of gate voltages $V_{1,2}$ in units of the conductance quantum G_Q. The curves are corrected for the lead resistance $R_l = 300\,\Omega$ using $G = (V/I - R_l)^{-1}$. Both QPCs feature flat conductance plateaus at integers of G_{Q}. Smooth steps between the conductance plateaus suggest reflectionless transmission between the free 2DES and the QPCs. This indicates smooth (parabolic) potential barriers in current (x-) direction. We parameterize our measurements with the coupled system of both QPCs in terms of the number of conducting 1D modes N of QPC_1 and M of QPC_2, which define the quantized conductance plateaus via $N,M = G_{1,2}/G_{\mathrm{Q}}$.

One of the nominally identical QPCs used in this experiment, QPC_1, has been thoroughly characterized by finite bias voltage spectroscopy measurements, see chapter 4 above.

6.2 Setup and basic concept of the measurements

The experimental data presented here are all direct current (dc) measurements using the current amplifier model 1211 of DL Instruments. As voltage sources for the gates and the source-drain voltage we used the model 7651 of Yokogawa. All measurements presented here were performed in a helium-3 evaporation cryostat and, if not stated otherwise, at a temperature of $T_B \simeq 250\,\mathrm{mK}$. In Fig. 6.3(a), we show a simplified circuit diagram of the

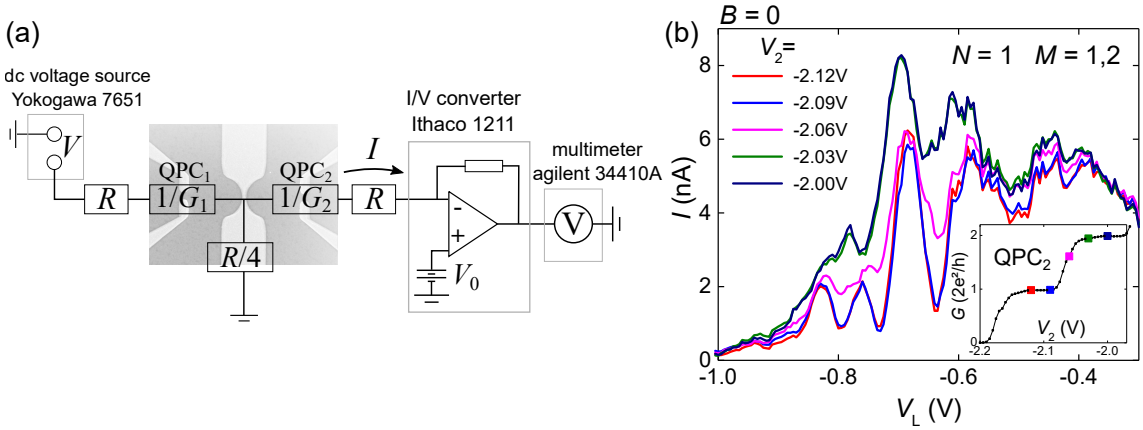

Figure 6.3: (a) Equivalent circuit diagram of the sample including the measurement instruments. (b) Measured detector current $I(V_L)$ at $B = 0$ for the emitter (QPC_1) tuned to the center of the first plateau ($N = 1$) at source-drain voltage $V = -1\,\mathrm{mV}$ while the detector (QPC_2) is tuned to various values between $M = 1$ and $M = 2$ by varying V_2. The detector conductance is indicated in the inset.

measurements described in this chapter. In section 2.2.1, we show further details of the experimental setup.

For the experiments we applied a source-drain voltage of $V = -1\,\mathrm{mV}$ across the emitter QPC while we measured the serial current I behind the second (detector) QPC. I is additionally influenced by a small offset input voltage V_0 caused by the I/V converter. In our experiments, we try to keep V_0 as low as possible. The QPCs are resistors that take values $1/G_{1(2)} = h/(N(M)2e^2)$. Every lead and its Ohmic contact (cf. crossed boxes in Fig. 6.1) represents a resistor R. The central region between the QPCs is grounded by four leads. Together they cause the side resistance $R/4$, cf. Fig. 6.3(a).

If not stated otherwise, we adjust the gate voltages such that the QPCs are tuned close to the centers of the respective conductance plateaus, cf. Fig. 6.2(b). To study the coupling between the two QPCs, we consider the current $I_{N,M}(V_L,B)$ flowing through both QPCs in series while (i) sweeping the voltage V_L applied to the concave lens gate and/or (ii) varying the external perpendicular magnetic field B. In the following we show the strong sensitivity of the serial current flowing through both QPCs as we change the number M of occupied 1D modes in QPC_2. The lower inset of Fig. 6.3(b) shows the pinch-off curve for QPC_2 with $M \leq 2$. In the main figure we present the detector current, i.e., the current through both QPCs in series (with V applied to QPC_1 and I measured behind QPC_2) as

a function of the lens gate voltage V_L at $B = 0$. The emitter QPC_1 is tuned to its first conductance plateau ($N = 1$) while the detector is tuned to various conductance values between $G_Q \leq MG_Q \leq 2G_Q$ as indicated in the lower inset. Traces $I(V_L)$ measured with the detector on one and the same plateau are almost identical even in small details. In contrast, we observe large variations between traces measured for different detector conductance. This result demonstrates that the current profile between the QPCs is directly related with the occupied eigenmodes of the QPCs. The latter stay unchanged as long as both QPCs remain on their respective plateaus. However, the mode structure and current profile rapidly change as soon as the conductance of one of the QPCs is changed.

6.3 Magnetic deflection

To study the divergence and lateral mode structure of the QPCs we perform magnetic deflection experiments without electrostatic focusing [21,22] while QPC_1 is set to conductance plateau N and QPC_2 is set to conductance plateau M. We apply a dc voltage of $V = -1\,\mathrm{mV}$ across the emitter QPC and measure the current I flowing to ground through the detector QPC, as a function of the perpendicular magnetic field B, cf. Fig. 6.4(a). Electrons move ballistically between the QPCs as their distance of $l \simeq 4.6\,\mu\mathrm{m}$ is smaller

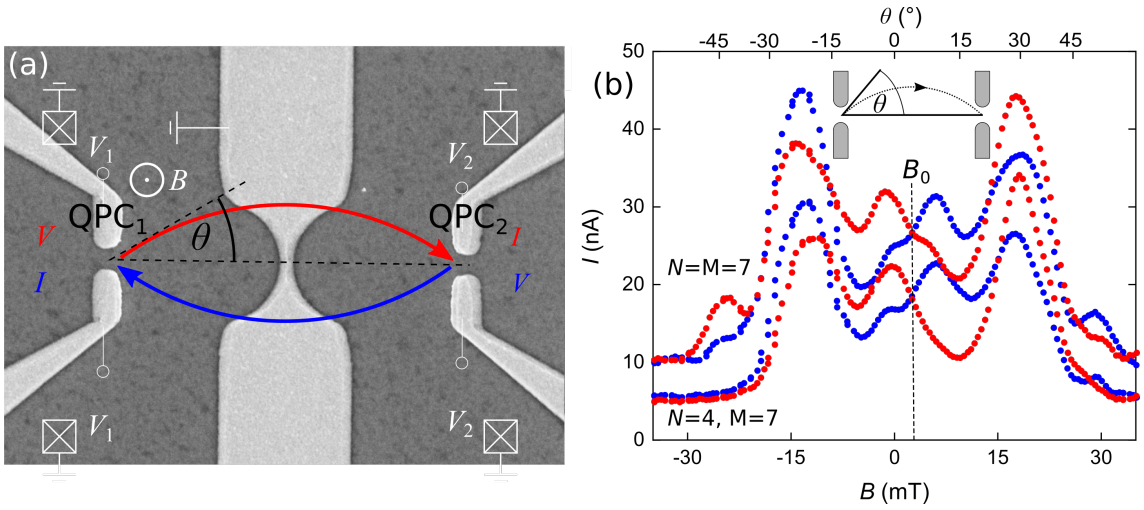

Figure 6.4: (a) Magnetic deflection experiment with grounded lens gate, $V_L = 0$. By exchanging the external voltage source for the source-drain voltage V and the current amplifier detecting I, we change the current direction (blue/red). (b) Measured detector current $I(B)$ while both QPCs are on their 7th plateau (upper curves) and the emitter QPC at $N = 4$ with the detector QPC at $M = 7$ (lower curves). Blue and red data points correspond to electron flow directions as indicated by the colored arrows in in panel (a).

than l_m. Classically, the magnetic field exerts the Lorentz force on ballistic electrons, causing them to propagate in a circle with the cyclotron radius $r_c(B) = m^\star v_F/|eB|$. To estimate the emission angle of ballistic electrons from the magnetic field dependence of the

serial current through both QPCs, $I(B)$, we in the following use the simplifying picture of a point-source-like electron emission from the QPC center. Using this picture, we geometrically derive at which angle θ ballistic electrons are emitted if they contribute to the current through the detector QPC at a given magnetic field, $\theta(B) = \arcsin(leB/2m^{\star}v_{\mathrm{F}})$, cf. Fig. 6.4(a). Our QPCs are aligned in series, such that ballistic carriers emitted at a larger angle reach the detector at a higher field.

In panel (b), we plot the measured serial currents $I(B)$ for electrons emitted by QPC_1 to be detected by QPC_2 (red curves) and the reversed current direction (blue curves). For each curve, the detector QPC is set to $M = 7$. For the lower curves, we set the emitter QPC to $N = 4$ and for the upper curves to $N = 7$. The approximate (within the picture of point-like electron emission from a QPC) emission angles $\theta(B)$ are shown on the top axis. The symmetry between both current directions is predicted by the Onsager-relations [91] for a multi-terminal device, here $I(B)|_{\leftarrow} = I(-B)|_{\rightarrow}$, where arrows indicate the opposite current directions. An offset of the symmetry point (vertical dashed line) is caused by a small residual perpendicular magnetic field of $B_0 \simeq 2.57\,\mathrm{mT}$. The residual field B_0 originates from slightly magnetized connector pins nearby the sample. Slight deviations from perfect symmetry can be attributed to the in-plane component of the residual field $\perp B$ or to magnetic impurities. Surprisingly, the $I(B)$ patterns do not show a maximum around $B = 0$, which would be expected for the serial transmission of two QPCs without additional potentials in the free 2DES.

The bimodal $I(B)$ patterns with maxima around $B = \pm 15\,\mathrm{mT}$ could in principle be related to disorder potentials, even if the mean free path exceeds the device size. In this regime we expect small angle scattering, e.g. originated by charged defects such as the ionized donor atoms, to have a small influence on the quantum mechanical phase of the carrier dynamics. However, even a single hard-wall, i.e., large angle scatterer can alter the ballistic properties completely by reflecting carriers and thereby generating a standing waves pattern.

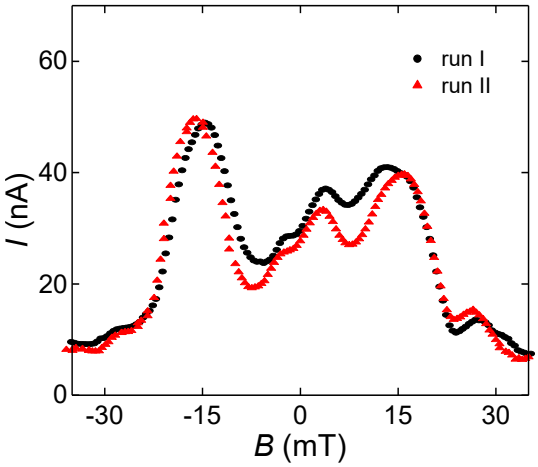

Figure 6.5: $I(B)$ through both QPCs, tuned to $N = M = 7$. Black dots: measured $I(B)$ in run I. Red triangles: same measurement after warming up, illuminating and cooling down the sample again (run II).

To experimentally explore the influence of disorder, we performed the some of our measurements twice in separate runs. However, between the two runs we warmed the sample up to room temperature, illuminated it with daylight and than cooled it back down. Because this procedure affects many defects by excitation and diffusion, the potential landscape induced by defects should vary between the two runs. We present a typical result in Fig. 6.5, which shows the measured currents through both QPCs as a function of the magnetic field for $N = M = 7$. The two curves are very similar with identical features for both runs.

We conclude that the traces $I(B)$ are not strongly influenced by disorder. Instead, as we will show in section 6.4.1 below, the bimodal $I(B)$ patterns are caused by a piezoelectric potential located at the waist of the lens gate.

6.3.1 Diffusive current contribution

Electrons which do not traverse both QPCs ballistically are either backscattered through the emitter or diffuse to the grounded side contacts. The resistance between the center region and ground is $\simeq 37\,\Omega$, small compared to the QPC resistances exceeding $1.8\,\mathrm{k}\Omega$ for $N \leq 7$ in our measurements. Nevertheless, the backscattering from the macroscopic, i.e., Ohmic leads connecting the region between the QPCs to ground causes a small diffusive contribution I_{diff} to the detector current, such that $I = I_{\mathrm{ball}} + I_{\mathrm{diff}}$. Here, I_{ball} is generated by carriers moving ballistically between emitter and detector. Below, we demonstrate how we achieve a clean a separation between the ballistic and diffusive contributions to the measured current $I(B)$.

Both, I_{ball} and I_{diff} can be directly determined from our magnetic deflection measurements. In Fig. 6.6(a) we plot $I(B)$ where we keep the detector QPC_1 fixed at $M = 7$ and open the

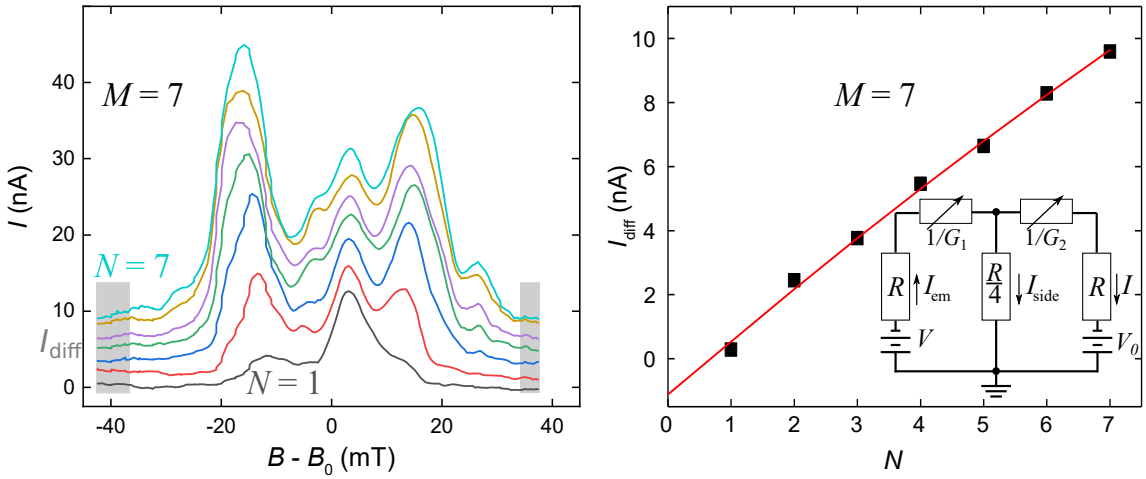

Figure 6.6: (a) $I(B)$ for detector QPC_2 with $M = 7$ and emitter QPC_1 opening from $N = 1$ to $N = 7$. (b) Black dots: magnetic field independent diffusive detector current contribution $I_{\mathrm{diff}}(N)$ obtained from $I(|B| > 35\,\mathrm{mT})$ for $N =\leq 7$ and $M = 7$ in panel (a), gray shaded areas. Red line: model curve according to equation 6.1 with $V_0 = -1.07\,\mu\mathrm{V}$ as fit parameter. Inset: simplified circuit diagram of the present sample.

emitter QPC_2 from $N = 1$ to $N = 7$. These measurements include the blue data points in Fig. 6.4(b). There is no lens defined between the QPCs as $V_{\mathrm{L}} = 0$. At high enough magnetic fields, here for $|B - B_0| > 35\,\mathrm{mT}$, the cyclotron diameter of the ballistic electron orbits becomes smaller than the distance between the two QPCs, $2r_{\mathrm{c}} = m^{\star} v_{\mathrm{F}}/|e(B-B_0)| < l = 4.6\,\mu\mathrm{m}$, such that ballistic carriers emitted from one QPC can no longer reach the second QPC. This is the case in the regions shaded in gray in Fig. 6.6(a). The current

flowing through the detector QPC for $|B - B_0| > 35\,\mathrm{mT}$ is diffusive and independent of B for moderate fields where Landau quantization is negligible. The diffusive current I_{diff} is caused by the voltage drop across the detector, QPC_2. In the inset of Fig. 6.6(b) we sketch a simplified circuit diagram of our setup which contains the Ohmic resistances relevant in the diffusive transport regime. For simplicity we assume identical resistances, R, of all leads indicated in Fig. 6.1 as crossed squares. Note that independent characterization measurements of the sample with all gates grounded, i.e. no QPCs and no lens defined, yielded indeed approximately identical lead resistances of $R = 144 \pm 0.5\,\Omega$ for the six leads of the sample. $1/G_1$ and $1/G_2$ are the tunable resistances of the two QPCs. The current amplifier connected to the detector QPC causes a small additional input offset voltage V_0 to the sample. Using Kirchhoff's circuit laws for the circuit sketched in panel (b) with the QPC conductances $G_1 = NG_{\mathrm{Q}}$ and $G_2 = MG_{\mathrm{Q}}$ we find

$$I_{\mathrm{diff}} = G_{\mathrm{Q}} M \frac{V R G_{\mathrm{Q}} N - V_0\,(5 R G_{\mathrm{Q}} N + 4)}{6 (R G_{\mathrm{Q}})^2 N M + 5 R G_{\mathrm{Q}} (N + M) + 4}. \tag{6.1}$$

The black squares in panel (b) show I_{diff} extracted from panel (a) next to a model curve according to equation 6.1 with the fit parameter $V_0 = -1.07\,\mu\mathrm{V}$.

6.3.2 Ballistic transmission

Aiming at a direct comparison with model predictions, we next subtract the B-field independent I_{diff} [cf. Fig. 6.6(b)] from the raw data [cf. Fig. 6.6(a)] and present $I^{\mathrm{ball}}_{N,M=7}(B) = I_{N,M=7}(B) - I^{\mathrm{diff}}_{N,M=7}(B)$ in Fig. 6.7.

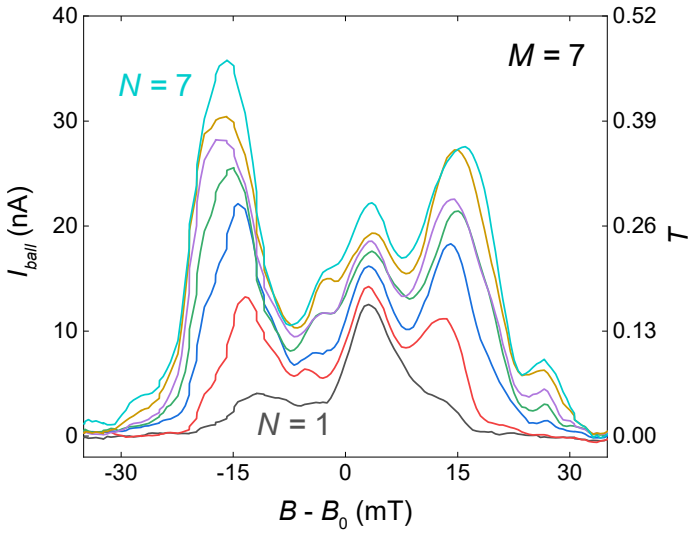

Figure 6.7: Same data as shown in 6.6a after subtraction of the diffusive current contribution, $I_{\mathrm{ball}}(B) = I(B) - I_{\mathrm{diff}}(B)$, for $N = 1,2,3..,7$ and $M = 7$. Right axis: corresponding total transmissions $T(B) = I_{\mathrm{ball}}(B)/V_{\mathrm{QPC}} G_Q$.

Following the Landauer-Büttiker formalism introduced in section 3.3, we define the total transmission of the N conducting modes as $T_{N,M=7}(B) = I^{\mathrm{ball}}_{N,M=7}(B)/V_{\mathrm{QPC}}G_Q$, shown on the right axis in Fig. 6.7. Here, V_{QPC} is the voltage drop across the emitter QPC only, i.e.

$$V_{\mathrm{QPC}} = \frac{V}{G_1\left[(R+1/G_1)+\left(4/R+\frac{1}{1/G_2+R}\right)^{-1}\right]}.$$

6.3.3 Calculated transmission matrix

To predict $T_{N,M}(B)$ we numerically solve the Schrödinger equation for a single electron moving in a 2D Fermi gas connected to ideal (reflectionless) leads. We account for the estimated dephasing length (cf. equation 3.10) of $l_\phi \simeq 0.5\,\mu$m by energy averaging, where l_ϕ is dominated by bias broadening. To mimic the measured mean free path of $l_{\mathrm{m}} \simeq 24\,\mu$m we include a weak homogeneous absorbing potential between the QPCs. To model the lateral confinement of the QPCs we use a hard wall potential, where its gate voltage dependent width and depth (at the center of the constrictions) are determined from the subband spacings plotted in Fig. 4.2 following the analysis shown in chapter 4. The opening of the constrictions towards the leads follow the semicircular shape of the gates. The lens potential controlled by the gate voltage V_{L}, cf. Fig. 6.1, is added on demand.

From the solution of the Schrödinger equation we extract the total transmission probability $T_{N,M}(B,V_{\mathrm{L}}) = \sum_{n,m} t_{n,m}$ of a ballistic and coherent electron through the two QPCs in series with the first (second) QPC set to the N-th (M-th) conductance plateau. Here, $t_{n,m}$ are the individual probabilities for an electron emitted from the nth mode of the emitter to transmit through the mth subband of the detector. In Fig. 6.8(a), we present the calculated $t_{n,m}(B)$ for $n = 1$ and $m = 1,2,3,4$. The serial transmission is similar to the convolution integral of the localized wavefunctions in QPC_1 and QPC_2. The individual $t_{n,m}(B)$ thus show alternating maxima/minima at $B = 0$ as n (or m) is changed by 1.

In our experiments, we performed measurements with up to seven occupied subbands in $\mathrm{QPC}_{1,2}$. The corresponding total transmission matrix with elements $t_{n,m}$ and $n,m \leq 7$ is presented in Fig. 6.8(b). We consider slowly varying QPC potentials and neglect coherent reflections into the QPCs. In this limit, $t_{n,m}$ do not depend on the gate voltages for $n \leq N$ and $m \leq M$ and can be reconstructed from the total transmissions as $t_{n,m} = T_{N,M} - T_{N-1,M} - T_{N,M-1} + T_{N-1,M-1}$. The Landauer formula relates $T_{N,M}(B,V_{\mathrm{L}})$ to the measured ballistic current, $T_{N,M}(B,V_{\mathrm{L}}) = I^{\mathrm{ball}}_{N,M}(B,V_{\mathrm{L}})/G_{\mathrm{Q}}V_{\mathrm{QPC}}$. For instance, the measured current for $N = M = 7$ contains contributions of all 49 elements of the transmission matrix.

6.3.4 Comparison between experiment and coherent model calculations

For a first direct comparison between experiment and coherent model calculations we consider $T(B)$ for $N = 1$ and $M = 7$. The measured data are plotted as blue dots in Fig. 6.9(a).

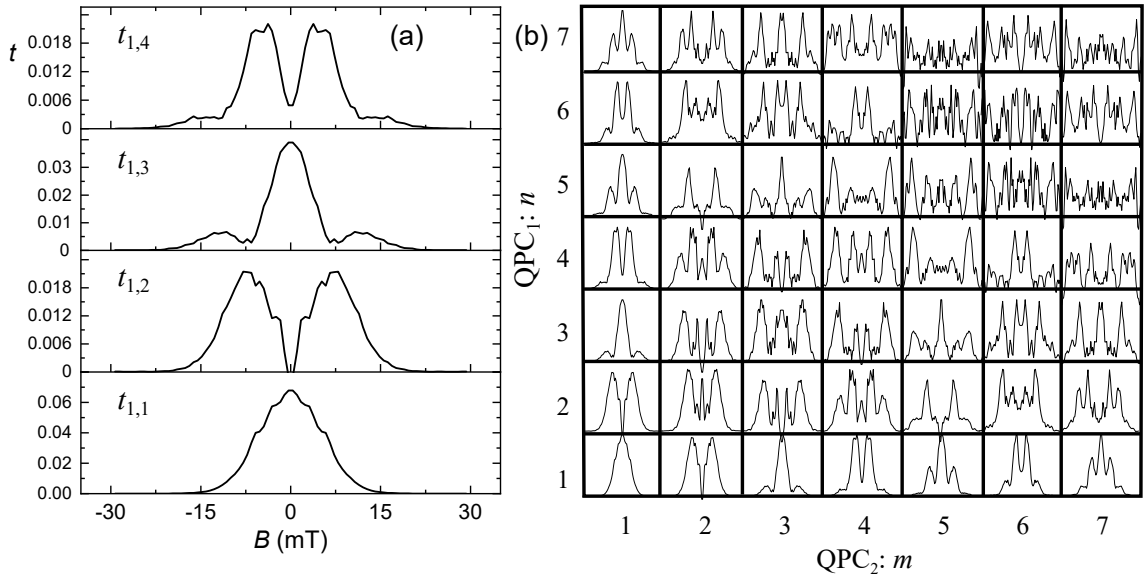

Figure 6.8: (a) Calculated transmission probabilities $t_{n,m}(B)$ for $n = 1$ and $m = 1,2,3,4$. The simulations were performed for $V_{\mathrm{L}} = 0$ (no lens) and a flat electrostatic potential between the perfectly aligned QPCs and show the average over energy to simulate temperature and source-drain voltage broadening. (b) Calculated $t_{n,m}(B)$ for $n,m \leq 7$. Each panel shows $t_{n,m}(B)$ between the nth mode of QPC_1 and the mth mode of QPC_2. $B = 0$ at vertical symmetry axes. For $N = M = 7$ the total transmission is the sum of all shown elements, $T_{N=7,M=7} = \sum_{n=1,m=1}^{N=7,M=7} t_{n,m}$.

The corresponding calculated transmission $T_{N=1,M=7}(B) = \sum_{m=1}^{7} t_{N=1,m}(B)$ assuming a flat 2DES without additional potentials and perfectly aligned QPCs is plotted as a dashed red line. This profile corresponds to the summation over all elements of the lower row in the transmission matrix shown in Fig. 6.8(b). While the widths of the patterns are comparable, we observe two characteristic differences between the experiment and the calculation: the measured data (i) show a decreased transmission around $B = 0$ and (ii) are asymmetric in B.

The decreased transmission around $B = 0$ is a consequence of a piezoelectric potential dip which is located at the lens waist and caused by strain developing during the cool down after the evaporation of the metal gates, see also section 6.4.1. Accounting for such a potential dip in the calculations results in the double peak structure in panel (a), dashed gray line. The dip splits the current peak centered at $B - B_0 = 0$ in two while the symmetry in magnetic field is preserved.

The additional breaking of the B symmetry in our measurements is a consequence of slight lateral shifts between the nanostructures, as shown in the AFM image in Fig. 6.9(b). The solid black line in panel (a) shows the calculated pattern after accounting for both the piezoelectric potential dip and slight lateral shifts of the nanonstructures. For better agreement with theory we used slightly smaller shifts than the ones extracted from the AFM data.

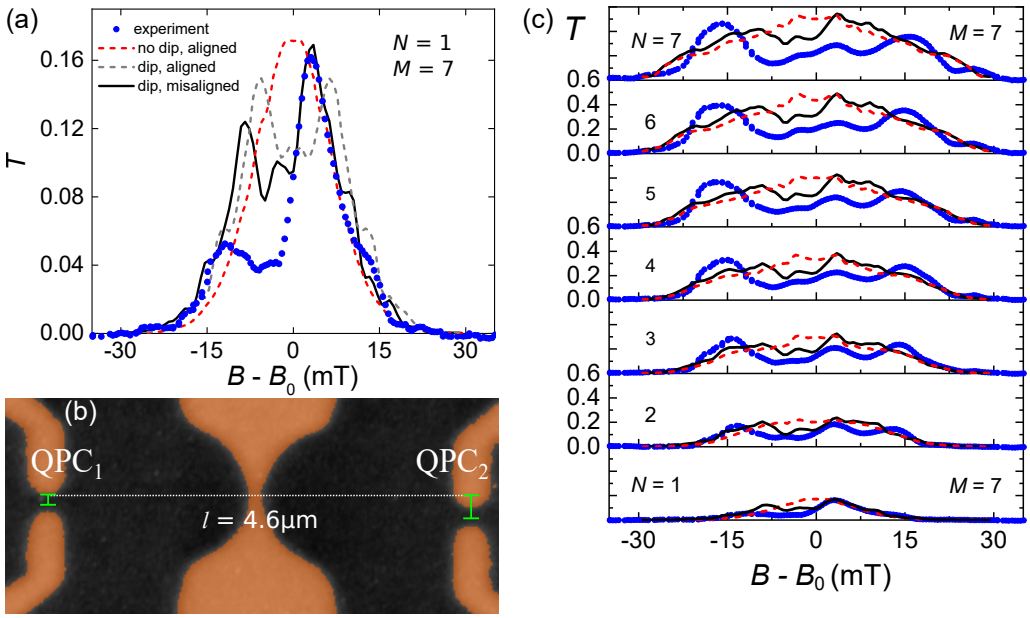

Figure 6.9: (a) Blue dots: measured $T(B)$ at $N = 1$ and $M = 7$. Lines are calculated $T_{N=1,M=7}(B)$. Dashed red line: for a flat 2DES (without dip) and perfect alignment of the QPCs. Dashed gray line: including the potential dip for perfectly aligned QPCs. Black solid line: including both the potential dip and the misalignment of the QPCs with respect to the lens. (b) AFM image of the sample surface. Light color corresponds to the metal gates. Green bars depict the lateral shifts of the QPCs from the waist of the lens (dashed horizontal line) by 80 nm and 260 nm, respectively. (c) Like (a) but for all for $N = 1,2,3,...7$ and without the calculated data for aligned QPCs with a potential dip at the lens waist.

For completeness, we additionally plot in Fig. 6.9(c) the measured total transmissions for all $N \leq 7$ as blue dots in direct comparison to (i) the calculated $T_{N,M=7}(B) = \sum_{n=1,m=1}^{N,M=7} t_{n,m}(B)$ assuming a perfect sample without shifts and the piezoelectric potential dip (red dashed line) and (ii) the calculated transmission accounting for the imperfections (black solid line). While the calculations for the realistic potential geometry still overestimate the transmission around $B - B_0 = 0$, accounting for the sample imperfections substantially improves the agreement with the experiment and reproduces its main features.

To reveal the mode structure of individual QPC subbands, we next consider the measured transmission differences $\Delta T_{N,M=7}(B) \equiv \left[I^{\text{ball}}_{N,M=7}(B) - I^{\text{ball}}_{N-1,M=7}(B)\right]/G_{\text{Q}}V_{\text{QPC}}$. Using $I^{\text{ball}}_{N,M}(B)/V_{\text{QPC}}G_Q = T_{N,M}(B) = \sum_{n=1,m=1}^{N,M} t_{n,m}(B)$, we aim at subtracting the contributions of the $(N-1) \times M$ lower mode to mode transmission probabilities, $\Delta T_{N,M=7} = \sum_{m=1}^{7} t_{N,m}$ for $N \leq 7$. These elements correspond to the summation over all elements in one row of the transmission matrix in Fig. 6.8(b).

In Fig. 6.10, we directly compare the measured $\Delta T_{N,M=7}(B)$ [panel (a)] to the bare model

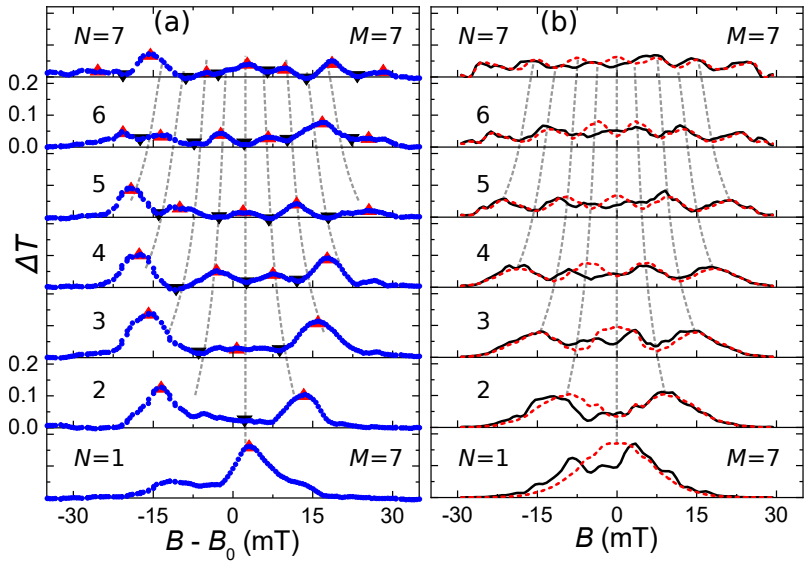

Figure 6.10: Measured (a) versus calculated (b) transmission differences $\Delta T_{N,M=7}$. Model curves in (b) for perfect symmetry and zero lens potential (red dashed) and with corrections of the QPC positions and accounting for the piezoelectric dip of the lens potential (solid black lines). Maxima and minima of $\Delta T_{N,M=7}$ are marked in panel (a) with red (black) triangles. Dashed gray lines [identical in (a) and (b)] connect the nth maxima for odd (even) N and the nth minima for even (odd) N.

predictions $\Delta T_{N,M=7} = \sum_{m=1}^{7} t_{N,m}$ for perfectly aligned nanostructures and a flat 2DES [red dashed lines in panel (b)]. Both, measured and predicted curves display a growing magnetic field range of finite I_{ball} as N is increased, confirming a larger aperture angle of carriers emitted from a QPC at higher modes. Our measured data roughly follow the features of the model curves, albeit they show additional fine structure and a reduced symmetry. The black solid lines in Fig. 6.10(b) are the result of the more realistic model taking into account (i) the slight lateral misalignment of the QPCs with respect to each other and the principal axis of the lens breaking the B-symmetry and (ii) the piezoelectric dip beneath the lens. These modifications improve the agreement between our model and experiments.

The comparison between our measurements and the model calculations demonstrates that a detailed knowledge and fine control of the sample properties are key for a successful engineering of the dynamics of ballistic carriers. The combination of (i) and (ii) results in additional features in $T(B)$ [cf. Fig. 6.9(c)] and $\Delta T(B)$ [cf. Fig. 6.10(b)] similar to our experimental observations, albeit the agreement is not perfect: Compared to our model, our measurements show enhanced transmissions of the outermost maxima in $\Delta T(B)$ for $N \lesssim 5$. This is also visible as an almost bimodal current distribution of the measured $T(B)$ in Fig. 6.9(c) (blue dots). We attribute the differences to the scattering properties of the electrostatic potential dip. Not knowing its detailed shape, we assume a parabolic dip with smooth edges. Compared to our measurements, it slightly underestimates the reduction of $(\Delta)T(B)$ around $B = 0$. Such deviations between theory and experiment illustrate our limited knowledge of the exact potential landscape. More accurate predictions

might be reached with self-consistent calculations solving the 3D Poisson and Schrödinger equations.

Next we focus on the interference pattern of the transmission curves $\Delta T_{N,M=7}$, which expresses the lateral coherence in our setup. The N maxima of each of the fully coherent model curves [red dashed lines in Fig. 6.10(b)] reflect the order of the lateral eigenmodes. The dashed gray lines in Fig. 6.10(b) connect the nth maxima for odd (even) N. They also cut through the nth minima for even (odd) N as expected for the interference pattern. In Fig. 6.10(a) the same lines (shifted in B) approximately connect corresponding maxima and minima of the measured data similar as for the model data including imperfections [blue lines in (b)]. This behavior is a fingerprint of the coherent mode structure of the QPCs.

6.3.5 Classical model calculations

In order to identify coherent effects we additionally compare our results with a classical simulation of the magnetic deflection experiment.

For the comparison, we implement the parabolic saddle point potential defined in equation 4.16 with the subband spacings shown in Fig. 4.2 and $R_0 = 400\,\mathrm{nm}$ in both the coherent and the classical calculation. To compute the current for classical electrons we sample the lateral distribution function of free electrons at the center of the emitter QPC (in current direction). We calculate the trajectory of each sampling point as a function of the perpendicular magnetic field B numerically and determine whether it transmits through the detector and hence contributes to the current. In the classical simulation we neglect trajectories that involve multiple reflections between the QPCs.[2]

In Fig. 6.11(a), we show the classically and quantum mechanically computed magnetic deflection transmission profiles $T_{N,M}(B)$ for a perfectly aligned geometry and without the electrostatic potential dip at the lens waist. The QPCs are set to the same conductance plateau, $N = M$. The quantum mechanical solution exhibits oscillations that reflect the mode structure of the waves emitted from the QPC. These coherent oscillations are absent in the transmission profile for classical electrons. The envelope of the transmission profile of coherent electrons coincides with the classical result for large magnetic field strengths. For small magnetic fields there are electron trajectories involving reflections between the QPCs that contribute to the current through the setup. These trajectories are included in the quantum mechanical calculation but are neglected in the classical calculation. They yield an overall enhanced transmission for small magnetic field strengths in the quantum mechanical calculation compared to our classical solution. In our experiments, coherent Fabry-Pérot-like oscillations caused by standing waves between the QPCs are averaged out, as expected for the dephasing length of $l_\phi = 500\,\mathrm{nm}$ due to bias broadening, cf. measured data in Fig. 6.7. In our quantum mechanical calculation we account for the broadening by energy averaging. Nevertheless, the quantum mechanical solution in Fig. 6.11(a) contains high frequency oscillations at small magnetic fields which are a remnant of the Fabry-Pérot

[2]The classical calculation was realized and provided by Max Geier from the Dahlem Center for Complex Quantum Systems at the FU Berlin.

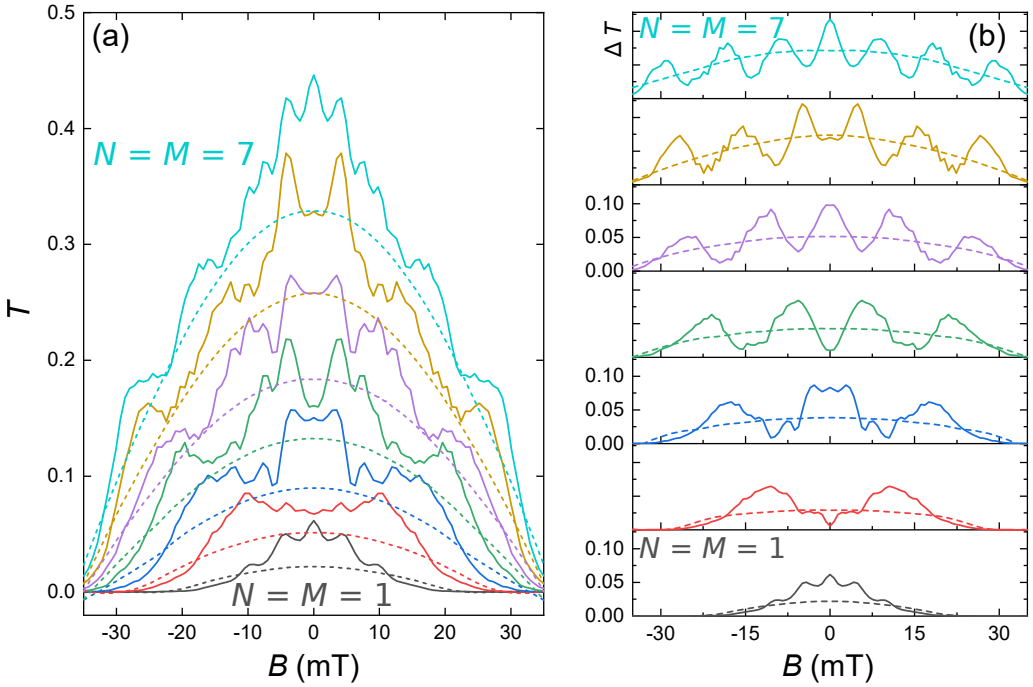

Figure 6.11: Comparison of quantum mechanically (solid lines) and classically (dashed lines) calculated (a) magnetic deflection transmission $T_{N=M}(B)$ and (b) corresponding first transmission differences $\Delta T_{N=M}(B)$ for a parabolic electrostatic QPC potential and a flat 2DES between two perfectly aligned QPCs. Both the emitter and the detector QPC are set to identical conductance plateaus with $N = M \leq 7$.

oscillations after averaging over the energy distribution of transmitting electrons. These remnants of the Fabry-Pérot oscillations are vulnerable to geometric imperfections and weak disorder contributing additional phase shifts to interfering paths.

In Fig. 6.11(b) we show the calculated first transmission differences $\Delta T_{N,M}(B) = T_{N,M}(B) - T_{N-1,M-1}(B)$ corresponding to panel (a) (with $N = M$). Since the coherent substructure is absent in the classical calculation, the first differences for the classical simulation show a smooth transmission maximum without oscillations, independently of N. In contrast, the quantum mechanical calculation clearly reflects the coherent QPC modestructure with N pronounced maxima for $\Delta T_{N=M}(B)$.

The lateral mode structure of the QPCs is visible in both, experimental results and quantum mechanical solution of their serial transmission, cf. Fig. 6.10(a,b). In contrast to the Fabry-Pérot-like oscillations discussed above, the lateral mode structure remains stable as long as the dephasing length is larger than the lateral distance of two adjacent maxima in the interference pattern of emitted electrons in real space. By choosing the bias voltage $V = -1\,\mathrm{mV}$ corresponding to a dephasing length $l_\phi = 500\,\mathrm{nm}$ (cf. Fig. 3.5), we are thus able to see the coherent lateral mode structure of the QPCs, while coherent Fabry-Pérot-like modes between the QPCs spaced by $l = 4.6\,\mu\mathrm{m}$ are averaged out.

6.4 Electrostatic focusing

For practical applications, we aim at maximizing the coupling of distant nanodevices without external magnetic fields. This can be realized by electrostatically refocusing the carriers emitted from one QPC to the other. For this purpose, we add a gate designed to define a concave spherical lens in the center between the two QPCs, cf. Fig. 6.1 [30, 31]. In a classical model with perfect geometry, the focusing properties are described by the electronic version of Snell's law with the refractive index for electrons defined as $n_\mathrm{r} = \sqrt{E_\mathrm{F}^0/E_\mathrm{F}^\mathrm{L}}$, where the Fermi energies below the lens gate E_F^L and elsewhere E_F^0 are assumed to be constants. As we are using a concave lens, focusing requires $n_\mathrm{r} > 1$ which we achieve by reducing E_F^L via applying $V_\mathrm{L} < 0$ to the lens gate. For the electrostatic focusing experiment, we set both the emitter QPC_1 and the detector QPC_2 to $N = M = 7$. In Fig. 6.12(a), we plot the calculated emitted current density using a realistic QPC potential geometry based on the measured QPC subband spacings, see chapter 4. The resulting electron beam (for zero B and no lens potential) is fairly wide and approximately matches the lens aperture, which we sketch for comparison.

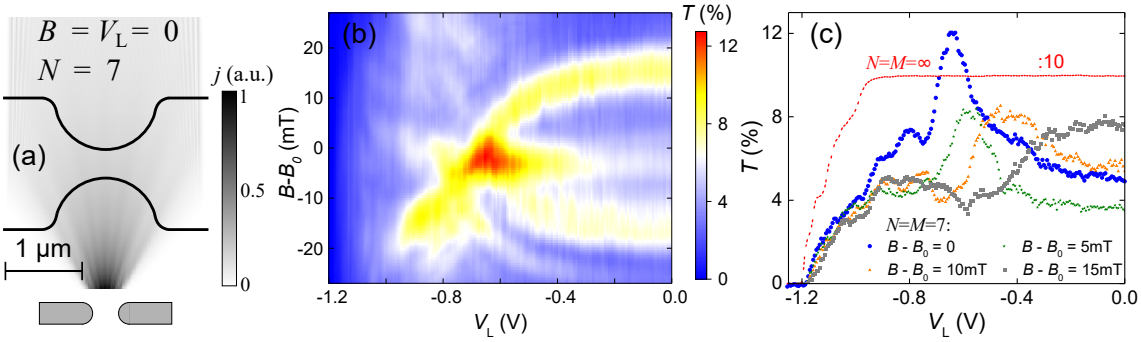

Figure 6.12: (a) Calculated current density emitted by QPC_1 modeled as hard wall potential for $N = 7$ at $B = V_\mathrm{L} = 0$ and without the electrostatic potential dip at the lens waist. We sketch the edge of the lens potential for comparison. (b) Measured serial transmission through both QPCs, $T(V_\mathrm{L},B)$ for $N = M = 7$ and QPC_1 as emitter. (c) $T(V_\mathrm{L})$ for various magnetic fields. For $B - B_0 = 0$ (blue) a pronounced maximum indicates focusing. Red dashed line: $T(V_\mathrm{L})$ of the lens gate without QPCs ($V_1 = V_2 = 0$).

To experimentally demonstrate the focusing effect, we combine electrostatic focusing and magnetic deflection and plot the measured transmission for $N = M = 7$ in Fig. 6.12(b). The magnetic deflection experiment shown in Fig. 6.7(a) (for $N = M = 7$) corresponds to the vertical cross section at $V_\mathrm{L} = 0$. While we decrease V_L, the current maxima bend inwards and eventually merge in a single peak at $B - B_0 = 0$ and $V_\mathrm{L} \simeq -0.64\,\mathrm{V}$, *a direct signature of electrostatic focusing*. In Fig. 6.12(c) we present various horizontal cuts $T(V_\mathrm{L})$ for constant B. Independent of B, the lens pinches off near $V_\mathrm{L} = -1.2\,\mathrm{V}$ similar as the lens' transmission curve without QPCs ($V_1 = V_2 = 0$), added as a red dashed line. Interestingly, the transmission maxima all lie within a range of V_L in which the lens itself has almost zero reflection, corroborating our interpretation in terms of electrostatic focusing.

6.4.1 Lens potential

While we measure electrostatic focusing as a function of the gate voltage V_L, model calculations are performed in terms of the electrostatic potential induced by the lens and parameterized by n_r or E_F^L. Aiming at a direct comparison, we present a detailed calibration of $n_\mathrm{r}(V_\mathrm{L})$ in this section.

The differences between the dispersion relations of light with the momentum $\propto 1/c$ and that of massive particles result in different refraction laws. The momentum of the relevant electrons is in our case proportional to its Fermi velocity v_F. In optics, the refractive index of a medium is defined as the ratio of the vacuum light speed c to the phase velocity c_m of light in the medium, $n_\mathrm{m} = c/c_\mathrm{m}$. In analogy, we define the relative refractive index of our electrostatic lens as $n_\mathrm{r} = v_\mathrm{F}^0/v_\mathrm{F}^\mathrm{L}$, where v_F^0 is the Fermi velocity of electrons in the bulk 2DES away from the lens and v_F^L its counterpart below the lens gate.

The focusing properties of a lens can be calculated by requiring a smooth transition between regions of different refractive index. In Fig. 6.13(a), we sketch two regions of different refractive indices (white/gray). Requiring the component of the momentum in the plane of the interface (along the y-axis) to remain constant yields Snell's law for light:

$$\text{for photons:} \quad n_\mathrm{m} = \frac{c}{c_\mathrm{m}} = \frac{\sin\delta_1}{\sin\delta_2}\,, \tag{6.2}$$

where δ_1 is the angle of incidence (in vacuum) and δ_2 the angle of refraction (in the lens). In contrast, we find a different refraction law for electron optics [30, 31]

$$\text{for electrons:} \quad n_\mathrm{r} = \frac{v_\mathrm{F}^0}{v_\mathrm{F}^\mathrm{L}} = \sqrt{\frac{E_\mathrm{F}^0}{E_\mathrm{F}^\mathrm{L}}} = \frac{\sin\delta_2}{\sin\delta_1}\,, \tag{6.3}$$

where we introduced the kinetic energies E_F^0 and E_F^L in the bulk 2DES away from the lens and below the lens gate, as sketched in Fig. 6.13(b). Using these kinetic energies, we define the electrostatic lens potential energy $\Phi_\mathrm{L} = E_\mathrm{F}^0 - E_\mathrm{F}^\mathrm{L}$. To achieve focusing for $n_\mathrm{r} > 1$, an optical lens must be convex while an electrostatic lens must be concave.

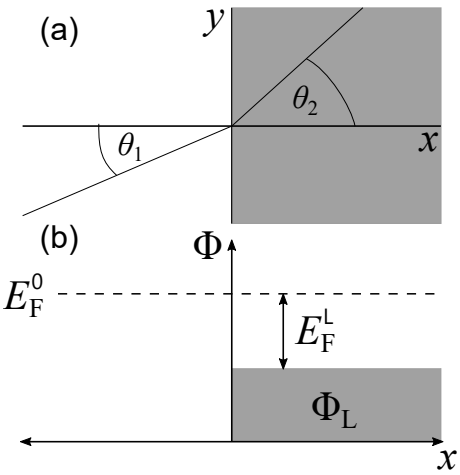

Figure 6.13: (a) Refraction at the interface between two regions with different refractive indices (white/gray). (b) Kinetic energies in the free 2DES E_F^0 and E_F^L in the region of finite lens potential Φ_L.

Below, we compare two different methods to experimentally calibrate the lens potential as a function of V_L: Landau-level reflection measurements [92] and a self-consistent approach by applying Snell's law for a given lens geometry. Comparison between the two methods reveals the dip of the lens potential discussed above.

6.4.1.1 Landau-level calibration

A viable method to calibrate the height of an electronic barrier is to measure the reflection of quantum Hall edge channels in a strong perpendicular magnetic field B. The edge channels are a consequence of the quantization of the density of states of the 2DES in Landau levels (LLs) with quantum number $l = 1,2,3,\ldots$. Taking into account the Zeeman splitting of the electron states, each LL results in two spin-resolved energy levels quantized at

$$E_{\pm}(l) = \hbar\omega_{\mathrm{c}}\left(l - \frac{1}{2}\right) \pm \frac{1}{2} g\mu_{\mathrm{B}} B\,, \tag{6.4}$$

where $\omega_{\mathrm{c}} = eB/m^{\star}$ is the cyclotron frequency, g is the Landé g-factor with $g \simeq -0.36$ in GaAs and μ_{B} the Bohr magneton. We denote the corresponding spin polarized edge channels by their filling factor $\nu = 1,2,3,\ldots$ defined as $\nu = 2E_{\mathrm{F}}^{0}/\hbar\omega_{\mathrm{c}}$. For instance at $\nu = 2.25$ the lowest two edge channels, corresponding to the lowest LL, are completely filled and one quarter of the states of (spin-up polarized) third level are also occupied.

For our calibration measurements, we apply a constant B such that the bulk 2DES (away from the gates) has an integer filling factor. By sweeping V_{L} we then gradually increase the lens barrier, hence decrease $E_{\mathrm{F}}^{\mathrm{L}}$ and the filling factor beneath the lens gate ν_{l}. Thereby, we detect the successive reflection of the individual edge channels at the barrier in terms of the corresponding resistance changes. In Fig. 6.14(a) we present an overview photograph of the wafer surface including bond pads and Ohmic contacts in the periphery. The position of the Ohmic contacts, labeled by numbers 1–6, are also indicated in panels (b) and (c), which show an SEM image of the central part of the lens gate and a sketch of the quantum Hall measurement set-up, respectively. In panel (c) we assume the filling factor of $\nu = 4$ in the bulk but $\nu_{\mathrm{l}} = 2$ below the lens gate, such that the third and the fourth edge channel (red) are reflected off the lens. As illustrated in Fig. 6.14(d), this reflection occurs for $\widetilde{E}_{\mathrm{F}}^{\mathrm{L}} < \nu_{\mathrm{L}}/2\,\hbar\omega_{\mathrm{c}} = \hbar\omega_{\mathrm{c}}$. Here $\widetilde{E}_{\mathrm{F}}^{\mathrm{L}}$ denotes the maximum of $E_{\mathrm{F}}^{\mathrm{L}}(y)$ taking into account a possible dip of $\Phi_{\mathrm{L}}(y)$ in the center of the lens. In our sketch $\widetilde{E}_{\mathrm{F}}^{\mathrm{L}}$ is centered in the gap between two LLs, such that below the lens gate [precisely at the minimum of $\Phi_{\mathrm{L}}(y)$] all states corresponding to filling factors $\nu = 1$ and 2 are occupied while states at higher energies, e.g. for $\nu = 3$ and 4, are empty. We expect to find the longitudinal resistance measured between contacts 3 and 2 across the lens [93, 94]

$$R_{32} = \frac{V_3 - V_2}{I_{41}} = \frac{h}{e}^{2}\left(\frac{1}{\nu_{\mathrm{L}}} - \frac{1}{\nu}\right)\,, \tag{6.5}$$

while applying a constant current between contacts 1 and 4. Likewise, between contacts 3 and 6 we expect to measure the transverse resistance across the lens gate

$$R_{36} = \frac{V_3 - V_6}{I_{41}} = \frac{h}{e}^{2}\frac{1}{\nu_{\mathrm{L}}}\,. \tag{6.6}$$

For simplicity we restrict the analysis of our calibration experiment to even filling factors ν and ν_{L} (and disregard features allocated to odd ν_{L}). In Fig. 6.15(a) we present the results of four terminal resistance measurements for the setups described by Eq. (6.6) and in panel (a) and according to Eq. (6.5) in panel (b). Each curve has been measured at constant B

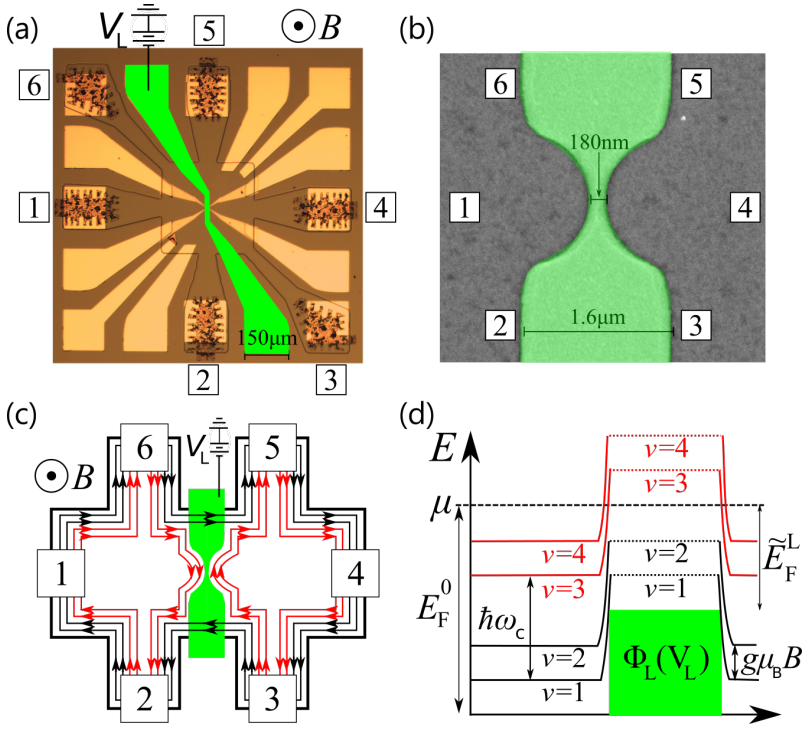

Figure 6.14: (a) Photograph of the sample with numbered Ohmic contacts and the lens gate highlighted in green. (b) SEM image of the concave shaped lens gate. (c) Sketch of edge channels at large B at integer filling factor $\nu_L = 2$ beneath the lens gate and $\nu = 4$ elsewhere. (d) Reflection of edge channels at the lens gate. Edge channels corresponding to the red quantized energy levels (with $\nu = 3,4$) are reflected at the lens barrier as their energy exceeds the chemical potential μ at the lens.

and bulk filling factors $\nu = 4,6,8,10,12$ while decreasing the filling factor beneath the lens gate by sweeping V_L from zero to the pinch-off point at $V_L = -1.2\,\mathrm{V}$. For a bulk quantum Hall measurement of the sample at $V_L = 0$, see Fig. 1.2(b).

Instead of the monotonous steps naively expected between resistance plateaus, we often find local resistance maxima. This phenomenon is related with an additional tunnel current between reflected edge channels via localized states below the thin barrier and has previously been observed in Ref. [94]. Where our measurements are close enough to the expected resistance plateaus (at the resistance values indicated by horizontal lines) we choose the center of these plateaus as calibration points $V_L(\nu_L)$ with

$$\frac{\widetilde{E}_F^L}{E_F^0} = \frac{\nu_L}{\nu}\,, \tag{6.7}$$

see Fig. 6.16(a) for the final calibration result. We assume that the chemical potential at the center of the plateaus lies exactly between two adjacent LLs, as sketched in Fig. 6.14(d). As expected, the calibration points obtained in this way turn out to be almost identical for the two alternative measurements presented in Fig. 6.15. The dependence $\widetilde{E}_F^L(V_L)$ is a

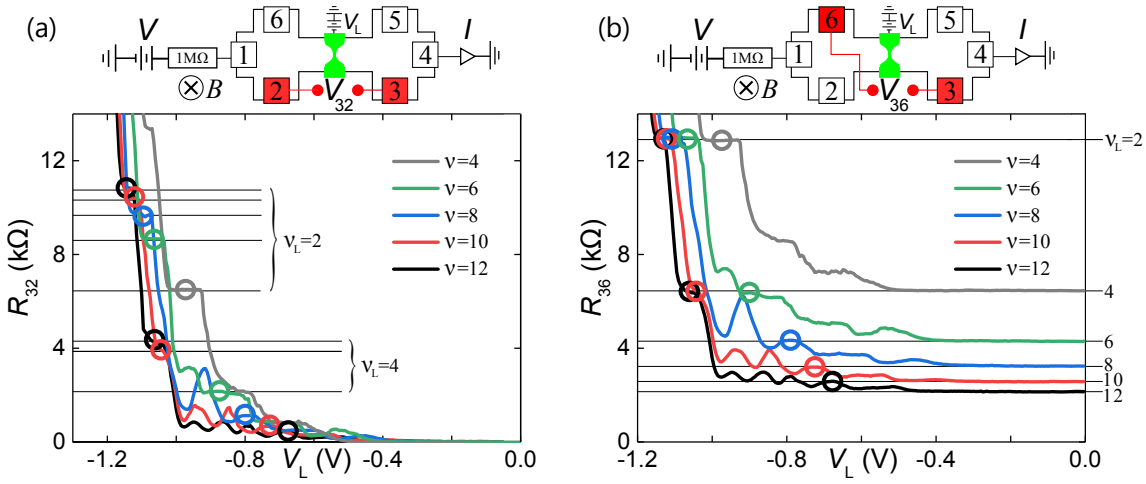

Figure 6.15: Longitudinal resistance $R_{32}(V_\mathrm{L})$ defined in Eq. (6.5) in panel (a) and transverse resistance $R_{36}(V_\mathrm{L})$ defined in Eq. (6.6) in (b). Each curve has been measured at constant B and fixed bulk filling factor ν with $V = -0.4\,\mathrm{V}$ applied at a $1\,\mathrm{M\Omega}$ series resistor causing an approximately constant current of $I \simeq 400\,\mathrm{nA}$ flowing from contact 1 into the grounded contact 4. Horizontal lines indicate plateaus expected at filling factors (ν,ν_L) according to Eq. (6.5) in (a) and Eq. (6.6) in (b) [not all expected plateaus are shown]. Our calibration points in the centers of the open circles are at identical values of V_L in (a) and (b). Top sketches: Four-terminal circuits of our Landau-level calibration measurements. A bulk ($V_\mathrm{L} = 0$) quantum Hall measurement of the present sample is shown in Fig. 1.2.

fingerprint of our heterostructure. The non-linear relation reveals a lens voltage dependent capacitance between the lens gate and the 2DES beneath. We conjecture that this behavior is related with a high-resistance conducting delta doped layer located between the wafer surface and the 2DES. This interpretation is supported by a finite longitudinal resistance $R_\mathrm{xx} \simeq 3\,\Omega$ at integer filling factors, compare Fig. 1.2(b). Since the carrier density (and mobility) in this layer likewise depends on the gate voltage, it causes a V_L-dependent screening between lens gate and 2DES.

In Fig. 6.16(b), we show the pinch-off curve $G(V_\mathrm{L})$ of the lens gate measured at $B = 0$ (solid line). Related with the concave shape of the lens gate it develops a few quantized conductance steps at integer multiples of G_Q, emphasized in the inset. They indicate a potential dip at the center of the lens forming a weakly confined QPC. Such a dip can be explained in terms of the piezoelectric effect of GaAs which gives rise to a sizable inhomogeneous built-in electric field below the lens gate. The piezo-field is caused by strain in response to stress at the metal-semiconductor interface built up during cool-down because of the different thermal expansion coefficients of the materials. The detailed build-in field depends on the geometry and orientation (as the piezo tensor is anisotropic) of the lens but can alter the potential $\Phi_\mathrm{L}(x,y)$ locally by up to several meV [95, 96]. Our LL calibration measures the absolute minimum of the barrier height, which is reduced at the dip located at the center of the lens. However, the focusing properties of the lens are predominantly determined by its curvature and potential further away from its center.

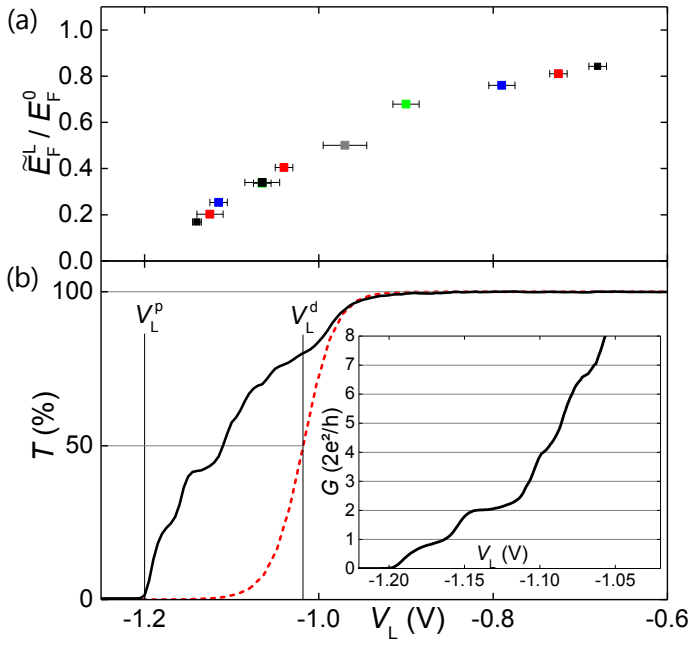

Figure 6.16: (a) Kinetic energy below the lens gate relative to the Fermi energy in the free 2DES as a function of lens gate voltage, $\widetilde{E}_F^L/E_F^0(V_L)$. Each point corresponds to a circle in Fig. 6.15 (same colors). Error bars correspond to the plateau widths in Fig. 6.15. (b) Solid black line: transmission through the lens gate, $T(V_L) = I(V_L)/I(V_L = 0)$ with $B = 0$ and no QPCs defined ($V_1 = V_2 = 0$). The pinch-off voltage is $V_L^p \simeq -1.2\,V$. Dashed red line: calculated transmission through a (one-dimensional 250 nm wide parabolic) barrier fitted to the depletion onset of the lens' pinch-off curve. It provides a rough estimate of the depletion voltage $V_L^d \simeq -1.02\,V$ where the 2DES is depleted beneath wide gates, i.e. outside of the central dip. Inset: For $V_L \lesssim V_L^d$ the lens conductance features two quantized conductance steps pointing to a 1D conducting channel through the central dip.

6.4.1.2 Self-consistent calibration

Our second calibration method aims at determining the lens potential in the wider concave regions away from the dip in its center. It relies on a self-consistent comparison of the measured focusing properties of the lens with our theoretical expectations. In Fig. 6.17 we present the transmission T through both QPCs in series tuned to their 7th conductance plateaus ($N = M = 7$). In panel (c) we re-plot the measured data $T(B,V_L)$ already presented in Fig. 6.12(b). To achieve a self-consistent calibration of the lens potential we first track the pronounced *measured* current maximum as a function of B and V_L, cf. dashed line in Fig. 6.17(c). Next, we track the corresponding maximum in the *calculated* transmission including the sample imperfections as a function of B and E_F^L, cf. dashed line in Fig. 6.17(b). By a point-by-point scaling of $(V_L,B) \to (E_F^L,B)$, we obtain the relation $E_F^L(V_L)$.

In addition to tracking the current maximum, we use the following features to quantitatively adjust the calibration result: (i) at the focus point measured at $V_L = -0.64\,V$

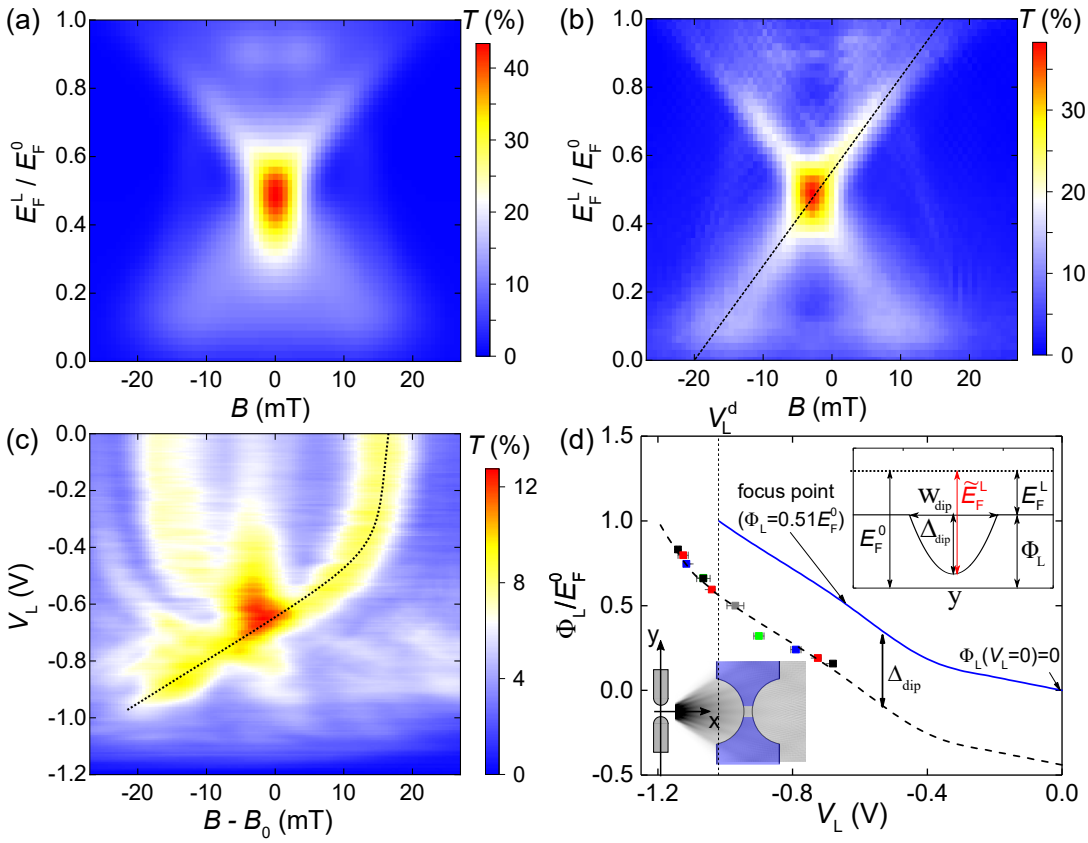

Figure 6.17: (a) Calculated serial transmission $T(E_{\mathrm{F}}^{\mathrm{L}},B)$ through two QPCs tuned to the 7th conductance plateau for a symmetric sample and a flat lens potential without potential dip. (b) Calculated $T(E_{\mathrm{F}}^{\mathrm{L}},B)$ including the slight lateral shifts between the QPCs and the lens potential dip at the lens waist. A dashed black line traces one of the main current maxima. (c) Measured transmission $T(V_{\mathrm{L}},B)$. A dashed black line traces one of the main current maxima. A point-by-point scaling of the two lines in (b) and (c) results in the calibration $E_{\mathrm{F}}^{\mathrm{L}}(V_{\mathrm{L}})$. (d) Comparison between the two calibration methods, plotting $\Phi_{\mathrm{L}}/E_{\mathrm{F}}^{0} = 1 - 1/n_{\mathrm{r}}^{2}$. The blue solid line indicates the result of the self-consistent and the colored symbols that of the LL lens calibration. The dashed black line is identical to the solid blue line but vertically shifted to fit the LL calibration points. The vertical shift can be interpreted as the dip depth Δ_{dip}. Top right inset: lateral model lens potential with parabolic dip, cf. main text. Bottom left inset: calculated quantum mechanical current density emitted from QPC_1 with $N = 7$.

our calculation predicts $E_{\mathrm{F}}^{\mathrm{L}} = 0.49E_{\mathrm{F}}^{0}$; (ii) we assume that the lens gate (away from its center, where it has a dip) has a negligible effect on the local potential at $V_{\mathrm{L}} = 0$ such that $\Phi_{\mathrm{L}}(V_{\mathrm{L}} = 0) = 0$; and (iii) we estimate the pinch-off point for the lens away from the center dip to occur at $V_{\mathrm{L}} \simeq -1.02\,\mathrm{V}$ which leads to $\Phi_{\mathrm{L}}(V_{\mathrm{L}} \simeq -1.02\,\mathrm{V}) = E_{\mathrm{F}}^{0}$.

In Fig. 6.17(d) we present the obtained relation as a solid line in comparison with our LL lens calibration (symbols). Assuming in our calculations a flat lens potential $\Phi_{\mathrm{L}}(V_{\mathrm{L}}) = E_{\mathrm{F}}^{0} - E_{\mathrm{F}}^{\mathrm{L}}(V_{\mathrm{L}})$ independent of y, we disregard the dip in the center of the lens. As such,

the self-consistent calibration approximately averages the lens potential weighted by the actual lateral current distribution (in y-direction). For $N = M = 7$ the lateral current distribution has two pronounced maxima away from the center of the lens. Underpinned by measured data, we argue that the current density is much smaller in the dip region, such that our second calibration mostly probes the lens potential away from its center.

With our second calibration method we predominantly determined the lens properties away from its center, hence outside its potential dip, while with our first calibration method we measured precisely the minimum of the electrostatic lens potential. Hence, we interpret the difference between the two results as being the depth of the dip. In Fig. 6.17(d) it is indicated as Δ_{dip}. Our data are consistent with a constant $\Delta_{\mathrm{dip}}(V_{\mathrm{L}})$, i.e., independent of V_{L}. This is expected if the electric field is generated by strain combined with the piezoelectric effect.

To model the 2D shape of the potential dip at the lens waist, we consider the pinch-off curve of the lens plotted in the inset of Fig. 6.16(b). Using the LL lens calibration we determine the corresponding one-dimensional subband spacing $\Delta E_{01} \simeq 0.7\,\mathrm{meV}$ from the step width between the two lowest quantized conductance plateaus. For a rough estimation we assume a parabolic potential dip in y-direction, which is centered in an otherwise flat barrier:

$$\Phi_{\mathrm{dip}}(y) = \Phi_{\mathrm{L}}(V_{\mathrm{L}}) - \Delta_{\mathrm{dip}} + \frac{1}{2} m^{\star} \omega_{\mathrm{dip}}^2 y^2 \qquad \text{for } |y| < W_{\mathrm{dip}}/2$$

$$\Phi_{\mathrm{dip}}(y) = \Phi_{\mathrm{L}}(V_{\mathrm{L}}) \qquad \text{for } |y| \geq W_{\mathrm{dip}}/2$$

where $\omega_{\mathrm{dip}} = \Delta E_{01}/\hbar$ is its curvature and $W_{\mathrm{dip}} = 2\hbar/\Delta E_{01}\sqrt{2\Delta_{\mathrm{dip}}/m^{\star}} \simeq 270\,\mathrm{nm}$ its width at $\Phi_{\mathrm{dip}}(y) = \Phi_{\mathrm{L}}(V_{\mathrm{L}})$, cf. top right sketch in Fig. 6.17(d). The dip width is indicated by the central gray region of the lens gate left out in the bottom left inset of Fig. 6.17(d). It is small enough to corroborate our assumption that the dip has only little influence on our second calibration method.

6.4.2 Comparison between experiment and coherent model calculations

The calibration $\Phi_{\mathrm{L}}(V_{\mathrm{L}})$ allows us to display coherent model calculations in the same coordinate system like our measurements. In Fig. 6.18 we directly compare the measured $T(B,V_{\mathrm{L}})$ [panel (a)] to the corresponding calculated transmission [panel (b)] for $N = M = 7$. In this calculation, we included the sample imperfections discussed above. The dashed lines in both panels are identical and serve as a guide for the eyes to facilitate comparison. The model calculations clearly reproduce the main features of our measurements in Fig. 6.18(a). For comparison, we also add the calculated $T(B,V_{\mathrm{L}})$ for a perfect sample, i.e. without lateral shifts of the nanostructure and without piezoelectric potential dip in Fig. 6.18(c). For the fairly wide electron beam at $N = 7$, accounting for the sample imperfections gives rise to only small deviations between the two scenarios.

Modulations in the transmission as a function of B (vertical cuts, constant V_{L}) can be interpreted in terms of the lateral mode structure of a QPC encoded in the current profile emitted from a QPC. To demonstrate the impact of the lens potential on the lateral

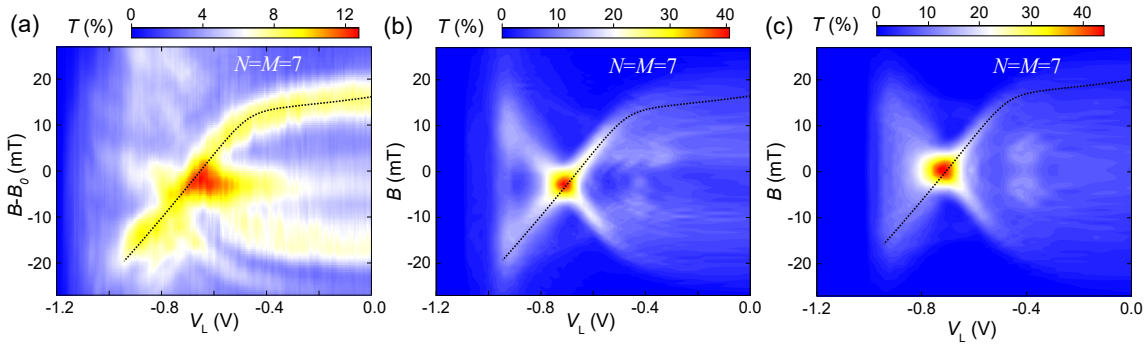

Figure 6.18: (a) Measured transmission as a function of lens voltage and magnetic field, $T(B,V_\mathrm{L})$. (b) Calculated $T(B,V_\mathrm{L})$ accounting for the sample imperfections due to the slight lateral shifts between the QPCs and the lens breaking the B-symmetry as well as a piezoelectric potential dip at the lens waist strongly decreasing the transmission around $B = 0$. (c) Calculated $T(B,V_\mathrm{L})$ for perfectly aligned QPCs and lens and a flat lens potential. Dashed lines in (a) and (b) are identical, dashed line in (c) is vertically shifted because of the perfect symmetry in the corresponding calculation.

current profile in real space, we display calculated beam profiles at finite lens potentials in Fig. 6.19.

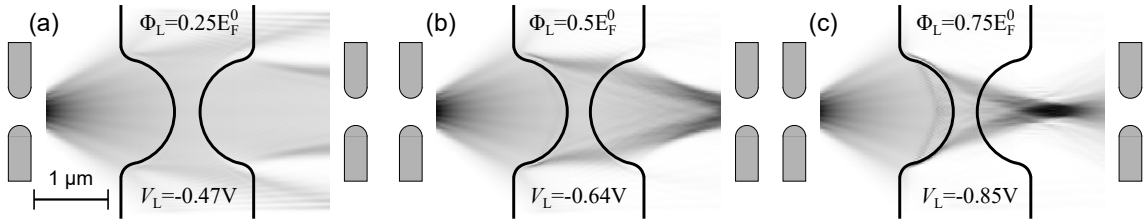

Figure 6.19: Calculated beam profiles for $N = 7$ and $B = 0$ for various lens potentials at finite lens voltages, $\Phi_\mathrm{L}(V_\mathrm{L})$. Dark (light) regions correspond to high (low) current density. We sketch the boundaries of the flat lens potential for comparison. (a) $\Phi_\mathrm{L}(V_\mathrm{L} = -0.47\,\mathrm{V}) = 0.25\,E_\mathrm{F}^0$ (Focal point behind the second QPC). (b) $\Phi_\mathrm{L}(V_\mathrm{L} = -0.64\,\mathrm{V}) = 0.5\,E_\mathrm{F}^0$ (Focal point on the second QPC). (c) $\Phi_\mathrm{L}(V_\mathrm{L} = -0.85\,\mathrm{V}) = 0.75\,E_\mathrm{F}^0$ (Focal point between the second QPC and the lens). For these calculations, we assumed perfect symmetry, a perfect lens without the central dip and a flat 2DES between gates.

For simplicity we consider a flat lens potential without the piezoelectric potential dip here. For $V_\mathrm{L} = 0$, the electron beam diverges into the free 2DES without any refraction or reflection from the lens gate, cf. Fig. 6.12(a). As we increase Φ_L by decreasing V_L, the part of the beam hitting the concave aperture is refracted towards the optical axis at the two lens boundaries and the focal point moves towards the lens. The relation $\Phi_\mathrm{L}(V_\mathrm{L})$, is known from our self-consistent lens calibration, cf. Fig. 6.17(d). For $\Phi_\mathrm{L}(V_\mathrm{L} = -0.47\,\mathrm{V}) = 0.25\,E_\mathrm{F}^0$ [cf. Fig. 6.19(a)], the beam is slightly collimated but the focal point still lies behind the second QPC. For this lens voltage (potential), an additional magnetic field is needed to

deflect the beam into the second QPC, cf. measured and calculated transmission maxima at finite B in Fig. 6.18. At the focal point around $\Phi_{\mathrm{L}}(V_{\mathrm{L}} = -0.64\,\mathrm{V}) = 0.5\,E_{\mathrm{F}}^{0}$, the beam is strongly collimated with the beam waist located on the second QPC for $B = 0$, cf. Fig. 6.19(b). For $V_{\mathrm{L}} < -0.64\,\mathrm{V}$, the refraction on the lens boundaries becomes so strong that the focal point moves between the second QPC and the lens, cf. calculated beam profile for $\Phi_{\mathrm{L}}(V_{\mathrm{L}} = -0.85\,\mathrm{V}) = 0.75\,E_{\mathrm{F}}^{0}$ in Fig. 6.19(c). In this regime, finite magnetic fields are needed to deflect the branches missing the second QPC into the latter, cf. measured and calculated transmission maxima at finite B for $V_{\mathrm{L}} < -0.64\,\mathrm{V}$ in Fig. 6.18.

To demonstrate the impact of the sample imperfections on a more narrow electron beam, we now consider the case of $N = M = 1$. In Fig. 6.20(a), we plot the measured

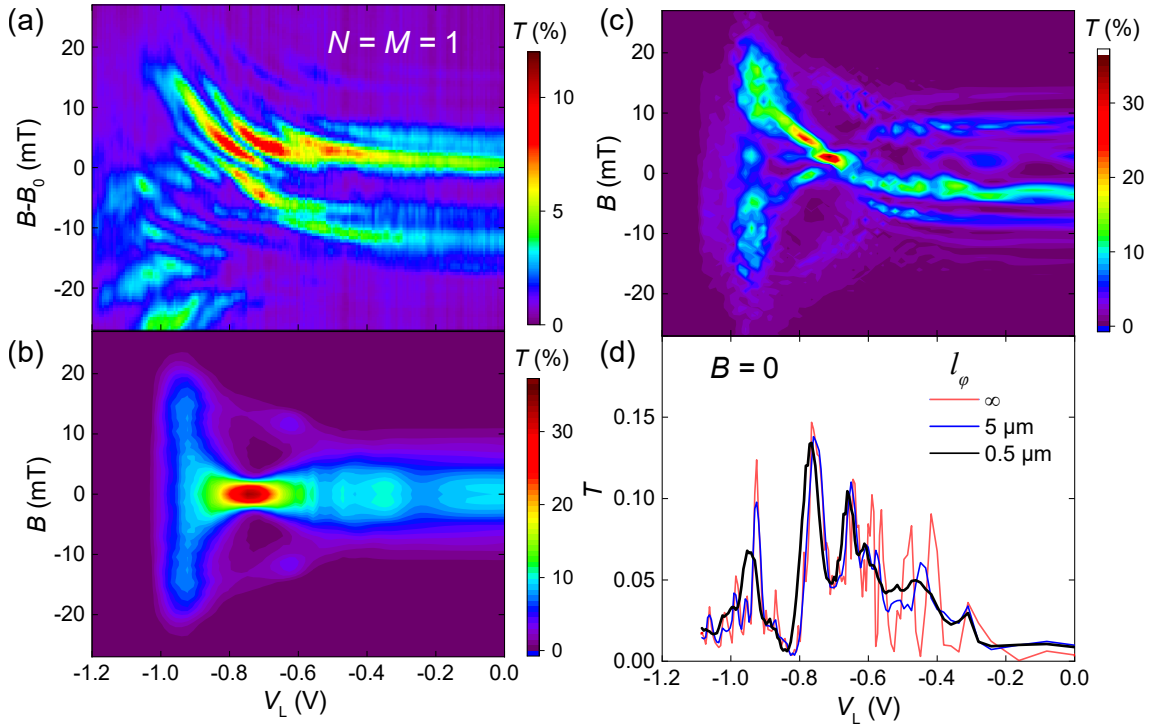

Figure 6.20: (a) Measured transmission $T(B,V_{\mathrm{L}})$ through both QPCs in series at $N = M = 1$ at a source drain voltage $V = -1\mathrm{mV}$. (b) Calculated $T(B,V_{\mathrm{L}})$ for $N = M = 1$ for a perfectly symmetric sample without electrostatic potential dip at the lens waist. (c) Calculated $T(B,V_{\mathrm{L}})$ for $N = M = 1$ for the lateral misalignments measured in (a) including a electrostatic potential dip at the lens waist as discussed in section 6.4.1. The dephasing length for the calculations in panels (b,c) is set to the estimated dephasing length in the experiment, $l_{\phi} = 0.5\,\mu\mathrm{m}$. (d) Calculated $T(B = 0,V_{\mathrm{L}})$ cuts for $N = M = 1$ as in (b) but with varying dephasing length l_{ϕ}.

$T_{N=M=1}(B,V_{\mathrm{L}})$. For comparison, we plot the predicted calculated transmission for a perfect sample in panel (b). Clearly, the much more narrow electron beam is strongly affected by the imperfections. Accounting for the imperfections discussed above results in the calculated data shown in panel (c). The traces of the measured $I(V_{\mathrm{L}},B = 0)$ (plotted

separately in Fig. 6.3(b), red solid line) display strong oscillations, which depend on the mode occupation of the QPCs, i.e., N and M. They are stronger for smaller N,M, lower temperature and smaller source drain voltage V, indicating an origin in terms of coherent standing waves (i) between the two QPCs or (ii) between emitter or detector QPC and the lens. Furthermore, (iii) the presence of the electrostatic potential dip at the center of the lens causes diffraction of the electron beam resulting in a modulated transmission profile $T(V_\mathrm{L} = 0,B)$ as seen both in experiment, Fig. 6.20(a) panel (b), and in the simulation accounting for the sample imperfections Fig. 6.20(c) as bent stripes of local transmission maxima. Due to the asymmetry of the sample, this diffraction results in oscillations of the transmission along horizontal cuts of the transmission profile, e.g., for $B = 0$.

As the interference pattern strongly depends even on slight disorder and the precise realization of the electrostatic potential, a one-to-one comparison with a numerical simulation is difficult. In order to qualitatively explain the oscillations in $I(V_\mathrm{L})$ in Fig. 6.3(b), we compare simulated $T(V_\mathrm{L},B = 0)$ cuts with varying dephasing length $l_\phi = 0.5\,\mu$m, $l_\phi = 5\,\mu$m and $l_\phi = \infty$ shown in Fig. 6.20(d). The fast oscillations for small negative lens voltages $V_\mathrm{L} > -0.6$V are consistent with an interpretation in terms of standing waves between the two QPCs as they are strong for a dephasing length much larger than the distance between the QPCs $l_\phi = \infty$ while they are averaged out for a dephasing length $l_\phi \leq 5\,\mu$m of the order of the distance between the QPCs. The oscillations at large negative lens voltages $V_\mathrm{L} < -0.6$V can originate both from (ii) coherent standing waves between the QPC and the lens and (iii) the lens voltage tuning the diffraction pattern through the $B = 0$ cut. The former exist only if the lens voltage V_L is negative enough such that electrons approaching a sufficiently smooth electrostatic potential $\Phi(V_\mathrm{L})$ are reflected if their forward momentum is smaller than $\sqrt{2m^\star(E_\mathrm{F}^0 - \Phi_\mathrm{L})}$. As the experiment was conducted at $T = 250\,$mK with a source drain voltage of $-1\,$mV corresponding to a dephasing length of $0.5\,\mu$m (cf. Fig. 3.5), oscillating current contributions due to standing waves between lens and the QPCs are averaged out. Thus, the simulation supports the conclusion that the large oscillations in the experimental data at $V_\mathrm{L} < -0.6\,$V of Fig. 6.3(b) are caused by (iii) the tuning of the diffraction pattern through the $B = 0$ cut. This conclusion is in agreement with the measured and simulated $T(V_\mathrm{L},B)$ profile for emitter and detector plateaus $N = M = 1$ Fig. 6.20(b,c), respectively. Note, that the simulated $T(V_\mathrm{L},B)$ profile in a symmetric geometry without electrostatic potential dip at lens waist does not exhibit these oscillations.

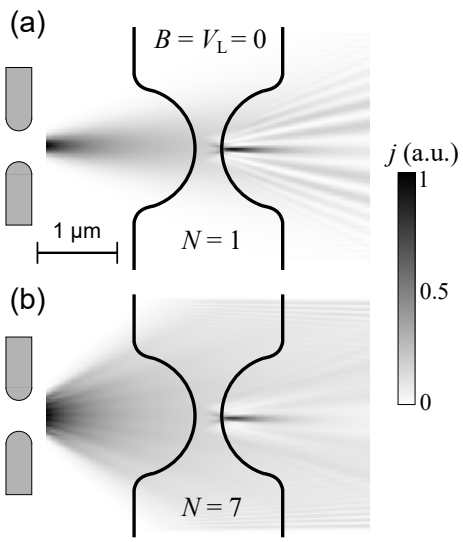

Figure 6.21: Calculated spatial current densities with $B = V_\mathrm{L} = 0$ for $N = 1$ (a) and $N = 7$ (b), accounting for the piezoelectric potential dip at the lens waist.

Using our numerical model, the magnetic field dependent oscillations of the serial current through the QPCs can be translated into modulations of the calculated current density in real space, cf. Fig. 6.21(a) for $N = 1$ and accounting for the piezoelectric potential dip

but an otherwise flat lens potential at $V_{\mathrm{L}} = 0$. Due to scattering off the potential dip, the beam fans out behind the lens. This effect is particularly strong for a narrow electron beam ($N = 1$) centered on the lens waist. For comparison, we add the calculated beam profile including the piezoelectric potential dip also for a wider electron beam at $N = 7$ in Fig. 6.21(b). Since the potential dip only affects a minor range of the beam width, the lateral current modulation is less pronounced here. Nevertheless, it manifests as a bimodal current distribution behind the lens. This explains the measured magnetic field dependent serial current, cf. Fig. 6.7 for $N \geq 3$.

7 Electron scattering in a ballistic and coherent cavity with quantum point contacts

Besides electrostatic lenses, electrostatic mirrors represent another tool to couple distant nanostructures via a region of free 2DES. Here, we study the coupled system of four QPCs and an elliptical mirror forming an open cavity in the ballistic and coherent transport regime.

7.1 Sample

We present an AFM picture of the sample in Fig. 7.1. The gate layout consisting of a mirror

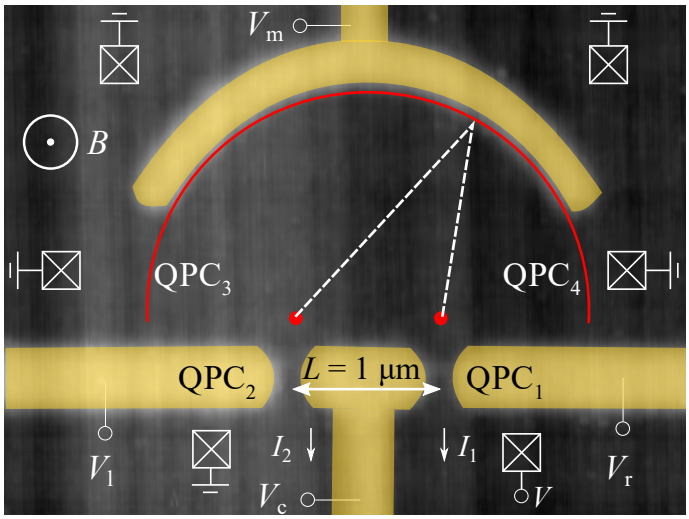

Figure 7.1: AFM image of Ti/Au gates (yellow) on the sample surface (dark). Negative gate voltages V_r,V_c,V_l and V_m are used to define four QPCs and a mirror following an elliptical arc (red line) in the 2DES 107 nm below the surface. Emitter QPC$_1$ and detector QPC$_2$ are located close to the two focal points of the elliptical arc (red dots). Crossed boxes indicate positions of Ohmic contacts far away from the nanostructure. We measure the currents I_1 and I_2 flowing through QPC$_{1,2}$ after applying a source drain voltage V at QPC$_1$ and leaving all other Ohmic contacts grounded. A perpendicular magnetic field B is added on demand.

gate and three split-gates forms a cavity with four QPCs. To realize the two narrow QPCs, (QPC_1 and QPC_2) used as emitter and detector for electrons, we keep the central gate at a constant negative voltage $V_c = -1.5\,\mathrm{V}$ depleting the 2DES below, while the other gate voltages $V_{r,l}$ are swept to control $QPC_{1,2}$ respectively. We define the electrostatic mirror by applying the gate voltage V_m. The geometry of the mirror follows an elliptic arc (red line) with the two corresponding focal points located close to the exits of the QPCs (red dots). Within the simplified ray-optics picture, every ballistic electron emitted from one of the two focal points is scattered onto the second focal point after one specular reflection of the elliptical mirror gate. By decreasing V_m, we decrease the size of the cavity, effectively shifting the focal points towards the centers of the QPCs. Using this concept, we intend to couple the two QPCs: we apply a source-drain voltage V at the emitter contact, such that electrons flow through the emitter QPC_1 into the cavity. Inside the cavity, electrons can scatter between each other or from the elliptical mirror and the QPC gates, before they either traverse the detector QPC_2, backscatter into the emitter QPC_1, or leave the cavity to the grounded side contacts. To characterize the cavity, we simultaneously measure the currents $I_1(V_\mathrm{m})$ and $I_2(V_\mathrm{m})$ flowing through QPC_1 and QPC_2 respectively, with a perpendicular magnetic field B added on demand, cf. Fig. 7.1. The sample was fabricated on wafer no. mbe8-309 [cf. A.1] with the corresponding Fermi energy $E_\mathrm{F}^0 = 11\,\mathrm{meV}$ and a measured elastic mean free path (after structuring the present sample) of $l_\mathrm{m} = 14\,\mu\mathrm{m}$. A detailed overview of the experimental setup used for the experiments described in this chapter is shown in section 2.2.2.

7.2 Cavity constrictions characterization

Before looking into the ensemble of the four QPCs and the elliptical mirror we start with the characterization of all individual components forming the cavity. In Fig. 7.2(a), we show an overview of the present sample layout with the gates used for the experiments (red) on the mesa representing the conducting areas of 2DES (blue). We additionally indicate the six Ohmic contacts located in the periphery of the mesa (crossed boxes). We bias the contact connected to the emitter QPC with an external source-drain voltage $V_1 < 0$, while keeping all other contacts grounded. The internal input offset voltage of the current amplifier connected to the detector QPC is adjusted as close as possible to the ground potential, $|V_2| \lesssim 10\,\mu\mathrm{V}$.

In panel (b) we show a magnified view of the cavity and its four openings labeled 1,2,3,4 connected to the free 2DES and Ohmic contacts. Each opening represents a QPC where we have determined the number of occupied spin-degenerate channels in the constriction, N_i. The present sample was designed to host two slightly different cavities, cf. 2nd mirror gate visible on the right in Fig. 7.2(b). To minimize the number of electrical connections in the setup, the mirror gates of both cavities were shorted and have the same potential. The distance between the two cavities (55 µm) is larger than the mean free path ($l_\mathrm{m} = 14\,\mu\mathrm{m}$). While we do not discuss the second cavity on the right hand side of the mesa, we account for an additional (lead) resistance $R_4^{'}$ due to the short of the mirror gates as shown in Fig. 7.2(b). Other gates of the second cavity are kept at ground potential and are not shown.

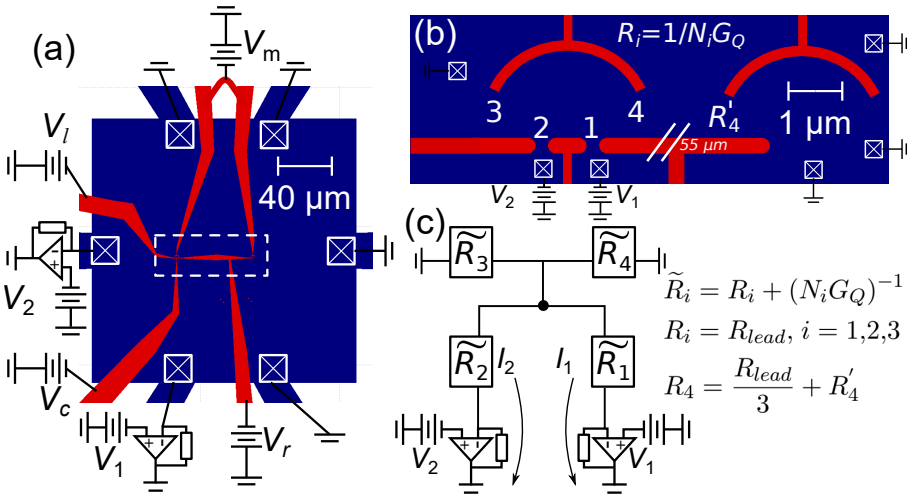

Figure 7.2: (a) Sample layout with gated structures connected to voltage sources (red) on the mesa (blue). Crossed boxes indicate Ohmic contacts in the periphery of the mesa. (b) Magnified view of the cavity and the Ohmic contacts connected to its leads. QPC_4 is connected to its lead via another constriction accounted for as R_4'. (c) Simplified circuit diagram of the setup.

In Fig. 7.2(c), we present a simplified equivalent circuit diagram including the components introduced above. The lead resistance $R_{lead} = 2645\,\Omega$ caused by RC low-pass filters at room temperature (2.2 kΩ), wire resistances (350 Ω), Ohmic contacts and 2DES (95 Ω) is practically identical for every lead within two percent accuracy. In table 7.1, we present all pairwise lead resistances between the six leads of the sample determined from I/V measurements with grounded gates.

$R(\Omega)$	Lead 1	Lead 2	Lead 3	Lead 4	Lead 5	Lead 6
Lead 1	-	5258	5297	5303	5313	5328
Lead 2	5258	-	5262	5267	5284	5300
Lead 3	5297	5262	-	5263	5276	5298
Lead 4	5303	5267	5263	-	5279	5296
Lead 5	5313	5284	5276	5279	-	5308
Lead 6	5328	5300	5298	5296	5308	-

Table 7.1: Pairwise resistances between the six leads of the sample, including wire- and RC filter resistances (cf. main text).

In the following, we first characterize the emitter and detector openings $QPC_{1,2}$ before discussing the larger cavity side openings $QPC_{3,4}$ and their leads.

7.2.1 Emitter and detector - QPC$_1$ and QPC$_2$

In Fig. 7.3 we present finite bias spectroscopy measurements for the emitter and detector QPC$_{1,2}$.

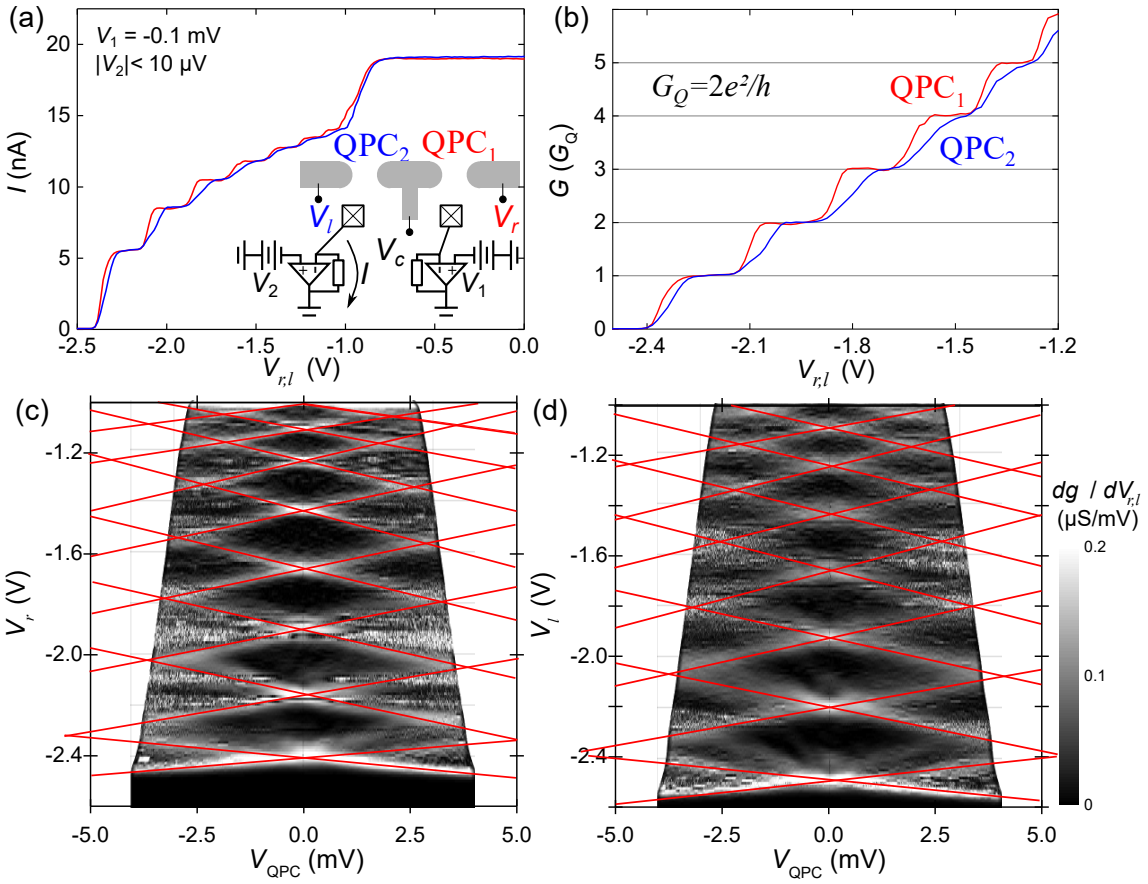

Figure 7.3: (a) Full pinch-off curves $I(V_{r,l})$ of QPC$_1$ (red) and QPC$_2$ (blue) measured separately while the central gate is kept constant at $V_c = -1.5\,\mathrm{V}$, depleting the 2DES below. (b) Solid lines: conductance $G(V_r)$ and $G(V_l)$ of both QPCs after subtraction of $2R_{lead} = 5.29\,\mathrm{k\Omega}$, including room temperature filters not used for (c,d). (c,d) Finite bias spectroscopy $dg/dV_{r,l}(V_{\mathrm{r,l}},V_{\mathrm{QPC}})$ of QPC$_{1,2}$, where V_{QPC} is the voltage drop over the respective QPC, cf. main text.

We keep the central gate at $V_c = -1.5\,\mathrm{V}$ and vary $V_{r,l}$ to control QPC$_{1,2}$ with the other QPC grounded, $V_{l,r} = 0$, cf. inset in Fig. 7.3(a). In the main panel of Fig. 7.3(a) we plot the full pinch-off curves $I(V_{\mathrm{r,l}})$ for both QPCs separately at $V_1 = -0.1\,\mathrm{mV}$, used for most of the experiments presented in this chapter. Fig. 7.3(b) displays the quantized conductance regime of both QPCs after subtraction of the lead resistance, featuring well defined conductance plateaus with smooth transitions, indicating reflectionless coupling of the 1D modes to the free 2DES. For experiments aiming at the coupling of both QPCs, we keep the QPCs at the centers of the plateaus at $G_{1,2}(V_{r,l}) = N_{1,2}G_Q$. To determine the

subband spacings of the QPCs, we measure the differential conductance $g = \mathrm{d}I/\mathrm{d}V$ as a function of the gate voltage and the source-drain voltage V serving as an energy reference. This allows us to extract their 1D subband spacings $\delta\epsilon(N_{1,2})$, analogous to the detailed QPC confinement potential characterization presented in chapter 4. In Fig. 7.3(c,d) we plot the differential transconductance $\mathrm{d}g/\mathrm{d}V_{r,l}$ of $\mathrm{QPC}_{1,2}$ which displays transitions between adjacent conductance plateaus in a diamond-like pattern, highlighted by red lines. Here, the x-axis shows the actual voltage drop over the QPC, $V_{\mathrm{QPC}} = V - 2R_{\mathrm{lead}}I$, after subtracting the parasitic voltage drop along the two leads. The first intersection points of the red lines at finite V_{QPC} indicate the subband spacings $\delta\epsilon_{N_{1,2}} = eV_{\mathrm{QPC}}$, plotted in Fig. 7.4.

Both QPCs feature almost identical decreasing subband spacings as the QPCs are opened by increasing the gate voltage. Moreover, the subband spacings found here are identical to the ones found for the QPC characterized in chapter 4 within the accuracy of the experiment. This is not surprising, since all three QPCs have a nominally identical gate geometry and are fabricated on the same heterostructure. Note, however, that the QPCs in this chapter are realized by keeping the central gate at $V_c = -1.5\,\mathrm{V}$ while controlling the conductance with the second gate defining the QPC, $V_{r,l}$. We thus expect an asymmetry of the lateral confinement potential [97] which increases with $|V_c| - |V_{r,l}|$. Our experimental data suggest that the asymmetry of the potential well does not affect the subband spacings of the QPCs, which is still compatible with a transition from a parabolic towards a hard-wall confinement potential caused by Coulomb screening [87].

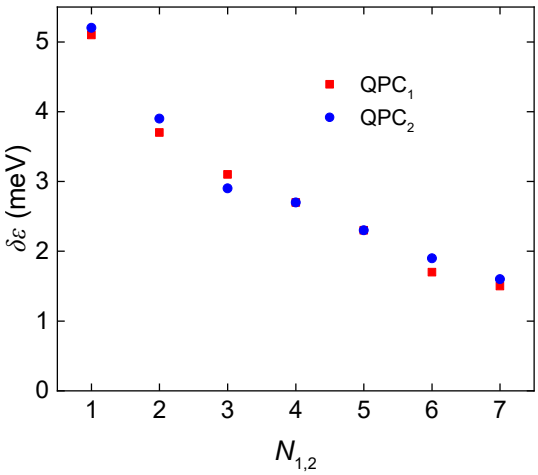

Figure 7.4: Subband spacings $\delta\epsilon(N_{1,2})$ of QPC_1 (red squares) and QPC_2 (blue dots).

7.2.2 Cavity side exits - QPC_3 and QPC_4

To determine the gate voltage dependent channel numbers of the wide QPCs QPC_3 and QPC_4, N_3 and N_4 as well as the resistance R_4' [cf. Fig. 7.2(b)], we perform various two terminal pinch-off measurements as a function of the voltages applied to the two gates forming the respective constriction V_l & V_m for QPC_3 and V_r & V_m for QPC_4 while keeping all other gates grounded. We present them in Fig. 7.5.

In the experiments with the coupled system including the cavity with its four exits, we tune QPC_1 and QPC_2 to the centers of their conductance plateaus $N_{1,2}$ at fixed QPC gate voltages $V_{r,l}(N_{1,2})$ while sweeping the mirror gate voltage V_{m}. To calibrate the cavity side exits *under exactly these conditions*, we present two-terminal pinch-off curves $I(V_{\mathrm{m}})$ with $V_{r,l}(N_{1,2})$ corresponding to the first three conductance plateaus $N_{1,2}$ = 1,2,3 [cf. Fig. 7.3(b)].

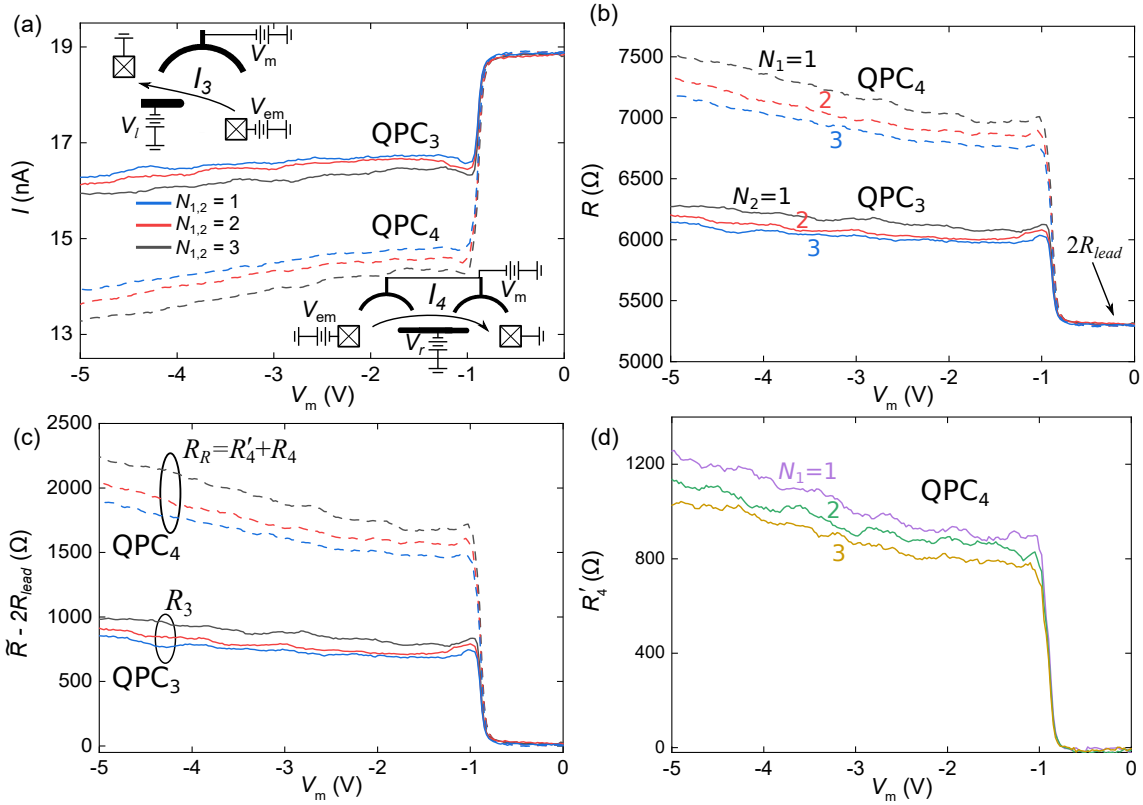

Figure 7.5: (a) Upper curves and sketch: $I_3(V_\mathrm{m})$ for $V_r = 0$ flowing through the left cavity exit with V_l corresponding to N_2 = 1,2,3. Lower curves and sketch: $I_4(V_\mathrm{m})$ for $V_l = 0$ flowing through the right cavity exit with V_r corresponding to N_1 = 1,2,3. Other contacts are floating, gates not shown are grounded. (b) Resistances $R_i = V/I_i$ with $V = 0.1\,\mathrm{mV}$ obtained from the currents shown in (a). In the transparent mirror regime, $R(-0.9\,\mathrm{V} < V_\mathrm{m} \leq 0) = 2R_{lead}$ corresponds to the resistance of the two leads. (c) Upper (lower) curves: resistance of the right (left) cavity exit, $R_R = R_4 + R_4'$ (R_3) after subtraction of the lead resistances (cf. main text). (d) Resistance R_4' of the additional constriction far away from the cavity, obtained from $R_4' = R_R - R_3$ (cf. main text).

To characterize the left opening of the cavity, we apply $V = 0.1\,\mathrm{mV}$ to a contact on one side of the constriction and measure the current $I_3(V_\mathrm{m})$ for $V_r = 0$ and V_l corresponding to N_2 = 1,2,3 flowing through it (cf. upper inset and upper curves). Similarly, for the right drain we measure $I_4(V_r,V_\mathrm{m})$ (cf. lower inset and lower curves). In both cases, we observe a drop in the current at the depletion voltage of the mirror, $V_\mathrm{m}^d \simeq -0.9\,\mathrm{V}$. Further decreasing V_m reduces the constriction size (field-effect) and leads to decreasing currents. Due to the additional constriction in the right drain of the cavity $I_4(V_\mathrm{m}) < I_3(V_\mathrm{m})$ in the depleted mirror regime.

In Fig. 7.5(b) we plot the total resistances $R_i = V/I_i$ with $V = 0.1\,\mathrm{mV}$ obtained from the measured currents shown in (a). The additional constriction enhances the total resistances of the right cavity drain (upper three curves) compared to those of the left exit (lower three curves). For $V_\mathrm{m} > V_\mathrm{m}^d$, the 2DES below the mirror gate is transparent and the constant

resistance corresponds to the total resistance of the two leads, $2R_{lead} = 5290\,\Omega$.

To extract the contribution of the constrictions to the measured total resistance, we plot the total resistances shown in panel (b) after subtraction of $2R_{lead}$ in Fig. 7.5(c). In this representation, we can directly read off the resistances of the left constriction $(N_3 G_Q)^{-1} = \widetilde{R} - 2R_{lead}$ for $V_l(N = 1,2,3)$ (lower curves). For the right cavity drain we have to subtract $\widetilde{R} - 2R_{lead} - R_4'$ for $V_r(N = 1,2,3)$ (upper curves). Note that we neglect ballistic effects and treat the extra constriction beyond the right exit as a serial Ohmic resistor, as the distance between QPC_4 and the extra constriction is substantially larger than the elastic mean free path.

Since the gate geometry of the left and right constriction of the cavity is nominally identical in terms of the gate geometry and $V_r(N_1) = V_l(N_2)$ [cf. Fig. 7.3(d)], in the following we assume identical resistances of the left and right cavity constriction, $(N_3 G_Q)^{-1} = (N_4 G_Q)^{-1}$. Under this assumption, we can separate the contributions $(N_4 G_Q)^{-1}$ and R_4' in the serial resistance $R_R = (N_4 G_Q)^{-1} + R_4'$. In Fig. 7.5(d) we plot $R_4'(V_\mathrm{m})$.

To quantitatively determine the various transmission coefficients between the four leads of the cavity, we need the number of spin-degenerate channels in each lead. For $\mathrm{QPC}_{1,2}$, $N_{1,2}(V_{r,l})$ can be determined from the pinch-off curves shown in Fig. 7.3(d).

In Fig. 7.6, we plot $\widetilde{R}_3 - 2R_{lead}$ (solid lines, left axis) and the corresponding $N_3 = [(\widetilde{R}_3 - 2R_{lead})G_Q]^{-1} = N_4$ (dashed lines, right axis). Our resonator represents an 'open' system in the sense that the number of spin-degenerate channels of the side constrictions $N_3 = N_4 \geq 13$ is much larger than the number of channels coupling into/out of the cavity via the QPCs, if we restrict our measurements to $N_{1,2} = 1,2$.

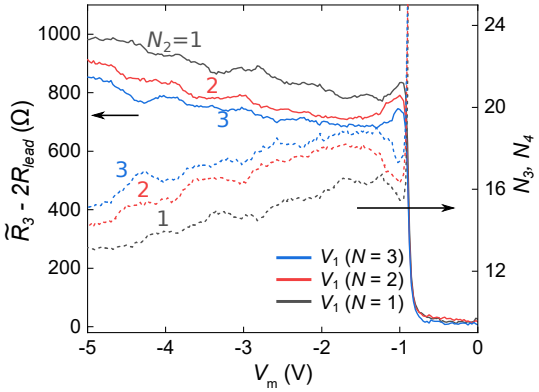

Figure 7.6: Solid lines, left axis: resistance of the left cavity constriction shown in 7.2b, $R_3(V_\mathrm{m})$ for $V_r = 0$ and V_l corresponding to $N_2 = 1,2,3$. Dashed lines, right axis: corresponding number of spin-degenerate channels $N_3 = 1/R_3 G_Q$.

7.3 Transmission and reflection at $B = 0$

Together with the calibration measurements of the individual QPCs shown above, applying the Landauer-Büttiker formalism to the present four terminal device (cf. section 3.3.1) now allows us to deduce the probability for electrons to return into QPC_1 from the measured emitter current I_1 (equation 3.21). In the same fashion, we can use equation 3.22 to indicate the transmission probability for electrons emitted by QPC_1 to traverse QPC_2 using the measured detector current I_2. Additionally, we in the following calculate the probability of electrons to be scattered through the larger side exits QPC_3 and QPC_4 using Kirchhoff's law. In this section, we only vary the size of the cavity by tuning V_m while keeping $B = 0$.

7.3.1 Reflection into the emitter QPC$_1$

The dimensions of the cavity ($< 2\,\mu$m) are much smaller than the measured elastic mean free path after structuring the present sample, $l_m = 14\,\mu$m. Hence, we expect the measured current $I_1(V_m)$ to contain ballistic components. In particular, the concave shape of the resonator supports ballistic backscattering of electrons emitted into the cavity back through the emitter QPC$_1$. We plot $I_1(V_m)$ for $N_1 = N_2 = 1,2$ and 3 in Fig. 7.7(a) mea-

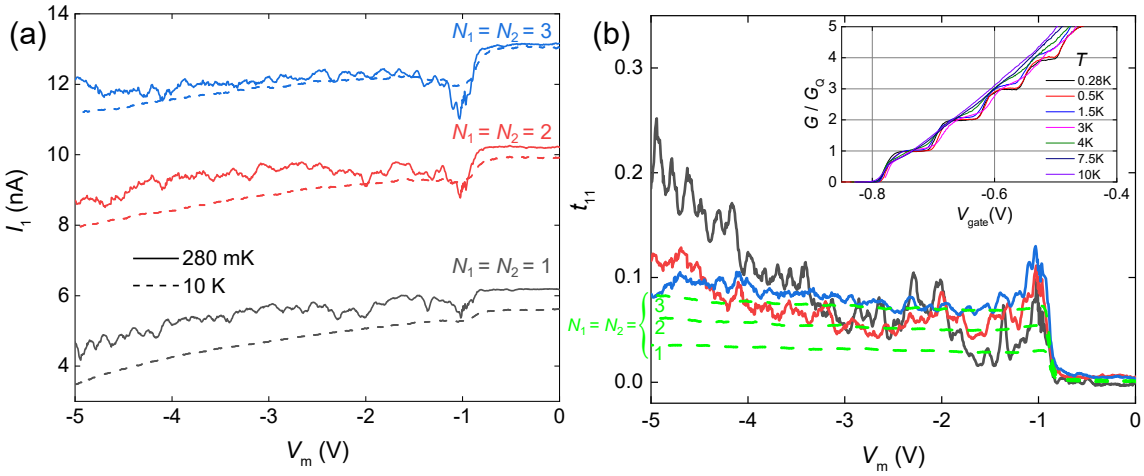

Figure 7.7: (a) Measured $I_1(V_m)$ at 280 mK (solid lines) and 10 K (dashed lines). (b) Reflection probabilities $t_{11}(V_m)$ for 280 mK. Dashed green lines: reflection probabilities assuming chaotic cavity physics for $N_1 = N_2 = 1,2,3$, calculated with equation 7.1. The inset shows the strong sensitivity of the QPC conductance to temperature, measured for another QPC. In the classical limit at high temperatures the conductance is expected to cut through the centers of the low-temperature plateaus.

sured at 280 mK (solid lines) and 10 K (dashed lines). For moderate voltages ($-1\,\text{V} < V_m$), the mirror gate is transparent for electrons at the Fermi edge, while for $V_m < -1\,$V the 2DES below the gate is depleted and the open cavity with four QPCs is formed. For both the data at 280 mK and 10 K, the formation of the cavity manifests as a drop in $I_1(V_m)$, as electrons are reflected back through QPC$_1$, decreasing the net current flowing into the cavity. For more negative values of V_m, the depleted area below the mirror gate increases, giving rise to a smaller cavity size. Comparing the data measured at the two temperatures, we find additional reproducible fine structures at 280 mK, which point to ballistic and coherent resonator modes.

The slight vertical offset between the data for the two temperatures originates from the temperature dependence of the QPC conductance. In the inset of Fig. 7.7(b) we show the pinch-off curve of a QPC with identical geometry fabricated on a different heterostructure, measured at various temperatures. As we increase the temperature, the conductance plateaus smear out due to thermal broadening. The conductance is in principle expected to feature temperature-independent fixed points as a function of energy, located at roughly multiple integers of e^2/h [98]. However, such points are less pronounced in the actual,

measured temperature dependence of the conductance as a function of gate voltage due to heating effects. For a fixed gate voltage set in the experiment, the conductance can therefore deviate from the quantized low temperature conductance as a function of temperature. The strong sensitivity of the QPC conductance on temperature makes a quantitative analysis of the currents at high temperature difficult, as N_1 and N_2 in equations 3.19 and 3.20 are not well controlled here. We thus translate only the measured $I_1(V_\mathrm{m})$ at low temperature directly to the corresponding reflection probabilities $t_{11}(V_\mathrm{m})$ using equation 3.21 with a source-drain voltage $V = -0.1\,\mathrm{mV}$, where G_1^{diff} and G_2^{diff} can be calculated from equation 3.16 and 3.18, respectively. We plot $t_{11}(V_\mathrm{m})$ in Fig. 7.7(b).

We observe a first local reflection maximum around the depletion voltage of the mirror, $V_\mathrm{m} = -1\,\mathrm{V}$, which is more pronounced for higher $N_1 = N_2$. For intermediate mirror voltages $-1.5\,\mathrm{V} > V_\mathrm{m} > -3\,\mathrm{V}$, $t_{11}(V_\mathrm{m})$ is oscillating close to the chaotic predictions

$$t_{11}(V_\mathrm{m}) = N_1 / \sum_{j=1}^{4} N_j(V_\mathrm{m}), \tag{7.1}$$

which we plot in Fig. 7.7(b) as dashed green lines for $N_1 = N_2 = 1,2,3$ for comparison. The gate voltage dependence of the chaotic prediction, cf. equation (7.1), is known from the V_m-dependence of the conducting channels $N_j(V_\mathrm{m})$ of all four QPCs forming the cavity, explained in detail in section 7.2 and $N_3(V_\mathrm{m}) = N_4(V_\mathrm{m})$ depicted in Fig. 7.6 (dashed lines). Further decreasing the cavity size with decreasing V_m, the reflection increases, most pronounced for lower $N_1 = N_2$. In particular, for $N_1 = N_2 = 1$, we observe a dramatic increase of the reflection probability up to around 25 %, which is more than 7 times the corresponding chaotic prediction.

7.3.2 Transmission through the detector QPC_2

Next, we consider the serial current I_2 flowing from the emitter QPC into the detector QPC via the cavity. In Fig. 7.8(a) we show the measured raw currents $I_2(V_\mathrm{m})$ for $N_1 = N_2 = 1,2,3$ at 280 mK (solid lines) and 10 K (dashed lines). Here, the depletion of the cavity shows as an abrupt increase of I_2 around $V_\mathrm{m} = -1\,\mathrm{V}$, as carriers are scattered into the detector via the cavity. Just like $I_1(V_\mathrm{m})$ [cf. Fig. 7.7(a)], the serial current $I_2(V_\mathrm{m})$ shows features of coherent resonator modes: at 280 mK, pronounced, reproducible maxima and fine structures occur, which are absent as the temperature is increased to 10 K.

Next, we use equation 3.22 to translate the measured detector currents $I_2(V_\mathrm{m})$ into the corresponding transmission probabilities $t_{21}(V_\mathrm{m})$ for electrons to transmit through QPC_1 and QPC_2 in series, plotted in Fig. 7.8(b). We again only consider the low temperature data due to the strong sensitivity of the QPC conductance on temperature, addressed in section 7.3.1. After subtracting the diffusive contribution, the coherent and ballistic features are clearly more pronounced than in the measured raw currents [panel (a)]: as we decrease the cavity size with V_m, the transmission strongly oscillates due to constructive and destructive interference. For comparison, we add the predictions of the transmission

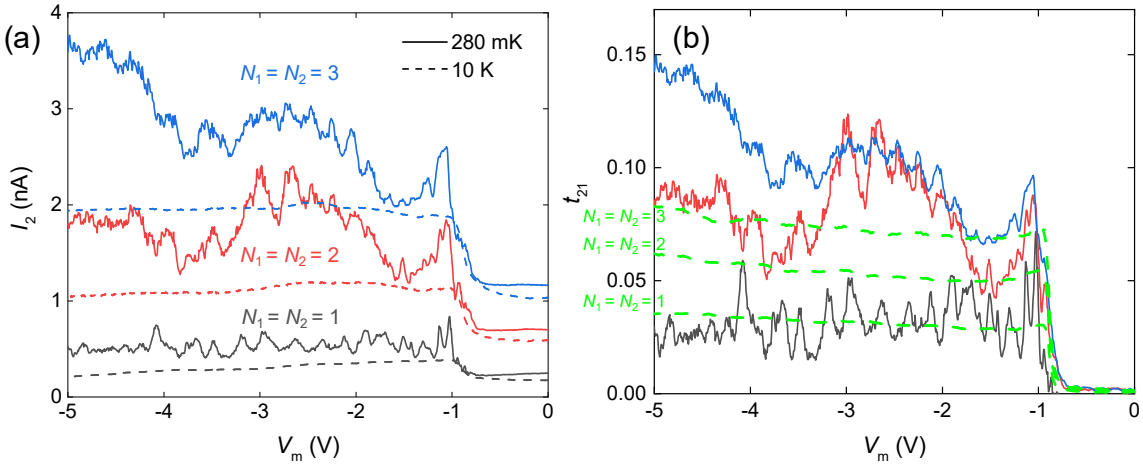

Figure 7.8: (a) $I_2(V_\mathrm{m})$ flowing through the detector QPC_2 for $N = 1,2,3$. Solid lines are data for 280 mK, dashed lines are for 10 K. (b) Transmission probabilities $t_{21}(V_\mathrm{m})$ for 280 mK. Dashed green lines: transmission probabilities assuming chaotic cavity physics for $N_1 = N_2 = 1,2,3$, calculated with equation 7.2.

for chaotic cavity physics,

$$t_{21}(V_\mathrm{m}) = N_2 / \sum_{j=1}^{4} N_j(V_\mathrm{m}) \tag{7.2}$$

for $N_1 = N_2 = 1,2,3$ as dashed green lines in Fig. 7.8(b). For $N_1 = N_2 = 1$, the oscillations in $t_{21}(V_\mathrm{m})$ feature the highest visibility. The transmission in this case oscillates around the corresponding chaotic prediction. In contrast, for $N_1 = N_2 = 2,3$ we observe an additional broad maximum between $-1.5\,\mathrm{V} > V_\mathrm{m} > -3.5\,\mathrm{V}$ superimposed on the oscillations. Here, the transmission is substantially higher than the chaotic prediction, pointing to ballistic focusing of electrons between QPC_1 and QPC_2. The highest transmissions are found for $N_1 = N_2 = 3$ as we go to very small cavity sizes by lowering V_m towards $-5\,\mathrm{V}$. Nevertheless, the total transmission does not exceed 15 % in the mirror voltage range considered here. Note that we do not apply $V_\mathrm{m} < -5\,\mathrm{V}$ to avoid leakage currents between the mirror gate and the 2DES.

7.3.3 Transmission through the side exits QPC_3 and QPC_4

In the previous two sections we have discussed backscattering of electrons emitted from QPC_1 into the same QPC in terms of the reflection probability $t_{11}(V_\mathrm{m})$ (see section 7.3.1) and the transmission through QPC_1 and QPC_2 in series, $t_{21}(V_\mathrm{m})$ (see section 7.3.2). Using unitarity of the scattering matrix (the equivalent of Kirchhoff's law), we calculate the transmission $t_{31}+t_{41}$ through QPC_3 and QPC_4, forming the wide side exits of the cavity:

$$t_{31} + t_{41} = 1 - t_{21} - t_{11}. \tag{7.3}$$

In Fig. 7.9, we re-plot the reflection $t_{11}(V_\mathrm{m})$ [panel (a)] and the transmission $t_{21}(V_\mathrm{m})$

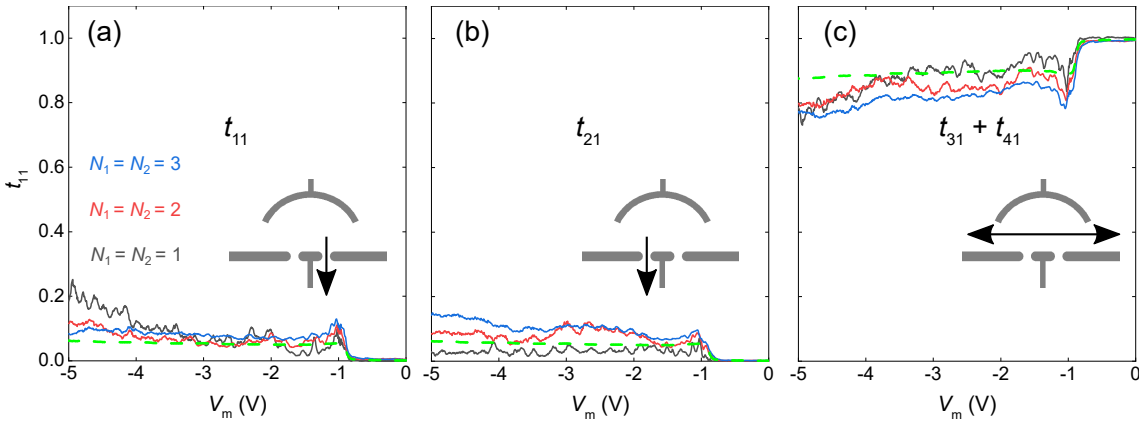

Figure 7.9: (a) Reflection probability back through emitter QPC$_1$, $t_{11}(V_\mathrm{m})$, (b) transmission probability through QPC$_1$ and QPC$_2$, $t_{21}(V_\mathrm{m})$ and (c) transmission probability through the side exits $(t_{31} + t_{41})(V_\mathrm{m})$ for $N_1 = N_2 = 1,2,3$ at 280 mK. The green dashed lines show the reflection/transmission prediction assuming chaotic cavity physics for $N_1 = N_2 = 2$.

[panel (b)] next to $(t_{31} + t_{41})(V_\mathrm{m})$ [panel (c)] for $N_1 = N_2 = 1,2,3$ and a temperature of 280 mK. For a completely transparent mirror gate, $V_\mathrm{m} > -0.8\,\mathrm{V}$, the cavity is absent and the current diffuses into leads 3 and 4, $t_{31} + t_{41} \simeq 1$. The depletion of the mirror around $V_\mathrm{m} \simeq -1\,\mathrm{V}$ results in increasing ballistic signals, t_{11},$t_{21} > 0$. Further decreasing V_m results in a trend to stronger overall t_{11} and t_{21}. This is expected, as the side exits QPC$_3$ and QPC$_4$ are becoming more narrow by decreasing V_m while QPC$_1$ and QPC$_2$ are not affected by it. However, for very negative mirror voltages, t_{11} and t_{21} substantially exceed the chaotic prediction. This points to enhanced (classical and/or coherent) backscattering through QPC$_1$ and focusing through QPC$_2$.

Nevertheless, throughout the entire V_m-range considered in the experiments, the main fraction of the current is scattered to the wide side drains of the cavity, $t_{31} + t_{41} >> t_{11} + t_{21}$.

7.3.4 Source-drain dependence

Next, we study the energy dependence of the V_m-dependent oscillations in the reflection (transmission) probabilities by measuring the currents I_1 and I_2 as a function of both the mirror gate voltage V_m as well as the source-drain voltage V applied to the lead of emitter QPC$_1$.

The confinement of electrons in a cavity gives rise to a discrete density of states characterized by the charging energy, e^2/C_cavity, where C_cavity is the self capacitance of our cavity. However, if the charging energy is much smaller than the line width, the discrete states can not be resolved and the density of states is continuous. The line width can be estimated semiclassically by substituting the quantum mechanical decay time $\tau = h/\Delta E$ by the classical time constant RC_cavity of the disc: $\Delta E \sim h/(RC_\mathrm{cavity})$, where $R = (\sum_{i=1}^{4} N_i G_\mathrm{Q})^{-1}$

denotes the effective resistance for charging the cavity. In this approximation, the ratio between charging energy and the line width is $e^2/(C_{\text{cavity}}\Delta E) = 0.5/\sum_{j=1}^{4} N_i$, which for $\sum_{i=1}^{4} N_i > 25$ as in our experiments is smaller than 0.02. Hence, we deal with an open cavity characterized by a continuous density of states. This implies that Coulomb blockade oscillations of the conductance of our cavity can not be resolved. An appropriate description of regular oscillations of the conductance as a function of applied voltages is the picture of standing waves of the quantum mechanical probability function caused by closed orbitals of multiple reflected electrons, the electronic analogue of Fabry-Pérot modes [58–60].

In Fig. 7.10(a,b), we present the source-drain dependence of the V_{m}-dependent oscillations in the reflection and transmission probability for $N_1 = N_2 = 1$, which showed the highest oscillation visibility. The x-axis represents a direct energy reference by means of the actual

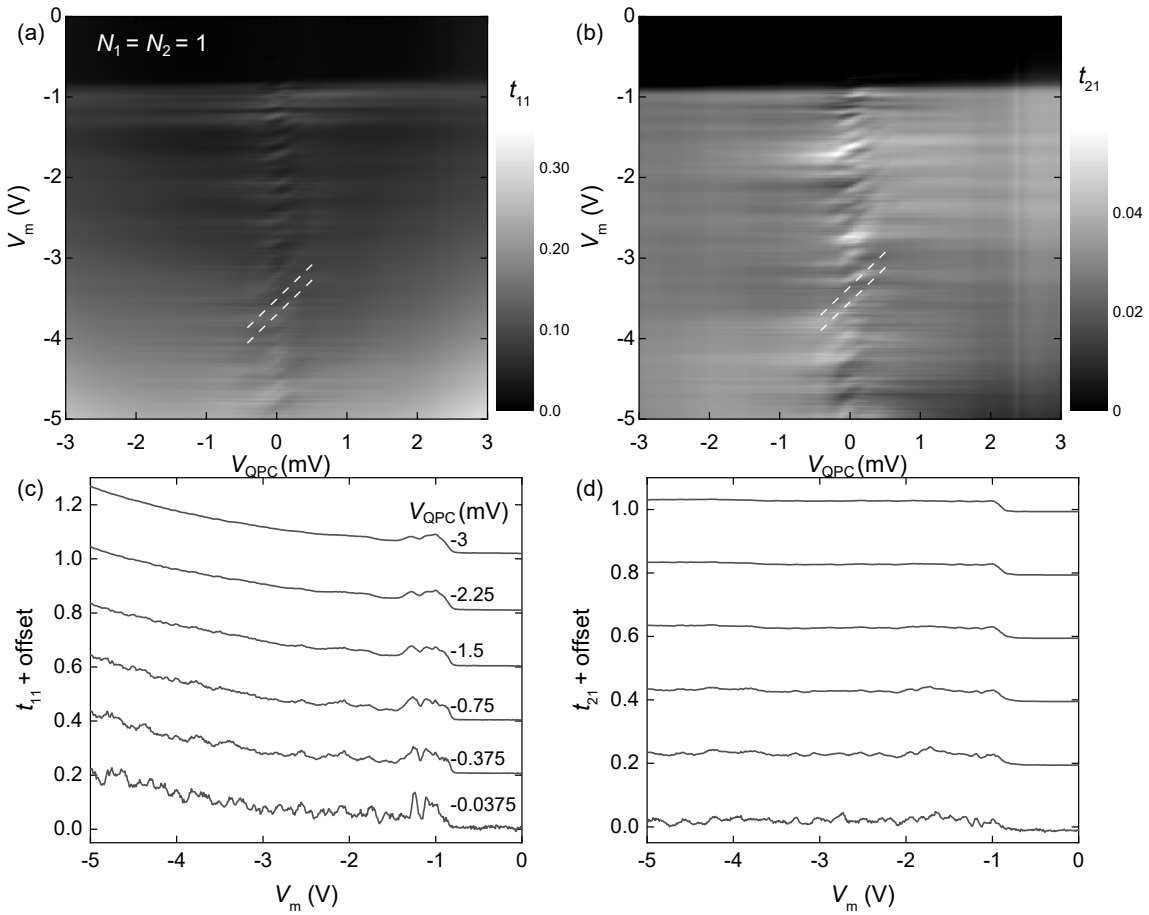

Figure 7.10: (a) Reflection probability into emitter QPC_1 as a function of source-drain- and mirror voltage, $t_{11}(V,V_{\text{m}})$ for $N_1 = N_2 = 1$, $B = 0$ and 280 mK. (b) Transmission probability into QPC_2, $t_{21}(V,V_{\text{m}})$. (c,d) Cuts of (a,b) along V_{m} for various V (data vertically shifted for clarity).

voltage drop over the emitter QPC_1,

$$V_{\mathrm{QPC}} = V \frac{G_1^{diff}}{N_1 G_Q},$$

with G_1^{diff} defined in equation 3.16. Both the reflection and the transmission probability show a blurred pattern of diagonal resonances around $V_{\mathrm{QPC}} = 0$, highlighted by dashed white lines as a guide for the eye. The stripes give rise to the pronounced oscillations found in the V_{m}-dependence in t_{11} and t_{21}. In Fig. 7.10(c,d) we present vertical cuts of the panels (a,b) for various V_{QPC}. Clearly, the oscillations are most pronounced for lower V_{QPC}. This suggests to interpret the diagonal stripes as a coherent interference pattern which blurs out due to bias smearing as the bias window gets larger. Since the dominant features are diagonal, the coherent cavity modes are sensitive to both V_{m} (used to control the size of the cavity) and V_{QPC} (used to control the width of the transport window between source- and drain leads).

In the inset of Fig. 7.11 we present a reference sample containing a QPC in strongly

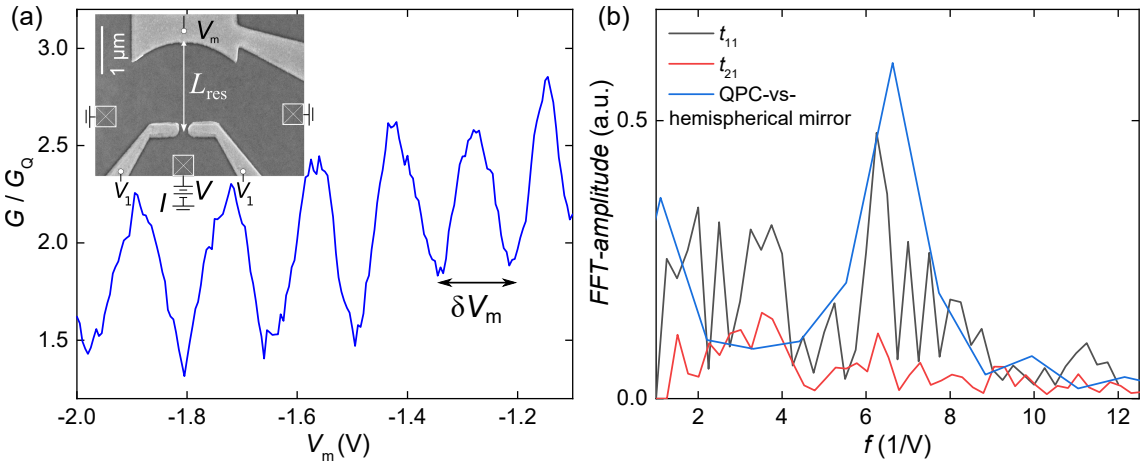

Figure 7.11: (a) Mirror gate voltage dependent conductance of a QPC set to $N = 4$, coupled to a hemisperical mirror, published in the appendix of Ref. [87]. (b) Fast Fourier transformation of $t_{11}(V_{\mathrm{m}})$ (red solid line) and $t_{21}(V_{\mathrm{m}})$ (black solid line) for $V = -50\,\mu\mathrm{V}$. Blue solid line: fast Fourier transformation of the pronounced Fabry-Pérot oscillations in (a).

coupled to a hemispherical mirror. In the main panel, we plot the measured conductance as a function of the mirror gate voltage V_{m}, while the QPC is set to $N = 4$. The strong oscillation in the conductance can be interpreted in analogy to the oscillations of the standing wave in a Fabry-Pérot resonator, while here, coherent electrons generate the standing wave. By increasing V_{m}, we decrease the area of 2DES depleted next to the mirror gate and thereby increase the length of the resonator (the distance between the QPC and the mirror). Per period of the conductance oscillation, the length of the resonator is reduced by half of the Fermi wavelength $\mathrm{d}L_{\mathrm{res}}/\mathrm{d}V_{\mathrm{m}} = 0.5\lambda_{\mathrm{F}}/\delta V_{\mathrm{m}}$ with the resonator length L_{res}. We determine the averaged period from the fast Fourier transform of the

oscillation, $\mathfrak{F}[I_1/V(V_\mathrm{m})]$ and find a strong peak around $f = 6.6\,\mathrm{V}^{-1}$, cf. blue solid line in Fig. 7.11(b). This corresponds to a period $\delta V_\mathrm{m} = 1/f = 150\,\mathrm{mV}$. With $\lambda_\mathrm{F} = 45\,\mathrm{nm}$, we finally estimate the rate of the depletion length reduction $\mathrm{d}L_\mathrm{res}/\mathrm{d}V_\mathrm{m} = 150\,\mathrm{nm/V}$. The sample in Fig. 7.11(a) was fabricated on the same heterostructure (A.1) and the QPC is nominally identical to QPC_1 and QPC_2. To compare the pronounced Fabry-Pérot frequency of the hemispherical mirror device to our elliptical cavity, we follow the same procedure and consider the fast Fourier transforms $\mathfrak{F}[t_{11}(V_\mathrm{m})]$ ($\mathfrak{F}[t_{21}(V_\mathrm{m})]$) at $V = -50\,\mu\mathrm{V}$, plotted as black solid (red solid) line in Fig. 7.11(b). Interestingly, both Fourier transforms show peaks around the characteristic Fabry-Pérot frequency obtained from the pronounced oscillations in Fig. 7.11(a). Note that the hemispherical mirror is designed such that it reflects the entire emitted electron beam directly back to the QPC. Ideally, this leads to the formation of a standing wave between the QPC and the mirror independently of the emission angle within the aperture of the mirror, causing a strong peak in the Fourier-spectrum. In contrast, the more complex geometry of the elliptical resonator gives rise to various trajectories that depend strongly on the emission angle of the QPC. Nevertheless, the good agreement between the peak frequencies obtained in the elliptical resonator and the hemispherical resonator suggests to interpret the periodic component of the V_m-dependent oscillations as Fabry-Pérot modes.

The visibility of the oscillations in $t_{11}(V_\mathrm{m})$ and $t_{21}(V_\mathrm{m})$ strongly drops with increasing $|V_\mathrm{QPC}|$ due to bias smearing, cf. Fig. 7.10. To obtain a better resolution of the cavity modes, we next consider the differential reflection and transmission coefficients δt_{11} and δt_{21} which we determined in analogy to t_{11} and t_{21} but replacing the terms $I_{1,2}/V$ in equation 3.19 and 3.19 by $\mathrm{d}I_{1,2}/\mathrm{d}V$, with $\mathrm{d}V = 20\,\mu\mathrm{V}$. This approach is similar to a lock-in measurement with a small ac-voltage superimposed on a dc-voltage offset. We plot the differential reflection and transmission cofficients as a function of V_m and V_QPC in Fig. 7.12(a,b).

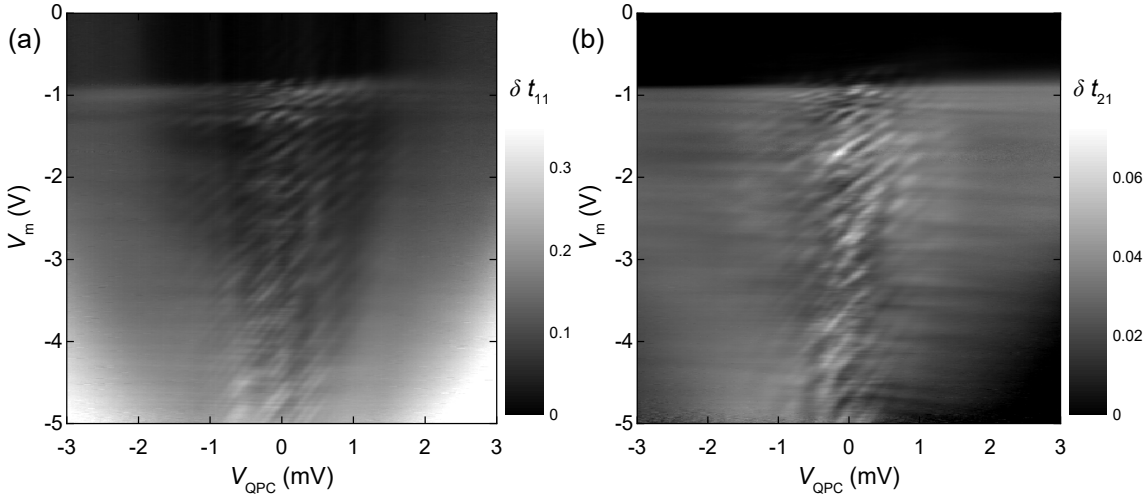

Figure 7.12: (a) Differential reflection coefficient, $\delta t_{11}(V_\mathrm{m},V_\mathrm{QPC})$ and (b) differential transmission coefficient $\delta t_{21}(V_\mathrm{m},V_\mathrm{QPC})$ for $N_1 = N_2 = 1$, $B = 0$ and $T = 280\,\mathrm{mK}$.

In this representation, the resolution of the cavity modes is much higher compared to the reflection/transmission plotted in Fig. 7.10, which were directly calculated from the measured raw data $I_{1,2}/V$ and thus reflect the bias smearing proportional to the full bias window $\propto eV$ relative to E_{F}^0. In contrast, in Fig. 7.12 we only consider the current flow within the narrow window $e\mathrm{d}V$ relative to the chemical potential at the source lead, which we control with V. This allows us to study the decoherence of single electron states due to electron-electron scattering on length scales shorter than the elastic mean free path [57].

The diagonal interference pattern is most pronounced in the differential reflection $\delta t_{11}(V_{\mathrm{m}},V_{\mathrm{QPC}})$, cf. Fig. 7.12(a). Here, we observe parallel diagonal stripes that are visible within a substantially larger V_{QPC}-range compared to the reflection data, cf. Fig. 7.10(a). The average spacing between two resonances along the V_{m}-axis coincides with the characteristic period obtained from the fast Fourier transform analysis of $t_{11}(V_{\mathrm{m}})$ and $t_{21}(V_{\mathrm{m}})$ for low V_{QPC} shown in Fig. 7.11. Moreover, the regular, equidistant nature of the interference pattern supports our interpretation of the cavity modes as Fabry-Pérot modes rather than conductance fluctuations. The latter are caused by the unique (random) disorder potential of the sample and are in general not equidistant in gate voltage [73].

The pattern in the differential detector transmission $\delta t_{21}(V_{\mathrm{m}},V_{\mathrm{QPC}})$, cf. Fig. 7.12(b), is less regular. One possible explanation for the lower visibility is the finite transmission of the *two* QPCs. In contrast, standing waves of the emitter QPC_1 only couple out of the cavity via *one* QPC (QPC_1).

Next, we repeat the Fourier analysis of the V_{m}-dependent oscillations for the much more pronounced pattern of the differential reflection/transmission. Since the main features are diagonal, they only acquire a phase shift in V_{m} as we vary V_{QPC}, while their frequencies in the Fourier spectrum remain unchanged. However, we expect the peak amplitudes to be sensitive to V_{QPC}, as we (i) vary the wavelength of electrons emitted into the resonator and (ii) modulate the phase space for electron-electron scattering. We present the fast Fourier transforms of $\delta t_{11}(V_{\mathrm{m}})$ and $\delta t_{21}(V_{\mathrm{m}})$ as a function of V_{QPC} in Fig. 7.13(a,b). Due to the high visibility of the V_{m}-dependent oscillations in the differential reflection beyond $|V_{\mathrm{QPC}}| > 1\,\mathrm{mV}$, the Fourier transformation shows peaks around the Fabry-Pérot frequency $f \simeq 6.6\mathrm{V}^{-1}$ in the same V_{QPC}-range, cf. Fig. 7.13(a). Interestingly, the visibility of the Fabry Pérot mode (proportional to the Fourier amplitude) is strongly modulated by V_{QPC}, giving rise to a pattern of resonances around $f \simeq 6.6\mathrm{V}^{-1}$. In contrast, there is no systematic V_{QPC}-dependence in the fast Fourier transform of the differential detector transmission [cf. Fig. 7.13(b)]. As we argued above, this could be related to the *two* partially transmitting QPCs in the detector transmission, compared to the reflection through a single QPC (QPC_1).

Next, we aim at extracting the dominant trajectory lengths from our bias voltage spectroscopy measurements. In the simple Fabry-Pérot picture, an increase (decrease) of V_{QPC} results in increasing (decreasing) wavelength of electrons in the resonator. Resonances occur, once the wavenumber between adjacent modes changes by $\Delta k = \pi/l$, where l is the length of the standing wave. Along the diagonal resonances in the differential reflection/transmission patterns, the variation in the resonator length (via V_{m}) and of the wavelength (via V_{QPC}) exactly compensate each other (constant phase condition). Assuming a parabolic dispersion relation in 1D, we can calculate the energy spacing between

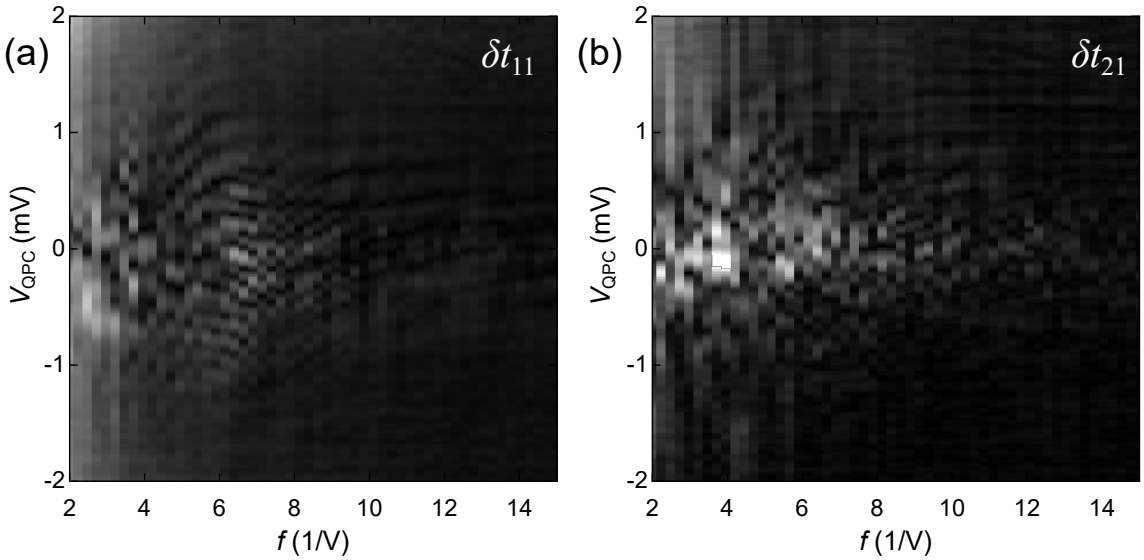

Figure 7.13: Fast Fourier transforms (FFT) of the differential reflection $\delta t_{11}(V_\mathrm{m})$ plotted in Fig. 7.12a and the differential transmission $\delta t_{11}(V_\mathrm{m})$ plotted in Fig. 7.12b, as a function of V_QPC. Light (dark) areas correspond to high (low) FFT amplitudes.

adjacent cavity modes at the Fermi energy,

$$\Delta E = \frac{\pi\hbar}{l}\sqrt{\frac{2E_\mathrm{F}^0}{m^\star}}. \tag{7.4}$$

In this picture, we treat the electron trajectories in the 2DES in 1D by 'unfolding' them after every reflection from a gate to result in an effective 1D trajectory length l. Exemplary classical calculated trajectories for a cavity based on the actual sample layout are shown in the appendix, Fig. A.5.

We interpret the V_QPC-dependent resonances in Fig. 7.13(a) as resonant conditions between the chemical potential of a cavity mode with the source-lead, $\mu_N = \mu_s$, where μ_s is tuned by V_QPC as sketched in the energy diagram in Fig. 7.14(a). We thus relate the spacing between two adjacent resonances as a function of V_QPC, ΔV_QPC, to the energetic difference between two adjacent cavity modes, $e\Delta V_\mathrm{QPC} = \Delta E$. In Fig. 7.14(a), we additionally indicate the chemical potential in the cavity and the drain lead behind the detector QPC_2, μ_c and μ_d, respectively. All local chemical potentials scale with the total source-drain voltage V applied at the emitter QPC_1. Assuming diffusive transport, we can calculate them from the measured, gate-voltage dependent resistances of the four QPCs (cf. section 7.2) using the diffusive sample resistance $R_{diff} = 1/G_1^{diff}$ and the effective resistances of the QPCs and their leads, $\tilde{R}_i = (N_i G_Q)^{-1} + R_i$, introduced in section

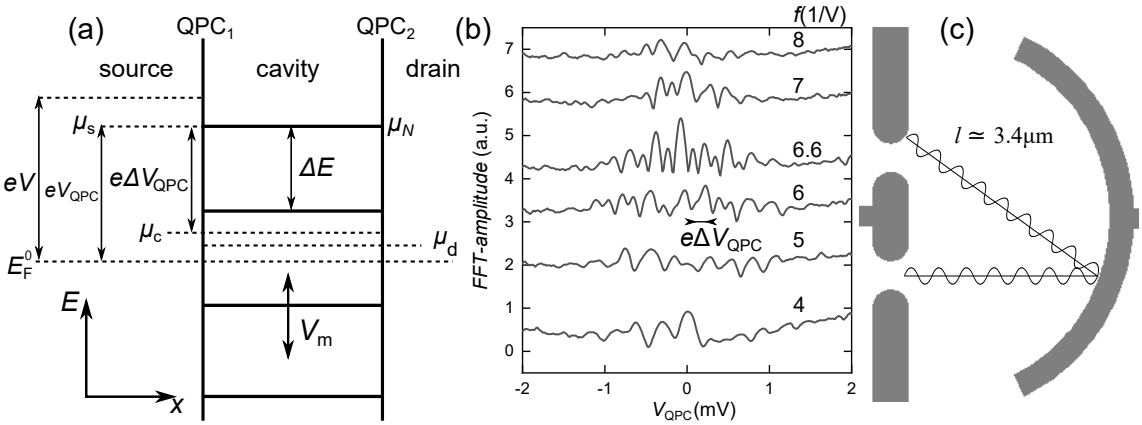

Figure 7.14: (a) Energy diagram of the cavity and the source- and drain leads, cf. main text. (b) Cuts along various frequencies of the fast Fourier transform of $\delta t_{11}(V_\mathrm{m})$, plotted as a function of V_QPC. Data are vertically shifted for clarity. (c) Standing electron wave with trajectory length $l \simeq 3.4\,\mu\mathrm{m}$, in very good agreement to the prediction obtained of the spacing of the resonances in panel (a), cf. main text.

3.3.1:

$$\mu_s = -eV\frac{R_{diff} - R_1}{R_{diff}}$$
$$\mu_c = -eV\frac{R_{diff} - \tilde{R}_1}{R_{diff}}$$
$$\mu_d = -eV\frac{R_{diff} - \tilde{R}_1}{R_{diff}}\frac{R_2}{\tilde{R}_2}.$$

To extract $\mu_s - \mu_c = e\Delta V_\mathrm{QPC}$ from our data, we plot cuts of the Fourier transform of the differential reflection coefficient for different frequencies around $f \simeq 6.6\mathrm{V}^{-1}$ as a function of V_QPC in Fig. 7.14(b). Within the window $4\,\mathrm{V}^{-1} \leq f \leq 8\,\mathrm{V}^{-1}$ we find the most pronounced resonances that exhibit a periodicity in V_QPC. Close to the Fabry-Pérot frequency around $f \simeq 6.6\mathrm{V}^{-1}$, the pattern covers the broadest V_QPC-range and the resonances show the highest visibility.

Using equation 7.4, we can calculate the trajectory length l for a given energetic cavity mode spacing. For the frequencies shown in Fig. 7.14(b), we find a characteristic spacing $\Delta E = 0.15\,\mathrm{meV}$ corresponding to $l = 3.2\,\mu\mathrm{m}$. This trajectory length is in good agreement with the dimensions of the cavity. In particular, it is compatible with the most simple standing wave expected for our cavity, which we illustrate in Fig. 7.14(c): the current density maximum of the narrow electron beam emitted from QPC_1 set to $N_1 = 1$ is reflected off the mirror towards the detector QPC. After an additional reflection from the upper detector QPC gate, a standing wave can be formed. The corresponding trajectory length of approximately $3.4\,\mu\mathrm{m}$ almost perfectly matches the trajectory length obtained from the energy spacings of adjacent cavity modes discussed above, $l = 3.2\,\mu\mathrm{m}$. This suggests to relate the pronounced Fabry-Pérot pattern to standing waves similar to the one illustrated

here. Other, more complex (longer) standing waves are possible, but expected to dephase faster with the bias voltage due to their increased trajectory length, contributing less to the diagonal (V_{QPC}-dependent) pattern.

Note that we find an identical trajectory length by directly reading off the spacing between two resonances (along the V_{QPC}-axis) in the differential reflection before the Fourier transform, cf. Fig. 7.12(a). However, the analysis above allows us to study the dependence of the Fabry-Pérot mode directly as a function of V_{QPC}.

To do so, we now focus on the dephasing and decoherence of electrons as a function of V_{QPC}, introduced in section 3.2.2 and consider:

(i) Dephasing of an electron ensemble excited within the energy window $E_{\mathrm{F}}^0 \leq E \leq E_{\mathrm{F}}^0 + eV_{\mathrm{QPC}}$ described by the dephasing length introduced in equation 3.10 (with $V' = V_{\mathrm{QPC}}$).

(ii) Decoherence of a single electron excited at energy $E_{\mathrm{F}}^0 + eV_{\mathrm{QPC}}$ described by the inelastic electron-electron scattering rate defined in equation 3.11 (with $\Delta = eV_{\mathrm{QPC}}$).

For our analysis, we neglect the small additional temperature broadening at the base temperature of 280 mK. In Fig. 7.15(a), we plot $V_{\mathrm{QPC}}(l_\phi)$ (black solid line) next to $V_{\mathrm{QPC}}(l_{e-e})$

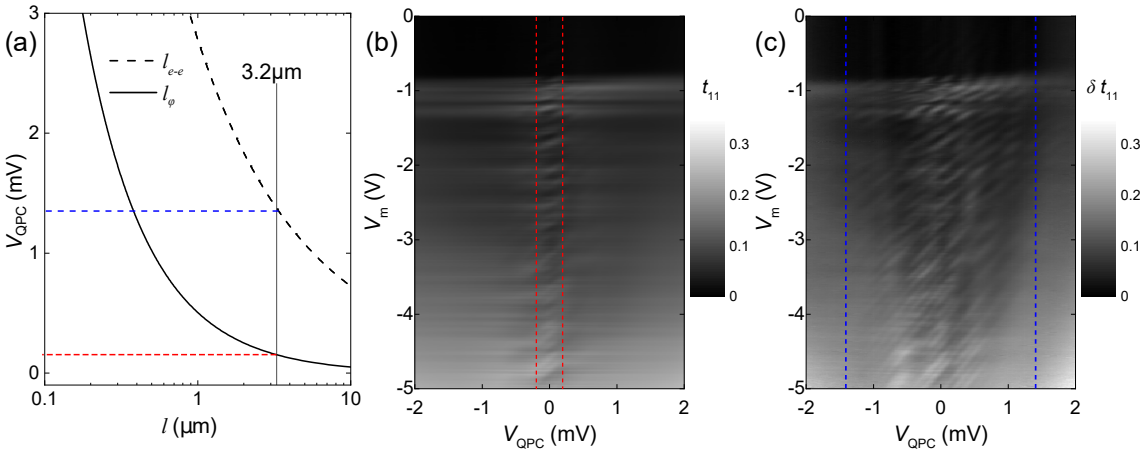

Figure 7.15: (a) Black solid line: electron dephasing length, cf. equation 3.10 and black dashed line: electron-electron scattering length for $T = 0$, cf. equation 3.11 as a function of the voltage drop into the cavity, V_{QPC}. (b) Measured reflection coefficient $t_{11}(V_{\mathrm{m}},V_{\mathrm{QPC}})$ and (c) differential reflection coefficient $\delta t_{11}(V_{\mathrm{m}},V_{\mathrm{QPC}})$ with vertical lines indicating the expected V_{QPC}-range for visible resonances obtained from the intersections in panel (a).

(black dashed line). We choose this representation instead of $l(V_{\mathrm{QPC}})$ because we are interested in finding the $|V_{\mathrm{QPC}}|$ for which (i) an electron ensemble dephases and (ii) single electrons suffer phase memory loss due to electron-electron scattering, as a function of their propagation distance. By increasing $|V_{\mathrm{QPC}}|$ for a given trajectory length l, the electron ensemble first dephases, before single electrons lose their phase memory, $|V_{\mathrm{QPC}}(l_\phi)| < |V_{\mathrm{QPC}}(l_{e-e})|$. This is in agreement with our experimental observation that the diagonal pattern in the measured reflection coefficient $t_{11}(V_{\mathrm{m}},V_{\mathrm{QPC}})$ vanishes for lower

$|V_{\mathrm{QPC}}|$ than in the differential reflection coefficient $\delta t_{11}(V_{\mathrm{m}},V_{\mathrm{QPC}})$. We plot both as a function of V_{QPC} in Fig. 7.15(b,c).

In panel (a) we additionally indicate the dominant trajectory length $l = 3.2\,\mu\mathrm{m}$ found in the analysis above as a vertical line. From the intersections with the dephasing length and the electron-electron scattering length dependence, we read off the corresponding $|V_{\mathrm{QPC}}|$ that is expected to limit the range of visible features in the reflection coefficient (due to dephasing of the electron ensemble) and the differential reflection coefficient (due to inelastic electron-electron scattering). We add vertical lines at the corresponding values of V_{QPC} in the panels (b,c) for direct comparison with the experimental data. For both the reflection [panel (b)] and the differential reflection [panel (c)], the prediction of the dephasing and inelastic electron-electron scattering model agrees well with the range of visible coherent features found in the experiment.

7.4 Combined electrostatic and magnetic field measurements

Another experimental parameter that can be used to manipulate coherent electrons consists in applying a perpendicular magnetic field B. In particular, magnetic field dependent measurements including ballistic and coherent cavities gave rise to a number of insightful publications [70–73, 99, 100]. In the first part of this section, we discuss the magnetic field dependent reflection probability $t_{11}(B,V_{\mathrm{m}})$ related to the cavity magnetoresistance, in the spirit of the publications cited above. The second part of this section treats the magnetic field dependent serial transmission through QPC_1 and QPC_2, $t_{21}(B,V_{\mathrm{m}})$.

7.4.1 Magnetic field dependent reflection

Cavities of dimensions smaller than the elastic mean free path and comparable to the coherence/dephasing length have been widely discussed in literature in terms of 'quantum chaos' in chaotic cavities both theoretically [69] and experimentally [70–73]. Next to chaotic cavities, also so called 'integrable' cavities have been theoretically predicted [101] and experimentally realized [99, 100]. The common method to characterize these cavities consists in measuring the magnetic field dependent resistance of the cavity. While the experiments cited above considered quantum dot-like structures with only two leads (two QPCs) serving as entrance and exit of the otherwise closed cavity, we here consider the case of an 'open' system by means of two additional side drains that are much wider than the QPCs, cf. Fig. 7.1. For the following measurements, we directly translate the measured cavity resistance $V/I_1(B,V_{\mathrm{m}})$ into the corresponding reflection probability $t_{11}(B,V_{\mathrm{m}})$ using equation 3.21.

In Fig. 7.16(a), we show $t_{11}(B,V_{\mathrm{m}})$ for $V = -0.1\,\mathrm{mV}$ and $N_1 = N_2 = 1$ at 280 mK in a 2D colorplot representation. Beyond the depletion voltage of the mirror ($V_{\mathrm{m}} < -0.9\,\mathrm{V}$) we observe a finite reflection probability modulated by both V_{m} and B. As almost the entire source-drain voltage drops along the emitter QPC, this measurement represents practically

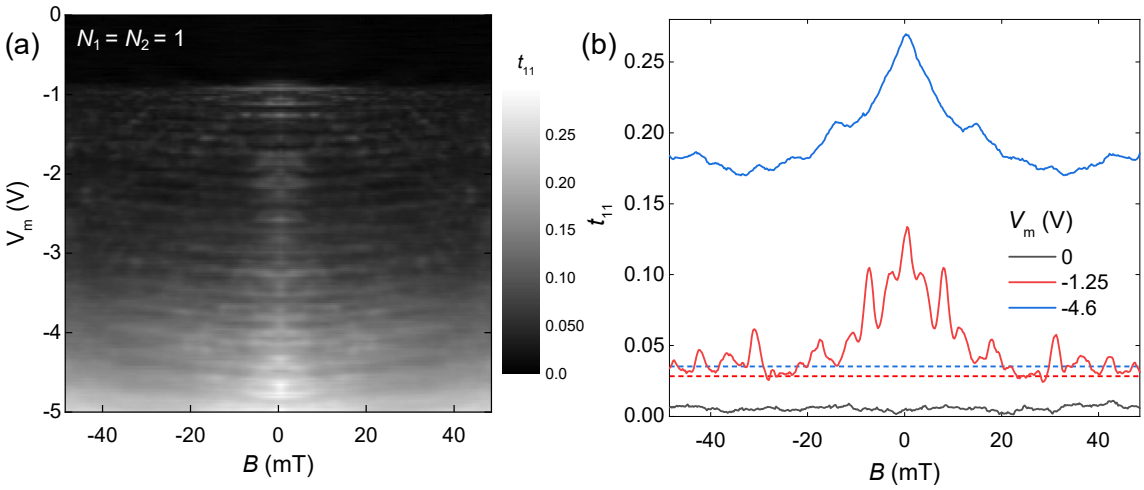

Figure 7.16: (a) Reflection probability $t_{11}(B,V_\mathrm{m})$ for $N_1 = N_2 = 1$ and $V = -0.1\,\mathrm{mV}$ at 280 mK. (b) Solid lines: cuts $t_{11}(B)$ along $V_\mathrm{m} = 0$, $-1.25\,\mathrm{V}$ and $-4.6\,\mathrm{V}$ (black, red and blue line). Dashed lines indicate the corresponding reflection probability assuming chaotic cavity physics.

a two-terminal measurement. Consequently, we find a mirror symmetry around $B = 0$, confirming the Onsager relations [91].

In Fig. 7.16(b), we plot cuts $t_{11}(B)$ for $V_\mathrm{m} = 0$, $-1.25\,\mathrm{V}$ and $-4.6\,\mathrm{V}$ (black, red and blue line). Clearly, the depleted cavity manifests as a reflection maximum at $B = 0$ (red and blue line) compared to the flat curve without cavity at $V_\mathrm{m} = 0$ (black line). This maximum can have both classical and quantum-mechanical contributions. Classically, our cavity layout can give rise to enhanced backscattering into the emitter QPC_1 at $B = 0$, while finite magnetic fields can cause a stronger coupling into the other QPCs. Quantum mechanically, constructive interference between time-reversed paths of electrons increases the probability of a particle to return to where it came from, compared to the classical case. This form of coherent backscattering was originally found in phase coherent, strongly disordered (diffusive) systems at low temperature [55], where it is termed weak localization effect. In this kind of samples, scattering events happen at spatially randomly distributed impurities. This effect is strongly B-dependent, as a magnetic field breaks time reversal symmetry. In contrast, we here present a system smaller than the elastic mean free path $l_\mathrm{m} = 14\,\mu\mathrm{m}$ - *i.e.* in the ballistic transport regime - with large angle scattering events occurring at the gate-defined boundaries.

Next to the pronounced reflection maximum at $B = 0$, we observe characteristic, reproducible oscillations in $t_{11}(B)$ which change strongly as we vary the cavity size with V_m, cf. Fig. 7.16. Similar to the weak localization effect, this behavior was originally found in phase-coherent diffusive systems and termed 'universal conductance fluctuations' [56], resulting from interference between different forward scattered paths. Due to their ballistic origin in our case, we denote them 'ballistic conductance fluctuations' (BCFs), in accordance with literature [70, 73].

For comparison, we add the predicted reflection probability assuming chaotic cavity physics

defined in equation 3.14 as dashed black, red and blue line in Fig. 7.16(b). While the reflection for $V_m = -1.25\,V$ is close to the chaotic prediction for $|B| > 20\,mT$, it dramatically exceeds the chaotic prediction for $V_m = -4.2\,V$, pointing to non-chaotic cavity dynamics as we decrease the size of the cavity.

7.4.1.1 Chaotic cavities

Ballistic microcavities have been widely discussed in the literature in terms of 'quantum billiard', in which electrons enter a cavity through one lead and leave the cavity through a second lead after multiple elastic reflections from the cavity boundaries. The quantum billiard model was motivated from a semiclassical point of view, in which electrons propagate along classical trajectories and additionally carry phase information. The dynamics of such cavities was investigated first theoretically by Jalabert et al. [69], who found 'chaotic' scattering dynamics for certain cavity geometries. To illustrate the characteristics of a chaotic system, we show an example in Fig. 7.17. Both figures show calculated classical

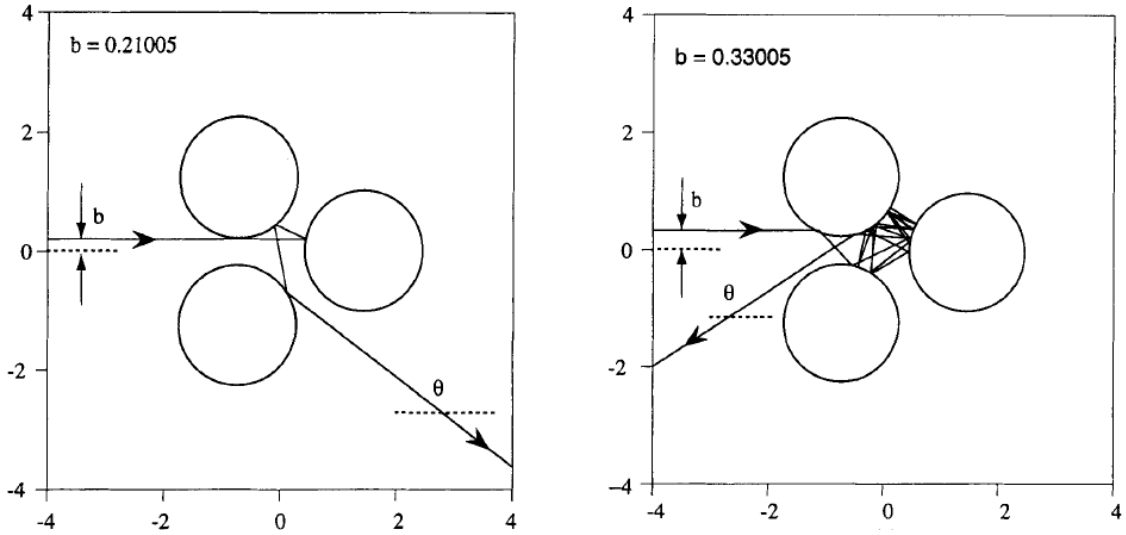

Figure 7.17: Calculated trajectories of a chaotic system. The trajectories strongly change with a small variation in the initial conditions (impact parameter b) of the system. Found in Ref. [102].

trajectories for a ballistic particle entering a scattering region for two different distances b to the symmetry axis (impact parameters). The particle propagates at constant velocity and scatters elastically with specular reflections from the circles. Comparing the two figures, we find that the trajectory changes dramatically while the impact parameter is just slightly varied: the strong sensitivity of the observable to only a small variation of the initial conditions is characteristic for a chaotic system. Using semiclassical arguments, it has been shown that the number of particles remaining in the scattering region after a time t follows an exponential law [103, 104] $N(t) = N_0 \exp(-\gamma t)$, with the classical escape rate γ and the number of incoming particles N_0. Assuming a constant particle

velocity v, the distribution of trajectory lengths inside the scattering region then scales like $N(L) \propto \exp(-\gamma_L L)$, with $\gamma_L = \gamma/v$. It is important to emphasize that the escape rate of the exact quantum mechanical solution for a 'quantum billiard' is determined by the underlying chaotic classical scattering [69].

To adapt these findings to magnetoresistance measurements in chaotic ballistic cavities, the convenient distribution function is

$$N(A) \propto \exp\left(\frac{-\alpha|A|}{2\pi}\right), \tag{7.5}$$

with the area enclosed by closed electron orbits A and the characteristic root-mean-squared area α^{-1} [69]. This distribution function is favorable because A and the experimental parameter B are linked by the Aharanov-Bohm relation $\varphi_0 = AB$, with the magnetic flux quantum $\varphi_0 = h/e$. By evaluating the Fourier spectrum of the oscillations, $S_g(f) = \mathfrak{F}[t_{11}(B)]$, we can relate the magnetic frequency f to an orbit area, $f = 1/B = A/\varphi_0$. The spectrum is thus a measure for the distribution of flux areas of trajectories contributing to conduction [70, 105]. For the area distribution function assuming chaotic scattering (equation 7.5), the functional form of the corresponding Fourier spectrum in the chaotic case is predicted to be [69]:

$$S_g(f) = S_g(0)[1 + (2\pi\alpha\varphi_0)\, f] \exp(-2\pi\alpha\varphi_0 f)\,. \tag{7.6}$$

From the BCFs in $t_{11}(B)$, we can thus extract statistical properties of the trajectories inside the cavity to reveal their dynamics.

In Fig. 7.18(a), we plot $t_{11}(B)$ at $N_1 = N_2 = 1$ and $V = -0.1\,\mathrm{mV}$ without cavity ($V_\mathrm{m} = 0$, black line) and for a cavity with decreasing size ($V_\mathrm{m} \leq -1\,\mathrm{V}$, colored lines). The experimental data show the average after measuring each curve ten times to increase the signal to noise ratio of the BCFs. We additionally indicate the average value of the chaotic prediction for the reflection (cf. equation 3.14) within $-1\,\mathrm{V} \geq V_\mathrm{m} \geq -5\,\mathrm{V}$ as a gray dashed line.

In Fig. 7.18(b), we show the Fourier transformation of the curves shown in panel (a), $\mathfrak{F}[t_{11}(B)]$ (dots) next to fits according to equation 7.6 (solid red lines) on a semi-logarithmic scale. On the 100 mT wide magnetic field range, we only consider oscillations with periods smaller than 25 mT. On the top axis, we show the flux area $A = f\varphi_0$ enclosed by electron trajectories. We use the measurement with transparent mirror gate ($V_\mathrm{m} = 0$) to obtain the noise-level of the measurement and indicate it as a dashed horizontal black line in all panels. This value was obtained from the average value of the spectrum for $V_\mathrm{m} = 0$. Decreasing V_m, we observe a steeper decay of the Fourier amplitude with f, corresponding to increasing decay constants α.

In Fig. 7.18(c), we plot the inverse of the decay constants found in the fits in (b). As explained above, α^{-1} can be interpreted as the root-mean-squared area enclosed by closed electron paths. Just like the shift of the decay to smaller frequencies, the inverse decay constants display the decreasing cavity size with decreasing V_m, in good agreement with the dimensions of the cavity. For $V_\mathrm{m} = 0$, the Fourier spectrum shows no significant decay: the open high mobility 2DES contains too few impurities to cause enhanced backscattering into

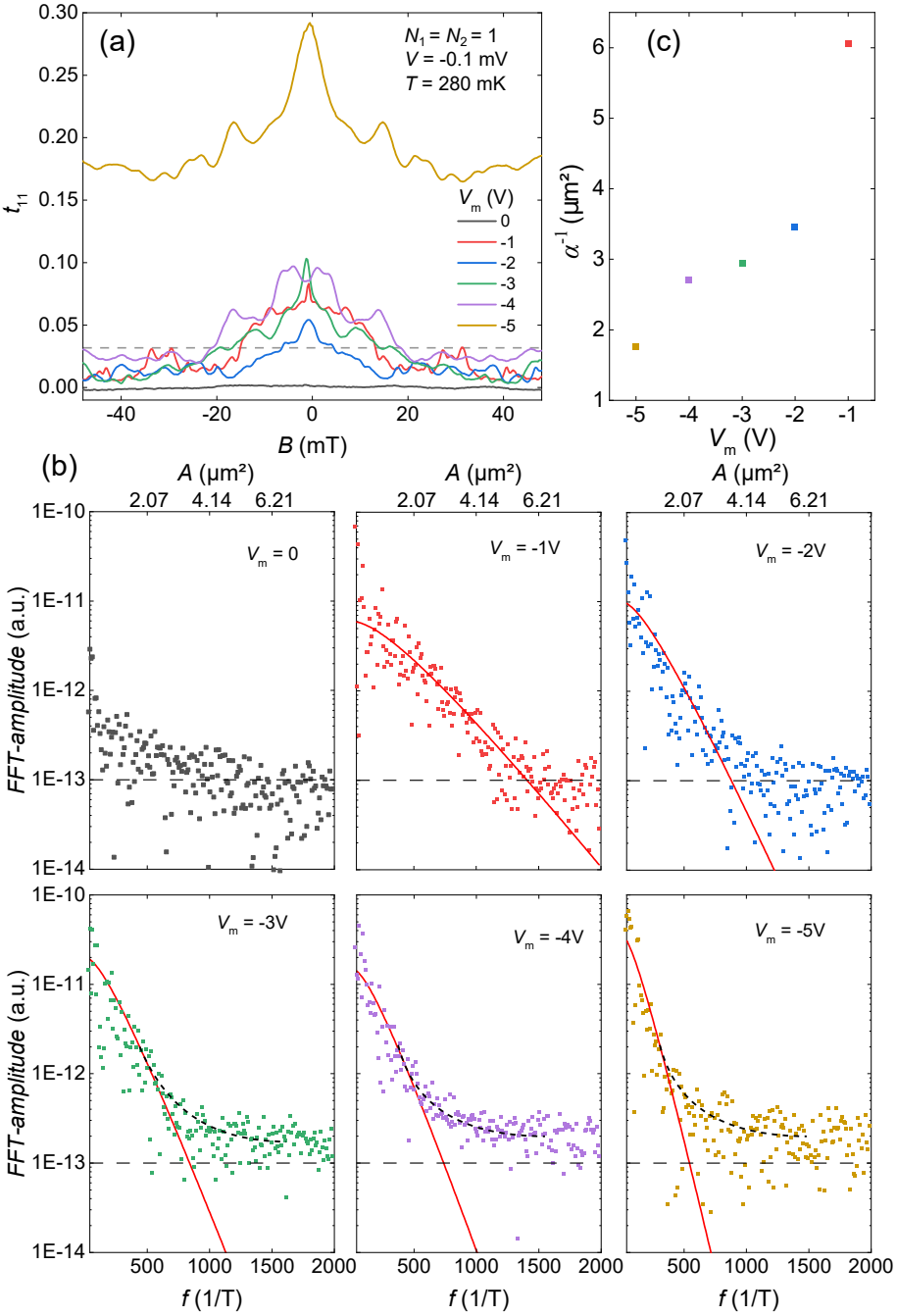

Figure 7.18: (a) Colored lines: $t_{11}(B)$ for $N_1 = N_2 = 1$ and $V = -0.1\,\mathrm{mV}$ at $T = 280\,\mathrm{mK}$ for various V_m. Dashed line: averaged chaotic prediction for t_{11}, cf. main text. (b) Colored dots: Fourier transformations of (a) plotted on semi-logarithmic scale. Solid red lines are fits of the decaying part of the spectrum according to equation 7.6 with fit parameters α and $S_g(0)$. (c) Root-mean-squared areas α^{-1} determined from the fits in (b) as a function of V_m.

the emitter QPC. With the mirror depleted, $V_m \leq -1\,V$, the fit to the chaotic prediction (red line) describes the data roughly over two decades. This agreement is worse than what has been found in other ballistic microcavities [70–73] and can be attributed to the geometry of our cavity: the larger area of our cavity (compared to those in the publications cited above) makes the magnetic flux more sensitive to the magnetic field ($\varphi = AB$), decreasing the resolution of the B-dependent oscillations. Additionally, the large cavity openings QPC_3 and QPC_4 lead to much shorter dwell times for electrons in our cavity. This causes in particular chaotic modes with multiple reflections to contribute less to the measured reflection amplitude. Finally, the magnetic field range of the measurements is likewise limited by the large cavity openings QPC_3 and QPC_4, as electrons leave the cavity already for fields $|B| > 60\,mT$ (based on a simple classical estimation of the cyclotron radius). Within the remaining magnetic field range, the conductance fluctuations in our open electron cavity are substantially less pronounced, giving rise to a weaker decay in the Fourier spectra.

For $V_m \leq -3\,V$, the data show a smooth transition down to a constant level, where they are not well described by the exponential fit anymore. Here, the data rather follow a power law distribution, cf. black dashed lines in Fig. 7.18(b). Similar deviations from the chaotic prediction for large frequencies have been observed before experimentally [72] and found in numerical calculations [106], who attributed the latter to fingerprints of non-chaotic, so-called integrable contributions.

7.4.1.2 Towards integrable cavities

Besides chaotic cavities, there are certain cavity geometries that lead to non-chaotic, so called 'integrable' dynamics. This concept is illustrated in Fig. 7.19. The two left panels

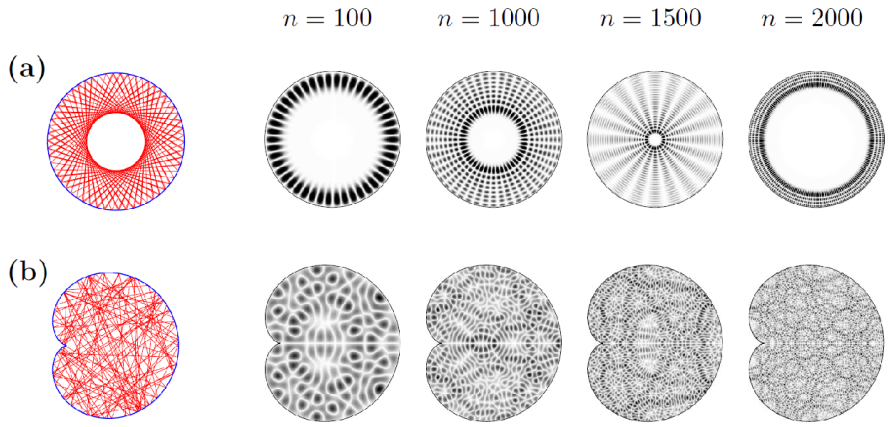

Figure 7.19: Left figures (red): calculated trajectories of a classical particle after 100 specular reflections from the boundaries. Right figures (black and white): calculated stationary eigenfunctions with quantum number n where dark areas correspond to high probability densities. Figures in (a) are for a circular (integrable) and (b) for a cardiod (chaotic) geometry, cf. main text. Copied from Ref. [107].

show the evolution of a classical particle after 100 reflections of the system boundaries for (a) an integrable circular and (b) a chaotic cardioid shape. While the circular geometry gives rise to a regular pattern with areas that are not traversed by the particle, the cardioid geometry results in an irregular pattern that spans the entire system. The latter represents an ergodic system, in which the particle fills the entire phase space after sufficiently many reflections. In contrast, for the circular geometry, the phase space traversed by the particle forms a torus smaller than the total system size, which is characteristic for an integrable system. Different characteristics are also found in the solution of the corresponding quantum mechanical problem [107], cf. black and white figures in Fig. 7.19. The probability density of the integrable circular geometry shows repetitive patterns with multiple symmetry axes and nodes in phase space. On the other hand, the chaotic cardiod gives rise to a complex pattern that equally fills the entire phase with respect to the symmetry axis of the geometry.

This motivated multiple groups to investigate circular microcavities which indeed showed two theoretically predicted features of integrability [72,99,100]. In the following, we present these predictions and compare them to our data.

Shape of the backscattering feature

Baranger et al. [101] derived a Lorentzian magnetic field dependence around the reflection maximum $t_{11}(B = 0)$ in coherent chaotic cavities:

$$t_{11}(B) = t_{cl}\left(1 + \frac{1}{1 + \left(\frac{2B}{\alpha\varphi_0}\right)^2}\right). \tag{7.7}$$

The first term denotes the classical reflection amplitude, t_{cl}. The second term describes the quantum mechanical interference contribution to the reflection, with the root-mean-squared area α^{-1} enclosed by electron paths with start- and end point at emitter QPC_1, introduced before in equation 7.5. The width of the reflection maximum can thus be related to the average flux area enclosed by electron paths with the same starting and endpoint. In contrast, they predicted a linear relation $t_{11}(B) \propto |B|$ around $B = 0$ for the integrable case. The qualitative difference between both regimes is a consequence of their different classical distribution of orbit areas [101].

In Fig. 7.20(a), we show $t_{11}(B,V_\mathrm{m})$ for $N_1 = N_2 = 2$ with cuts along different V_m plotted in Fig. 7.20(b). The latter figure demonstrates that our tunable structure permits to switch between chaotic and integrable behavior: for $V_\mathrm{m} = -4.68\,\mathrm{V}$ [blue line in Fig. 7.20(a)], we find a Lorentzian $t_{11}(B)$ profile indicating chaotic behavior [blue line in Fig. 7.20(b)]. We additionally plot a fit to the clearly Lorentzian feature using equation 7.7 (red dashed line). From the fit, we find $\alpha = 3.12 \times 10^{12}\,\mathrm{m}^{-2}$, corresponding to a flux area $\alpha^{-1} = 0.32\,\mu\mathrm{m}^2$, which is substantially smaller than the cavity size. This is in contrast to earlier results using fully-circular microcavities: here, the peaks were comparable to the cavity dimensions and could be readily explained by electrons propagating along the cavity boundaries in a

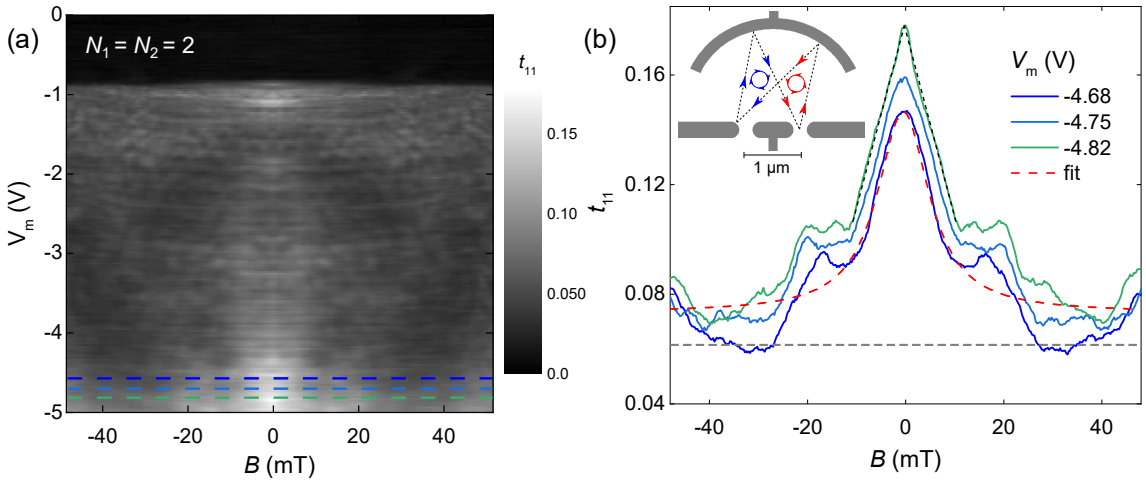

Figure 7.20: (a) t_{11} for $N_1 = N_2 = 2$ and $V = -0.1\,\mathrm{mV}$ at 280 mK as a function of the perpendicular magnetic field B and V_m. (b) Line cuts of $t_{11}(B)$ as indicated in (a) for $V_\mathrm{m} = -4.68\,\mathrm{V}$ (blue line), $V_\mathrm{m} = -4.75\,\mathrm{V}$ (turquoise line) and $V_\mathrm{m} = -4.82\,\mathrm{V}$ (green line). Red dashed line: Lorentzian fit using equation 7.7, indicating chaotic cavity modes (see text). The black dashed lines are a guide to the eye highlighting the linear B-dependence around $t_{11}(B = 0)$, indicating integrable cavity modes. Inset: sketch of a backscattering trajectory with two closed orbits of opposite magnetic flux, cf. main text.

closed loop [70,99]. In our half-elliptical geometry, closed loops are unlikely, since emitted electrons are reflected from the mirror towards the detector, rather than along the mirror gate. Closed paths thus require additional reflections from the QPC- and the mirror gates, as illustrated schematically in Fig. 7.20(b). These kind of trajectories necessarily include intersections, which leads to flux areas with opposite directions of rotations (blue, red). Since the magnetic flux is a directed vector quantity, the accumulated net area corresponds to the difference of both orbits. Consequently, the flux can cancel out completely for identical areas [108,109], or give rise to net areas that are substantially smaller than the cavity itself [72]. As we further decrease the cavity size with V_m, the shape of the reflection maximum feature evolves into a clearly triangular V-shape at $V_\mathrm{m} = -4.82\,\mathrm{V}$ [green line in Fig. 7.20(a)], pointing to an integrable cavity regime [green line in Fig. 7.20(b) with black dashed lines as guide for the eye]. Note that we find similar line shapes for comparable voltages at $N_1 = N_2 = 1$, cf. Fig. 7.16(b). However, a clear *transition* from a Lorentzian (chaotic) to a triangle (integrable) was found only at $N_1 = N_2 = 2$.

To demonstrate the coherent nature of the V-shaped reflection maximum, we show $t_{11}(B)$ at $N_1 = N_2 = 2$ and $V_\mathrm{m} = -4.82\,\mathrm{V}$ for temperatures T increasing from 280 mK to 5 K in Fig. 7.21. Due to the strong sensitivity of the QPC conductance on temperature (cf. inset of Fig. 7.7(b)) and to facilitate comparison, we vertically shifted the curves. For the base temperature, we clearly find a triangular, non-Lorentzian resistance peak, corresponding to an integrable cavity ($T = 280\,\mathrm{mK}$, solid black line). While the peak shape remains triangular for $T = 0.55\,\mathrm{K}$ (solid red line), the triangular structure smears out for higher temperatures and transforms into a smooth maximum ($T = 2.5\,\mathrm{K}$) before it vanishes at

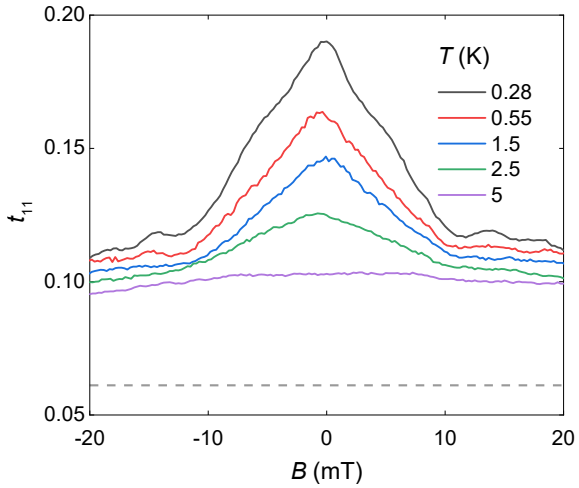

Figure 7.21: Temperature dependence of the V-shaped reflection maximum $t_{11}(B,V_\mathrm{m} = -4.82\,\mathrm{V})$ shown in Fig. 7.20. Dashed gray line: chaotic prediction of the reflection probability.

$T = 5\,\mathrm{K}$. The same behavior has been found within the first experimental realization of an integrable electron cavity in a 2DES [99]. Chang et al. concluded that phase coherence of the electrons giving rise to the integrable feature is destroyed as the dephasing length due to thermal broadening is becoming shorter than the characteristic trajectory lengths contributing to conduction.

7.4.2 Magnetic field dependent transmission

In the previous section, we have discussed the magnetic field dependent reflection probability $t_{11}(B)$ related to the measured *emitter* current I_1. Next, we consider the magnetic field dependence of the simultaneously measured *detector* current I_2 and the corresponding transmission probability $t_{21}(B)$ through both QPCs in series, which can be obtained from equation 3.22 for not too high magnetic fields. In the first part of this section, we investigate the coupling of both QPCs with grounded mirror gate, $V_\mathrm{m} = 0$, by only applying a perpendicular magnetic field. In the second part, we look at their coupling while additionally varying the cavity size with V_m.

7.4.2.1 QPCs coupled via magnetic field

Classically, the application of a perpendicular magnetic field exerts the Lorentz force on electrons, giving rise to cyclotron motion. For not too high fields, the magnetic field dependent cyclotron radius is defined as:

$$r_c(B) = \frac{m^\star v_\mathrm{F}}{|eB|}. \tag{7.8}$$

The vertical alignment of our QPCs requires finite magnetic fields to bend electron trajectories from the emitter into the detector, analog to earlier 'magnetic focusing' experiments [29,110]. In Fig. 7.22(a), we plot $I_1(B)$ (solid black line, left axis) for $N_1 = N_2 = 1$ and the mirror gate grounded, $V_\mathrm{m} = 0$. For comparison, we add the simultaneously mea-

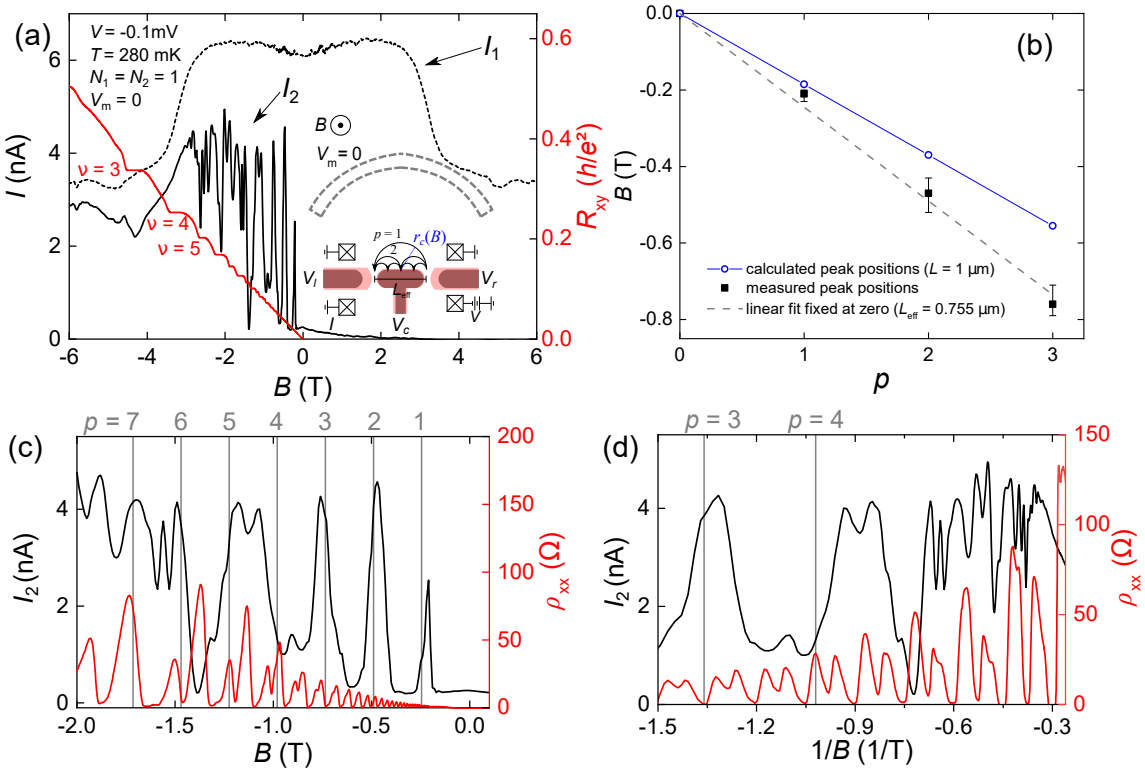

Figure 7.22: (a) Left axis, black solid line: $I_2(B)$ at $V_\mathrm{m} = 0$ for $N_1 = N_2 = 1$ and black dashed line: $I_1(B)$. Right axis, red line: Hall resistance $R_{xy}(B)$ measured in the bulk (without QPCs). The inset shows the corresponding circuit diagram and sketches magnetic focusing. The red shaded areas schematically show the depleted areas after applying $V_{0,r,l}$, see main text. (b) Black squares: position of the first three (p = 1,2,3) peaks from (a). Dashed gray line: linear fit fixed at zero, corresponding to an effective lateral spacing $L_{eff} = 0.755\,\mu\mathrm{m} < L$ between the QPCs, cf. main text. Blue circles: calculated positions of the first three magnetic focusing maxima, assuming the lithographic spacing L between the QPCs. (c) Magnified $I_2(-2\,\mathrm{T} < B < 0.1\,\mathrm{T})$ from (a) with vertical lines indicating the peak positions obtained from the linear fit in (b) for $p \leq 7$. (d) Black line: I_2 with vertical lines p = 3,4 from (c) added for orientation, next to bulk Shubnikov-de Haas oscillations (red line), plotted against $1/B$.

sured emitter current $I_1(B)$ as a dashed black line. Other than $I_2(B)$, $I_1(B)$ is asymmetric, as only for $B < 0$ electrons are bent towards the detector. Here, we observe a series of peaks in $I_1(B)$, highlighted in a magnified view in Fig. 7.22(c). For small magnetic fields, we expect classical cyclotron motion (skipping orbits) along the intermediate gate (cf. Fig. 7.1) that can give rise to magnetic focusing. As we increase $|B|$, Landau quantization as well as Zeeman splitting (cf. equation 6.4) compete with the energies of the electro-

static 1D QPC subbands [spaced by $\varepsilon(N)$]. Consequently, for high fields, edge channel transport within the quantum Hall regime [cf. measured $R_{xy}(B)$ red curve, right axis in Fig. 7.22(a)] gives rise to additional features.

From the *lithographical* lateral distance between the QPCs, $L = 1\,\mu\text{m}$ (cf. Fig. 7.1), we derive the focusing conditions for electrons propagating in classical cyclotron motion:

$$|B| = \frac{2m^\star v_\text{F}}{eL}, \tag{7.9}$$

where $L = 2pr_c$ and the positive integer p accounting for $p-1$ reflections off the intermediate gate before reaching the detector, as sketched in the inset of Fig. 7.22(a).

In Fig. 7.22(b), we compare the measured peak positions (black squares) to the fields calculated from the focusing condition in equation 7.9 (blue circles) for p = 1,2 and 3, assuming $L = 1\,\mu\text{m}$. As expected from the periodic focusing condition, the measured peaks are approximately equidistant within error bars related to their widths, pointing to classical cyclotron motion with specular reflections from the intermediate gate. However, we find a higher slope compared to the calculated fields, cf. linear fit fixed at zero (dashed gray line). We exclude interactions with the mirror gate to cause these deviations, as the distance between the grounded mirror gate is larger than the cyclotron radius of the first magnetic focusing peak, cf. inset of Fig. 7.22(a). Instead, we attribute the different slopes to the electrostatic potentials defining the QPCs: while the central gate is always kept at a constant voltage $V_c = -1.5\,\text{V}$, $\text{QPC}_{1,2}$ are controlled by varying $V_{r,l}$. On the first conductance plateau, we have $V_r = V_l = -2.25\,\text{V} < V_0 = -1.5\,\text{V}$ (cf. Fig. 7.3). Consequently, the outer QPC-gates defined by $V_{r,l}$ cause a larger depleted region (red shaded areas) than the intermediate gate, effectively lowering the lateral distance of the QPCs L_{eff}. This effect is particularly strong at $N_1 = N_2 = 1$, where $\delta V_{gate} = |V_{r,l}| - |V_c|$ is largest. From a linear fit to the experimental data in Fig. 7.22(b) (dashed gray line), we determine $L_{eff} = 0.755\,\mu\text{m}$, slightly larger than the lithographic vertical extent of the intermediate gate ($0.75\,\mu\text{m}$). This is in very good agreement with the depletion rate $\delta l/\delta V = 150\,\text{nm/V}$ determined in section 7.3.4.

Panel (c) shows a magnified view of the first peaks in $I_2(B)$ with gray vertical lines indicating the classical magnetic focusing conditions $|B(L_{eff})|$ for $p \leq 7$. Additionally, we plot the Shubnikov-de Haas (SdH) oscillations measured in the bulk with no QPCs defined (red line). The first two $I_2(B)$ peaks are clearly distinguishable due to the intermediate pronounced minima: here, the ballistic orbits skip the detector and $I_2(B)$ is diffusive. This suggests an interpretation of the first two peaks as orbits with zero ($p = 1$) or one ($p = 2$) reflection on the intermediate gate. However, for $p > 2$, the assignment of the peaks to the classical periodicity in B becomes difficult, as contributions of different p begin to overlap. The resolution of the peaks is limited by the narrow constriction size of the detector QPC at $N_2 = 1$ (approximately 80 nm, see QPC calibration measurements in chapter 4). Second, the round shape of the QPC-gates can lead to deviations of the estimation of the focusing conditions, which does not take into account the shape of the QPCs. Third, and most importantly, as $|B|$ is increased, Landau quantization of electrons becomes stronger and the semiclassical skipping orbits gradually transform into quantum mechanical edge states [29,111]. For high fields, $|B| > 3\,\text{T}$, the Landau quantization energy dominates the 1D subband spacing of the QPCs, $\varepsilon(N = 1) = 5.2\,\text{meV}$, cf. Fig. 4.2. At

these fields, we observe a transition from the spin-degenerate 1D QPC-subbands to spin split Landau levels [11].

In Fig. 7.22(d), we compare $I_2(B)$ to the periodicity of the SDH oscillations by plotting the data in $1/B$, with the vertical lines for $p = 3{,}4$ from (c) added for orientation. While the SdH oscillations show the expected periodicity with increasing Zeeman-splitting (double-peaks), $I_2(B)$ turns out to be neither periodic in B nor $1/B$. In literature, these kind of oscillations have been described as interference between occupied edge channels [111].

In Fig. 7.23 we translate the measured detector current $I_2(B)$ into the probability to traverse QPC_1 and QPC_2 in series, $t_{21}(B)$, while keeping $V_m = 0$. Note that the cavity (and hence QPC_3 and QPC_4) are not defined here, such that we can omit the last term in the equation for $T_{21}(B)$ (cf. equation 3.20). The magnetic focusing maxima lead to transmissions of beyond 60 %, making magnetic focusing in this geometry much more efficient than the typical transmissions for (electrostatic) focusing at $B = 0$ found in this and other samples, see chapter 5. In the edge-channel regime for very high fields, $B < -3\,\mathrm{T}$, the transmission probability increases to more than 80 %.

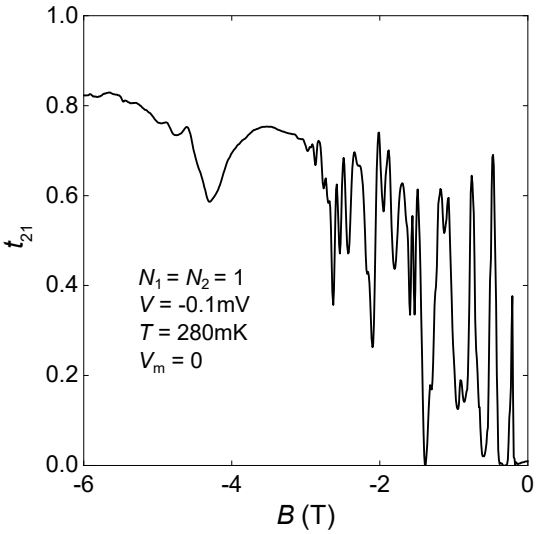

Figure 7.23: Serial transmission probability through QPC_1 and QPC_2 as a function of B, for $N_1 = N_2 = 1$ and $V_m = 0$.

Next, we open up the QPC-constrictions and additionally consider $I_2(B)$ at $N_1 = N_2 = 2{,}3$ and 4 while still keeping the mirror grounded ($V_m = 0$). In Fig. 7.24(a), we plot the corresponding transmissions as a function of B within the range of the first two pronounced magnetic focusing maxima shown in Fig. 7.22. For all $N_1 = N_2$, we find a pronounced first order magnetic focusing peak around $B \simeq -0.2\,\mathrm{T}$. The peak widths increase with $N_{1,2}$, reflecting the increasing emission angles as the QPCs are opened up, cf. section 4.4. Other than for $N_1 = N_2 = 1$ (solid black line), $t_{21}(B)$ does not drop to zero behind the second magnetic focusing peak around $B \simeq -0.45\,\mathrm{T}$, as the beams are becoming too wide and skipping orbits propagating along the intermediate gate begin to overlap. While we found the highest transmission of the first magnetic focusing peak around $B \simeq -0.2\,\mathrm{T}$ for $N_1 = N_2 = 2$ (solid red line), the second focusing peak around $B \simeq -0.45\,\mathrm{T}$ is strongest for only one conducting channel with systematically decreasing amplitudes for higher $N_1 = N_2$. At $N_1 = N_2 = 3{,}4$, the second peak becomes less pronounced and additional oscillations develop. As these oscillations are weakened at lower $N_{1,2}$ (less conducting subbands), they might be attributed to interference between different transverse modes.

Surprisingly, we find a feature before the first magnetic focusing peak around $B \simeq -50\,\mathrm{mT}$ with a trend to more negative B for increasing $N_{1,2}$, cf. area shaded in gray in panel (a) and the magnified view in Fig. 7.24(b). Drawing the corresponding skipping orbit with $r_c(B = -50\,\mathrm{mT}) = 1.7\,\mu\mathrm{m}$ [see sketch in panel (b)] shows that this feature is compatible

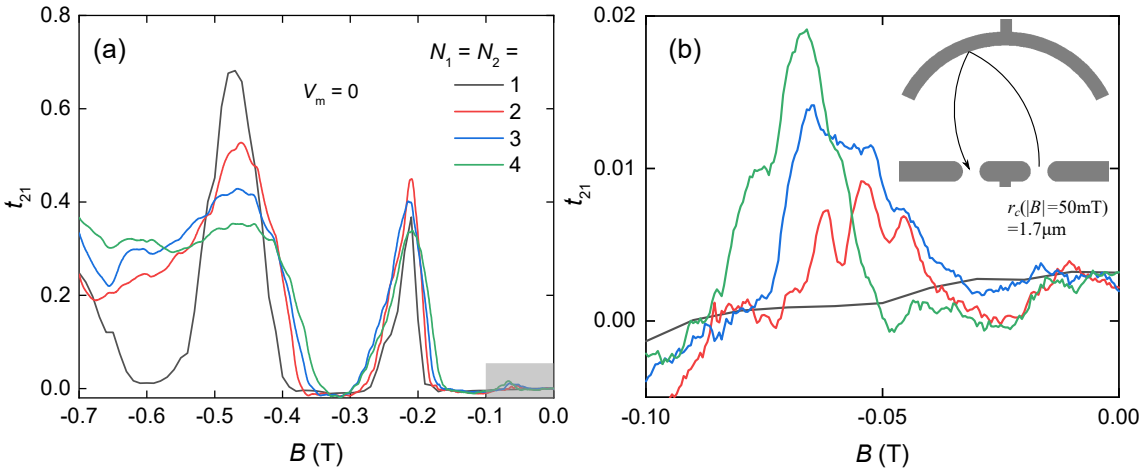

Figure 7.24: (a) $t_{21}(B)$ for $V_\mathrm{m} = 0$ for $N_1 = N_2 = 1,2,3$ and 4 with $V = -0.1\,\mathrm{mV}$. Data in the gray frame are plotted separately in (b). Sketch: cyclotron orbit for $r_c(B = -50\,\mathrm{mT})$, compatible with ballistic focusing via a reflection off the mirror, indicating a piezoelectric potential modulation within the 2DES caused by the mirror gate even at $V_\mathrm{m} = 0$.

with magnetic focusing via one specular reflection off the mirror gate. This points to the presence of a finite piezoelectric potential below the curved mirror gate, causing reflections even for a grounded mirror gate at $V_\mathrm{m} = 0$, similar to the piezoelectric potential discussed in section 6.4.1.

7.4.2.2 QPCs coupled via the cavity in a magnetic field

To further investigate the connection between the features around $B = -50\,\mathrm{mT}$ and the mirror gate, we now additionally apply a negative gate voltage and consider $t_{21}(B,V_\mathrm{m})$ for $N_1 = N_2 = 2$, cf. Fig. 7.25(a). Again, we find the prominent magnetic focusing feature at $B = -0.2\,\mathrm{T}$ which is not affected by V_m, as the distance to the mirror is larger than the corresponding cyclotron orbit, cf. sketch in Fig. 7.22(a). For more positive B, we find increasing transmissions precisely around $B = -50\,\mathrm{mT}$, confirming the connection between the feature found at $V_\mathrm{m} = 0$ and the mirror gate. As we move the mirror closer to the QPCs by decreasing V_m, the transmission maximum bends towards lower absolute magnetic fields (larger r_c).

To describe the bent features in the $t_{21}(B,V_\mathrm{m})$ map, highlighted by black dashed lines in panel (a), we use a frequently used semiclassical picture, in which electrons carry phase information while moving along classical trajectories. In Fig. 7.25(d) we show classical cyclotron orbits corresponding to various coordinates of the $t_{21}(B,V_\mathrm{m})$ map in panel (a), highlighted in the same color: at ($V_\mathrm{m} = -1\,\mathrm{V}, B = 0$, cyan trajectory and circle), electrons are propagating straight and are scattered from the mirror towards the detector [cyan trajectory in panel (d)]. At ($V_\mathrm{m} = -1\,\mathrm{V}, B = -50\,\mathrm{mT}$, red), electrons are focused into the detector via a curved trajectory after one reflection off the mirror. By decreasing V_m, we move the mirror towards the QPCs [dashed arc in panel (d)]. For ($V_\mathrm{m} = -1.5\,\mathrm{V}, B = 0$,

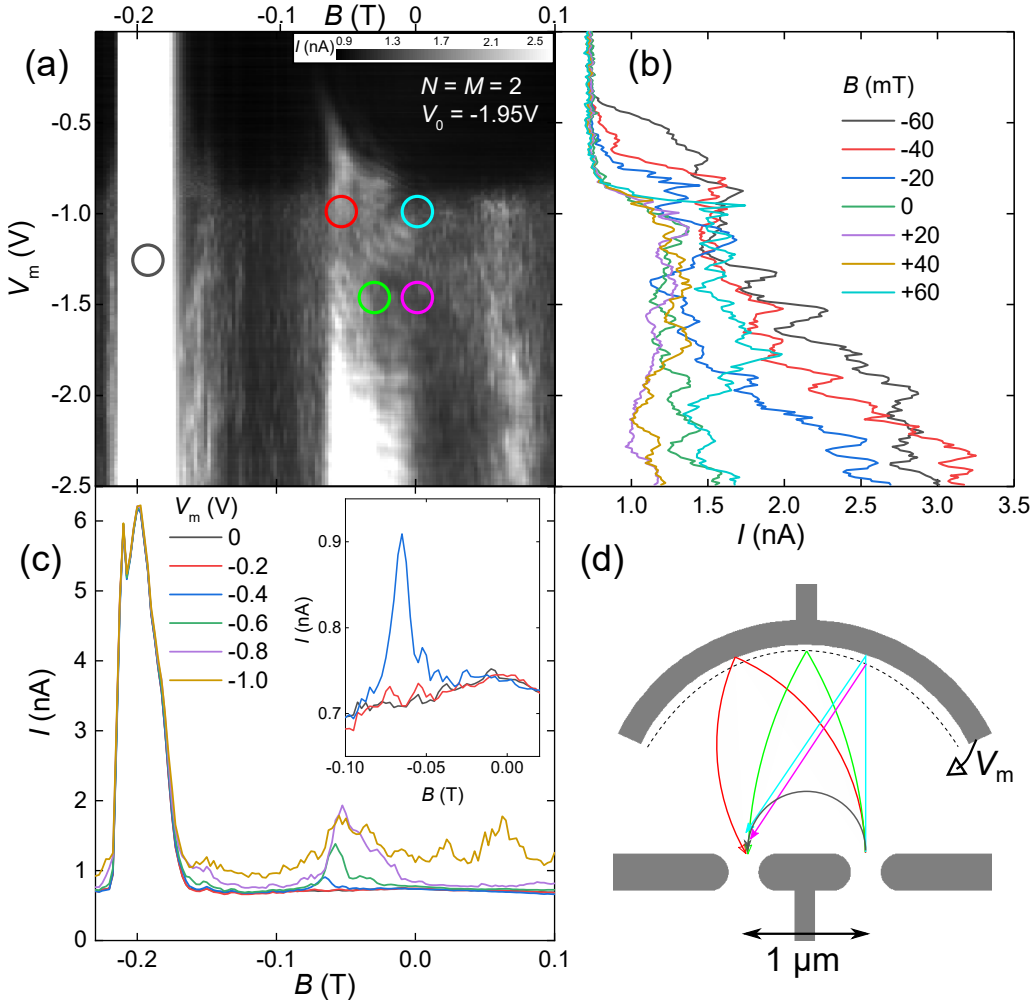

Figure 7.25: (a) $t_{21}(B,V_\mathrm{m})$ for $N_1 = N_2 = 2$ and $V = -0.1\,\mathrm{mV}$. (b) Cuts $t_{21}(V_\mathrm{m})$ for different B. (c) Cuts $t_{21}(B)$ for different V_m. (d) Sketch of various electron trajectories at coordinates (V_m,B) of the map in (a), marked with circles in the respective color.

purple), electrons propagate parallel to the trajectories for more positive V_m (with $B = 0$). For trajectories at $B < 0$, ($V_\mathrm{m} = -1.5\,\mathrm{V}$,$B = -25\,\mathrm{mT}$, green) shifting the mirror towards the QPCs requires more positive B to keep the orbit focused into the detector.

Quantum mechanically, the electrons' phase can be modulated by both, variations in B and V_m. Consequently, a constant phase condition in the (B, V_m) parameter space gives rise to bent, arc-like features like the ones found in our experiment [cf. dashed black lines as guide for the eye in Fig. 7.25(a)], as well as in earlier works with open electron resonators [112].

In Fig. 7.25(b), we plot cuts $t_{21}(V_\mathrm{m})$ along various values of B. The oscillating features demonstrate the alternating constructive and destructive interference, as we vary the resonator size with V_m. Fig. 7.25(b) shows cuts $t_{21}(B)$ for decreasing V_m. Clearly, the cavity related focusing peak shifts to more positive B as we decrease V_m, demonstrating the sen-

sitivity of the cavity modes to both V_m and B. In contrast, the direct magnetic focusing maximum around $B = -200\,\mathrm{mT}$ is not affected by V_m, as the corresponding cyclotron radius is smaller than the distance from the emitter QPC to the mirror gate, gray trajectory in Fig. 7.25(d).

8 Parabolic cavity

Making use of ballistic electron optics we next present an approach to couple two distant nanostructures via a parabolic cavity.[1] We present an SEM image of an exemplary sample in Fig. 8.1(a).

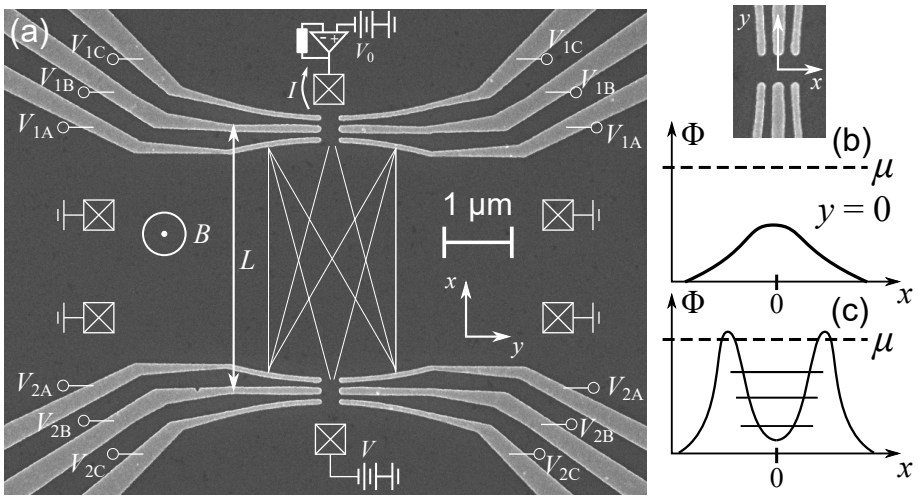

Figure 8.1: (a) SEM image of a sample. Light areas show gated structures on the sample surface (dark). Crossed boxes mark Ohmic contacts, negative voltages V_{ij} with $i = 1{,}2$ and $j = \mathrm{A,B,C}$ define nanostructures 1,2 with pairs of split gates labeled A,B,C. We measure the serial current I flowing through structure 1 after applying a source drain voltage V to the lead of structure 2. All other Ohmic contacts (crossed boxes) are electrically grounded. Thin lines show two ideal trajectories coupling both structures after specular reflections off the parabolic mirrors. Two different devices with distances $L = 2.8\,\mu\mathrm{m}$ and $L = 4\,\mu\mathrm{m}$ with different parabolic mirror gates were studied. (b) Illustration of the longitudinal electrical potential component $\Phi(x)$ for $y = 0$ through a QPC defined by three pairs of split gates. (c) $\Phi(x)$ for $y = 0$ the case where outer split gates form tunneling barriers defining a quantum dot (cf. main text).

The two nanostructures labeled 1,2 consist of three thin ($\approx 90\,\mathrm{nm}$ wide) pairs of split-gates labeled A,B,C respectively. We control the electrical potential in the 2DES below each

[1] The measurements presented in this chapter were conducted by I. Sampaio, who also took over the optical lithography process for the sample. The concept and design of the samples based on EBL was developed and realized by J. Freudenfeld and J. Meister. The single QPC characterization measurements can be found in I. Sampaio's masterthesis (Ref. [49]). Section 8.2 of this thesis contains data from Ref. [49] but additionally accounts for the finite lead resistance in the measurements.

split gate by the voltages V_{ij} with $i = 1,2$ and $j = \mathrm{A,B,C}$. The split gates labeled A form the mirrors of a cavity located between the two nanostructures. They have a parabolic shape with their focal point located close to the central orifice of the opposite split-gate respectively. Ideally, for this design, electrons emitted from one of the two nanostructures are focused into the second nanostructure after two specular reflections off the parabolic mirror gates, cf. white trajectories in Fig. 8.1. We aim at demonstrating the focusing effect by measuring the serial current I flowing through the two nanostructures in series after applying a source-drain voltage V to the the lead of the emitter nanostructure for different mirror voltages. The central region of 2DES is electrically grounded via four Ohmic contacts. The samples shown in this chapter were fabricated on wafer number mbe8-309 grown by V. Umansky (see growth protocol in section A.1) hosting a 2DES 107 nm below the wafer surface. The 2DES Fermi energy is $E_{\mathrm{F}}^{0} = 11\,\mathrm{meV}$ and the measured mean free path after processing of the present samples $l_{\mathrm{m}} \simeq 35\,\mu\mathrm{m}$. A detailed overview of the experimental setup used for the experiments in this chapter is shown in section 2.2.1.

Depending on the gate voltages V_{ij}, various confinement potential configurations can be realized. In the following we describe the two limiting cases.

Quantum point contact

Each pair of split-gate features a constriction. By adjusting the respective gate voltage, it can be tuned to a classical pinhole or to a QPC. For $V_{i(\mathrm{A,C})} > V_{i\mathrm{B}}$, the electrical potential below split-gate B in the center of the nanostructure is higher than the electrical potential below the outer split-gates A and C. In Fig. 8.1(b) we show an illustration of the longitudinal electrical potential component Φ_x at the center of the 1D-channel at $y = 0$. In this regime, the gate voltages $V_{i\mathrm{B}}$ are used to tune to control the strongest lateral confinement at the maximum Φ_x and the nanostructure represents a QPC. Additionally, the gate voltages $V_{i(\mathrm{A,C})}$ are used to fine tune the longitudinal channel length of the QPC. In particular, $V_{i\mathrm{A}}$ are used to control the distance between the parabolic mirrors

Quantum dot

In contrast, for $V_{i(\mathrm{A,C})} < V_{i\mathrm{B}}$ the electrical potential below the outer gates can be higher than below the central split-gate cf. Fig. 8.1(c). For a proper choice of gate voltages, the outer potential wells exceed the chemical potential and thereby form quantum dot with discrete states [113]. In this regime, the outer gates represent tunneling barriers that are controlled by the gate voltages $V_{i(\mathrm{A,C})}$ while the energies of the localized states are varied with $V_{i\mathrm{B}}$. The transition between the quantum point contact and the quantum dot regime is described in detail in Ref. [77].

8.1 Concept

In the spirit of ballistic electron optics, we assume that electrons emitted into the cavity propagate along perfectly straight trajectories and only scatter from the system bound-

aries (the gates) via specular reflections. Furthermore, the ideal trajectories sketched in Fig. 8.1(a) (white solid lines) require a perfect cavity geometry. To design the cavity, we treat the QPCs as classical pinholes without a characteristic 1D mode structure. In Fig. 8.2(a), we place one pinhole at the vertex of one of the two parabolic mirror gates. The latter follows the parabola equation $x'(y') = ay'^2$ (dashed black lines), where a is the curvature of the parabola. The second mirror obeys the parabola equation of a vertically

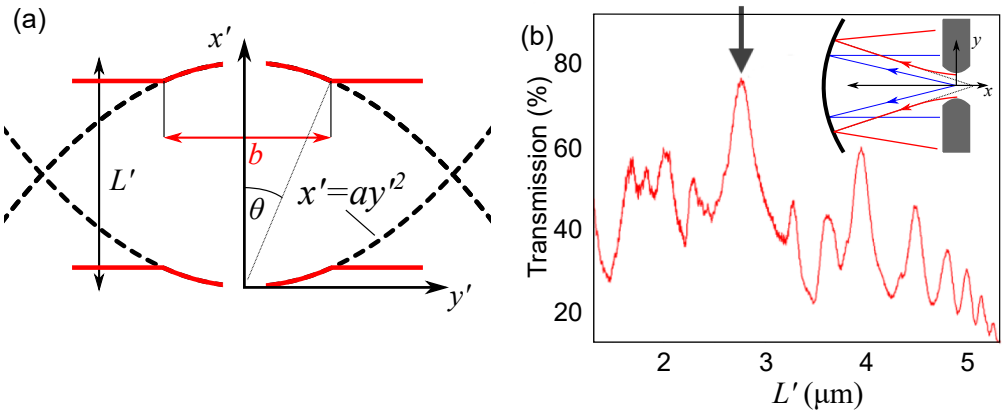

Figure 8.2: (a) Sketch of the cavity geometry. The parabolic mirrors (red solid line) obey a parabola equation with curvature a (black dashed line) within a lateral region $|y'| < b/2$ and are straight for $|y'| > b/2$. (b) Exemplary calculated serial transmission through two mirror constrictions for $a = 0.0833\,\mu\text{m}^{-1}$ and $b = 4.3\,\mu\text{m}$ as a function of the distance L' between their vertices [cf. panel (a)] with both mirror constrictions set to $G = 3G_Q$ respectively. Inset: illustration of a pinhole serving as a point source of electrons (blue trajectory) and a parabolic mirror.

flipped copy of the first parabola, spaced by a distance L' along the x'-axis. We define a maximum lateral extent b of the parabolic mirrors, such that the minimum distance between the two structures along the x'-axis does not cause a too high side resistance, $R_{side} << 1/G_Q$, as we intend to study an *open* resonator. At the same time, we make sure that the aperture b is large enough to collect electrons emitted at an angle $|\theta| \leq 35°$ with respect to the x'-axis. This angle is chosen such that electrons are captured by the mirror for up to four conducting channels, cf. Fig. 4.8. For $|y'| > b/2$, the mirrors are straight and run parallel to the y'-axis, cf. red solid line. The vertices of the mirrors are left out to form the orifices of the nanostructures.

With the parameters a and b set, we next run coherent numerical calculations (cf. section 3.5) to find the optimum spacing L' between the two mirror vertices maximizing the transmission through the system, cf. Fig. 8.2(b). In our calculations, we describe the pinhole using a realistic parabolic saddle point potential which reproduces the typical emission angles in our experiments, cf. section 6.3. Even though we are considering specular reflections off perfect mirrors and a perfectly flat 2DES without disorder potentials, the theoretical transmissions found in the calculations are limited to approximately 80 %. We attribute the upper limit to the actual funnel-like emission of electrons from the QPC, cf. sketch in Fig. 8.2(b) and explanations in section 4.4: other than the simplified ray-optics

picture suggests, the QPCs do not represent perfect point sources emitting electrons from the center of the constriction (blue trajectories). Instead, the entire quantum well formed in the constriction is populated with electrons depending on the lateral QPC potential relative to the local chemical potential. As the lateral electrostatic potential drops towards the free 2DES, the transverse electron momentum changes and the emission follows a funnel shape (red trajectories). Extrapolating the straight course of the red trajectories back through the QPC (black dashed lines), we find that the effective focal point of the parabolic cavity slightly varies with the emission angle. In other words, our parabolic mirrors have a slight astigmatism due to the funnel-like emission of the QPCs. Despite the upper transmission limit, we choose L' for a given a and b such that our device operates close to the calculated transmission maximum. Note that the calculated L' for maximum transmission only deviates by 10 % from the simple geometrical estimation of the focal point based on point-sources, $f = 1/4a$. We follow that the idealized trajectories sketched in Fig. 8.1(a) are major contributors to the serial transmission through both mirrors rather than chaotic cavity modes which couple much stronger to the open side drains of the cavity.

Summarizing the concept introduced above, we conclude that the simple geometrical optics picture is a starting point for the design of the present structure, even though more complex mirror shapes would be required to maximize the coupling between the two pinholes.

8.2 Transmission enhancement via the cavity

In Fig. 8.3, we show pinch-off curves for a device with a distance $L = 4\,\mu\text{m}$ between split-

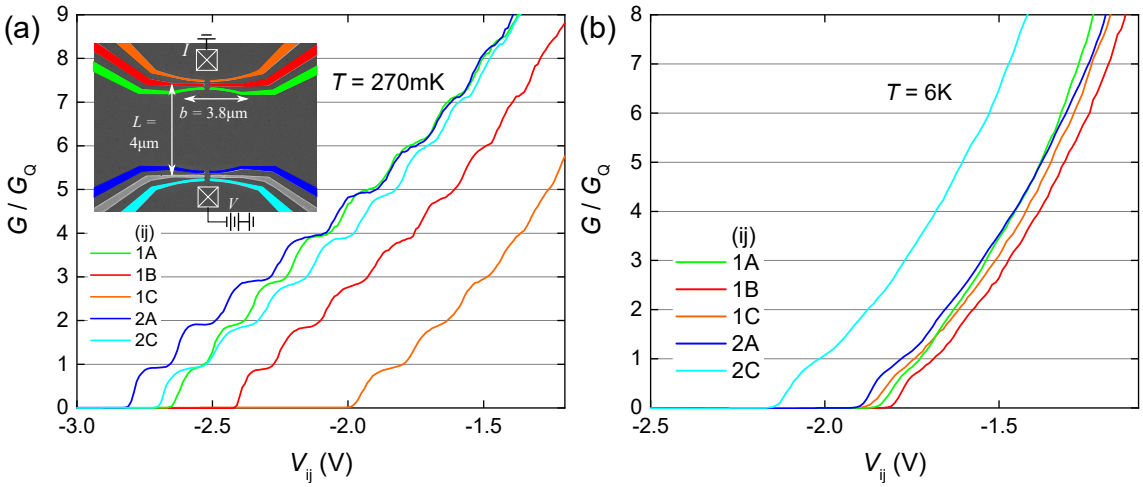

Figure 8.3: Individual pinch-off curves of the split-gates highlighted in the respective color in the top left inset at a temperature of 270 mK [panel (a)] and 6 K [panel (b)]. The missing split-gate 2B did not respond to the applied gate voltage for the device shown here. The SEM image shown in the inset is not true to scale.

gates 1B and 2B and a lateral extent of the mirrors with parabolic shape $b = 3.8\,\mu\text{m}$.

The mirror curvature is $a = 0.0625\,\mu\text{m}^{-1}$. In Fig. 8.3(a), we display the pinch-off curves of the individual split-gates measured at a temperature of 270 mK. Split-gate 2B was not functional due to a disconnected bond wire. At this temperature, all working split-gates feature a discrete 1D subband spectrum, as we observe pronounced conductance plateaus in all pinch-off curves. In Fig. 8.3(b), we show the pinch-off curves measured at a temperature of 6 K. Here, the thermal excitations cause energy broadening, such that the conductance plateaus smear out and the QPCs lose their characteristic 1D modestructure. In this regime, the constrictions are better described as classical pinholes with a Gaussian lateral emission pattern.

Comparing the two panels, we also observe a strong shift in gate voltages for the individual pinch-off curves. This shift occurred for all gates after frequently sweeping the corresponding gate voltage in the measurements. We believe that this behavior is related to a leakage current leading to frozen negative charges trapped between the gates and the 2DES. Since we have not been facing this problem in the other samples presented in this work, we suspect the application of a plasma etching procedure in O_2 prior to the evaporation of the gate layer, performed only during the fabrication for this set of samples to cause this problem.

To couple two distant QPCs for a fully operational device with the present geometry, we ideally aim at setting the maximum lateral confinement potential of QPC_1 and QPC_2 with the two central split-gates 1B and 2B, while using the split-gates 1A and 2A as mirrors of the parabolic cavity. By decreasing V_{1A} and V_{2A} beyond the depletion voltage, we increase the depleted area below the respective gates and thereby lower the effective cavity size. The additional split-gates 1C and 2C can be used to tune the longitudinal channel length to control the beam profile.

However, to reduce the number of gates swept and to still characterize the focusing properties of the parabolic mirrors, we in the following apply a source-drain voltage V to QPC_2 (emitter) defined by split-gate 2A and measure the serial current I flowing through QPC_1 (detector) defined by split-gate 1A. We keep all other gates at the ground potential. We set the detector to a conductance of $G(V_{1A} = -1.66\,\text{V}) \approx 2G_Q$, cf. Fig. 8.3(b). We now step the emitter gate voltage V_{2A} and simultaneously measure the lateral carrier emission spectrum in a magnetic deflection experiment, introduced in section 6.3. We plot $I(V_{2A},B)$, in a 2D colorplot representation in Fig. 8.4(a) for orientation. In Fig. 8.4(b) we show cuts $I(B)$ for various values of the emitter split-gate voltage V_{2A}. Independently of V_{2A}, we find a current maximum around $B \approx 9\,\text{mT}$. Note that the expected magnetic focusing maximum is located at $B = 0$ due to the symmetry of the design. However, a broken y-symmetry due to lithography imperfections or electrostatic (disorder) potentials in the intermediate region between the 2DES can give rise to the observed shift in B.

To extract the ballistic component $I_{ball}(B)$ of the measured current we next look at $I(V_{2A},B = 40\,\text{mT})$, plotted in Fig. 8.4(c). The corresponding cyclotron radius $r_c(B = 40\,\text{mT}) = 2.1\,\mu\text{m}$ is small enough that carriers can no longer be ballistically focused into the opposite QPC via specular reflections and cyclotron motion for the present gate geometry (assuming a free 2DES without additional elastic scattering between the two QPCs). We thus define this as the magnetic field independent diffusive contribution I_{diff} to the total current $I(B) = I_{ball}(B) + I_{diff}$.

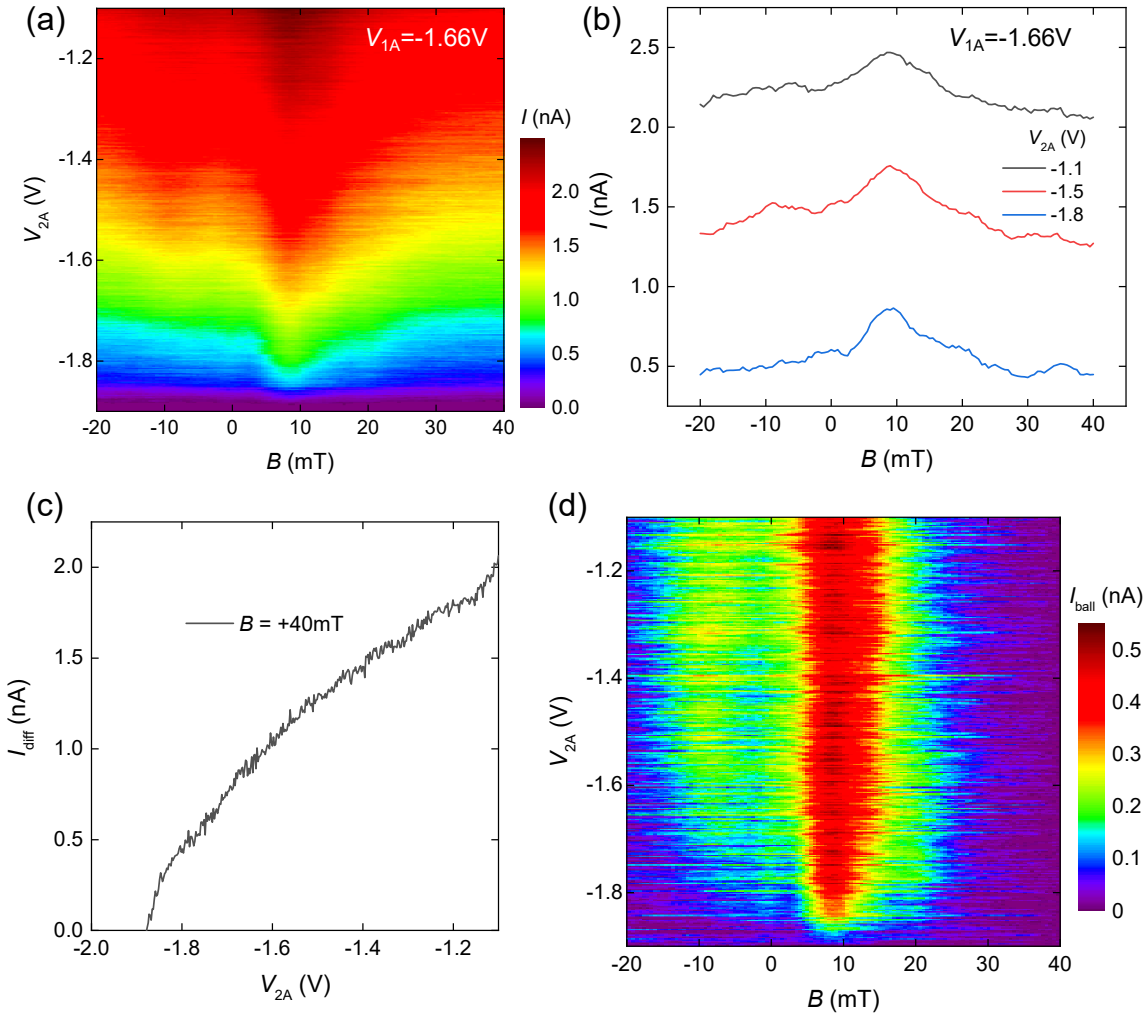

Figure 8.4: (a) Serial current as a function of the emitter QPC voltage and magnetic field, $I(V_{2A},B)$ with the detector QPC fixed at $G(V_{1A} = -1.66) \approx 2G_Q$. Other gates are grounded. (b) Cuts along $I(B)$ for various V_{1A}. (c) Cut along $I(V_{2A},B = 40\,\mathrm{mT})$, identified as the diffusive current contribution I_{diff}, cf. main text. (d) $I_{ball}(V_{2A},B)$ after subtraction of the diffusive current contribution of the total current.

In Fig. 8.4(d), we finally plot the ballistic current after subtraction of the diffusive component, $I_{ball}(B) = I(B) - I_{diff}$.

To quantify the ballistic transmission $T = I_{ball}/I_0$ we need to know the total current I_0 flowing through the emitter into the cavity. To determine I_0, we consider the equivalent circuit diagram of the present setup sketched in Fig. 8.5(a). The emitter (detector) QPC is represented by an Ohmic resistor $R_{2A} = 1/G(V_{2A})$ [$R_{1A} = 1/G(V_{1A})$]. Their serial lead resistances consisting of a 2.2 kΩ RC low-pass filter resistance at room temperature, 50 Ω wire resistance and 120 Ω due to Ohmic contact and 2DES resistance sum up to $R_{\mathrm{lead}} \simeq 2370\,\Omega$. The central region between both QPCs is grounded via four leads, such that we define the side resistance $R_{\mathrm{side}} = R_{\mathrm{lead}}/4$. The total sample resistance R_{tot} is

thus

$$R_{tot} = R_{\text{lead}} + R_{2\text{A}} + \left(\frac{1}{R_{\text{side}}} + \frac{1}{R_{1\text{A}} + R_{\text{lead}}} \right)^{-1} . \tag{8.1}$$

Using Ohm's law, we calculate the total current I_0 flowing into the cavity $I_0 = V/R_{tot}$, where $V = 0.1\,\text{mV}$ is the source-drain voltage applied in the experiments. We plot I_0 as a function of the emitter voltage $V_{2\text{A}}$ in Fig. 8.5(b) (black dashed line, right axis). Finally, we extract the ballistic transmission from $I_{ball}(V_{2\text{A}},B = 9\,\text{mT})$, cf. Fig. 8.4(d), via $T(V_{2\text{A}},B = 9\,\text{mT}) = I_{ball}(V_{2\text{A}},B = 9\,\text{mT})/I_0$, plotted in Fig. 8.5(b). For the emitter voltage $V_{2\text{A}} = -1.1\,\text{V}$, the ballistic serial transmission through both QPCs is only around 2 %. As we decrease the emitter constriction size with decreasing $V_{2\text{A}}$, we decrease both the lateral width of the electron beam and (ii) the size of the cavity. We observe a smooth increase of the transmission as we decrease $V_{2\text{A}}$. Towards the pinch-off of the emitter constriction, the transmission finally saturates around 7.5 %. We did not consider the transmission very close to the pinch-off of the emitter as the division by small numbers gives rise to artificially high transmissions.

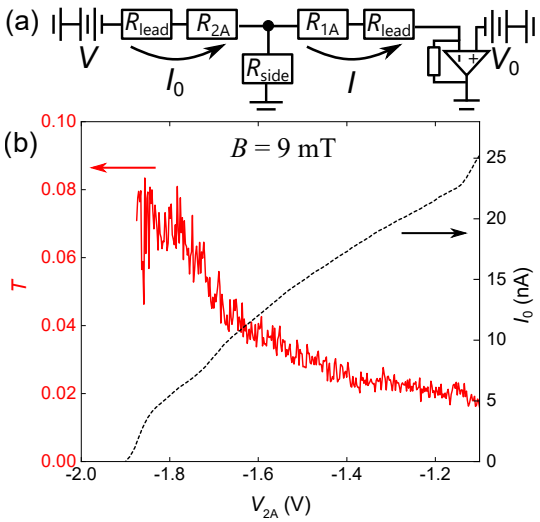

Figure 8.5: (a) Equivalent circuit diagram of the sample. (b) Black dashed line, right axis: calculated I_0 as a function of the emitter QPC gate voltage $V_{2\text{A}}$. Red solid line, left axis: ballistic transmission $T = I_{ball}/I_0$ at $B = 9\,\text{mT}$, cf. main text.

9 Summary and outlook

Within the present thesis, we explored the ballistic transport of electrons between distant QPCs. Below, we summarize the most important results and give an outlook for the project.

In chapter 4, we first showed that the actual potential landscape of a gate-defined QPC resembles a bathtub-like confinement potential for multiple occupied subbands ($N \geq 4$), which undergoes a transition to a parabolic saddle-point potential close to pinch-off of the QPC. The transition is caused by Coulomb screening inside the constriction. In the following, we investigated three different sample geometries containing multiple distant QPCs:

In chapter 6, we considered two nominally identical QPCs spaced by 4.6 µm in a three terminal configuration. In a magnetic deflection experiment, we were able to find generic features of the two QPCs' eigenmodes encoded in the serial transmission through both QPCs. By comparing our experiments to coherent model calculations, we demonstrated how the laterally coherent mode structure of the serial transmission changes, if we vary the number of occupied subbands in the two QPCs. Deviations from the expected transmission profiles for a perfect sample could be mainly attributed to lithographic imperfections and a piezoelectric potential dip created by an intermediate lens-shaped gate between the QPCs, rather than strong (large-angle scattering) disorder potentials. Moreover, by combining magnetic deflection and electrostatic refraction using the lens gate, we found evidence for electrostatic focusing of ballistic electrons. Comparing our experiments to our model calculations, we were also able to calibrate the spatial electrostatic lens potential as a function of the voltage applied to the lens gate, as well as to reconstruct the electron beam pattern between the two QPCs.

In chapter 7 we investigated a ballistic and coherent electronic cavity. The cavity was realized by two narrow QPCs and an elliptical mirror gate, which formed two wider QPCs acting as side drains of the cavity. The cavity was 'open' by means of a continuous density of states and no resolvable Coulomb blockade oscillations. In this regime, the coherent oscillations of the conductance found in the experiments are described by Fabry-Pérot-like cavity modes. We characterized the latter using bias spectroscopy and found good agreement with the prediction for the dephasing of the electron ensemble as well as the decoherence of single electrons due to inelastic electron-electron scattering. Moreover, we found indications for a transition from chaotic to integrable cavity dynamics, as we decreased the size of the cavity in magnetotransport experiments.

In chapter 8 we considered an open ballistic cavity formed by parabolic mirrors with QPCs located close to their focal points. In this experiment, we operated at an elevated electronic temperature of around 6 K, where the QPCs are better described as classical pinholes

without coherent mode structure. We successfully demonstrated how the transmission through the two pinholes can be enhanced by decreasing the size of the cavity.

However, in all three devices, the serial transmission stayed limited below 15 %, which we mainly attributed to small-angle scattering from the disorder potential caused by remote impurities as well as the funnel-like emission process of ballistic electrons from a QPC. This mechanism leads to slightly different emission angles for different occupied subbands, making it impossible to design an electron-optics-based coupling gate (like a lens or mirror) which focuses the entire beam pattern. To further optimize the serial transmission efficiency and to avoid the problem described above, future sample geometries could be tailored for a specific mode, for example the fundamental mode ($N = 1$) using the predictions of coherent model calculations.

Once the ballistic and coherent coupling between two distant QPCs is maximized, the next step consists in replacing the split-gate based QPCs shown in chapters 6 and 7 by quantum dots, for instance based on the gate layout presented in chapter 8. With additional QPCs acting as charge detectors in close vicinity to the two dots, two distant charge or spin qubits with a readout could be formed, which interact by the exchange of ballistic and coherent electrons via the intermediate region of grounded 2DES. Nevertheless, the feasibility of this approach requires further investigation, as the coherent coupling is a complicated function of gate layout, disorder potential and not least electronic excitations.

A Appendix

A.1 Heterostructure: Umansky wafer no. mbe8-309

In Fig. A.1, we show the growth protocol of the wafer material used for the experiments shown in this thesis. The wafer material was provided by V. Umansky from the Weizmann Institute of Science.

Process Name: mbe8-309.mbe
Description:: as 8-304 but with delta 300 sp
Substrate Type : Semi-Insulating
Run Time : 01:51:16.8
Creation Date: 13-08-2007 08:27:50 Date of Last Change 13-08-2007 11:11:22

#	Material		X%	Y%	N(Si)	(A/min)	Thick	Time	Temp	SL	To
001	Ga4AS4					160.0	0750.0	00:04:41.2	570		
002	Ga4AS4:Si				3.0e+17	160.0	0100.0	00:00:37.5	600		
003	Ga4AS4					160.0	0120.0	00:00:45.0	600		
004	AS4	(Ga4)				160.0	0080.0	00:00:30.0	600		
005	AlGa4AS4		26.0			216.2	0270.0	00:01:14.9	650		
006	Ga4AS4					160.0	0060.0	00:00:22.5	600		
007	AS4	(Ga4)				160.0	0070.0	00:00:26.2	640	033	005
008	AS3	(Ga3)				100.0	0060.0	00:00:36.0	600		
009	AlGa3AS3		26.0			135.1	0270.0	00:01:59.8	600		
010	Ga3AS3					100.0	0060.0	00:00:36.0	600		
011	AS3	(Ga3)				100.0	0040.0	00:00:24.0	600	005	009
012	AS3	(Ga3)				100.0	0010.0	00:00:06.0	600		
013	Ga3AS3					100.0	0600.0	00:06:00.0	630		
014	AS3	(Ga3)				100.0	0060.0	00:00:36.0	600		
015	AlGa3AS3		25.0			133.3	0300.0	00:02:15.0	630		
016	Ga3AS3					100.0	0005.6	00:00:03.3	630		
017	AS2	(Ga2)				60.0	0080.0	00:01:20.0	600		
018	AS2:Si	(Ga2)			1.0e+18	60.0	0088.0	00:01:28.0	600		
019	AlGa3AS3		25.0			133.3	0020.0	00:00:09.0	600		
020	Ga2AS2					60.0	0002.8	00:00:02.7	600		
021	AS2	(Ga2)				60.0	0030.0	00:00:30.0	600		
022	AlGa2AS2		25.0			80.0	0030.0	00:00:22.5	580		
023	rAlGa2AS2		34.0			90.9	0170.0	00:01:59.8	600		
024	AlGa2AS2		34.0			90.9	0020.0	00:00:13.2	600		
025	AlGa2AS2:Si		34.0		1.7e+18	90.9	0150.0	00:01:39.0	600		
026	AlGa2AS2		34.0			90.9	0250.0	00:02:45.0	600		
027	Ga2AS2					60.0	0100.0	00:01:39.9	580		

Figure A.1: Growth protocol of the heterostructure used for the experiments presented in this thesis. The carrier density of the wafer material is $n_s = 3.1 \times 10^{11}\,\mathrm{cm}^{-2}$ at a mobility of $\mu = 6.1 \times 10^{6}\,\mathrm{cm}^2/\mathrm{Vs}$ (measured on the bare wafer material without further processing).

A.2 Sample fabrication parameters

Optical lithography

Mesa

- Spin-coating positive resist AZ MiR 701: 3 s at 800 rpm, 30 s at 6000 rpm
- Prebake: 60 s at 90°C
- Exposure time: 17 s in hard contact mode
- Postbake: 60 s at 110°C
- Development: 30 s in AZ 726, stopping in H_2O
- Etching: 100 nm deep in a piranha solution H_2O:H_2SO_4:H_2O_2 (100:1:8)
- Stopping of the etching process in H_2O

Ohmic contacts

- Spin-coating negative resist AR-N 7520-18: 45 s at 4000 rpm
- Prebake: 60 s at 90°C
- Exposure time: 0.6 s in hard contact mode
- Postbake: 90 s at 90°C
- Development: 35 s in AR 300-47:H_2O (1:5), stopping in H_2O
- Plasma etching in Electronic Diener Femto, 20 s in 0.5 mbar O_2
- Evaporation of 60 nm AuGe, 10 nm Ni, 60 nm AuGe
- Lift-off in acetone followed by an isopropanol bath
- Annealing procedure in AO 500-2103035 oven (Dr. Eberl MBE-Komponenten)
  - flush-mode on (in 300 mbar N_2)
  - ramp to 100°C in 5 s
  - hold temperature for 180 s
  - flush-mode off
  - ramp to 360°C in 5 s
  - hold temperature for 120 s
  - ramp to 480°C in 5 s
  - hold temperature for 50 s
  - ramp to 100°C in 5 s

  - flush-mode on
  - hold temperature for 2 s
  - end

Gates

- Spin-coating negative resist AR-N 7520-18: 45 s at 4000 rpm
- Prebake: 60 s at 90°C
- Exposure time: 0.6 s in hard contact mode
- Postbake: 90 s at 90°C
- Development: 35 s in AR 300-47:H_2O (1:5), stopping in H_2O
- Evaporation of 10 nm Ti, 90 nm Au
- Lift-off in acetone followed by an isopropanol bath

Electron beam lithography with Raith 150 two

- Nanostructure
  - Spin-coating of adhesion promoter AR300-80, 45 s at 4000 rpm, 2 min hot plate at 150°C, acetone bath followed by isopropanol bath
  - Spin-coating EBL resist ARP 669.029 (PMMA 600k): 1 s at 800 rpm, 30 s at 5000 rpm
  - Prebake: 180 s at 150°C
  - Electron beam acceleration voltage: 5 kV
  - Electron beam aperture: 7 µm
  - Electron beam exposure dose: 50 µC/cm^2
  - Development: 45 s in MIBK:isopropanol (1:3), stopping in isopropanol
  - Evaporation of 5 nm Ti, 35 nm Au
  - Lift-off in acetone followed by an isopropanol bath
- Insulating PMMA layer
  - Spin-coating of adhesion promoter AR300-80, 45 s at 4000 rpm, 120 s min hot plate at 150°C, acetone bath followed by isopropanol bath
  - Spin-coating EBL resist PMMA 950k A4: 1 s at 800 rpm, 30 s at 5000 rpm
  - Prebake: 180 s at 150°C
  - Electron beam acceleration voltage: 5 kV

  - Electron beam aperture: 60 µm
  - Dose to cross-link PMMA for the insulating later: 2400 µC/cm^2
  - Removing unexposed PMMA in acetone followed by an isopropanol bath
- Top gate
  - Spin-coating of adhesion promoter AR300-80, 45 s at 4000 rpm, 120 s min hot plate at 150°C, acetone bath followed by isopropanol bath
  - Spin-coating EBL resist ARP 679.04 (PMMA 950k): 1 s at 800 rpm, 60 s at 6000 rpm
  - Prebake: 180 s at 150°C
  - Electron beam acceleration voltage: 5 kV
  - Electron beam aperture: 20 µm
  - Dose 2400 µC/cm^2
  - Development: 45 s in MIBK:isopropanol (1:3), stopping in isopropanol
  - Evaporation of 5 nm Ti, 55 nm Au
  - Lift-off in acetone followed by an isopropanol bath

A.3 Textbook calculation of the transfer- and scattering matrix

Knowing the electron energy and the electrostatic potential in every region, we can write the wave numbers in leads 1 and 2 at zero potential, cf. Fig. 3.8:

$$k = \frac{\sqrt{2m^\star E}}{\hbar}$$

and in the region of finite potential

$$k' = \frac{\sqrt{2m^\star \left(E - \Phi_0\right)}}{\hbar}.$$

For $\Phi_0 < E$ both k and k' are real, while for $\Phi_0 > E$ the wave number in the scattering region k' becomes imaginary and the wavefunction amplitude in the barrier is decaying exponentially with x.

We write the wavefunctions in the different regions of constant potential:

$$\psi(x) = \begin{cases} a_1 e^{ikx} + b_1 e^{-ikx}; & x < -x_0 \\ c e^{ik'x} + d e^{-ik'x}; & -x_0 \leq x \leq x_0 \\ a_2 e^{-ikx} + b_2 e^{ikx}; & x > x_0. \end{cases}$$

Using continuity at $\psi(x = -x_0)$ we obtain

$$a_1 e^{-ikx_0} + b_1 e^{ikx_0} = ce^{-ik'x_0} + de^{ik'x_0}.$$

Similarly, continuity at $\psi'(x = x_0)$ implies

$$cike^{ik'x_0} - dik'e^{-ik'x_0} = -a_2 ike^{-ikx_0} + b_2 ike^{ikx_0}.$$

A.4 Parabolic saddle-point potential model

The observation of quantized conductance in quantum point contacts directly raised the question about the electrostatic potential resulting in a series of flat plateaus with smooth transitions as a function of the gate voltage. For electrostatically defined QPCs, the course of the field lines gives rise to a smooth potential landscape forming the QPC. Consequently, the parabolic saddle-point potential is frequently used to describe the spatial electrostatic QPC potential in the 2DES. The corresponding analytic form around the constriction center is:

$$\Phi(x,y) = \Phi_0 + \Phi_x(x) + \Phi_y(y) = \Phi_0 - \frac{1}{2}m^\star\omega_x^2 x^2 + \frac{1}{2}m^\star\omega_y^2 y^2$$

where Φ_0 is the potential energy at the saddle point with $x = y = 0$, ω_x and ω_y are the curvatures of the parabolic potential barrier Φ_x in current direction and the confinement potential Φ_y in transverse direction, respectively. Fig. A.2 illustrates $\Phi(x,y)$ in a 3D-

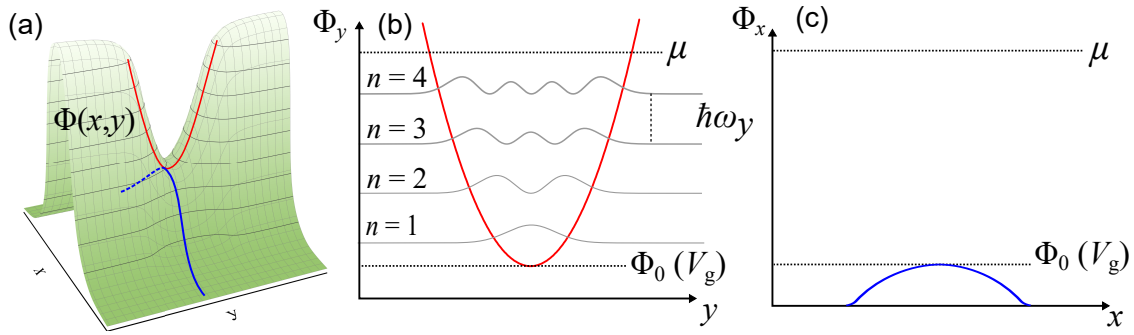

Figure A.2: (a) Illustration of parabolic saddle-point potential within the QPC-constriction around the saddle point $\Phi(x = y = 0)$. (b) Cut along the lateral parabolic confinement potential $\Phi(x = 0,y)$, corresponding to the red parabola in (a). Equidistant energy levels indexed n spaced by $\hbar\omega_y$ are formed with respect to $\Phi_0(V_g)$ and the chemical potential μ. The corresponding eigenfunctions are the Hermite functions (gray lines). (c) Cut along the longitudinal parabolic barrier $\Phi(y = 0,x)$ with the vertex Φ_0, corresponding to the blue parabola shown in (a).

representation, additionally including smooth transitions to the free 2DES with $\Phi(x,y) = 0$. The transverse parabolic confinement potential Φ_y around the saddle-point [cf. panel (b)] results in equidistant energy-levels $E_n = \hbar\omega_y(n - 1/2) + \Phi_0$ with the corresponding

eigenfunctions given by the well-known Hermite functions (gray lines). The longitudinal potential Φ_x [cf. panel (c)] represents a parabolic barrier.

In the most simple model, the potential at the saddle point depends on the gate voltage, $\Phi_0(V_\mathrm{g})$, while the curvatures ω_x and ω_y are constants. A variation in gate voltage then causes the whole saddle to vertically shift with respect to the chemical potential at the Fermi edge, while its shape remains unchanged. Under these assumptions, Büttiker calculated the quantized conductance through the parabolic saddle-point potential [84]:

$$G(V_\mathrm{g}) = G_\mathrm{Q} \sum_{n=1}^{N} \frac{1}{1 + e^{-\pi e_n(,V_\mathrm{g})}} \tag{A.1}$$

with

$$e_n(V_\mathrm{g}) = \frac{2\left(\mu_\mathrm{F} - \hbar\omega_y(n - 1/2) - \Phi_0(V_\mathrm{g})\right)}{\hbar\omega_x}. \tag{A.2}$$

where μ_F is the fixed chemical potential at the Fermi edge. The coupling constant $\delta\Phi_0/(e\delta V_\mathrm{g})$ describing the capacitance between the QPC gates and 2DES can be determined by finite bias spectroscopy measurements, cf. section 4.3. Here, we assume an

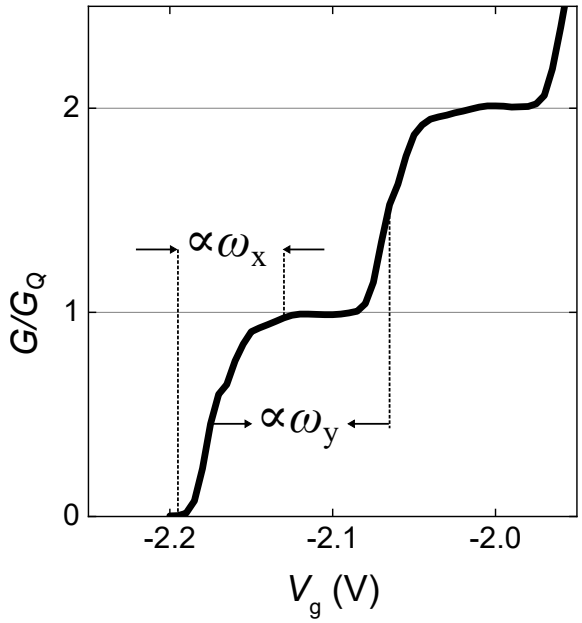

Figure A.3: Applying the parabolic saddle-point potential for a constant capacitance between 2DES and gate, the separation between conductance plateaus is proportional to $\hbar\omega_y$ while the width of transitions scales with $\hbar\omega_x$.

arbitrary energy scale of the offset potential that depends *linearly* on the gate voltage ($\Phi_0 \propto V_\mathrm{g}$), corresponding to a constant capacitance between the QPC gate and the 2DES. In this case, the functional form of equation A.1 gives rise to equidistant conductance steps in gate voltage. The spacing between steps is then proportional to the energy spacing of subsequent subbands ($\hbar\omega_y$), as indicated in Fig. A.3. The parabolic barrier in current

direction sets the stepwidth of transitions between plateaus proportional to $\hbar\omega_x$. Well pronounced conductance plateaus thus occur for $\omega_y \geq \omega_x$. Note that smooth transitions between subsequent conductance plateaus are a fingerprint for a smooth parabolic confinement potential with adiabatic (reflectionless) coupling to the free 2DES: non-adiabatic couplings between a QPC and its leads would result in enhanced back-scattering and deviations from the theoretical plateau values NG_Q. An elongated barrier would give rise to (Fabry-Pérot type) resonances at energies above the barrier and lead to conductance oscillations with $G_N < NG_Q$ along the plateaus [77]. Reflectionless coupling of a QPC to its leads can be achieved with a parabolic (or sharper) barrier in the direction of current flow as long as the potential gradients are also small within the lengths scale of the Fermi wavelength. For adiabatic coupling the lateral profile of the current emitted from a QPC resembles the eigenmodes of the transverse potential. In the case of parabolic lateral confinement these are the eigenstates of the 1D-harmonic oscillator, i.e. Hermite functions [cf. Fig. A.2(b)].

A.4.1 Finite anharmonicity

Small corrections to the parabolic saddle-point potential scenario with constant capacitance occur by accounting for finite anharmonicity of the lateral potential component. In Fig. A.4(a), we plot individually measured pinch-off curves for two QPCs (black dots).

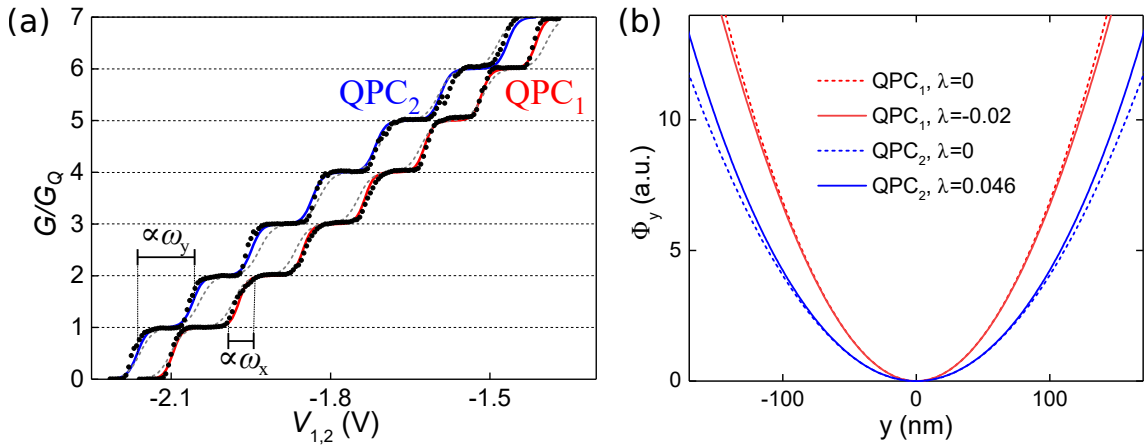

Figure A.4: (a)Pinch-off curves of both QPCs for $N \leq 7$ (black data points). Solid lines: model curves according to equation A.6 with fit parameters from table A.1 (red: QPC_1, blue: QPC_2). Dashed gray lines: model curves assuming parabolic potentials with $\lambda = 0$. ω_y is proportional to the stepwidth and ω_x to the width of the curved transition regions between plateaus. (b) Potential wells $\Phi_y(x = 0,y)$ resulting from fitting the harmonic ($\lambda = 0$) conductance formula to QPC_1 (red dashed line) and QPC_2 (blue dashed line). Solid lines show the corresponding wells accounting for finite anharmonicity with ($\lambda < 0$) for QPC_1 and ($\lambda > 0$) for QPC_2.

Taking a close look to the data we find that the spacings between plateaus are not perfectly equidistant: while QPC_1 shows a trend to decreasing spacings for higher conductance

plateaus, QPC_2 features slightly increasing spacings. Attributing these deviations to a finite anharmonic (non-parabolic) component, we expand the symmetric lateral confinement potential in lowest relevant order

$$\Phi_y = \frac{1}{2} m^\star \omega_y^2 y^2 \left(1 + \lambda \left(\frac{y}{y_0}\right)^2\right) ,$$

where $|\lambda| \ll 1$ determines the degree of anharmonicity and $y_0 = 100\,\mathrm{nm}$ sets the length scale. The solution of the Schrödinger equation for this anharmonic oscillator can be reduced to the solution of the depressed qubic equation [114]

$$\left(\frac{2}{\hbar\omega_y}\nu_n\varepsilon_n\right)^3 - \frac{2}{\hbar\omega_y}\nu_n\varepsilon_n = \lambda\kappa_n \,, \tag{A.3}$$

where ε_n is the nth eigen energy with $n = 1,2,3,\ldots$ and $\nu_n = (2n-1)^{-1}$. The parameter κ_n can be approximated with [114]

$$\kappa_n = \frac{1.1924 + 33.2383(n-1) + 56.2169(n-1)^2}{1 + 43.6106(n-1)}$$

with high accuracy. For $\lambda\kappa_n \leq \dfrac{2}{3\sqrt{3}}$ the three roots of Eq. (A.3) are

$$\varepsilon_n(\lambda,\omega_y) = \frac{\hbar\omega_y}{\sqrt{3}\nu_n} \cos\left[\frac{1}{3}\arccos\left(\frac{3\sqrt{3}}{2}\lambda\kappa_n\right) - \frac{2\pi s}{3}\right] , \tag{A.4}$$

where the parameter s takes the values 0, 1 or 2. Analysis of the harmonic limit with $\lambda = 0$ establishes that $s = 0$ provides the correct solution of the eigenvalue problem. For $\lambda\kappa_n > \dfrac{2}{3\sqrt{3}}$ the only real valued root is

$$\varepsilon_n(\lambda,\omega_y) = \frac{\hbar\omega_y}{\sqrt{3}\nu_n} \cosh\left[\frac{1}{3}\mathrm{arcosh}\left(\frac{3\sqrt{3}\lambda\kappa_n}{2}\right)\right] . \tag{A.5}$$

Note that κ_n grows quickly with n. As a consequence, for $n = 1$ Eq. (A.4) is valid for $|\lambda| \lesssim 0.32$ and Eq. (A.5) for $|\lambda| \gtrsim 0.32$, while for $n = 7$ Eq. (A.5) applies already for $|\lambda| \gtrsim 0.045$.

Using Büttikers formula for the quantized transmission through a parabolic saddle point potential [84], while replacing the eigenenergies of the harmonic oscillator with our results for the slightly anharmonic oscillator, we find

$$G(\lambda,V_i) = G_\mathrm{Q} \sum_{n=1}^{N} \frac{1}{1 + e^{-\pi e_n(\lambda,V_i)}} \tag{A.6}$$

with

$$e_n(\lambda,V_i) = \frac{2\left(\mu_F - \Phi_0(V_i) - \varepsilon_n(\lambda,\omega_y)\right)}{\hbar\omega_x} ,$$

	ω_y/ω_x	λ
QPC_1	2.02	-0.017
QPC_2	1.65	0.046

Table A.1: Parameters describing the QPC potentials obtained by fitting equation A.6 to the measured data in figure A.4a.

$\epsilon_n(\lambda,\omega_y)$ is given by Eq. (A.4) with $s = 0$ or Eq. (A.5), depending on λ as discussed above. The solid lines in Fig. A.4(a) are model curves representing Eq. (A.6) with the curvatures ω_x and ω_y as well as the anharmonicity parameter λ as fit-parameters. In table A.1, we list the ratios ω_y/ω_x as well as λ for both QPCs. Energies $\hbar\omega_{x,y}$ can be determined with a known energy reference by performing finite bias measurements. Our main result is $|\lambda| \ll 1$ corresponding to almost parabolic saddle point potentials. As indicated in Fig. A.4(a), ω_x determines the width of the conductance steps, while the plateau width is proportional to ω_y and would be independent of N for a parabolic confinement. Non harmonic confinement with $\lambda \neq 0$ causes deviations from this behavior. The anharmonicity of our lateral confinement potentials can be directly seen in Fig. A.4(b) which displays $\Phi_y(y)$ for the harmonic case ($\lambda = 0$) for QPC_1 and QPC_2 (red/blue dashed line) as well as the corresponding wells with finite anharmonicity (red/blue solid lines).

Summarizing the above, the parabolic saddle point potential with constant curvature describes the pinch-off curves of hypothetical QPCs without screening qualitatively well. The agreement can even be improved by accounting for a weak anharmonic component of the lateral confinement potential. Nevertheless, this model is in contradiction to the measured subband spacings of the same QPC: in chapter 4 we demonstrate that Coulomb screening causes a transition of the QPC potential from a parabolic potential of variable curvature close to pinch-off towards a hard-wall potential as the QPC is opened up by increasing the gate voltage.

A.4.2 Code to fit (an)harmonic QPCs

The following shows a Python script which can be used to fit (an)harmonic QPCs from measured conductance pinch-off curves within the model discussed in the previous section.

```
1  import scipy
2  import numpy
3  import matplotlib
4  import numpy as np
5  import os
6  import matplotlib.cm as cm
7  import matplotlib.mlab as mlab
8  import matplotlib.pyplot as plt
9  get_ipython().magic(u'matplotlib inline')
10 from scipy import interpolate
11 #from scipy.optimize import *
12 #from __future__ import division
13 from scipy.optimize import curve_fit
14 #!/usr/bin/env python
```

```
#<examples/doc_model1.py>
from numpy import sqrt, pi, exp, linspace, loadtxt
from lmfit import  Model
import matplotlib.pyplot as plt
import csv
from numpy import exp,arange
from pylab import meshgrid,cm,imshow,contour,clabel,colorbar,axis,title,show
import pylab

#Constants
hbar=1.0545718e-34

# Equation:
#ax^3 + bx^2 + cx + d = 0
#x^3/(2n+1) - x/(2n+1) - la(4/3+8n/9) = 0   (ax^3+cx+d=0)
#with  a=(1/(2n+1))**3,  b=0,  c=-1/(2n+1)
#and  d=-la*((1.1924+33.2383*n+56.2169*(n**2))/(1+43.6106*n))
#D(n,la): Diskriminante

def a(n):
    return (1/(2*n+1))**3

def c(n):
    return (-1/(2*n+1))

def d(n,la):
    return -la*((1.1924+33.2383*n+56.2169*(n**2))/(1+43.6106*n))

def p(n):
    return c(n)/a(n)

def q(n,la):
    return d(n,la)/a(n)

def D(n,la):
    return -4*a(n)*(c(n))**3-27*((a(n))**2)*((d(n,la))**2)

def k0(n,la):
    return 2*np.sqrt(-p(n)/3)*np.cos((1/3)*np.arccos(((3*q(n,la))\
                        /(2*p(n)))*np.sqrt(-3/p(n)))-2*np.pi*0/3)

def k1(n,la):
    return 2*np.sqrt(-p(n)/3)*np.cos((1/3)*np.arccos(((3*q(n,la))\
                        /(2*p(n)))*np.sqrt(-3/p(n)))-2*np.pi*1/3)

def k2(n,la):
    2*np.sqrt(-p(n)/3)*np.cos((1/3)*np.arccos(((3*q(n,la))\
                        /(2*p(n)))*np.sqrt(-3/p(n)))-2*np.pi*2/3)

def r(n,la):
    -2*(np.abs(q(n,la))/q(n,la))*np.sqrt(-p(n)/3)*np.cosh((1/3)\
        *np.arccosh(-np.sqrt(-3/( p(n)))*3*np.abs(q(n,la))/(2*p(n))))

def e(n,la):
    if (D(n,la)>0):
        return 2*np.sqrt(-p(n)/3)*np.cos((1/3)\
        *np.arccos(((3*q(n,la))/(2*p(n)))*np.sqrt(-3/p(n)))-2*np.pi*0/3)
```

```
72      else:
73          return -2*(np.abs(q(n,la))/q(n,la))\
74      *np.sqrt(-p(n)/3)*np.cosh((1/3)*np.arccosh(-np.sqrt(-3/( p(n)))\
75      *3*np.abs(q(n,la))/(2*p(n))))
76
77 # Load data-set
78
79 data = loadtxt('C:/Users/freudenfeld/Desktop/Programme/python/data/qpc1y.dat')
80 #x = data[:, 0]
81 x = np.linspace(0, 21, num=161)
82 y = data[:, 1]
83
84
85 from lmfit import minimize, Minimizer, Parameters, Parameter, report_fit
86
87 def fcn2min(params, x, y):
88      T=np.linspace(0, 0, num=161)
89      r = params['r']     # ratio of omega_y/omega_x
90      la = params['la']  # anharmonicity lambda
91      for n in range(0,7):
92          T = T+1/(1+np.exp(-2*np.pi*(x-0.5*r*(e(n,la)))))
93      return (T-y)
94
95 params = Parameters()
96 params.add('r', value=3, min=2, max=5)
97 params.add('la', value=0.01, min=0, max=0.05)
98
99 minner = Minimizer(fcn2min, params, fcn_args=(x, y))
100 kws  = {'options': {'maxiter':1000}}
101 result = minner.minimize()
102 result.params
103
104 final = y + result.residual
105 report_fit(result)
106 plt.plot(x, y, 'o')
107 plt.plot(x, final, 'r')
108 params2=result.params
109 v = params2.valuesdict()
```

A.5 Classical trajectories in a (half) elliptical cavity

In Fig. A.5, we show calculated classical trajectories of electrons in a cavity adapted to the gate layout of the sample discussed in chapter 7.

To compute the current for classical electrons we sample the lateral distribution function of free electrons at the center of the emitter QPC (in current direction). We calculate the trajectory of each sampling point as a function of the perpendicular magnetic field B numerically by assuming a constant velocity (v_F) as well as specular reflections from the gated structures (solid black lines). [1]

[1] The classical calculation was realized and provided by Max Geier from the Dahlem Center for Complex Quantum Systems at the FU Berlin.

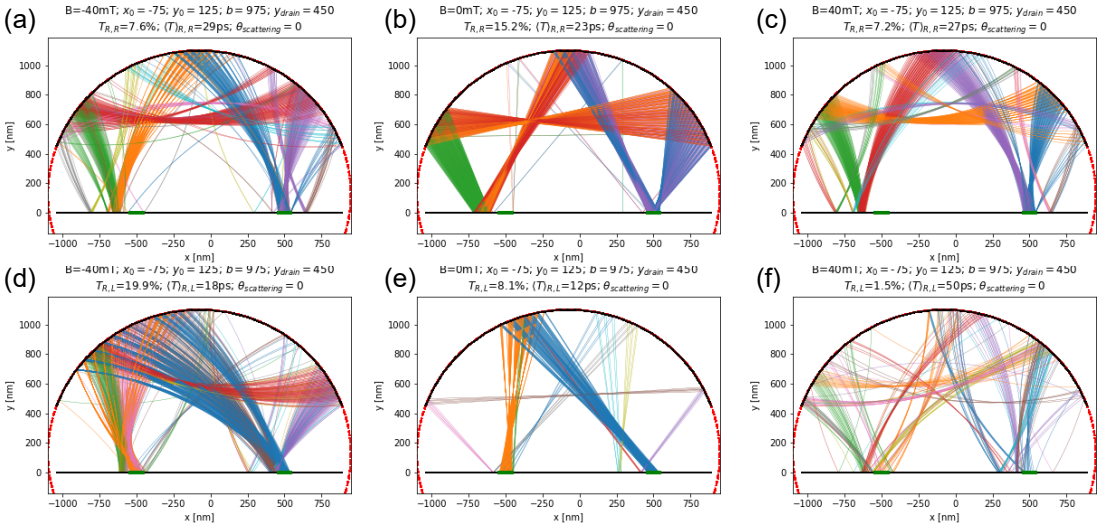

Figure A.5: Calculated classical trajectories for a ballistic resonator adapted to the actual sample geometry. Upper panels: trajectories contributing to $t_{11}(B)$ at $B = -40\,\mathrm{mT}$ (a), $B = 0$ (b) and $B = +40\,\mathrm{mT}$ (c). Lower panels: trajectories contributing to $t_{21}(B)$ at $B = -40\,\mathrm{mT}$ (d), $B = 0$ (e) and $B = +40\,\mathrm{mT}$ (f).

The upper (lower) panels show trajectories that contribute to the reflection into QPC_1, t_{11} (the transmission into QPC_2, t_{21}). Panels (a,d); (b,e) and (c,f) correspond to constant magnetic fields $B = -40\,\mathrm{mT}$; $B = 0$ and $B = +40\,\mathrm{mT}$, respectively. For clarity, we change the color of the branches after each reflection off a gate.

Note that these trajectories show exemplary trajectories for the above gate layout. We neglect the curvature of the QPC tips, which can give rise to a different, chaotic scattering behavior of the incident branches. However, as we argue in chapter 7, we intend to treat the actual two-dimensional trajectories in the cavity as 1D trajectories with a total length l, by 'unfolding' them after every reflection from a gate. We determine l for $B = 0$ by source-drain spectroscopy measurements as shown in section 7.3.4.

B Publications

In the following, we acknowledge the contribution of each author for the published and planned publications used in this thesis.

- Chapter 4: Electrostatic potential shape of gate-defined quantum point contacts, M. Geier *et al., Phys. Rev. B 101.* 165429 (2020)

  J. Freudenfeld fabricated the sample presented in chapter 4 and carried out the experiment, analyzed the data and prepared the data visualization for publication. The second sample presented in this publication (but not shown in chapter 4) was fabricated and measured by J. T. Silva. M. Geier compared the measured QPC subband spacings to the lateral hard-wall and the lateral parabolic confinement potential model. V. Umansky, D. Reuter and A. D. Wieck provided the wafer material. J. Freudenfeld, M. Geier and S. Ludwig wrote the manuscript. P. W. Brouwer and S. Ludwig supervised the project.

- Chapter 6: Coherent electron optics with ballistically coupled quantum point contacts, J. Freudenfeld *et al., Phys. Rev. Lett. 125.* 107701 (2020)

  J. Freudenfeld fabricated the sample and carried out the experiment, analyzed the data and prepared the data visualization for publication. M. Geier developed the theoretical models used for the numerical quantum mechanical as well as classical calculations. V. Umansky provided the wafer material. J. Freudenfeld, M. Geier, P. W. Brouwer and S. Ludwig wrote the manuscript. P. W. Brouwer and S. Ludwig supervised the project.

- Chapter 7: Electron scattering in a ballistic and coherent cavity *(In preparation)*

  J. Freudenfeld fabricated the sample, carried out the experiment and prepared the data visualization for publication. J. Freudenfeld and S. Ludwig analyzed the data. M. Geier developed the theoretical models used for comparison to the measurements. V. Umansky provided the wafer material. J. Freudenfeld, M. Geier and S. Ludwig wrote the manuscript. P. W. Brouwer and S. Ludwig supervised the project.

Bibliography

[1] R. Landauer, "Can a length of perfect conductor have a resistance?" Physics Letters A, vol. 85, no. 2, pp. 91 – 93, 1981. [Online]. Available: http://www.sciencedirect.com/science/article/pii/0375960181902309

[2] B. J. van Wees, H. van Houten, C. W. J. Beenakker, J. G. Williamson, L. P. Kouwenhoven, D. van der Marel, and C. T. Foxon, "Quantized conductance of point contacts in a two-dimensional electron gas," Phys. Rev. Lett., vol. 60, pp. 848–850, Feb 1988. [Online]. Available: https://link.aps.org/doi/10.1103/PhysRevLett.60.848

[3] D. A. Wharam, T. J. Thornton, R. Newbury, M. Pepper, H. Ahmed, J. E. F. Frost, D. G. Hasko, D. C. Peacock, D. A. Ritchie, and G. A. C. Jones, "One-dimensional transport and the quantisation of the ballistic resistance," Journal of Physics C: Solid State Physics, vol. 21, no. 8, p. L209, 1988. [Online]. Available: http://stacks.iop.org/0022-3719/21/i=8/a=002

[4] M. Hashisaka, Y. Yamauchi, S. Nakamura, S. Kasai, K. Kobayashi, and T. Ono, "Measurement for quantum shot noise in a quantum point contact at low temperatures," Journal of Physics: Conference Series, vol. 109, no. 1, p. 012013, 2008. [Online]. Available: http://stacks.iop.org/1742-6596/109/i=1/a=012013

[5] M. A. Topinka, B. J. LeRoy, S. E. J. Shaw, E. J. Heller, R. M. Westervelt, K. D. Maranowski, and A. C. Gossard, "Imaging coherent electron flow from a quantum point contact," Science, vol. 289, no. 5488, pp. 2323–2326, 2000. [Online]. Available: http://science.sciencemag.org/content/289/5488/2323

[6] B. Brun, F. Martins, S. Faniel, B. Hackens, G. Bachelier, A. Cavanna, C. Ulysse, A. Ouerghi, U. Gennser, D. Mailly, S. Huant, V. Bayot, M. Sanquer, and H. Sellier, "Wigner and kondo physics in quantum point contacts revealed by scanning gate microscopy," vol. 5, p. 4290, 06 2014.

[7] H. van Houten, L. W. Molenkamp, C. W. J. Beenakker, and C. T. Foxon, "Thermo-electric properties of quantum point contacts," Semiconductor Science and Technology, vol. 7, no. 3B, p. B215, 1992. [Online]. Available: http://stacks.iop.org/0268-1242/7/i=3B/a=052

[8] C. Rossler, K.-D. Hof, S. Manus, S. Ludwig, J. P. Kotthaus, J. Simon, A. W. Holleitner, D. Schuh, and W. Wegscheider, "Optically induced transport properties of freely suspended semiconductor submicron channels," Applied Physics Letters, vol. 93, no. 7, p. 071107, 2008. [Online]. Available: http://link.aip.org/link/?APL/93/071107/1

[9] J. G. Williamson, H. van Houten, C. W. J. Beenakker, M. E. I. Broekaart, L. I. A. Spendeler, B. J. van Wees, and C. T. Foxon, "Hot-electron spectrometry with quantum point contacts," Phys. Rev. B, vol. 41, pp. 1207–1210, Jan 1990. [Online]. Available: http://link.aps.org/doi/10.1103/PhysRevB.41.1207

[10] T.-M. Chen, M. Pepper, I. Farrer, D. A. Ritchie, and G. A. C. Jones, "Magnetic focusing with quantum point contacts in the non-equilibrium transport regime," Applied Physics Letters, vol. 103, no. 9, p. 093503, 2013. [Online]. Available: https://doi.org/10.1063/1.4819489

[11] C. Rössler, M. Herz, M. Bichler, and S. Ludwig, "Freely suspended quantum point contacts," Solid State Communications, vol. 150, no. 17–18, pp. 861 – 864, 2010. [Online]. Available: http://www.sciencedirect.com/science/article/pii/S0038109810000906

[12] A. M. Lunde, A. De Martino, A. Schulz, R. Egger, and K. Flensberg, "Electron-electron interaction effects in quantum point contacts," New Journal of Physics, vol. 11, no. 2, p. 023031, 2009. [Online]. Available: http://stacks.iop.org/1367-2630/11/i=2/a=023031

[13] A. P. Micolich, "What lurks below the last plateau: experimental studies of the 0.7 × 2 e 2 / h conductance anomaly in one-dimensional systems," Journal of Physics: Condensed Matter, vol. 23, no. 44, p. 443201, 2011. [Online]. Available: http://stacks.iop.org/0953-8984/23/i=44/a=443201

[14] F. Bauer, J. Heyder, E. Schubert, D. Borowsky, D. Taubert, B. Bruognolo, D. Schuh, W. Wegscheider, J. von Delft, and S. Ludwig, "Microscopic origin of the '0.7-anomaly' in quantum point contacts," Nature, vol. 501, p. 73–78, 2013. [Online]. Available: www.nature.com/nature/journal/v501/n7465/full/nature12421.html

[15] M. Field, C. G. Smith, M. Pepper, D. A. Ritchie, J. E. F. Frost, G. A. C. Jones, and D. G. Hasko, "Measurements of coulomb blockade with a noninvasive voltage probe," Phys. Rev. Lett., vol. 70, pp. 1311–1314, Mar 1993. [Online]. Available: http://link.aps.org/doi/10.1103/PhysRevLett.70.1311

[16] Ji Yang, Chung Yunchul, Sprinzak D., Heiblum M., Mahalu D., and Shtrikman Hadas, "An electronic mach–zehnder interferometer," Nature, vol. 422, p. 415, Mar. 2003.

[17] M. G. Prokudina, S. Ludwig, V. Pellegrini, L. Sorba, G. Biasiol, and V. S. Khrapai, "Tunable nonequilibrium luttinger liquid based on counterpropagating edge channels," Phys. Rev. Lett., vol. 112, p. 216402, May 2014. [Online]. Available: http://link.aps.org/doi/10.1103/PhysRevLett.112.216402

[18] H. van Houten, C. W. J. Beenakker, J. G. Williamson, M. E. I. Broekaart, P. H. M. van Loosdrecht, B. J. van Wees, J. E. Mooij, C. T. Foxon, and J. J. Harris, "Coherent electron focusing with quantum point contacts in a two-dimensional electron gas," Phys. Rev. B, vol. 39, pp. 8556–8575, Apr 1989. [Online]. Available: http://link.aps.org/doi/10.1103/PhysRevB.39.8556

[19] S. Chesi, G. F. Giuliani, L. P. Rokhinson, L. N. Pfeiffer, and K. W. West, "Anomalous spin-resolved point-contact transmission of holes due to cubic rashba spin-orbit coupling," Phys. Rev. Lett., vol. 106, p. 236601, Jun 2011. [Online]. Available: https://link.aps.org/doi/10.1103/PhysRevLett.106.236601

[20] Lo Shun-Tsung, Chen Chin-Hung, Fan Ju-Chun, Smith L. W., Creeth G. L., Chang Che-Wei, Pepper M., Griffiths J. P., Farrer I., Beere H. E., Jones G. A. C., Ritchie D. A., and Chen Tse-Ming, "Controlled spatial separation of spins and coherent dynamics in spin-orbit-coupled nanostructures," Nature Communications, vol. 8, p. 15997, Jul. 2017. [Online]. Available: https://www.nature.com/articles/ncomms15997#supplementary-information

[21] J. J. Koonen, H. Buhmann, and L. W. Molenkamp, "Probing the potential landscape inside a two-dimensional electron gas," Phys. Rev. Lett., vol. 84, pp. 2473–2476, Mar 2000. [Online]. Available: http://link.aps.org/doi/10.1103/PhysRevLett.84.2473

[22] P. Khatua, B. Bansal, and D. Shahar, "Single-slit electron diffraction with aharonov-bohm phase: Feynman's thought experiment with quantum point contacts," Phys. Rev. Lett., vol. 112, p. 010403, Jan 2014. [Online]. Available: http://link.aps.org/doi/10.1103/PhysRevLett.112.010403

[23] P. H. Beton, B. R. Snell, P. C. Main, A. Neves, J. R. Owers-Bradley, L. Eaves, M. Henini, O. H. Hughes, S. P. Beaumont, and C. D. W. Wilkinson, "The resistance of two quantum point contacts in series," Journal of Physics: Condensed Matter, vol. 1, no. 40, p. 7505, 1989. [Online]. Available: http://stacks.iop.org/0953-8984/1/i=40/a=026

[24] D. A. Wharam, M. Pepper, H. Ahmed, J. E. F. Frost, D. G. Hasko, D. C. Peacock, D. A. Ritchie, and G. A. C. Jones, "Addition of the one-dimensional quantised ballistic resistance," Journal of Physics C: Solid State Physics, vol. 21, no. 24, p. L887, 1988. [Online]. Available: http://stacks.iop.org/0022-3719/21/i=24/a=002

[25] L. P. Kouwenhoven, B. J. van Wees, W. Kool, C. J. P. M. Harmans, A. A. M. Staring, and C. T. Foxon, "Transition from ohmic to adiabatic transport in quantum point contacts in series," Phys. Rev. B, vol. 40, pp. 8083–8086, Oct 1989. [Online]. Available: https://link.aps.org/doi/10.1103/PhysRevB.40.8083

[26] P. Coleridge, R. Taylor, A. Sachrajda, and J. Adams, "Anti-collimation of ballistic electrons by a potential barrier," Surface Science, vol. 305, no. 1, p. 448–452, 1994. [Online]. Available: http://www.sciencedirect.com/science/article/pii/0039602894909342

[27] K. Liu, H. Lin, V. Umansky, and S. Hsu, "Carrier density dependent electric transport of serially connected two quantum point contacts," Physica E: Low-dimensional Systems and Nanostructures, vol. 42, no. 4, p. 1122–1125, 2010, 18th International Conference on Electron Properties of Two-Dimensional Systems. [Online]. Available: http://www.sciencedirect.com/science/article/pii/S138694770900530X

[28] H. van Houten and B. C.W.J., "Principles of solid state electron optics," Confined electrons and plasmons, 1995. [Online]. Available: https://www.lorentz.leidenuniv.nl/beenakkr/mesoscopics/fulltext/172_108_Burstein.pdf

[29] H. van Houten, C. W. J. Beenakker, J. G. Williamson, M. E. I. Broekaart, P. H. M. van Loosdrecht, B. J. van Wees, J. E. Mooij, C. T. Foxon, and J. J. Harris, "Coherent electron focusing with quantum point contacts in a two-dimensional electron gas," Phys. Rev. B, vol. 39, pp. 8556–8575, Apr 1989. [Online]. Available: https://link.aps.org/doi/10.1103/PhysRevB.39.8556

[30] J. Spector, H. L. Stormer, K. W. Baldwin, L. N. Pfeiffer, and K. W. West, "Electron focusing in two-dimensional systems by means of an electrostatic lens," Applied Physics Letters, vol. 56, no. 13, pp. 1290–1292, 1990. [Online]. Available: http://scitation.aip.org/content/aip/journal/apl/56/13/10.1063/1.102538

[31] U. Sivan, M. Heiblum, C. P. Umbach, and H. Shtrikman, "Electrostatic electron lens in the ballistic regime," Phys. Rev. B, vol. 41, pp. 7937–7940, Apr 1990. [Online]. Available: http://link.aps.org/doi/10.1103/PhysRevB.41.7937

[32] L. W. Molenkamp, A. A. M. Staring, C. W. J. Beenakker, R. Eppenga, C. E. Timmering, J. G. Williamson, C. J. P. M. Harmans, and C. T. Foxon, "Electron-beam collimation with a quantum point contact," Phys. Rev. B, vol. 41, pp. 1274–1277, Jan 1990. [Online]. Available: https://link.aps.org/doi/10.1103/PhysRevB.41.1274

[33] V. Umansky and M. Heiblum, "Chapter 6 - mbe growth of high-mobility 2deg," in Molecular Beam Epitaxy. Oxford: Elsevier, 2013, pp. 121 – 137. [Online]. Available: http://www.sciencedirect.com/science/article/pii/B9780123878397000063

[34] R. Dingle, H. L. Störmer, A. C. Gossard, and W. Wiegmann, "Electron mobilities in modulation-doped semiconductor heterojunction superlattices," Applied Physics Letters, vol. 33, no. 7, pp. 665–667, 1978. [Online]. Available: https://doi.org/10.1063/1.90457

[35] S. Adachi, "Gaas, alas, and alxga1-xas: Material parameters for use in research and device applications," Journal of Applied Physics, vol. 58, no. 3, pp. R1–R29, 1985. [Online]. Available: https://doi.org/10.1063/1.336070

[36] K. v. Klitzing, G. Dorda, and M. Pepper, "New method for high-accuracy determination of the fine-structure constant based on quantized hall resistance," Phys. Rev. Lett., vol. 45, pp. 494–497, Aug 1980. [Online]. Available: https://link.aps.org/doi/10.1103/PhysRevLett.45.494

[37] L. Shubnikov and W. J. De Haas, "Na new phenomenon in the change of resistance in a magnetic field of single crystals of bismuth," Nature, vol. 126, 1930. [Online]. Available: https://doi.org/10.1038/126500a0

[38] M. Reed, W. Kirk, and P. Kobiela, "Investigation of parallel conduction in gaas/alxga1-xas modulation-doped structures in the quantum limit," IEEE Journal of Quantum Electronics, vol. 22, no. 9, pp. 1753–1759, 1986.

[39] M. Grayson and F. Fischer, "Measuring carrier density in parallel conduction layers of quantum hall systems," Journal of Applied Physics, vol. 98, no. 1, p. 013709, 2005. [Online]. Available: https://doi.org/10.1063/1.1948529

[40] L. J. van der Pauw, "A method of measuring specific resistivity and hall effect of discs of arbitrary shape," Philips Research Reports, vol. 13, no. 1, 1958. [Online]. Available: http://electron.mit.edu/~gsteele/vanderpauw/vanderpauw.pdf

[41] A. N. Broers, "Resolution limits for electron-beam lithography," IBM Journal of Research and Development, vol. 32, no. 4, pp. 502–513, 1988.

[42] W. H. Teh and C. G. Smith, "Fabrication of quasi-three-dimensional micro/nanomechanical components using electron beam cross-linked poly (methyl methacrylate) resist," Journal of Vacuum Science & Technology B: Microelectronics and Nanometer Structures Processing, Measurement, and Phenomena, vol. 21, no. 6, pp. 3007–3011, 2003. [Online]. Available: https://avs.scitation.org/doi/abs/10.1116/1.1629290

[43] R. Nanofabrication, "Raith150 two," 2019. [Online]. Available: https://www.raith.com/products/raith150-two.html

[44] Janis, "He-3-svsd insert - standard sample loading, sample in vacuum for storage dewar," 2019. [Online]. Available: https://www.janis.com/Products/productsoverview/He-3Systems/HE-3-SVSDUltraLowTemperatureCryostat.aspx#

[45] F. Pobell, "Matter and methods at low temperatures," Springer-Verlag, Berlin, 1992.

[46] "Model 1211 current preamplifier," DL Instruments. [Online]. Available: http://dlinstruments.com/wp-content/uploads/2013/04/1211.pdf

[47] M. Steinacher, "Low noise/high stability i to v converter sp983 with lsk389a," Physics Basel, 2014. [Online]. Available: https://www.physik.unibas.ch/fileadmin/user_upload/physik-unibas-ch/02_Department/04_Infrastructure_Services/Electronics_Lab/LNHS_IV_Converter_SP983_Datasheet_LSK389A_1_2.pdf

[48] ——, "Low noise/high stability i to v converter sp983 with if3602," Physics Basel, 2014. [Online]. Available: https://www.physik.unibas.ch/fileadmin/user_upload/physik-unibas-ch/02_Department/04_Infrastructure_Services/Electronics_Lab/LNHS_IV_Converter_SP983_Datasheet_IF3602_1_2.pdf

[49] I. C. Sampaio, "Electron optics in a parabolic cavity with two quantum point contacts," Master thesis, Department of Physics, Freie Universität Berlin, 2018.

[50] P. Drude, "Zur elektronentheorie der metalle," Annalen der Physik, vol. 306, no. 3, pp. 566–613, 1900. [Online]. Available: https://onlinelibrary.wiley.com/doi/abs/10.1002/andp.19003060312

[51] R. Landauer, "Spatial variation of currents and fields due to localized scatterers in metallic conduction," IBM Journal of Research and Development, vol. 1, no. 3, pp. 223–231, 1957.

[52] W. Walukiewicz, H. E. Ruda, J. Lagowski, and H. C. Gatos, "Electron mobility in modulation-doped heterostructures," Phys. Rev. B, vol. 30, pp. 4571–4582, Oct 1984. [Online]. Available: https://link.aps.org/doi/10.1103/PhysRevB.30.4571

[53] B. J. van Wees, H. van Houten, C. W. J. Beenakker, J. G. Williamson, L. P. Kouwenhoven, D. van der Marel, and C. T. Foxon, "Quantized conductance of point contacts in a two-dimensional electron gas," Phys. Rev. Lett., vol. 60, pp. 848–850, Feb 1988. [Online]. Available: https://link.aps.org/doi/10.1103/PhysRevLett.60.848

[54] Y. Aharonov and D. Bohm, "Significance of electromagnetic potentials in the quantum theory," Phys. Rev., vol. 115, pp. 485–491, Aug 1959. [Online]. Available: https://link.aps.org/doi/10.1103/PhysRev.115.485

[55] B. L. Altshuler, D. Khmel'nitzkii, A. I. Larkin, and P. A. Lee, "Magnetoresistance and hall effect in a disordered two-dimensional electron gas," Phys. Rev. B, vol. 22, pp. 5142–5153, Dec 1980. [Online]. Available: https://link.aps.org/doi/10.1103/PhysRevB.22.5142

[56] P. A. Lee and A. D. Stone, "Universal conductance fluctuations in metals," Phys. Rev. Lett., vol. 55, pp. 1622–1625, Oct 1985. [Online]. Available: https://link.aps.org/doi/10.1103/PhysRevLett.55.1622

[57] A. Yacoby, U. Sivan, C. P. Umbach, and J. M. Hong, "Interference and dephasing by electron-electron interaction on length scales shorter than the elastic mean free path," Phys. Rev. Lett., vol. 66, pp. 1938–1941, Apr 1991. [Online]. Available: http://link.aps.org/doi/10.1103/PhysRevLett.66.1938

[58] C. G. Smith, M. Pepper, H. Ahmed, J. E. F. Frost, D. G. Hasko, R. Newbury, D. C. Peacock, D. A. Ritchie, and G. A. C. Jones, "Fabry-perot interferometry with electron waves," Journal of Physics: Condensed Matter, vol. 1, no. 45, pp. 9035–9044, nov 1989. [Online]. Available: https://doi.org/10.1088%2F0953-8984%2F1%2F45%2F026

[59] J. A. Katine, M. A. Eriksson, A. S. Adourian, R. M. Westervelt, J. D. Edwards, A. Lupu-Sax, E. J. Heller, K. L. Campman, and A. C. Gossard, "Point contact conductance of an open resonator," Phys. Rev. Lett., vol. 79, pp. 4806–4809, Dec 1997. [Online]. Available: https://link.aps.org/doi/10.1103/PhysRevLett.79.4806

[60] M. P. Jura, M. A. Topinka, M. Grobis, L. N. Pfeiffer, K. W. West, and D. Goldhaber-Gordon, "Electron interferometer formed with a scanning probe tip and quantum point contact," Phys. Rev. B, vol. 80, p. 041303, Jul 2009. [Online]. Available: https://link.aps.org/doi/10.1103/PhysRevB.80.041303

[61] A. Mittal, R. Wheeler, M. Keller, D. Prober, and R. Sacks, "Electron-phonon scattering rates in gaas/algaas 2deg samples below 0.5 k," Surface Science, vol. 361-362, pp. 537 – 541, 1996. [Online]. Available: http://www.sciencedirect.com/science/article/pii/0039602896004645

[62] J. J. Lin and J. P. Bird, "Recent experimental studies of electron dephasing in metal and semiconductor mesoscopic structures," Journal of Physics: Condensed Matter, vol. 14, no. 18, pp. R501–R596, apr 2002. [Online]. Available: https://doi.org/10.1088%2F0953-8984%2F14%2F18%2F201

[63] A. V. Chaplik, "Energy spectrum and electron scattering processes in inversion layers," SOVIET PHYSICS JETP, vol. 33, pp. 997–1000, Nov 1971. [Online]. Available: http://www.jetp.ac.ru/cgi-bin/dn/e_033_05_0997.pdf

[64] G. F. Giuliani and J. J. Quinn, "Lifetime of a quasiparticle in a two-dimensional electron gas," Phys. Rev. B, vol. 26, pp. 4421–4428, Oct 1982. [Online]. Available: https://link.aps.org/doi/10.1103/PhysRevB.26.4421

[65] B. ALTSHULER and A. ARONOV, "Chapter 1 - electron–electron interaction in disordered conductors," vol. 10, pp. 1 – 153, 1985. [Online]. Available: http://www.sciencedirect.com/science/article/pii/B9780444869166500077

[66] K. K. Choi, D. C. Tsui, and K. Alavi, "Dephasing time and one-dimensional localization of two-dimensional electrons in GaAs/al$_x$ga$_{1-x}$As heterostructures," Phys. Rev. B, vol. 36, pp. 7751–7754, Nov 1987. [Online]. Available: https://link.aps.org/doi/10.1103/PhysRevB.36.7751

[67] S. Q. Murphy, J. P. Eisenstein, L. N. Pfeiffer, and K. W. West, "Lifetime of two-dimensional electrons measured by tunneling spectroscopy," Phys. Rev. B, vol. 52, pp. 14 825–14 828, Nov 1995. [Online]. Available: https://link.aps.org/doi/10.1103/PhysRevB.52.14825

[68] S. Datta, Electronic Transport in Mesoscopic Systems, ser. Cambridge Studies in Semiconductor Physics and Microelectronic Engineering. Cambridge University Press, 1995.

[69] R. A. Jalabert, H. U. Baranger, and A. D. Stone, "Conductance fluctuations in the ballistic regime: A probe of quantum chaos?" Phys. Rev. Lett., vol. 65, pp. 2442–2445, Nov 1990. [Online]. Available: https://link.aps.org/doi/10.1103/PhysRevLett.65.2442

[70] C. M. Marcus, A. J. Rimberg, R. M. Westervelt, P. F. Hopkins, and A. C. Gossard, "Conductance fluctuations and chaotic scattering in ballistic microstructures," Phys. Rev. Lett., vol. 69, pp. 506–509, Jul 1992. [Online]. Available: https://link.aps.org/doi/10.1103/PhysRevLett.69.506

[71] M. J. Berry, J. H. Baskey, R. M. Westervelt, and A. C. Gossard, "Coherent electronic backscattering in ballistic microstructures," Phys. Rev. B, vol. 50, pp. 8857–8860, Sep 1994. [Online]. Available: https://link.aps.org/doi/10.1103/PhysRevB.50.8857

[72] M. J. Berry, J. A. Katine, R. M. Westervelt, and A. C. Gossard, "Influence of shape on electron transport in ballistic quantum dots," Phys. Rev. B, vol. 50, pp. 17 721–17 724, Dec 1994. [Online]. Available: https://link.aps.org/doi/10.1103/PhysRevB.50.17721

[73] Chan, Clarke, Marcus, Campman, and Gossard, "Ballistic conductance fluctuations in shape space." Physical review letters, vol. 74 19, pp. 3876–3879, 1995.

[74] K.-F. Berggren and M. Pepper, "Electrons in one dimension," Philosophical Transactions of the Royal Society A: Mathematical, Physical and Engineering Sciences, vol. 368, no. 1914, pp. 1141–1162, 2010. [Online]. Available: https://royalsocietypublishing.org/doi/abs/10.1098/rsta.2009.0226

[75] T. Rejec and Y. Meir, "Magnetic impurity formation in quantum point contacts," Nature, vol. 442, no. 7105, p. 900–903, 2006. [Online]. Available: https://www.nature.com/articles/nature05054

[76] E. J. Koop, A. I. Lerescu, J. Liu, B. J. van Wees, D. Reuter, A. D. Wieck, and C. H. van der Wal, "The influence of device geometry on many-body effects in quantum point contacts: Signatures of the 0.7 anomaly, exchange and kondo," Journal of Superconductivity and Novel Magnetism, vol. 20, no. 6, p. 433–441, 2007. [Online]. Available: https://link.springer.com/article/10.1007/s10948-007-0289-5

[77] J. Heyder, F. Bauer, E. Schubert, D. Borowsky, D. Schuh, W. Wegscheider, J. von Delft, and S. Ludwig, "Relation between the 0.7 anomaly and the kondo effect: Geometric crossover between a quantum point contact and a kondo quantum dot," Phys. Rev. B, vol. 92, p. 195401, Nov 2015. [Online]. Available: http://link.aps.org/doi/10.1103/PhysRevB.92.195401

[78] J. Freudenfeld, M. Geier, V. Umansky, P. W. Brouwer, and S. Ludwig, "Coherent electron optics with ballistically coupled quantum point contacts," Phys. Rev. Lett., vol. 125, issue 10, p. 107701, Sep 2020. [Online]. Available: https://doi.org/10.1103/PhysRevLett.125.107701

[79] R. Taboryski, A. Kristensen, C. B. Sørensen, and P. E. Lindelof, "Conductance-quantization broadening mechanisms in quantum point contacts," Phys. Rev. B, vol. 51, pp. 2282–2286, Jan 1995. [Online]. Available: https://link.aps.org/doi/10.1103/PhysRevB.51.2282

[80] K. J. Thomas, J. T. Nicholls, N. J. Appleyard, M. Y. Simmons, M. Pepper, D. R. Mace, W. R. Tribe, and D. A. Ritchie, "Interaction effects in a one-dimensional constriction," Phys. Rev. B, vol. 58, pp. 4846–4852, Aug 1998. [Online]. Available: https://link.aps.org/doi/10.1103/PhysRevB.58.4846

[81] W. Hew, K. Thomas, I. Farrer, D. Anderson, D. Ritchie, and M. Pepper, "Tuning the confinement strength in a split-gate quantum wire," Physica E: Low-dimensional Systems and Nanostructures, vol. 40, no. 5, pp. 1645 – 1647, 2008. [Online]. Available: http://www.sciencedirect.com/science/article/pii/S1386947707006364

[82] C. Rössler, S. Baer, E. de Wiljes, P.-L. Ardelt, T. Ihn, K. Ensslin, C. Reichl, and W. Wegscheider, "Transport properties of clean quantum point contacts," New Journal of Physics, vol. 13, no. 11, p. 113006, nov 2011. [Online]. Available: https://iopscience.iop.org/article/10.1088/1367-2630/13/11/113006

[83] A. M. Burke, O. Klochan, I. Farrer, D. A. Ritchie, A. R. Hamilton, and A. P. Micolich, "Extreme sensitivity of the spin-splitting and 0.7 anomaly to confining potential in one-dimensional nanoelectronic devices," Nano Lett., vol. 12, no. 9, pp. 4495–4502, Sep. 2012. [Online]. Available: https://pubs.acs.org/doi/abs/10.1021/nl301566d

[84] M. Büttiker, "Quantized transmission of a saddle-point constriction," Phys. Rev. B, vol. 41, pp. 7906–7909, Apr 1990. [Online]. Available: https://link.aps.org/doi/10.1103/PhysRevB.41.7906

[85] A. P. Micolich and U. Zülicke, "Tracking the energies of one-dimensional sub-band edges in quantum point contacts using dc conductance measurements," Journal of Physics: Condensed Matter, vol. 23, no. 36, p. 362201, aug 2011. [Online]. Available: https://iopscience.iop.org/article/10.1088/0953-8984/23/36/362201

[86] S. Laux, D. Frank, and F. Stern, "Quasi-one-dimensional electron states in a split-gate gaas/algaas heterostructure," Surface Science, vol. 196, no. 1, pp. 101 – 106, 1988. [Online]. Available: http://www.sciencedirect.com/science/article/pii/0039602888906711

[87] M. Geier, J. Freudenfeld, J. T. Silva, V. Umansky, D. Reuter, A. D. Wieck, P. W. Brouwer, and S. Ludwig, "Electrostatic potential shape of gate-defined quantum point contacts," Phys. Rev. B, vol. 101, issue 16, p. 165429, Apr 2020. [Online]. Available: https://doi.org/10.1103/PhysRevB.101.165429

[88] D. A. Wharam, U. Ekenberg, M. Pepper, D. G. Hasko, H. Ahmed, J. E. F. Frost, D. A. Ritchie, D. C. Peacock, and G. A. C. Jones, "Empirical relation between gate voltage and electrostatic potential in the one-dimensional electron gas of a split-gate device," Phys. Rev. B, vol. 39, pp. 6283–6286, Mar 1989. [Online]. Available: https://link.aps.org/doi/10.1103/PhysRevB.39.6283

[89] S. A. Self, "Focusing of spherical gaussian beams," Appl. Opt., vol. 22, no. 5, pp. 658–661, Mar 1983. [Online]. Available: http://ao.osa.org/abstract.cfm?URI=ao-22-5-658

[90] V. S. Tsoi, "Focusing of electrons in a metal by a transverse magnetic field," JETP Lett., vol. 19, p. 70, 1974. [Online]. Available: http://www.jetpletters.ac.ru/ps/1772/article_26958.shtml

[91] H. B. G. Casimir, "On onsager's principle of microscopic reversibility," Rev. Mod. Phys., vol. 17, pp. 343–350, Apr 1945. [Online]. Available: https://link.aps.org/doi/10.1103/RevModPhys.17.343

[92] D. Taubert, C. Tomaras, G. J. Schinner, H. P. Tranitz, W. Wegscheider, S. Kehrein, and S. Ludwig, "Relaxation of hot electrons in a degenerate two-dimensional electron system: Transition to one-dimensional scattering," Phys. Rev. B, vol. 83, p. 235404, Jun 2011. [Online]. Available: https://link.aps.org/doi/10.1103/PhysRevB.83.235404

[93] M. Büttiker, "Absence of backscattering in the quantum hall effect in multiprobe conductors," Phys. Rev. B, vol. 38, pp. 9375–9389, Nov 1988. [Online]. Available: https://link.aps.org/doi/10.1103/PhysRevB.38.9375

[94] R. J. Haug, A. H. MacDonald, P. Streda, and K. von Klitzing, "Quantized multichannel magnetotransport through a barrier in two dimensions," Phys. Rev. Lett., vol. 61, pp. 2797–2800, Dec 1988. [Online]. Available: https://link.aps.org/doi/10.1103/PhysRevLett.61.2797

[95] P. M. Asbeck, C.-P. Lee, and M. . F. Chang, "Piezoelectric effects in gaas fet's and their role in orientation-dependent device characteristics," IEEE Transactions on Electron Devices, vol. 31, no. 10, pp. 1377–1380, Oct 1984.

[96] T. Tanaka, H. Furukawa, and D. Ueda, "A gaas power fet with zero-temperature-coefficient," pp. 557–560, Dec 1997.

[97] F. Wakaya, J. Takahara, S. Takaoka, K. Murase, and K. Gamo, "Confinement potential in an asymmetrically biased quantum point contact," Japanese Journal of Applied Physics, vol. 35, no. Part 1, No. 2B, pp. 1329–1332, feb 1996. [Online]. Available: https://doi.org/10.1143%2Fjjap.35.1329

[98] V. Senz, T. Heinzel, T. Ihn, S. Lindemann, R. Held, K. Ensslin, W. Wegscheider, and M. Bichler, "Analysis of the temperature-dependent quantum point contact conductance in relation to the metal-insulator transition in two dimensions," Journal of Physics: Condensed Matter, vol. 13, no. 17, pp. 3831–3837, apr 2001. [Online]. Available: https://doi.org/10.1088%2F0953-8984%2F13%2F17%2F303

[99] A. M. Chang, H. U. Baranger, L. N. Pfeiffer, and K. W. West, "Weak localization in chaotic versus nonchaotic cavities: A striking difference in the line shape," Phys. Rev. Lett., vol. 73, pp. 2111–2114, Oct 1994. [Online]. Available: https://link.aps.org/doi/10.1103/PhysRevLett.73.2111

[100] Y. Lee, G. Faini, and D. Mailly, "Shape-averaged weak localization in chaotic and integrable ballistic cavities," Chaos, Solitons & Fractals, vol. 8, no. 7, pp. 1325 – 1336, 1997, chaos and Quantum Transport in Mesoscopic Cosmos. [Online]. Available: http://www.sciencedirect.com/science/article/pii/S0960077997000222

[101] H. U. Baranger, R. A. Jalabert, and A. D. Stone, "Weak localization and integrability in ballistic cavities," Physical Review Letters, vol. 70, no. 25, p. 3876–3879, Jun 1993. [Online]. Available: http://dx.doi.org/10.1103/PhysRevLett.70.3876

[102] T. Yalçinkaya and Y. Lai, "Chaotic scattering," Computers in Physics, vol. 9, no. 5, pp. 511–539, 1995. [Online]. Available: https://aip.scitation.org/doi/abs/10.1063/1.168549

[103] R. Blümel and U. Smilansky, "Classical irregular scattering and its quantum-mechanical implications," Phys. Rev. Lett., vol. 60, pp. 477–480, Feb 1988. [Online]. Available: https://link.aps.org/doi/10.1103/PhysRevLett.60.477

[104] P. Gaspard and S. A. Rice, "Scattering from a classically chaotic repellor," The Journal of Chemical Physics, vol. 90, no. 4, pp. 2225–2241, 1989. [Online]. Available: https://doi.org/10.1063/1.456017

[105] R. Taylor, M. Leadbeater, G. Whittington, P. Main, L. Eaves, S. Beaumont, I. McIntyre, S. Thoms, and C. Wilkinson, "Universal conductance fluctuations in the magnetoresistance of submicron-size n+-gaas wires and laterally confined n–gaas/(alga)as heterostructures," Surface Science, vol. 196, no. 1, pp. 52 – 58, 1988. [Online]. Available: http://www.sciencedirect.com/science/article/pii/0039602888906644

[106] W. A. Lin, J. B. Delos, and R. V. Jensen, "Order and chaos in semiconductor microstructures," Chaos: An Interdisciplinary Journal of Nonlinear Science, vol. 3, no. 4, pp. 655–664, 1993. [Online]. Available: https://doi.org/10.1063/1.165994

[107] A. Bäcker, "Eigenfunctions in chaotic quantum systems," Habilitationsschrift, Fakultät Mathematik und Naturwissenschaften der Technischen Universität Dresden, 2007. [Online]. Available: https://tud.qucosa.de/api/qucosa%3A23663/attachment/ATT-0/

[108] P. G. de Gennes and M. Tinkham, "Magnetic behavior of very small superconducting particles," Physics Physique Fizika, vol. 1, pp. 107–126, Sep 1964. [Online]. Available: https://link.aps.org/doi/10.1103/PhysicsPhysiqueFizika.1.107

[109] C. W. J. Beenakker and H. van Houten, "Boundary scattering and weak localization of electrons in a magnetic field," Phys. Rev. B, vol. 38, pp. 3232–3240, Aug 1988. [Online]. Available: https://link.aps.org/doi/10.1103/PhysRevB.38.3232

[110] K. Aidala, R. Parrott, T. Kramer, E. Heller, R. Westervelt, M. Hanson, and A. Gossard, "Imaging magnetic focusing of coherent electron waves," Nature Physics, vol. 3, pp. 464–468, 2007. [Online]. Available: https://doi.org/10.1038/nphys628

[111] T. Stegmann, D. E. Wolf, and A. Lorke, "Magnetotransport along a boundary: from coherent electron focusing to edge channel transport," New Journal of Physics, vol. 15, no. 11, p. 113047, nov 2013. [Online]. Available: https://doi.org/10.1088%2F1367-2630%2F15%2F11%2F113047

[112] D. S. Duncan, M. A. Topinka, R. M. Westervelt, K. D. Maranowski, and A. C. Gossard, "Aharonov-bohm phase shift in an open electron resonator," Phys. Rev. B, vol. 64, p. 033310, Jun 2001. [Online]. Available: https://link.aps.org/doi/10.1103/PhysRevB.64.033310

[113] R. C. Ashoori, "Electrons in artificial atoms," Nature, vol. 379, Feb 1995. [Online]. Available: https://doi.org/10.1038/379413a0

[114] A. Dasgupta, D. Roy, and R. Bhattacharya, "Simple systematics in the energy eigenvalues of quantum anharmonic oscillators," Journal of Physics A: Mathematical and Theoretical, vol. 40, no. 4, p. 773, 2007. [Online]. Available: http://stacks.iop.org/1751-8121/40/i=4/a=013

Acknowlegment

Danke an:

Stefan, für die über fünf Jahre lange Zusammenarbeit und dafür, dass ich das spannende Projekt meiner Masterarbeit in München auch bei Dir als Doktorand in Berlin fortsetzen durfte.

Piet und Max, für Euren Input aus der Theorie und die sehr produktive Zusammenarbeit, welche für mich extrem lehrreich war.

Das Paul-Drude-Institut, für die Gelegenheit zur Erstellung meiner Dissertation.

Meine Kollegen/Bürogenossen Sergey, Nick, Hannes, Ludwig, Carl-Johan, Ian, Yefei, Johannes, Jan, Irene, Filipp und Jorge, für die gegenseitige Unterstützung in allen Bereichen, die nötige Portion Humor und kultige Abende zwischen "the sad place", Augustiner und Hausvogteiplatz.

Angela Riedel, Kerstin Ehrensack sowie die PDI-Werkstatt um Jörg Pfeiffer, für die ständige Hilfsbereitschaft, die technische Unterstützung und Ihre freundliche, lockere Art.

Holger Grahn, für das immer offene Ohr und die Geduld bei der PRL-Veröffentlichung.

Sebastian Meister, für die technische Unterstützung bei der Elektronenstrahllithographie sowie Sander Rauwerdink, Walid Anders und Werner Seidel für die Hilfe bei der optischen Lithographie.

Meine Münchner Jungs, für die vielen Besuche und gemeinsamen Wochenenden/Urlaube, die für die nötige Abwechslung gesorgt haben.

Meine Berliner Fraktion um Lena, Claire und Ben für die Unterstützung und schöne Zeit im wilden Berlin, sowie an meine Fußballkollegen von SG Rotation, welche für den sportlichen Ausgleich gesorgt haben.

Nicht zuletzt meine Familie, die mir durch die Unterstützung das Studium und die Doktorarbeit ermöglicht bzw. stark erleichtert hat, sowie für die immer schöne und harmonische gemeinsame Zeit in München, Berlin und Frankreich.